# Experimental and numerical characterization of functional properties of sand molds produced by additive manufacturing (3D printing by jet binding) in a fast foundr

Saptarshee Mitra

▶ **To cite this version:**

Saptarshee Mitra. Experimental and numerical characterization of functional properties of sand molds produced by additive manufacturing (3D printing by jet binding) in a fast foundr. Other [cond-mat.other]. Ecole nationale supérieure d'arts et métiers - ENSAM, 2019. English. NNT : 2019ENAM0043 . tel-02466819v2

**HAL Id: tel-02466819**

**https://pastel.hal.science/tel-02466819v2**

Submitted on 6 Feb 2020

**HAL** is a multi-disciplinary open access archive for the deposit and dissemination of scientific research documents, whether they are published or not. The documents may come from teaching and research institutions in France or abroad, or from public or private research centers.

L'archive ouverte pluridisciplinaire **HAL**, est destinée au dépôt et à la diffusion de documents scientifiques de niveau recherche, publiés ou non, émanant des établissements d'enseignement et de recherche français ou étrangers, des laboratoires publics ou privés.

HESAM UNIVERSITÉ

Arts et Métiers Sciences et Technologies

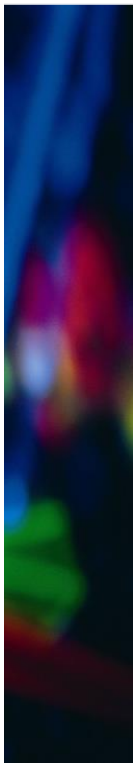

2019-ENAM-0043

École doctorale n° 432 : Sciences des Métiers de l'ingénieur

# Doctorat

## T H È S E

**pour obtenir le grade de docteur délivré par**

## l'École Nationale Supérieure d'Arts et Métiers

**Spécialité " Mécanique-matériaux "**

*présentée et soutenue publiquement par*

**Saptarshee MITRA**

le 15 novembre 2019

# Experimental and numerical characterization of functional properties of sand molds produced by additive manufacturing (3D printing by binder-jetting) in a fast foundry

Directeur de thèse : **Mohamed EL MANSORI**
Co-encadrement de la thèse : **Antonio RODRÍGUEZ DE CASTRO**
Co-encadrement de la thèse : **Marius COSTIN**

**Jury**

| | |
|---|---|
| **M. Michel BELLET**, Professeur des Universités, CEMEF, Mines ParisTech | Président |
| **M. Liam BLUNT**, Professeur des Universités, CPT, University of Huddersfield, England | Rapporteur |
| **M. Jean-Yves HASCOET**, Professeur des Universités, GeM, Ecole Centrale Nantes | Rapporteur |
| **M. Ismail LAZOGLU**, Professeur des Universités, MARC, Koc University, Turkey | Examinateur |
| **M. Mohamed EL MANSORI**, Professeur des Universités, MSMP-EA-7350, Arts et Métiers ParisTech | Examinateur |
| **M. Antonio RODRÍGUEZ DE CASTRO**, Maître de Conférences, Arts et Métiers ParisTech | Examinateur |
| **M. Marius COSTIN**, Researcher in NDT, Institute List – CEA Saclay | Examinateur |

T H È S E

**Arts et Métiers - Campus de Aix-en-Provence**
**Laboratoire MSMP (EA-7350)**

# Abstract:

Nowadays, traditionally manufactured sand molds and cores for metal casting are being progressively replaced by additively processed sand molds in aerospace/automotive industry, facilitating the production of quality cast parts with complex shapes. The type of additive manufacturing technology used to manufacture 3DP parts in foundries is known as powder-binder-jetting process. In this technology, the molds are produced without the use of any kind of additive tools and in a completely automated way using the layer based construction method. One of the most popular binder systems used in the manufacturing of 3DP mold is a furan-based resin binder, which holds the grain particles together. Their amounts and ratios can influence significantly the 3D printed mold properties, affecting casting quality. Therefore, it is essential to characterize the effects process parameters on the functionality of the 3DP molds. In the present work, the mechanical behavior of 3DP sand molds with varying printing process parameters was first investigated, followed by mass transport properties. To do so, a series of three-point bending strength tests, density measurements, porosity measurements and permeability tests were performed on the 3DP molds. Furthermore, the influence of time, temperature and binder volume fraction on the mechanical and mass transport properties was also investigated. Advanced modelling of the pore space was performed by using the reconstructed images provided by X-ray computed tomography, following different steps: X-ray CT scanning of small 3DP mold specimen, 3D volumetric reconstruction of data, numerical simulations for the prediction of permeability from the reconstructed volume, and pore network modelling for the determination of the pore size distribution. Experiments were also designed to investigate the 3D printed molds in terms of mold erosion during metal casting, in order to select the molding parameters to print 3D printed parts not only with good mechanical and mass transport properties but also to minimize the mold erosion during metal casting. Furthermore, a reverse engineering method for determination of the erosion resistance of sand molds has been established, to study the volume of the eroded surface.



***Keywords:*** Additive manufacturing; Binder jetting; 3D-printed casting sand mold; Casting; 3-Point bending strength; Permeability; Pore Size Distribution; Throat Size Distribution; X-ray tomography; Numerical simulations; Pore network modelling; Mold Erosion; Cast iron;

# Résumé:

Les techniques traditionnelles pour la production des moules et des noyaux en sable utilisés en fonderie pour la coulée de métaux sont actuellement en cours de remplacement par des méthodes de fabrication additive, afin d'aider l'industrie aérospatiale/automobile à fabriquer des pièces de forme complexe d'une manière pratique. Le but de ce travail de recherche est d'étudier les propriétés fonctionnelles des moules imprimés en 3D utilisés lors de la coulée des pièces de forme complexe pour des applications d'ingénierie. Premièrement, le comportement mécanique des moules en sables imprimés en 3D a été analysé et caractérisé pour de différents paramètres du processus d'impression. Ensuite, les propriétés mécaniques et de transport de masse des moules en sable 3DP ont été étudiées. Les pièces imprimées en 3D pour la fonderie sont souvent fabriquées avec un type de technologie de fabrication additive appelé « *powder-binder-jetting process* » (processus de projection de liant de poudre). Des mesures sur trois points de la force de flexion, la densité, la porosité et la perméabilité, ont été effectués sur les moules fabriqués avec la technologie additive. En plus, l'influence de la température et de la fraction volumique du liant sur les propriétés mécaniques et de transport de masse a également été étudiée. Par ailleurs, la perméabilité des moules en sable imprimé a aussi été caractérisée par micro-tomographie de rayons X, permettant la modélisation avancée de la microstructure poreuse en suivant plusieurs étapes : 1) tomodensitométrie de petits échantillons de moules 3DP, 2) reconstruction volumétrique 3D de données, 3) simulation numérique pour la prédiction de la perméabilité à partir de volumes reconstruits et 4) modélisation du réseau de pores pour déterminer la distribution de la taille des pores et des constrictions. Des expériences ont également été conçues pour étudier les moules imprimés en 3D en termes de leur érosion lors de la coulée des métaux. Cela a permis d'identifier les paramètres optimaux du procédé d'impression 3D des moules, non seulement en termes de leurs propriétés mécaniques et de transport de masse, mais aussi pour minimiser l'érosion du moule durant la coulée métallique. Une méthode de détermination de la résistance à l'érosion des moules en sable a également été proposée, sur la base de la mesure du volume de la surface érodée à l'aide d'une technique d'ingénierie inverse moderne.



***Mots clés:*** Fonderie; Fabrication additive; Moules sable impression 3D; Coulée métallique; Flexion trois points; Perméabilité; Distribution de tailles de grains; Tomographie par rayons X; Simulations numériques; Distribution de tailles de pores; Modélisation réseau de pores; Mold Erosion; Fonte;

*“Dedication, hard work all the time, and belief.” – Cristiano Ronaldo*

# Acknowledgments

Undertaking this PhD has been a truly life-changing experience for me and it would not have been possible to do without the support and guidance that I received from many people.

Firstly, I would like to express my sincere gratitude to my thesis director Prof. Mohamed EL MANSORI, and my supervisors, Dr. Antonio RODRÍGUEZ DE CASTRO and Dr. Marius COSTIN for allowing me to conduct this research under their guidance. I am especially grateful for the confidence, motivation and the freedom they gave me to do this work. Their constant encouragement and advice helped me at all the time of research, publiclations and in writing of this thesis, despite their busy agenda. Without a coherent and illuminating instruction, this thesis would not have reached its present form. I could not have imagined having a better advisor and mentor for my Ph.D study.

Besides my advisors, I would like to thank the members of jury: Prof. Michel BELLET, Prof. Liam BLUNT, Prof. Jean-Yves HASCOET and Prof. Ismail LAZOGLU, for accepting to review my manuscript and to participate in the defense of this thesis. I express my gratitude to the members of the jury for their insightful comments and encouragement, but also for the interesting questions which incented me to widen my research from various perspectives.

I wish to express my gratitude to Dr. Antonio RODRÍGUEZ DE CASTRO, who helped me to learn techniques in the characterization of gas flow through porous media, during my stay in Laboratory MSMP - Arts et Métiers ParisTech - Châlons-en-Champagne, France. I am also very grateful to Dr. Marius COSTIN who kindly helped me with a great efficiency for the Non-Destructive characterization of 3DP sand mold using X-Ray CT, to extract information at different scales, including micro-scale, during my stay in CEA-LIST - Department of Imaging & Simulation for Non-Destructive Testing - Gif-sur-Yvette, France.

I extend my sincere thanks to all members of the MSMP, and all those who contributed directly or indirectly to the dissertation. I also express my gratitude to all these experts with whom I have had the opportunity to discuss and learn: Dr. Tharmalingam SIVARUPAN, for sharing his expertise in 3D printing technology of sand mold; Dr. Agnès FABRE and Dr. Marie BEDEL, for generously sharing their expertise in teaching students and for their helpful suggestions whenever I had problems during practical sessions for 1st year Engineering students; Mr. Jérémie BOURGEOIS, Mr. Julien NEGRE, and Mr. Wayan GERAUD, for their assistance in the 3D printing of sand specimens and during metal casting operations; Mr.

Fabrice GUITTONNEAU, for his assistance during the analysis of 3D printed specimens using electron microscope.

I also want to give all my gratitude to my family, and especially to my parents, whose love and support have been a constant motivation. Without their support, I would never finish this thesis and I would never find the courage to overcome all the difficulties during this work. My thanks go to my grandmother Mrs. Manjusree Mitra, my father Capt. Prabir Kumar MITRA, my mother Mrs. Keya MITRA and my brother Mr. Rajarshee MITRA for their confidence and their love during all these years. I would like to extend my warmest thanks and appreciation to my beloved fiancée, Miss. Karima TIBRAYEM. If this work has sometimes prevented us from sharing important moments of life, know that I never stopped thinking about you.

Furthermore, a special thanks to all my doctoral colleagues, Dr. Benjamin GUILLOT, Dr. Hazem MUBARAK, Dr. Hadrien WEIL, Dr. Maxime GELINEAU, Dr. Clément MAUDUIT, Dr. Antonin SANITAS, Dr. François GODET, Dr. Nicolas SPITZ, Mr. Mohamed KBIBOU, Mr. Hugo TRYLA, Mr. Hassan CHOUHAD and Mme. Lisa GERMAIN, who have constantly encouraged me during these years in the laboratory.

Last but not the least, I also wish to thank Mme. Grazyna CAUQUIL, Mme. Laurence COMBARIEU, Mme. Marie FERNANDEZ and Mme. Celine THOMAS for helping me to resolve administrative issues.

# TABLE OF CONTENTS

**List of Figures…….....xi**

**List of Tables……...xvii**

**1. GENERAL INTRODUCTION ..... 1**

1.1 Research Objectives ..... 3

1.1.1 Research Question 1: ..... 3

1.1.2 Research Question 2 ..... 4

1.1.3 Research Question 3: ..... 4

1.1.4 Research Question 4: ..... 5

1.1.5 Research Question 5: ..... 6

1.2 Thesis Roadmap ..... 7

**2. STATE OF ART ..... 9**

2.1 Casting processes ..... 9

2.2 3D Printing technology in casting applications ..... 11

2.3 Powder Binder Jetting (PBJ) ..... 13

2.4 Process characteristics and physics involved in the process ..... 16

2.4.1 Layering of Powdered Material, Vertical Dimensional Control ..... 16

2.4.2 Interaction of a single droplet of binder with the particle ..... 16

2.5 Mold fabrication via Powder Binder Jetting technology ..... 17

2.5.1 Powder Bed Compaction ..... 17

2.5.2 Print-head characteristics ..... 18

2.5.3 Binder selection ..... 18

2.6 Influence of process parameters on the quality of 3DP molds ..... 20

2.6.1 Effect of grains size and shape ..... 20

2.6.2 Effect of binder on mold properties ..... 21

2.6.3 Effect of curing time ..... 23

2.7 Modelling Powder binder jetting process ..... 24

**3. EXPERIMENTAL CHARACTERIZATION OF 3DP MOLDS FOR FOUNDRY PURPOSES ..... 25**

3.1 Optimum print orientation of 3DP molds ..... 25

3.1.1 Introduction and Objective ..... 25

3.1.2 Printing procedure ..... 26

3.1.3 Printing Parameters ..... 28
3.1.4 Heat treatment and natural curing ..... 29
3.1.5 Results ..... 30
3.1.5.1 Relative water content ..... 30
3.1.5.2 Loss on Ignition ..... 30
3.1.5.3 3PB Strength ..... 31
3.1.6 Conclusions ..... 34
3.2 Effect of curing process parameters on 3DP sand mold ..... 34
3.2.1 Introduction and Objective ..... 34
3.2.2 Materials ..... 35
3.2.3 Design of ageing mechanism experiment ..... 36
3.2.4 Printing procedure and parameters ..... 36
3.2.5 Curing process ..... 41
3.2.6 Density and porosity ..... 42
3.2.7 Loss on Ignition (LOI) testing ..... 43
3.2.8 Three-point Bending test ..... 44
3.2.9 Gas permeability test ..... 45
3.2.10 Results ..... 46
3.2.10.1 Mass loss ..... 46
3.2.10.2 3PB strength ..... 47
3.2.10.3 Permeability ..... 48
3.2.11 Discussion ..... 49
3.2.12 Conclusion ..... 53
3.3 Effect of Binder percent on 3DP sand mold ..... 54
3.3.1 Introduction and Objective ..... 54
3.3.2 Materials ..... 55
3.3.3 3D Printing stage ..... 55
3.3.4 Curing stages ..... 57
3.3.5 Loss on Ignition tests ..... 59
3.3.6 Porosity measurements ..... 60
3.3.7 Three-Point bending tests ..... 61
3.3.8 Permeability tests ..... 61
3.3.9 Results and discussion ..... 66
3.3.9.1 Evolution of binder content during curing as a function of the initial binder content 66
3.3.9.2 3PB strength as a function of the initial binder content for different curing conditions ..... 68

3.3.9.3 Permeability as a function of the initial binder content for different curing conditions ..... 72
3.3.10 Conclusion ..... 78
**4. PERMEABILITY CHARACTERIZATION OF 3DP MOLDS USING X-RAY CT AND ADVANCED POROSITY MODELLING ..... 80**
4.1 Introduction ..... 80
4.2 Scanning Electron Microscope (SEM): General functioning ..... 81
4.3 Basic aspects in X-ray micro-computed tomography (X-ray µ-CT) ..... 82
4.4 Processing reconstructed images ..... 84
4.5 Experimental setup ..... 86
4.6 Analysis of tomographic images of 3DP mold ..... 88
4.6.1 Introduction ..... 88
4.6.2 Grain Morphology: Grain Size Distribution (GSD) and Sphericity ..... 90
4.6.2.1 Analysis method ..... 90
4.6.2.2 Results and discussion ..... 94
4.6.3 Direct pore scale modelling ..... 96
4.6.3.1 Introduction ..... 96
4.6.3.2 Lattice Boltzmann: Theory and Implementation ..... 97
4.6.3.3 Calculation of permeability using LBM ..... 104
4.6.3.4 Implementation of LBM to predict permeability of 3DP sand mold ..... 105
4.6.3.5 Experimental approach: Local porosity and permeability ..... 109
4.6.3.6 Results and discussion ..... 110
4.6.4 Pore scale modelling with pore network models ..... 114
4.6.4.1 Introduction ..... 114
4.6.4.2 Chord Length distribution ..... 117
4.6.4.3 Pore network extraction from µ-CT images: pore and throat size distributions ..... 122
4.6.4.4 Results and discussion ..... 125
4.7 Model efficiency ..... 132
4.8 Conclussion ..... 134
**5. MELT INTERACTION WITH 3DP MOLD SURFACE ..... 136**
5.1 Introduction ..... 136
5.2 Experimental design and Methodology ..... 137
5.3 Results and discussion ..... 142
5.4 Conclusion ..... 148
**6. CONCLUSIONS AND FUTURE PERSPECTIVES ..... 149**
6.1 Summary ..... 149

6.2 Conclusion ..... 149
6.3 Perspectives ..... 150
**7. BIBLIOGRAPHY ..... 152**
**8. Annex : Terminology ..... 165**

## List of Figures:

Figure 1 (a) Ancient Greece; bronze statue casting circa 450BC, (b) Iron works in early Europe: cast-iron cannons from England circa 1543 [4] ..... 9

Figure 2. Traditional sand-casting process; (a) Assembled molds, (b) Pouring liquid metal and (c) final solidified casting without the riser. ..... 10

Figure 3. Schematic representation of particle binder bonding and resin ..... 13

Figure 4. Schematic representation of a 3D printer: (a) lowering the build platform, layering with material and (b) printing process using binder, (c) final part ..... 14

Figure 5. Powder binder jetting process ..... 15

Figure 6. (a) Simplified model of binder dropping of binder by print-head over powder bed, (b) an SEM image of particle binder bonding along with (c) a schematic representation of interaction of a droplet of binder with the particle. ..... 17

Figure 7. Binder categories ..... 19

Figure 8. Factors influencing mold properties ..... 20

Figure 9. Main Effect Plot of chemically bonded sand mold properties [27]. ..... 22

Figure 10. (a,b) The effect of furan resin content with curing time and temperature on tensile strength [66]; (c) Shrinkage and (d) hardness of cores with varying resin content [26]. ..... 23

Figure 11. Schematic representation for binder droplet spacing ..... 26

Figure 12. Schematic design of parts to be printed over job-box ..... 27

Figure 13. Schematic design (a) top view, and (b) side view of the 3DP box with the specimens inside. Each layer has 5 3DP bars with an angle difference of 137.508°; the golden angle ..... 28

Figure 14. 3DP Boxes that with the 3PB test bars inside (a,b,c,d), specimens for LOI test (e), 3DP bars printed with an angle difference of 137.508° ..... 29

Figure 15. Relative water content over curing time ..... 30

Figure 16. Loss on ignition over curing time ..... 31

Figure 17. 3PB strength over curing time ..... 32

Figure 18. 3PB strength over part printing position ..... 33

Figure 19. Grain size distribution ..... 35
Figure 20. Schematic design of printed specimen on Catia ..... 36
Figure 21. Schematic design of a Job-Box (NetFabb) ..... 37
Figure 22. 3D sand printer used in the present experiments ..... 37
Figure 23. Printing recipe on ExOne 3D printer ..... 38
Figure 24. 3D printed 3PB test bars and permeability specimens ..... 38
Figure 25. Effects of curing temperature and time on the precision of the sand samples ..... 40
Figure 26. Precision of the 3D printed samples ..... 41
Figure 27. KERN Laboratory precision balance ..... 43
Figure 28. Ovens used for accelerated curing ..... 43
Figure 29. LOI test crucible with(a) powdered 3DP specimens, (b) immediately after taking out of the oven at 900 °C and (c) after cooling it to 150 °C, before measuring the mass loss 44
Figure 30. Universal strength machine for the 3PB test [78], (a) front view and (b) bar dimensions ..... 45
Figure 31. Universal machine used for the gas permeability test[79] ..... 46
Figure 32. Critical effect of curing time and temperature on mass loss of specimens ..... 47
Figure 33. Critical effect of curing time and temperature on 3PB strength of specimens ..... 48
Figure 34. Permeability of the samples vs. curing time at different temperatures ..... 49
Figure 35. Furan binder chain reaction ..... 49
Figure 36. 3PB strength vs. mass loss for the three curing temperatures ..... 50
Figure 37. 3PB strength vs. curing time and temperatures ..... 51
Figure 38. Permeability vs. mass loss for the three curing temperatures ..... 52
Figure 39. Permeability vs. curing time and temperatures ..... 53
Figure 40. Scanning electron microscope (SEM) image of the 3DP sample, (a, b) zoom showing the resin bridges ..... 57
Figure 41. Samples heat treated inside oven for accelerated curing ..... 58
Figure 42. Heat-treated 3DP samples with 1.45% binder, (a,b) cylinders and (c,d) bars ..... 58

Figure 43. LOI test (a) 3DP samples, (b) immediately after taking out of the oven at 900 °C 60

Figure 44. Perm-meter setup ..... 65

Figure 45. Mass loss as a function of curing time for three curing temperatures ..... 67

Figure 46. Binder saturation vs porosity of specimens ..... 67

Figure 47. Variation of strength with binder, curing temperature and time ..... 68

Figure 48. Effect of curing parameters on 3PB strength ..... 69

Figure 49. SEM image of 3DP specimen showing resin bridges between particles ..... 70

Figure 50. Resin bonding bridge of adjacent sand particles ..... 71

Figure 51. SEM image of 3DP specimen showing cracking of resin bridges at 200°C ..... 72

Figure 52. Effect of binder content on f vs. $Q_m$ rate for uncured samples at 25°C ..... 73

Figure 53. Effect of curing time on the relationship between f and $Q_m$ at different temperatures and binder contents ..... 74

Figure 54. Relationship between apparent permeability and mass flow rate for uncured samples at 25°C ..... 76

Figure 55. Evaluation of the inertial effects for uncured samples at 25°C and a binder content of 1.02%: (a) Darcy's law fit. Black symbols represent experimental measurements. The red dashed line represents Darcy's law fit; (b) Forchheimer number at different flow rates. ..... 77

Figure 56. Variation of permeability with binder, curing temperature and time ..... 77

Figure 57. Variation of permeability with binder content, curing temperature and time ..... 78

Figure 58. Schematic representation of SEM ..... 81

Figure 59. Schematic representation of principle of X-ray tomography ..... 82

Figure 60. 3DP specimen ..... 83

Figure 61. (a) The projection profile of attenuated X-ray radiography through a 3DP specimen received by the detector and (b) Reconstructed pixel data of 3DP specimen ..... 83

Figure 62. Main steps of 3D image reconstruction ..... 83

Figure 63. Steps of image processing with Fiji-ImageJ, (a) cropped stack; (b) using median filter; (c) otsu's thresholding; (d) binary image ..... 85

Figure 64. (a) Cross section of raw image; (b) median filtered image of (a); (c) is binary image of (a); (d) is binary image of (b) ..... 86

Figure 65. Different views and schemes of the experimental X-ray µ-CT setup showing: (a) the robotic X-ray inspection platform, (b) a schematic design of the sample holder (c) the sample holder and (d) a zoom-in view including the dimensions of the sample ..... 87

Figure 66. Grain size distributions and sphericity ..... 94

Figure 67. Combined (a) grain size distribution for small grains and big grains, and (b) sphericity distribution ..... 95

Figure 68. (a) Examples of silica grain with different sphericity number in the BG specimen. (b) SEM image of a 3DP specimen, showing the silica grains ..... 95

Figure 69. Govering equations with LBM ..... 97

Figure 70. Streaming before and after propagation in lattice cells ..... 99

Figure 71. Diagram showing the velocity discretization in D2Q9 and D3Q19 lattice scheme 99

Figure 72. Images of different dimensions used to determine the Representative Volume Element (RVE) of the BGLB specimen. Pores are displayed in white and silica sand grains in black on the binary image. ..... 106

Figure 73. Representative volume element (RVE), for BGLB specimen ..... 108

Figure 74. Visualization of steps in conversion of a µ-CT image for velocity distribution simulation in the case of the SGHB specimen (200 voxels): (a) 2D slice of the binary volume and (b) converted image for simulation with pore space (dark blue pixel), grains (yellow pixel) and grain boundary interface (light blue pixel) where the bounce-back boundary condition is implemented. (c) Simulated velocity distribution through a cross-section. ..... 109

Figure 75. Velocity map in lattice units through specimens of, (a) 50, (b) 100, (c) 150, and (d) 200 voxel. (Warmer colors represent higher velocity) ..... 111

Figure 76. Effect of input geometry volume on the computed value of permeability ..... 113

Figure 77. Pores and throats identified by medial axis algorithm ..... 116

Figure 78. The clustering of overlapping maximal balls into families, where white arrows indicate the pore–throat chain [133] ..... 117

Figure 79. Binary images of the 3DP specimens (SGLB, SGHB, BGLB and BGHB) ..... 118

Figure 80. CLD for BGLB specimen ..... 119

Figure 81. CLD for BGHB specimen ..... 120

Figure 82. CLD for SGLB specimen ..... 121

Figure 83. CLD for SGHB specimen ..... 122

Figure 84. ALL specimens used for the pore network extraction ..... 123

Figure 85. X-ray µ-CT image for all specimens used for PNM ..... 124

Figure 86. Extracted pore network for (a) SGLB, (b) SGHB, (c) BGLB and (d) BGHB specimens ..... 126

Figure 87. Pore and throat size distribution ..... 127

Figure 88. Combined (high binder +low binder) pore size and throat size distribution for (a) small grains and (b) big grains ..... 127

Figure 89. Relationship between surface area and volume of all pores in all three samples . 128

Figure 90. Drainage curve ..... 130

Figure 91. Throat distribution ..... 131

Figure 92. Comparison of permeability for different methods ..... 138

Figure 93. Schematic design of mold erosion experiment ..... 138

Figure 94. Steps involved, (a) 3D printing of sand mold, (b) melting iron, (c) casting process and (d) eroded molded with the respective positioning of thermocouples ..... 139

Figure 95. Temperature as noted during casting by thermocouples ..... 139

Figure 96. Tested slabs as used to study the melt interaction with 3DP sand mold. (a) LB specimen, (b) cleaned LB specimen, (c) HB specimen and (d) cleaned HB specimen ..... 140

Figure 97. (a) Thermal deformation testing machine, and (b) zoomed view ..... 141

Figure 98. Temperature noted on the back part of testing slab during casting ..... 142

Figure 99. Cut section of the testing slabs, (a,b) zoomed view of the side section of interaction ..... 143

Figure 100. For LB specimen, (a) laser scanning of testing slabs, (b) cloud data points from scanned data, (c) meshing of cloud data, (d) surface generation and measuring deformation ..... 144

Figure 101. For HB specimen, (a) laser scanning of testing slabs, (b) cloud data points from scanned data, (c) meshing of cloud data, (d) surface generation and measuring deformation ..... 144

Figure 102. Bar specimens used form thermal deformation testing, (b) zoomed view of LB specimen, and (d) zoomed view of HB specimen ..... 146

Figure 103. Temperature as noted for the HB and LB specimens ..... 147

## List of Tables:

Table 1. Lists the publication/conference title, incorporated as chapters ..... 8

Table 2 The process parameters used for printing the specimens. ..... 28

Table 3. Printing process parameters used with ExOne S-Print furan machine..... 39

Table 4. Printing process parameters used with ExOne S-Print furan machine..... 56

Table 5. Experimental parameters..... 59

Table 6. All results for 3PB strength and permeability..... 74

Table 7. Results showing the pore connectivity and tortuosity..... 93

Table 8. Results from image analysis..... 96

Table 9. Results from permeability simulation ..... 112

Table 10. Results from pore network modelling..... 129

Table 11. Results from MIP ..... 131

Table 12. Permeability measured with different methods..... 133

Table 13. Results from laser scanned specimens ..... 146

Table 14. Results from thermal deformation test..... 147

# 1. GENERAL INTRODUCTION

Hybrid casting is an advanced additive mold manufacturing technique, in which the computer model design is integrated with 3D printing in order to fabricate sand molds to produce castings. This offers an excellent opportunity for foundry industries to rethink old/traditional metal casting approaches and to manufacture complex design using computer models. In hybrid casting, the molds are produced without the use of any kind of additive tools and in a completely automated way using the layer-based construction method. The 3D printer generates successive overlaying layers until the full mold is fabricated. The numerous advantages offered by this innovative casting process include a huge reduction in mold manufacturing time and the improved quality of metal castings. Besides, the absence of tooling costs makes this process particularly economical, and much complex geometry that cannot be manufactured using traditional sand casting can be reconsidered. 3D printers are generally faster, easier to use and cheaper than other add-on technologies. It is also possible to make foundry sand molds of extremely small dimensions and very thin parts. Modern foundry industries gradually use this Hybrid Casting technology because they provide ease of sand molding with good surface finish. The furan-based resin is one of the most popular binders used to hold the grain particles together in the manufacturing of 3DP molds. The amounts and ratios of furan binder can influence significantly the 3D printed mold properties resulting in altered casting quality. With rising importance on hybrid casting, there is a need to study and optimize the 3D printing process parameters, which affect the mold properties and have a major impact on the quality of casting.

The present PhD project focuses on the modeling of the 3DP technology to produce functional molds for metal casting in terms of stiffness and permeability. This is expected to assist the aerospace/automotive industry in the selection of the optimum process parameters allowing the minimization of the casting defects. The Low-Pressure-Sand-Casting (LPSC) platform of the Mechanics, Surfaces and Materials Processing (MSMP) laboratory was used to experimentally address these issues. In particular, the ExOne 3DP Machine provided valuable results for the study of the effect of 3DP process parameters (e.g., amount of binder / X-resolution of the Furan droplets, speed of the printer head, and compaction of the mold) on the functionalities of the molds. This work investigates the effects of aging time and temperature on the properties of 3DP at different binder contents, which will facilitate the selection of the optimum binder percent for a given cast product. Also, CEA LIST has several

X-ray imaging devices which were used to inspect the 3DP molds in order to find defects or other anomalies. A high-resolution computed tomography scanner was used to characterize small samples, which allowed in extracting structural information (i.e. the grain size and its distribution, porosities of the mold, etc.). The link between the structural properties of the printed molds and the influence of processing parameters, allowed in defining the functional rules for the design of sand molds.

| **Primary Research Objective** |
| --- |
| To define functional rules for the design of 3D printed sand molds |

The following research works were conducted:

- ✓ Understanding the effects of the process parameters used during 3D printing on the functionality of the molds (mainly binder content, recoating speed and grain size) and selecting a rigorous experimental method to characterize the mechanical strength and mass transport properties of the 3D printed mold.

- ✓ Characterizing the mechanical strength and permeability of the 3DP parts produced under different ageing conditions, in order to improve the understanding of the mechanisms controlling the curing stage.

- ✓ Characterizing the behavior of the 3DP molds through non-destructive volumetric image analysis (X-Ray tomography). Computation of permeability from numerical simulations performed on the obtained 3D digital images and comparison to experimental results.

- ✓ Studying the processes involved during the interaction of melt with the 3DP sand mold and measuring the volumetric erosion of mold by means of reverse engineering techniques.

## 1.1 Research Objectives

### 1.1.1 Research Question 1:

The Rapid Prototyping (RP) technology also termed as layered based manufacturing or additive fabrication has become a fast growing and ever-changing family of technologies. Various process parameters are involved in these technologies, such as build direction, printing orientation, recoating speed and binder droplet resolution. For a sand mold to be functional, it is important to consider the application and the direction of the metal casting as, in general, the top (Z axis) or upward facing surfaces of a 3D printed sand mold present better surface finish. Rapid manufacturing of sand molds with PBJ 3D printing consists of 2 major steps: first a fine layer of powder is deposited over the job-box, and then a liquid binds the material according to the desired shape as described on the different slices of the CAD. The same process is repeated until the last layer of the CAD is 3D printed. There exist 2 important steps which highly influence the quality of the functional 3DP sand mold depending on its print orientation. Firstly, the accuracy on the Z axis depends on the defined height of the powdered layer, and thus, which varies slightly from one layer to the other depending on the powder particles, as they are compacted by the recoater. Secondly, the accuracy of the XY axis hinge on the print head (X, Y resolution) movement instrument, which is precise and regular. For these reasons, parts for which the dimensional accuracy is needed should be placed on the XY plane rather than on Z axis. An example of droplet orientation over powder bed is shown in section 3. In order to study the bonding of particles in the powder bed, it was of crucial importance to study the print orientation in the job-box.

| **Research Objective 1** |
| --- |
| How does print orientation of molds made from 3D Printed sand molding materials affect their mechanical properties? |

This research was designed to classify penetrating materials (furan binder) over powder beds for the ExOne 3D printing machine, as it was crucial to understand the optimum print orientation and to recommend a solution to overcome the above-mentioned issue. Therefore, the sand molds were printed at an angle different from the famous golden or Fibonacci angle (137.508°) with the objective of obtaining less anisotropic properties The optimum build location and orientation of the prototypes being produced by a state-of-the-art ExOne 3D printer installed at MSMP laboratory in Aix-en-Provence was determined.

It was found in this research that the parts manufactured using 3DP technologies present anisotropic mechanical properties, which means that they have different properties depending on the printing axis. Usually, the mechanical properties are not as suitable on the Z axis as they are on the X and Y axis. By orientating the part in different directions, there can be a significant difference in the print quality, hence varying mold properties.

### 1.1.2 Research Question 2

Access to a 3D printer is limited to large scale companies due to its high investment cost. Therefore, 3DP specimens need to be transported to various locations while preserving their original dimensional accuracy. However, safe transportation of the 3D printed parts for direct casting applications or for the characterization of the printed specimens is challenging given their fragile and complex nature.

Once a part is 3D printed, clearing the loose sands on the build platform is time consuming as the printed part should not be damaged while cleaning or during the part removal process from the powder bed. Some researchers need 3D printed specimens with high dimensional accuracy, but deep cleaning of the printed specimens can alter the dimensional accuracy of the part, also affecting the surface properties of the printed specimen.

| **Research Objective 2** |
| --- |
| How do 3D Printed sand molds cure within the job-box? |

For this reason, a sand mold assembly was printed inside a 3D printed cover and transported straight after printing so that it can cure during transportation. It was found in this research that the sand molds printed inside a 3D printed cover would have similar mechanical properties but with less amount of moisture as compared to the parts 3D printed without a cover, which is an added advantage of curing while storing or transportation of mold assembly from one place to another. This will help the storage or transportation of a 3DP mold specimen for casting application or for the research work with controlled rate of curing, and hence achieving good mechanical properties.

### 1.1.3 Research Question 3:

Although additive manufacturing of sand molds has enabled designers to commercialize and implement this technology in industry, little is known about the curing behavior of such

molds during storage. Knowledge of how the ageing process affects the resulting material properties is critical in the design of the functionality of the molding materials.

| **Research Objective 3** |
| --- |
| What is the influence of curing process parameters on the mechanical strength and permeability of 3DP molds? |

To do so, the accelerated curing mechanisms were experimentally investigated using a set of 3DP samples produced with chemically-bonded sand used in casting applications. The evolution of the permeability and the three-point bending strength of the samples was monitored over a long time and related to the amount of binder present in the 3DP mold. The experimental results extended our understanding of curing mechanisms and provided rigorous criteria for the choice of ageing parameters.

It was found in this research that 3D printed molds can be stored at room temperature for a long time before being used for casting, roughly preserving the initial properties. Therefore, the objective of the present research work is to study the effects of curing parameters, i.e., curing time and temperature, on the strength and permeability of the 3DP sand molds.

### 1.1.4 Research Question 4:

As explained earlier, the functional properties of the 3D printed sand mold directly depend on the various printing process parameters, such as the compacting force on the powder bed (by re-coater), the volume and resolution of binder droplet over powder bed in the job-box, and the curing conditions. Many foundries encounter a wide variation in casting properties under uncontrolled conditions within a few hours due to the change in the physical properties of the 3D printed sand mold, e.g., three-point bending (3 PB) strength, gas permeability etc. These properties are further dependent on certain variables - moisture and binder content - which brings about a radical change for the 3D printed specimen. The change in the binder content will affect the 3 PB and permeability. Higher amounts of binder lead to increased strength of 3DP mold, but also to increased gas generation during metal casting and low permeability values. Low permeability values may lead, in turn, to casting defects, including porosities, blow holes, scabbing, and misruns. Consequently, it is necessary to evacuate the gas in an efficient manner in order to obtain a sound casting product with a minimum of defects. For these reasons, the success of this novel technology is strongly conditioned by the production

of sufficiently permeable sand molds with convenient mechanical strength for their manipulation.

| **Research Objective 4** |
| --- |
| What is the influence of the amount of binder on the mechanical strength and mass transport properties of 3DP molds? |

For this reason, the evolution of permeability and mechanical strength of the 3DP sand molds during the curing stage was studied in a recent research work using characterization methods for a unique value of binder content. However, the effects of binder percent on permeability and 3PB strength have still not been studied to the best of our knowledge. Such effects are expected to play a crucial role on the functionality of the casted parts for the above-mentioned reasons. To fill this gap, the present research study focuses on the effect of binder mass fraction on permeability and mechanical strength of printed molds for different curing temperatures and times. It was found in this research that the mechanical strength of the printed 3DP parts/molds is deeply dependent on the amount of binder (change in X resolution) and the curing process.

### 1.1.5 Research Question 5:

Foundry industries use casting process numerical simulation tools (mold filling and alloy solidification), to improve the yield and to reduce the manufacturing cost before the real time metal casting. However, inaccurate implementation of material physical properties (i.e. local mold porosity, permeability, and strength) reduces the reliability of the numerical results. Non-destructive in situ method like 3D X-ray micro computed tomographic imaging can be used to obtain accurate characterization of 3D printed sand mold specimens (i.e., local microscopic porosity, density, permeability, and strength) as required for casting simulations. Permeability is an important property of 3DP sand mold, which directly affects the casted part quality. Also, porosity, grain size distribution, average grain diameter, pore size distribution, average pore diameter, throat size distribution and average throat diameter are essential inputs when predicting flow in any porous medium, so this is also the case of 3DP molds. Moreover, the 3D images of the pore space provided by X-ray micro computed topography (μ-CT) can also be used for direct numerical computation of multiphase fluid flow and reliably determine permeability.

| Research Objective 5 |
| --- |
| How to predict permeability of sand molds through X-ray CT characterization? |

X-ray µ-CT is an effective and efficient tool not only to non-destructively visualize the interior of the object, but also to provide the necessary resolution to quantitatively analyze the 3DP sand molds. It was hypothesized that the digital image analysis of sand molds and the numerical simulations using lattice Boltzmann method (LBM) computer simulation and Pore Network Modelling (PNM) could be a reliable alternative (non-destructive testing) to traditional permeability measurements, as they provide more details of the tortuous microstructure.

For this reason, an additional objective of the present work is to study the geometrical and mass transport properties of 3D tomographic reconstructions of samples of 3D printed sand mold using LBM numerical simulations. Also, X-ray µ-CT was combined with LBM to determine the permeability of 3DP sand mold specimen. The resulting values of permeability were then compared with the experimental values and the predicted analytical values. In addition to the LBM simulations, a pore network modelling (PNM) was also performed to extract physically realistic pore network structures from high resolution 3D X-ray CT images of 3DP sand molds.

## 1.2 Thesis Roadmap

*Chapter 1* provides a general introduction of the thesis along with the defined objectives, followed by *Chapter 2* which provides an introduction to additive manufacturing of 3DP sand molds and cores in foundry using powder-binder-jetting technology. The theoretical information of process steps and physical basis of powder binder jetting technology in sand molding was summarized. In *Chapter 3*, the experimental procedure followed to manufacture the 3DP molds is presented, along with the basis of the proposed methods for characterizing permeability and mechanical strength within a given range of printing process parameters. *Chapter 4* is devoted to a non-destructive characterization of 3DP molds using Micro-focus X-ray computed tomography (CT) and its application for permeability characterization. Finally, the results presented in *Chapters* 3 and 4 are used in *Chapter 5* to study the erosion phenomena that occurs at the liquid metal-sand mold interface during the metal casting, and experiments are performed to investigate the 3D printed molds in terms of mold erosion related to metal casting.

The current thesis integrates material from three papers presented by the author. Chapter 3.2 uses material from References [1] coauthored with Dr. Antonio Rodríguez de Castro and Prof. Mohamed El. Mansori. Meanwhile, Chapter 3.3 is based on Reference [2] coauthored with Dr. Antonio Rodríguez de Castro and Prof. Mohamed El. Mansori. Finally, Chapter 4 is based on Reference [3], coauthored with Prof. Mohamed El. Mansori, Dr. Antonio Rodríguez de Castro, and Dr. Marius Costin. A list of the mentioned works is presented in Table 1.

**Table 1. Lists the publication/conference title, incorporated as chapters**

| Publication Title/Chapter | Status | Link |
|---|---|---|
| The effect of ageing process on three-point bending strength and permeability of 3D printed sand molds (*Chapter 3*) | Published (2018) | https://dx.doi.org/10.1007/s00170-018-2024-8 |
| On the rapid manufacturing process of functional 3D printed sand molds (*Chapter 3*) | Published (2019) | https://dx.doi.org/10.1016/j.jmapro.2019.04.034 |
| Study of the evolution of transport properties induced by additive processing sand mold using X-ray computed tomography (*Chapter 4*) | Published (2019) | https://doi.org/10.1016/j.jmatprotec.2019.116495 |
| On quality assessment of 3D printed sand mold using non-destructive X-ray micro Computed Tomography (µ-CT) - *DIRCT2019* | Presented (2019) | https://www.dir2019.com/Programme#Add.1 |

# 2. STATE OF ART

This chapter begins with a bibliographic review of sand casting in foundry, focusing on the traditional technique. Then, the additive manufacturing technology and its use in foundries to print sand molds for metal casting is introduced. Finally, the theoretical and physical basis of powder binder jetting technology underlying the developments in sand molding is summarized.

## 2.1 Casting processes

Casting is one of the earliest methods for metal shaping in the history of civilization. Archaeological data indicate that the origin of casting process was around 5,000 years ago. Some examples of ancient casting parts are displayed in Fig. 1. These processes consist in pouring a molten metal into a mold (sand or metallic) with a cavity of the shape to be manufactured and allowing it to solidify within the mold. When solidified, the desired metal object is taken out of the mold either by breaking the disposable sand mold or taking the mold apart when a reusable metallic mold is used. The solidified object is called casting. Sand casting is the most widely used metal casting process in manufacturing, and almost all casting metals can casted in sand molds. Sand castings can range in size from very small to extremely large. Some notable examples of items manufactured in modern industry by sand casting processes are engine blocks, machine tool bases, cylinder heads, pump housings, and valves.

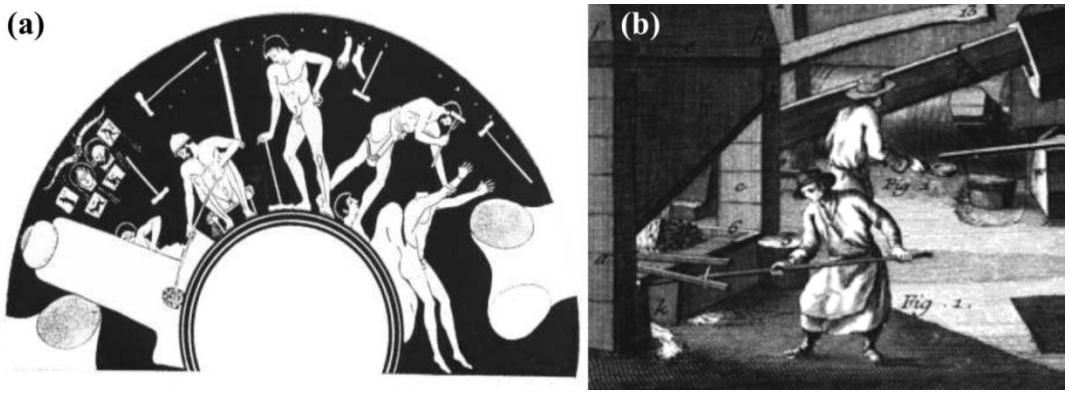


**Figure 1** (a) Ancient Greece; bronze statue casting circa 450BC, (b) Iron works in early Europe: cast-iron cannons from England circa 1543 [4]

Modern providers of industrial castings make use of the above-mentioned techniques and improve them based on the understanding of the fundamental principles of fluid flow, heat transfer on molds and casting, thermodynamics and metallurgical microstructural

developments. These engineering methods are used to assist the design of casting systems allowing the fabrication of quality metal castings, by minimizing the impact of defects.

Producing a quality metal casting requires a good design effort to:

- Create a proper gating system (metal pouring basin, sprue and runner) to let the molten metal flow into the mold cavity free from inclusions and gas bubbles.
- Provide a riser which will feed the liquid metal on to the casting cavity as the liquid metal is cooled and solidified (liquid metals shrink when cooling and most liquid metals shrink as they solidify).
- Control the heat flow from the mold cavity to the atmosphere so that all significant shrinkage defects are located in the riser.

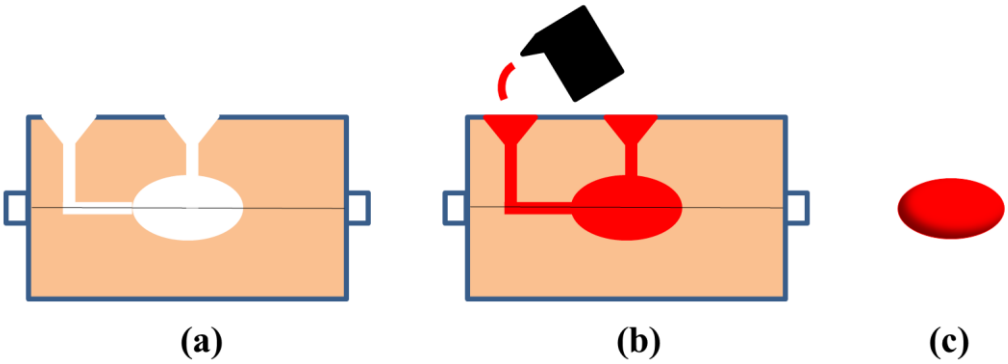


**Figure 2.** Traditional sand-casting process; (a) Assembled molds, (b) Pouring liquid metal and (c) final solidified casting without the riser.

The key to a successful and sound metal casting design is systematic combination of experience and engineering science. The main stages of the designing process are listed below.

*i.* *Design of the part to be cast*

Identify the purpose of casting, the shape, the size, the tolerances (manufacturing), by taking into account dimensional change during the casting processes.

*ii.* *Selection of Material for designed Part to be Cast*

Mechanical and physical properties of material, including castability, thermal properties and fluid flow properties.

*iii.* *Design and production of the patterns for the molds and cores*

Gating system and riser channel design, based on Fluid Mechanics and Heat Transfer concepts.

*iv.* *Selection of the casting process*

Type of mold (sand or metallic mold), mold size and roughness, mold permeability (for sand molds) and production cost.

*v.* *Post-processing of the casting*

Subtractive machining, heat treatment, welding.

*vi.* *Quality control of cast parts*

Mechanical and physical properties, destructive or non-destructive testing.

In the system design stage, simulation of the filling and solidification of the proposed part is most valuable. Nowadays, modern computers are commonly combined with powerful software packages to give a preview of mold filling and illustrating the path of solidification. Such simulations are essential to reduce the time between design and prototype castings by avoiding a trial and error approach for the design of both gating system and riser. Although there exist many possible solutions to cast geometries with traditional casting method, the high investment costs in complex parts make 3D printing technology an excellent alternative for the foundry industries, and an opportunity to rethink old casting approaches by using computer models. The Rapid Prototyping (RP) technology, also termed as layered based manufacturing or additive fabrication, is rapidly growing and evolving, and 3D-printed sand molds have been proven to be an effective way for rapid prototyping and manufacturing of sand molds for metal casting. Consequently, 3D printing of complex molds for casting of metals is currently used by different companies like ExOne, 3D Systems, and Viridis3D.

## 2.2 3D Printing technology in casting applications

Additive Manufacturing (AM), commonly referred as Three-Dimensional Printing (3DP) was invented at MIT as a rapid prototyping technique to build three-dimensional parts directly from computer design model in layers [5–8]. Commercial scale 3D sand printers were invented at Massachusetts Institute of Technology (MIT) to build three-dimensional (3D) parts directly from a computer design model [6,7,9–12]. In 3DP processes, 3D CAD design data are sliced to print up a mold layer upon layer by binding granular material. AM is defined as the process of joining particles from 3D design data to form an object layer upon layer, which is just opposite to subtractive manufacturing. Three-dimensional printing (3DP) of sand molds using binder jetting technology overcomes challenges faced in the traditional production method, e.g., limitations in terms of part complexity and size, production time and

cost (which depends on the quantity and the part complexity [13,14], optimization in part design/design freedom for any castable alloys [13–15].

Nowadays, 3DP has become the standard method for the production of molds and cores in the casting industry, with applications in various areas, such as aircraft, automobiles, and medical. This process of rapid prototyping has been widely accepted due to its significant potential to reduce the cost of manufacturing highly complex components [13–15]. Amongst all the rapid tooling and manufacturing processes, 3DP makes the most sense for quick integration into existing industries as it can produce high quality and complex sand molds with the required properties for better casting solutions within a short time frame[16]. Furthermore, the use of binder jetting technique for the production of optimized part designs results in reductions in weight up to 33% compared to the traditional sand mold making process or even any other 3D printing techniques [17].

The layer-based 3DP technology produces porous parts by binding individual particles, which generates permeable molds that are suitable for metal casting despite their lower mechanical strength. And is, therefore, a measure of ease through which the gas generated can flow. It should be noted that molds with excessively high levels of mechanical strength may give rise to hot tearing and high residual stress, which is not convenient for casting [18,19]. In the case of casting molds, ceramics are used as particle materials to provide refractoriness, and a liquid binder is used to ensure cohesion between particles.

Qualitatively, the liquid binder forms capillary bridges between the sand grains as schematically shown in Fig. 3, and the curvature of the liquid interface generates a capillary pressure that causes attraction between grains and high stiffness of the 3D printed parts. This generates a network of sand grains connected by resin bridges hence a complex mold can be printed for metal casting.

The interstices between the grains of sand in the 3D printed parts permit the evacuation of air during the filling of the mold as well as the flow of the gases generated during filling and solidification of the alloy. These gases will be evacuated more or less rapidly depending on the permeability of the sand [20,21]. Good permeability of the mold reduces casting defects formed by trapping of gas pockets within the liquid alloy and subsequently improves the filling ability. While high permeability may lead to metal penetration defect due to large inter-sand grain spacing.

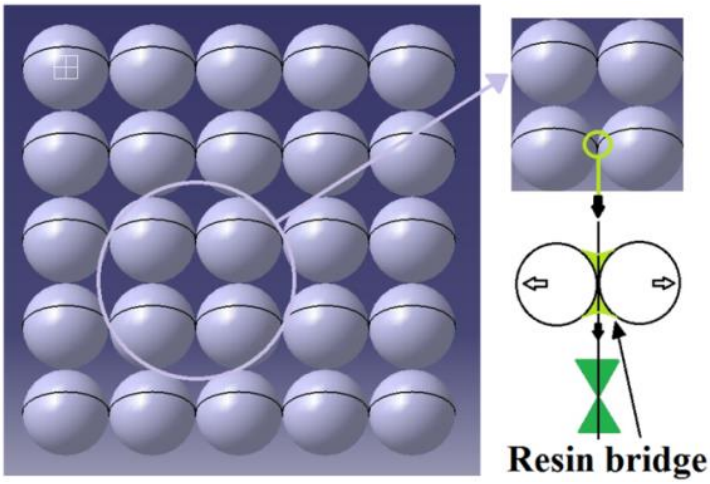


**Figure 3.** Schematic representation of particle binder bonding and resin

The flexural strength of the mold is a function of the grain size, binder content present in the mold and sand compaction [22,23]. Indeed, liquid binder blocks gas flow through the sand, resulting in more gas being trapped during pouring of the alloy leading to gas defects. So, more percentage of binder present leads to more flexural strength and shrinkage but generates excessive gas during casting operations [24–27]. The volume of the gas generated while filling depends on the proportion of the binder however, excessive binder produces too much gas and hence poor quality of the casting[25] and lack of filling [28]. Therefore, it is much necessary to evaluate mechanical and functional 3D printed sand mold properties of the printed mold.

Among various existing binders, organic furan binders are commonly used in foundries for 3DP of sand molds to cast light alloys [18,19,25,28–31]. The main advantage of furan binder is that it cures at room temperature and possesses good mechanical strength[29]. The furan binder condensation reaction produces water, which tends to slow down the rate of curing and hence affects the 3-point bending strength and permeability[32]. Increase in aging time of the 3DP part results in more water being evaporated from specimen.

### 2.3 Powder Binder Jetting (PBJ)

In this section, an overview of the process of sand binder jetting is provided. Sand additive manufacturing uses the technology of Powder Binder Jetting (PBJ), which constitutes of distinct stages which are repeated continuously to fabricate a 3D component. As compared to other additive manufacturing techniques, PBJ technology presents the particular advantage of not releasing heat during the process of printing, which results in no induced residual stress,

and is considered as the standard method for the production of 3DP molds and cores. PBJ process can be used to manufacture large 3DP components and is often more economical or cost-effective than any other existing additive manufacturing technology. Among all processes, the PBJ process is considered the most scalable. A schematic representation of some key stages of the process is shown in Fig. 4.

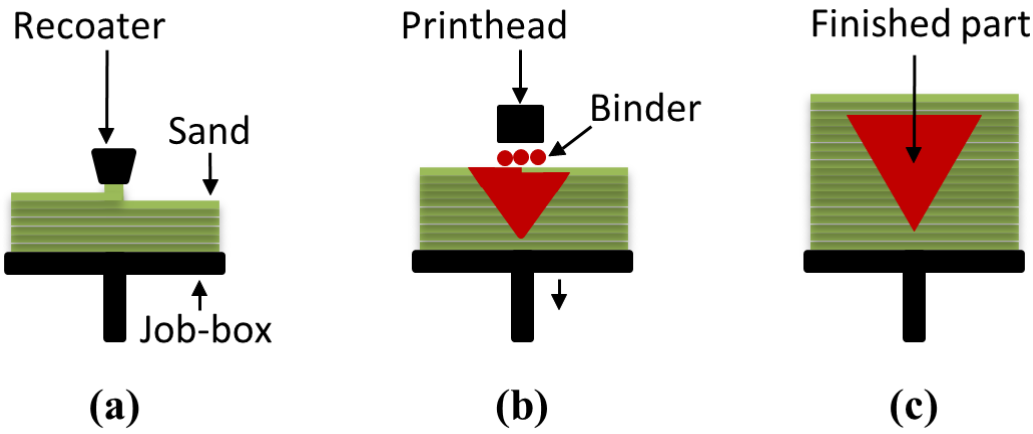


**Figure 4.** Schematic representation of a 3D printer: (a) lowering the build platform, layering with material and (b) printing process using binder, (c) final part

The PBJ process consists of the following steps:

1. Sand is spread over the build platform using an automated roller.
2. The sand bed is then applied with a compacting force by the help of the re-coater.
3. The print head nozzle injects the liquid binding adhesive on top of the sand bed.
4. Binding of sand grains by providing cohesion during drying and curing, Fig 5.
5. The build platform is lowered by the required layer thickness in Z direction.
6. The object is formed where the sand powder is bound to the liquid binding agent.
7. Unbounded sand remains in a position surrounding the printed object.
8. The entire process is repeated until the required object is printed.

A CAD model of the desided part is first created. From the CAD part design, the images are processed sliced into matrix [33] and converted into different formats, such as STL [34] or the recently developed Additive Manufacturing File AMF [35]. While the traditional STL file only deals with the geometry, the AMF file allows the modification of materials and textures [33]. The newly introduced format ASTM AMF file is a massive development for the 3D image processing for additive manufacturing and will be replacing most of the other formats available [35–37]. Unlike its predecessor STL file format, AMF file format has native support for color, textures, materials, lattices, and constellations.

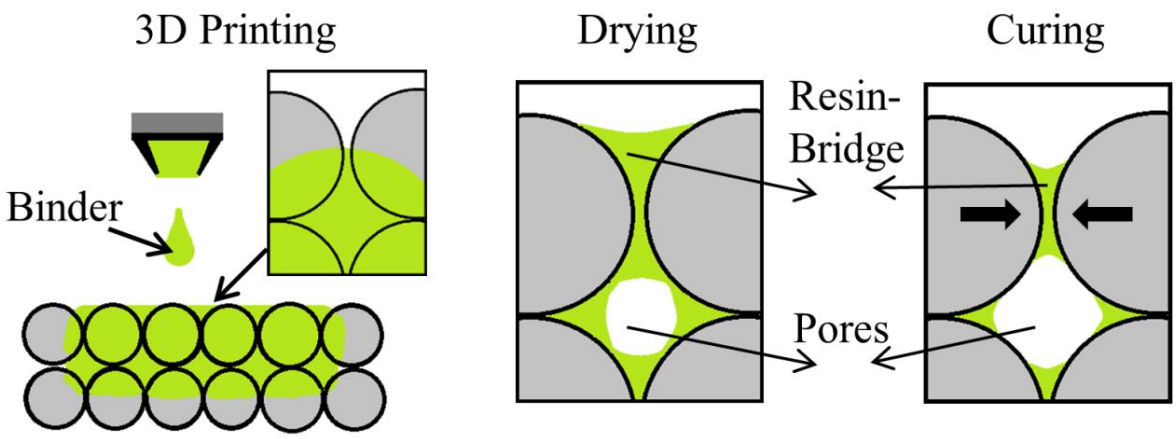


**Figure 5.** Powder binder jetting process

The process of powder binder jetting starts with an empty build platform. At the corner of the job box, the platform is sealed to prevent sand leakage. The recoater then spreads uniform layers of particles on the build platform [7,38]. At the beginning of the printing process, few layers are printed to get an even strong layer of powder bed over which the part will be printed. The print head then moves over the powder and drops binder uniformly onto the layer in X and Y direction. The print head represents a matrix-like arrangement (line of nozzles) and can be accessed over the entire build platform. This line of nozzles corresponds to the driving pattern by print head, as determined by the data model. During the movement of the print head the data updates in rapidly, hence forming the provided image. The print-head uses Drop-on-Demand (DoD) technology, schematized in Fig. 6(a). The binder droplets are formed in the print head due to rapid pressure fluctuations, which are later ejected through a micro-sized nozzle, similarly to the case of ink-jet printing [39]. The binder droplet leaves the micro-nozzle as a free flying droplet. Due to such behavior of droplet, only particular binder material is used [40,41]. Given that the mechanical properties of sand packs mainly depend on the cohesion properties of the binder, the binder liquid should exhibit convenient shear viscosity to fill the interstices without flowing down by gravity. The final step in the printing process is the lowering of the powder build platform in Z direction. After lowering of the power bed build platform (Job-Box), it is once again filled with powdered particles with the help of the recoater. This layer thickness corresponds to the vertical distance the build platform moved while lowering of the powder build platform in Z direction. The entire process characteristics involved during printing will be discussed in the next section.

## 2.4 Process characteristics and physics involved in the process

Most of the features of the 3DP process are related to the nature of the additive process. The rate of the building is restricted by the speed at which the binder can be delivered to the powder bed. In most cases, the amount of solid particles and binder is the same when printing a part. Hence, on a volumetric basis, the part printing rate is limited to twice the flow rate of a binder [8,9]. Past researches have also been conducted to study the steps involved during the process of additive manufacturing.

(a) The layering of powdered material and vertical dimensional control.
(b) The interaction of a single droplet of the binder with the particle.

### 2.4.1 Layering of Powdered Material, Vertical Dimensional Control

After each layer is printed, successive layers are added. The added layer weight produces a compression over the powder bed which leads to loss of vertical dimensional control. Past researchers [6] have proved experimentally, the primary cause for the increase in compression arises from the weight of the sand particles on the powder bed. It was confirmed that the powder bed layer with a higher packing density are more resistant towards vertical dimensional change occurred due to compression of following loading [6]. To control the vertical dimension of the print, a vibratory mechanism was developed, which vibrates the layer of distributed powder to compact the powder in order to gain high packing density [42,43] .

### 2.4.2 Interaction of a single droplet of binder with the particle

The key parameters for achieving excellent mechanical properties of the Powder Binder Jetting process are directly dependent on the adhesion ability of adjacent sand particles sticking to each other and on the cohesion properties between binder and sand particles. The deposition of the liquid binder droplet over the powdered particle substrate tends to form a new interface between them like wettability, spreading, evolution and adhesion. These forces provide strong bonds between the powdered particles. On the other hand, the wettability of the powder bed by the liquid binder is influenced by the movement of the print-head and the angle at which the binder contacts the powder bed. Therefore, the speed of the print head needs to have the desired rate of movement over the powder bed to suitably drop the binder. As shown in Fig. 6(b) and 6(c), a nearly cylindrical binder bridge is formed between two sand particles, which are modelled as spheres. Under the effect of surface tension, the sand

particles bond closer and a strong binder-particle bridge is formed. The solvent used in PBJ process is relatively volatile in nature and tends to evaporate in time, which results in shrinkage of the solid sand skeleton and stronger inter-particle bridges [26].

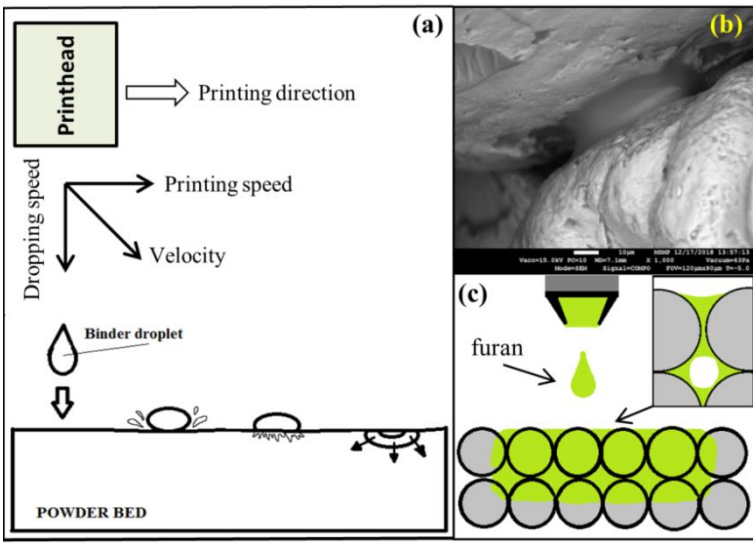


**Figure 6.** (a) Simplified model of binder dropping of binder by print-head over powder bed, (b) an SEM image of particle binder bonding along with (c) a schematic representation of interaction of a droplet of binder with the particle.

## 2.5 Mold fabrication via Powder Binder Jetting technology

### 2.5.1 Powder Bed Compaction

Packing density is generally defined as the compactness of a substance. During the preparation of powder bed, the recoater spreads uniform layers of powder on the build platform. Then, each layer is compacted by the recoater to get high packing density of the part. It should be noted that the layers with higher packing density are more resistant towards vertical dimensional change arising from compression of subsequent loadings [6]. Also, the strength and permeability of the printed part are dependent on the compaction density. The packing density of the spherical particles is around 0.60 when un-vibrated and 0.64 when vibrated [44,45]. Apart from the presence of vibration, the critical parameters affecting the packing density are the particle shape, size distribution [46] and also the resin binder content. Indeed, packing density is higher for nearly-spherical particles with regular shape [47], and increases with the sphericity [48] of the particles.

Expendable molds used in casting processes are commonly made from quasi-spherical silica grains. Quartz is the only stable form of silica polymorph at normal ambient conditions, and

the density value of α-Quartz (Silica) is known to be 2648 $kgm^{-3}$. Therefore, the overall density of a given pack of quartz grains can be calculated by multiplying the density value of quartz by (1 - ε), where ε is the global porosity of the type of packing:

- Simple cubic packing = $\pi/6 \times 2648$ kg $m^{-3}$ = 1376.96 kg $m^{-3}$
- Centred cubic packing = $\pi\sqrt{3}/8 \times 2648$ kg $m^{-3}$ = 1800.64 kg $m^{-3}$
- Face-Centred Cubic = $\pi/ 3\sqrt{2} \times 2648$ kg $m^{-3}$ = 1959.52 kg $m^{-3}$

It is reminded here that the theoretical maximum porosity for a simple cubic packing of uniform sand grain size is ε = (1- π/6) and is obtained with a simple cubic packing.

### 2.5.2 Print-head characteristics

A droplet of the binder is formed only when an electric heat charge is dispersed through the print head and forms a vapor bubble [49]. The mass and the velocity of the binder droplet is a function of the shape and size of the print-head and the physical and chemical composition of the binder [49]. Also, both the firing signal profile and the dimensional stability and accuracy of the orifice, influence the frequency at which binder droplets are generated as well as their volume and velocity [41,49]. During the PBJ process, the number of nozzles is closely proportional to the time required for printing one layer [31]. In this regard, previous works showed that the performance in printing (amount of binder, droplet spacing, etc) is hugely affected by increasing number of nozzles [50].

### 2.5.3 Binder selection

The binder system plays an important role during the additive manufacturing process of powder binder jetting. Indeed, the strength of the printed part is a function of the amount of binder as well as the thickness of the powdered layer [51].

The binder system must meet several requirements.

- **a.** The binder needs to have excellent bonding properties, to interact with the powder bed over the build platform (wettability and penetration) and should also have enough strength during the part removal process.
- **b.** The surface tension should be below that of water, which will allow it to spread, and facilitate the penetration into the pores.

**c.** The binder should exhibit low viscosity values, so that it can be easily deposited over the powder bed.

In the foundries, a significant amount of sand molds and cores are bonded chemically with 1-3% of binder [52,53]. Although most of them are organic, there are also some inorganic binders. There are three main types of binders in casting processes, (a) vapor cured-cold box, (b) no-bake and (c) heat cured.

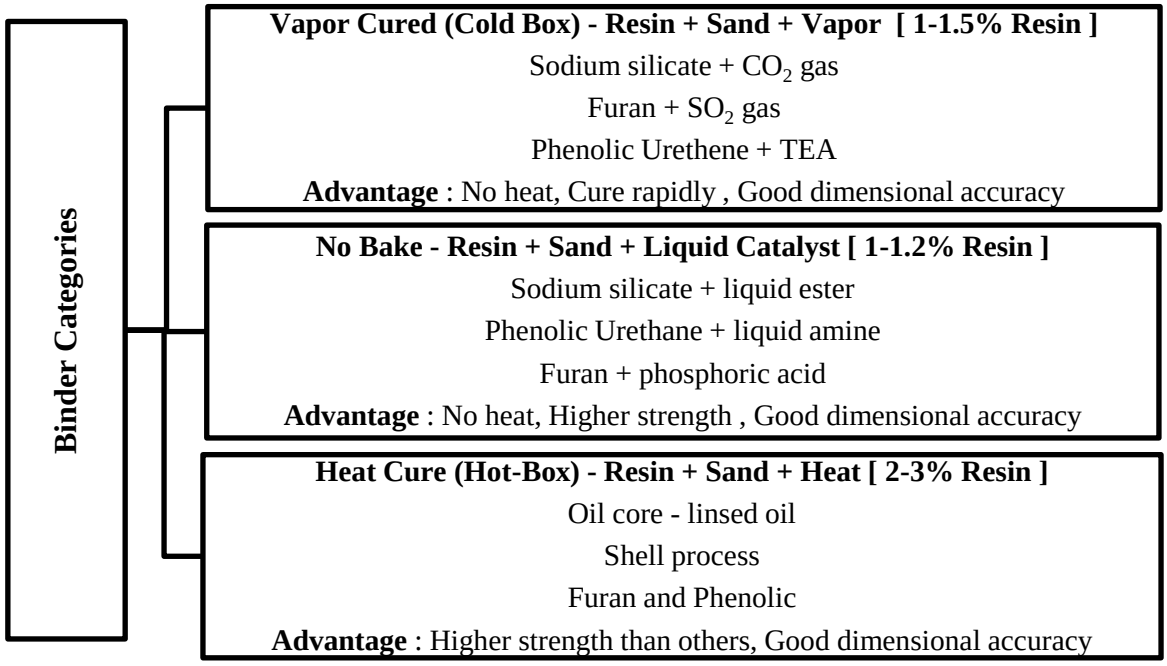


**Figure 7.** Binder categories

The purpose of adding binder and catalyst [54] is to give additional cohesion and strength to the powder, to ease the mold to retain its shape under a change in pressure, temperature, and erosion when comes in contact with liquid metal. In general, resin bonded sand in casting consists of 93-99% silica and 1-3% binder [52,53]. The amount of binder present in the mold can be characterized by Loss On Ignition (LOI) experiments to differentiate the impurities present in the mixture.

The most common types of resins used in casting processes are phenolic and furan [55,56]. Phenolic acid cured binders are relatively cheaper and are used mainly for the production of larger parts. The resin present is phenol-formaldehyde (PF) or urea-formaldehyde (UF) [55]. Furan resin binders are more expensive than phenolic ones but provide with suitable mold and core strength. They cure rapidly and possess excellent mold and core strength. The main advantage of furan over phenolic binder is that it produces less odor and smoke during the

process of casting due to free phenol level and low formaldehyde [32]. Previous studies have provided significant insight towards their differences on mechanical properties of a sand mold for casting application [53].

## 2.6 Influence of process parameters on the quality of 3DP molds

In the Powder Binder Jetting process there are many different parameters which affect the quality of the 3DP molds (Fig. 8), including mold physical properties, printing parameters and curing parameters. Among the numerous process parameters, the current literature review will only focus on the following ones:

- ✓ Effect of grains size and shape
- ✓ Effect of binder
- ✓ Effect of curing time

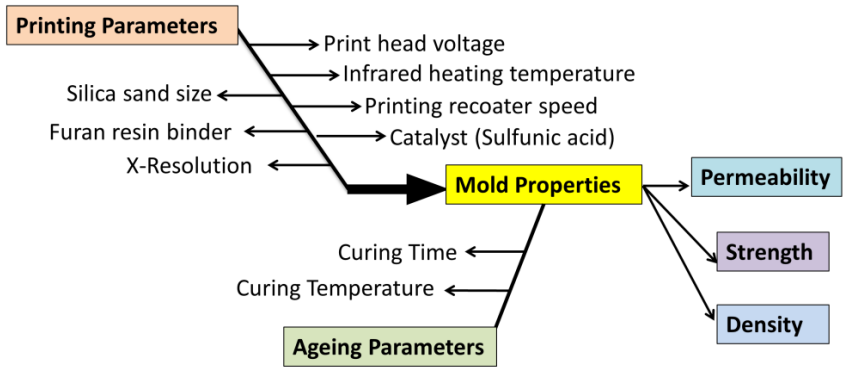


**Figure 8.** Factors influencing mold properties

### 2.6.1 Effect of grains size and shape

Grain Fineness Number analysis is a method for identifying the average grain size of the sand. This method consists in estimating the total number of meshes per inch of the sieve from which the sand particle of uniform shape and size will pass through. It is nearly proportional to the surface area per unit of weight of the sand particle. Sand is a material, regardless of chemical composition, which falls between 1/12-1/500in. (0.05-2.0mm) or 10-250 mesh [57]. Typical range for grain fineness for an acceptable casting is 25 to 170 [58]. When the size of the sand particle is modified to improve the surface finish, this strongly influences the behavior of the gas penetration in sand mold [31]. Moreover, the shrinkage of the sand mold is affected with increasing or decreasing grain size [27].

Also, the shape of the grain affects the surface finish of a casting. Grain shape can be categorized into three components: angular, sub-angular, and rounded [58]. The roughness values Ra and Rz should be measured in all the three planes (XY, YZ, ZX) of the printed mold in order to evaluate the quality of the surface finish. It can be noted that the size of the sand particle has a direct relationship with the preceding quantities, and also influences the rate of gas evacuation through the 3D printed model. Despite providing better surface finish, a finer particle size distribution prevents the gasses from escaping during pouring of the metal. On the contrary, coarser particles would facilitate the evacuation of gasses while providing a rough surface finish [57,58].

When the sand grain fineness number is increased, this results in more sand particles being coated for a constant amount of binder. This provides less strength to the cross-linked bond in between two adjacent sand particles, leading to reduced mechanical properties. It was also identified that the shrinkage of cores increases with finer sand particles, as increasing number of sand particles results in increasing number of resin bridges which shrinks during the process of curing and leads to more shrinkage [26,27]. Also to characterize the physical properties and the deformation behavior of silica sand grain, many analyses were performed using x-ray tomography [59–61].

### 2.6.2 Effect of binder on mold properties

Chemically bonded sand cores and molds are commonly used in foundries to obtain excellent surface finish properties and mechanical strength or collapsibility . In order to optimize the hardness and dimensional accuracy of the resin bonded sand molds, the effect of binder composition on the shrinkage of the cores and molds. In this sense, the effects of the quantities and ratios of the components present in a binder ( i.e., crosslinking agents, resin, and catalyst) were previously analyzed [25–27]. The amount of binder content affects the mechanical properties and shrinkage of the printed mold [26,27]. The main reason for the shrinkage mechanism is explained in terms of the evaporation tendency of the solvent during curing. Bridges are formed in between adjacent sand particles during the cross-linking polymerization reaction of a resin, and shorten when the solvent present in the resin bridges gradually evaporates, which leads to shrinkage of the core [26,27]. It was identified that, a greater amount of resin used in the binder leads to increase in shrinkage of cores [26], Fig. 10. The catalyst used as an activator also influences the shrinkage of the mold. It was stated that a

higher percentage of catalyst leads to increase the rate of curing and hence resulting in the higher initial rate of shrinkage.

Moreover, the percentage of binder directly influences the hardness of the mold, which affects, in turn, the dimensional accuracy of the 3D printed sand mold [27]. Previous research works proved that the hardness of the mold reduces with a reduction in the percentage of the resin binder. Also, reducing the amount of activator reduces the rate of reaction between the sand particle and the binder, and hence reduces the mold strength[26]. It was identified that, by using a high amount of binder with the inadequate ratio between mold and cast, leads to high permeability issues and hence resulting in the release of more amount of toxic gas [20,21]. Mathematical tools and software were developed in the past to identify the shrinkage, porosity and filling problems during casting [62–65]. 3DP molds were also compared with other chemically bonded samples, showing that printed parts had a higher burnout temperature and has better mechanical properties [25].

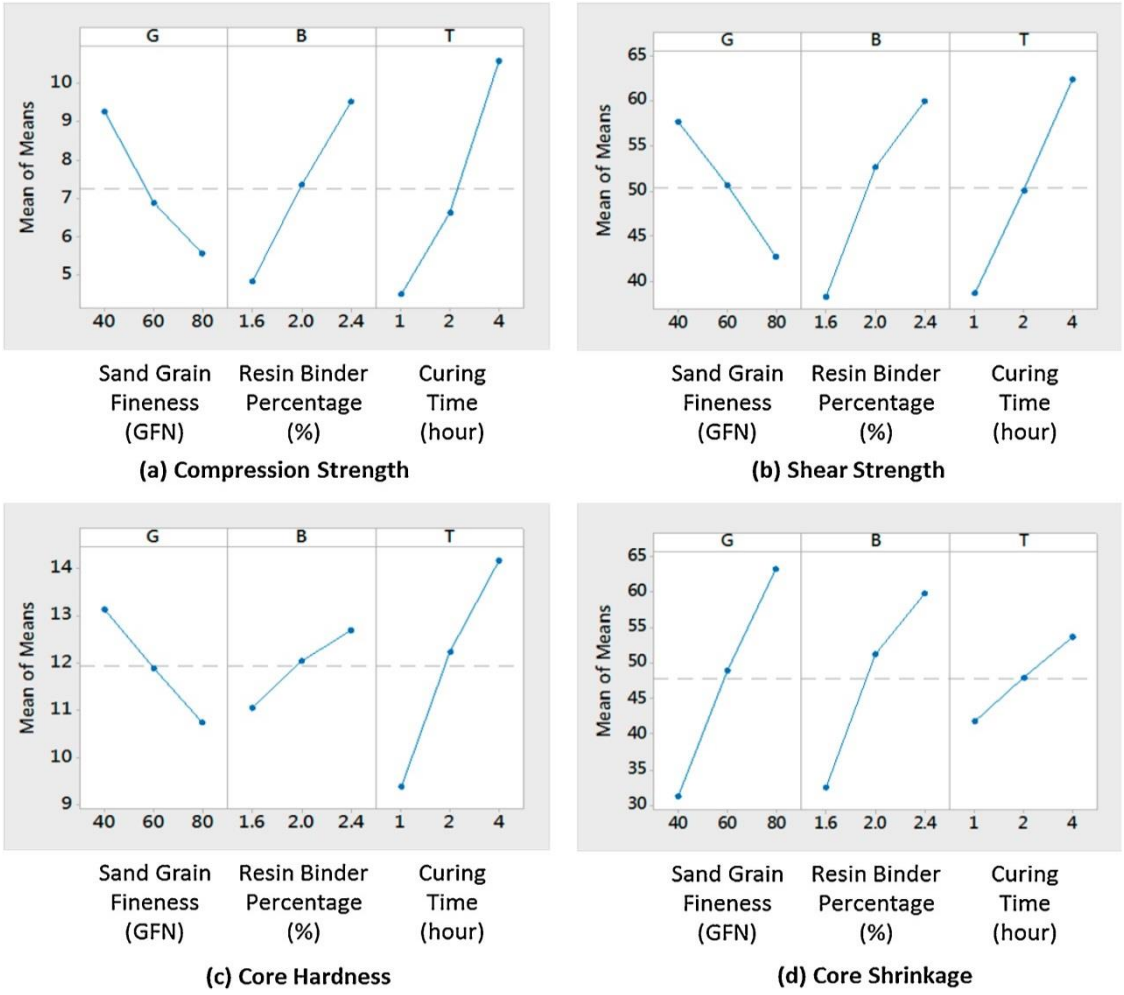


**Figure 9.** Main Effect Plot of chemically bonded sand mold properties [27].

### 2.6.3 Effect of curing time

The effect of curing mechanism of furan resin binder was previously characterized by using infrared spectroscopy method [29], concluding that the thermal strength can be improved by using modified (modified with different agents i.e. sorbitol, polyester polyol, phenol and acetonr) furan resins [29]. Two different stages coexist during curing, as explained in the literature [26]. The first phase begins when the sand mixes with the introduced binder and tends to perform polymeric crosslinking with the provided resin at an initial rate controlled by the catalyst. The second phase of curing begins, when the resin gets in contact with the oxygen present in the air, and then polymerizes to form a stable bond between the sand particles. Most shrinkage arises during curing, due to the evaporation of the solvent, as mentioned above [26,27]. Furthermore, it was identified that the compression strength, shear strength, and core hardness increase with increasing curing time, Fig. 9. The underlying reason for such increase in the mechanical properties is hardening of resin bridges between the sand particles arising during curing.

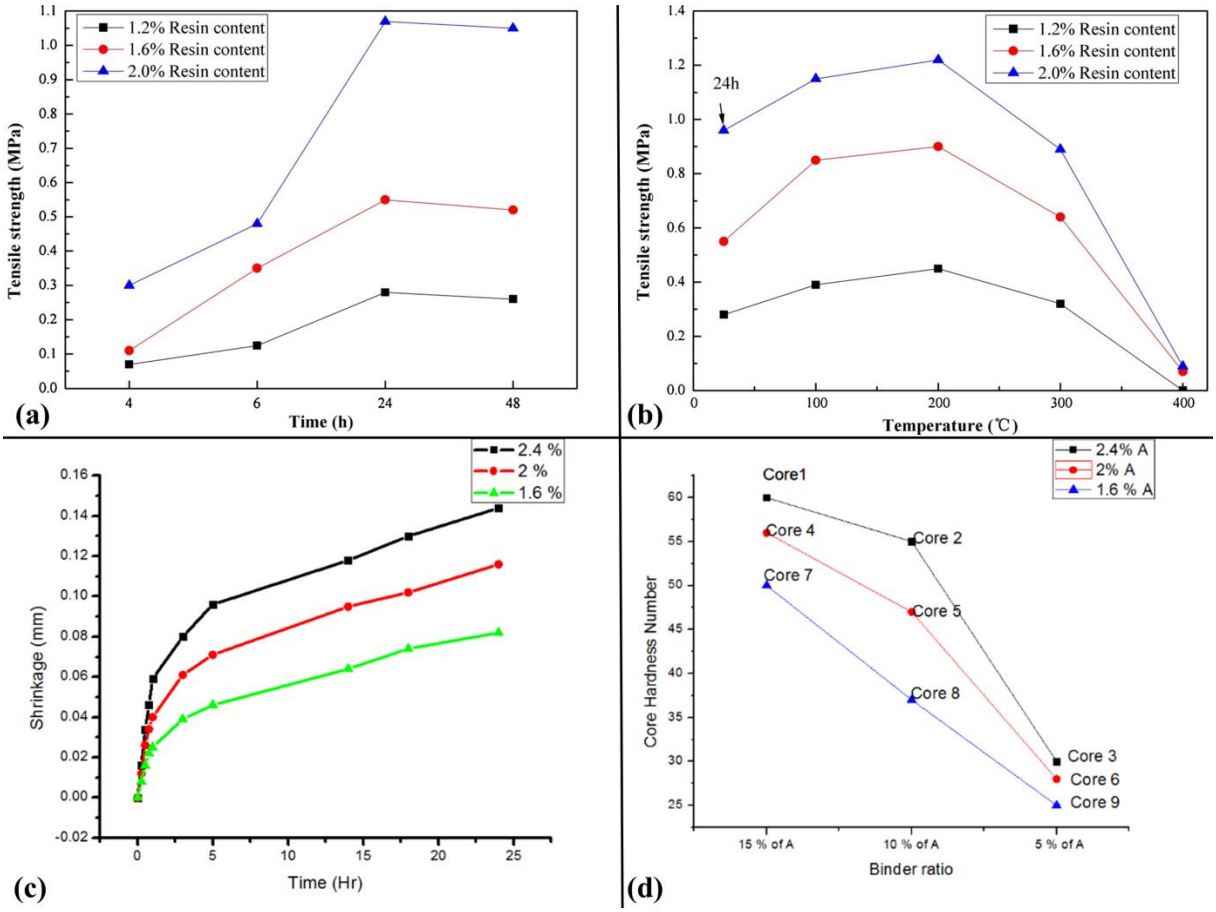


**Figure 10.** (a,b) The effect of furan resin content with curing time and temperature on tensile strength [66]; (c) Shrinkage and (d) hardness of cores with varying resin content [26].

The compressive strength of a mold ought to be high enough to withstand the different impacts during handling and transfer from the molding place to the pouring area, as well as other impact loads that might occur in the process. It is the ability of a printed mold to stay together until it is filled with molten metal and hold the shape of its internal core cavity until the casting has solidified completely. The tensile strength of the resin bonded mold is also an important parameter as it is essential for mold handling and easy de-coring after casting. It was found that tensile strength of resin bonded mold increased with the increasing resin binder content, and the 48 h tensile strength is less than the 24 h tensile strength because of moisture absorption [66], as illustrated in Fig. 10a and 10b. As shown in Fig. 10, for the same temperature, the retained tensile strength of resin bonded mold increased with the increasing binder percent. When the binder percent is fixed for the resin bonded mold, the tensile strength first increases and then it tends to decrease with the increase in temperature. It was also found that the retained tensile strength is maximum when heat treated at 200 °C. The reason stated was that low roasting temperatures cause secondary hardening of resin bridges which increases the retained tensile strength. In contrast, high roasting temperatures burn the resin bonding bridges of sand mold, hence reducing the tensile retained strength.

## 2.7 Modelling Powder binder jetting process

In order to properly characterize processes, there is a need to perform physics-based modeling. These models must be able to predict the variation of as built and functional mold properties for the different values of the process parameters, and can be divided into micro-, meso- and macro-scale models.

- **i.** Micro-models provide information about the sand powder bed. (Sand grain size, pore size, porosity, permeability).
- **ii.** Macro-models utilize the provided dimensions from micro-models for the measurement of surface quality, produced due to the different arrangement of grain shape and sizes affecting the geometrical characteristics. (Surface Roughness).
- **iii.** Meso-scale models are dedicated to the calculation of strength dependent mechanical properties of the printed mold. (Density, ultimate bending strength, erosion)

# 3. EXPERIMENTAL CHARACTERIZATION OF 3DP MOLDS FOR FOUNDRY PURPOSES

In this chapter, three different series of experiments were performed to study the properties of 3DP molds. The procedure to manufacture the 3DP mold together with the physical basis of the characterization method will be presented. The experimental procedure followed to manufacture the 3DP molds is presented, along with the basis of the proposed methods for characterizing permeability and mechanical strength within a given range of printing process parameters.

## 3.1 Optimum print orientation of 3DP molds

### 3.1.1 Introduction and Objective

3D-printers of sand molds have been proven to be an effective way for rapid prototyping as well as rapid manufacturing of casting parts. The heavy investment cost of these production machines hinders its penetration into family owned foundries or research organizations even though accessing these facilities from other organizations permit the use of this technology. Minimizing the cost and safe storage and transportation can be a challenge. Consequently, access to a 3D printer is limited to large scale companies and 3DP specimens need to be stored or transported to various locations with high dimensional accuracy. However, safe storing or transportation of the 3D printed parts for direct casting applications or for the characterization of the printed specimens is challenging due to their fragile nature and complex assemblies.

The aim of this study was to optimize the time and cost of production, storage and transportation of such molds, with the required optimized properties, to other location or within the same company. Parts of a sand mold assembly can be printed inside a 3D printed cover and transported straight after printing so that it can cure during transportation. The unbounded sand present around the 3DP part can help reduce the water/moisture content produced due to polycondensation (polymerization and condensation) of binder. Also the cover ensures that the parts can safely stay together for a particular assembly. Printing a cover around the parts may only consume extra binder and activator; otherwise it will be waste/loose sand cannot be recycled for 3D printing due to premixing the acid activator.

This research aims at comparing the mold sample properties between immediately- and delayed-cleaning procedures. It was hypothesized that the parts printed inside the 3DP cover would have similar 3PB strength with reduced water content with the time of storing, which is an added advantage of curing while storing/transportation of mold assembly from one place to another. This will help the storage of a 3DP mold specimen for casting application or for the research work with controlled rate of curing, and hence achieving good mechanical properties. The way the 3D printer drops the binder over binder bed is symmetrical, but it changes when a part is rotated over the build platform, Fig. 10. It was also important to understand the optimum print orientation and to recommend a solution to overcome this issue and hence producing molds with less anisotropic properties by printing at an angle difference of the famous golden or Fibonacci angle which equal to 137.508°.

### 3.1.2 Printing procedure

A 3DP cover with sizable allowance along was printed surrounding the specimens, which can be easily dismantled once taken out of the job box and/or curing and heat treatment. The 3DP mold specimens were printed inside a 3DP cover with loosely packed sand powder around it. Subsequently the printed sand mold box is removed from the build platform of the 3D printer and is used for direct transportation to different locations for casting application or for the research work. A 200×150×50 $mm^3$, rectangular box was designed around the 3PB specimens, Fig.11, with a thickness of 10 mm, and the upper layer was made comparatively thinner than the other sides, to ease the cleaning process once delivered to its destination without any damage to the printed specimens and also by controlling the rate of curing from variation of temperature causes during transportation.

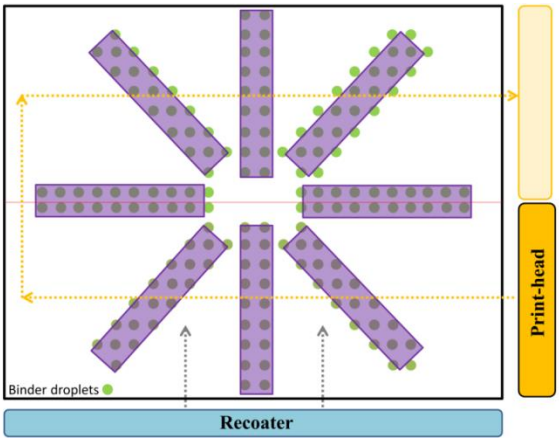


**Figure 11.** Schematic representation for binder droplet spacing

Two such 3DP Boxes (five 3DP bars inside) and together with 15 bars, were designed in a CAD software program, and were then printed, Fig. 11, using ExOne's s-print 3D sand mold printer. The printing process was repeated 3 times with the same process parameters, Table 2, in order to have a total of 6 boxes with a total of 30 (5×6) 3PB test specimens.

The first experiment was designed to compare the 3PB strength of the parts printed with (inside)/without the 3DP cover before/after heat treatment.

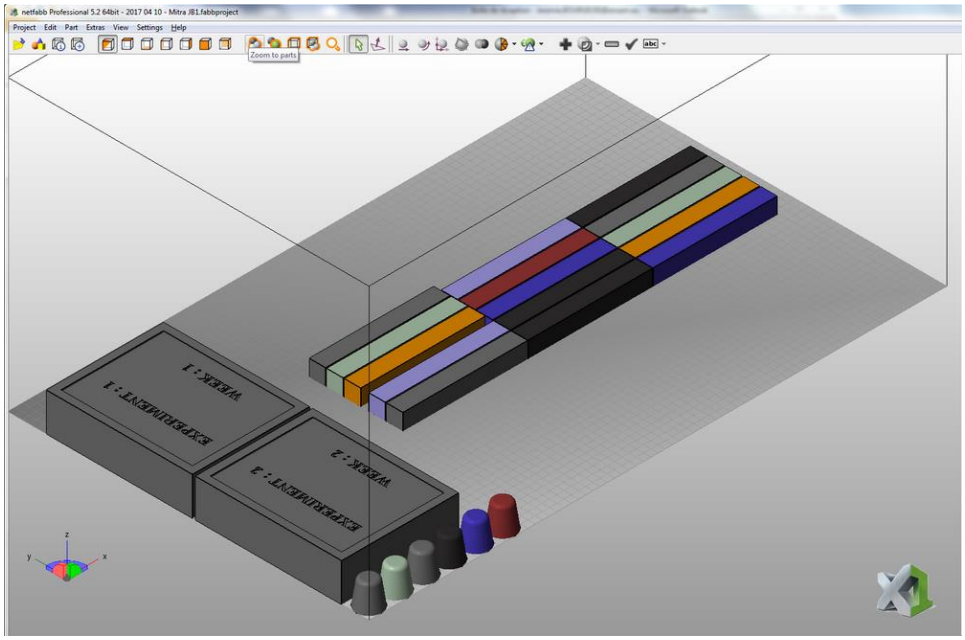

**Figure 12.** Schematic design of parts to be printed over job-box

The second experiment was designed, Fig.12, to assess the effect of print orientation on the 3PB strength; the first test specimens was in the X axis and the following were organized to have an angle difference of the famous golden or Fibonacci angle 137.508° to the previous. There were 5 test bars in the first layer and the rest were in the next 14 such layers in order to have no coincidence of any previous angle in the XY plane. Each bar was numbered from 1(0°/x-axis) to 71. The designed bars were inside a cylindrical cover in order to preserve the specimen for better curing and to naturally reduce the moisture content. The bars were then tested for 3PB strength.

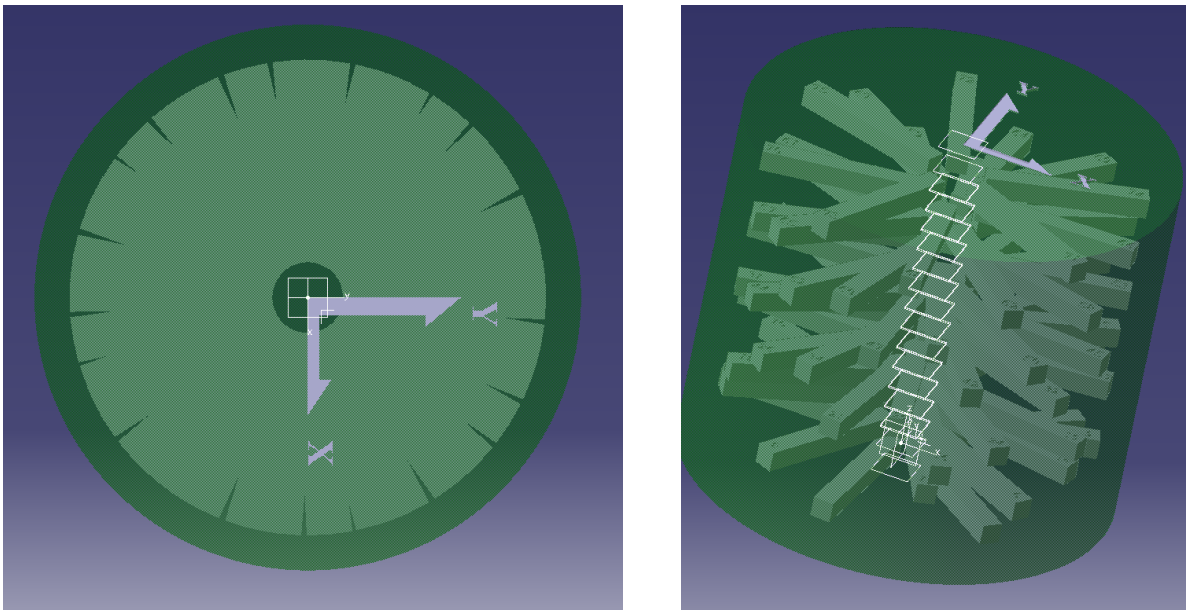

**a.** **b.**

**Figure 13.** Schematic design (a) top view, and (b) side view of the 3DP box with the specimens inside. Each layer has 5 3DP bars with an angle difference of 137.508°; the golden angle

### 3.1.3 Printing Parameters

The printing process parameters used, Table. 2, was based on the recommendation from the previous publication [67] for better 3PB strength.

**Table 2 The process parameters used for printing the specimens.**

| | |
|---|---|
| Recoating speed | 0.130 m/s (10%) or 0.182 m/s (14%) |
| X Resolution | 120 µm |
| Y Resolution | 101.6 µm |
| Z-resolution/Layer thickness | 280 µm |
| Print head voltage | 78V |
| Activator content(sulfonic acid) | 0.18% of the weight of sand |
| Infrared heating temperature | 32°C |
| Layers printed before printing each Job-Box | 13 |

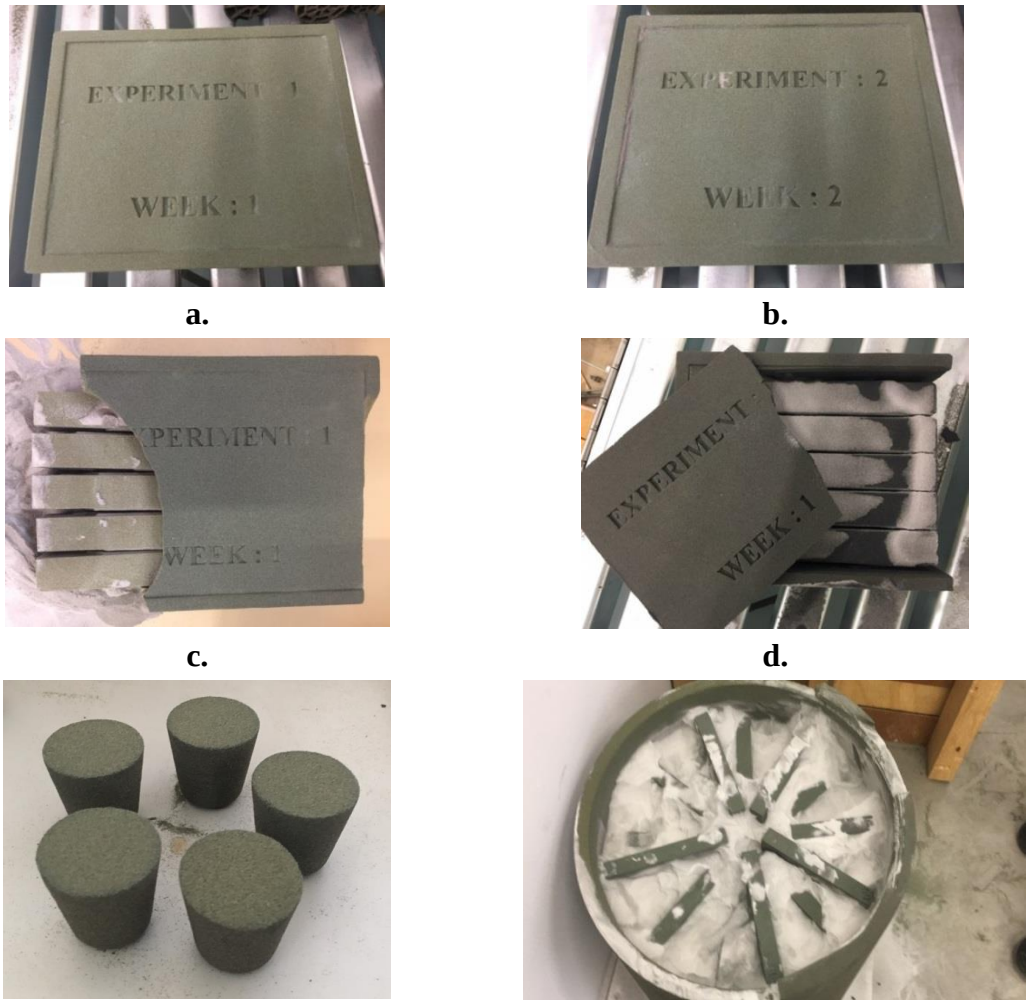


**Figure 14.** 3DP Boxes that with the 3PB test bars inside (a,b,c,d), specimens for LOI test (e), 3DP bars printed with an angle difference of 137.508°

### 3.1.4 Heat treatment and natural curing

Past research proved that high amount of binder present in a mold increases the strength of the mold, but the more amount gas will be generated during pouring liquid metal, resulting in shrinkage, incomplete filling and gas defects [19–22]. Hence, it is necessary to understand the influence of time and temperature on the strength of the 3DP bars present inside the 3DP box. At controlled room temperature, it is only the water which tends to evaporate gradually with time. At 100°C, since the boiling temperature of water is 100°C, here it is only the water which evaporates faster than at room temperature. So curing up to 192 hours (imitate the transport time) at room and 100°C temperature were chosen, in order to remove sufficient amount of moisture from the 3DP specimen, also retaining adequate strength. Two 3DP boxes with bars were printed and kept at room temperature, and two other boxes were printed and

were heat treated at 100°C for first 24 hours and were then cured at controlled room temperature for a period of 192 hours. Both the type of bars present inside the 3DP boxes was then compared as a function of LOI and mechanical 3PB strength and also the designed bars inside the cylindrical cover were also tested for 3PB strength.

### 3.1.5 Results

#### 3.1.5.1 Relative water content

The specimens were cured at room temperature for a maximum period of 192 hours. There is an increase in weight of the loose powder bed inside the box during the curing period, Fig.15, due to the absorption of water from the printed parts; fine sand particles adsorb water due to their high surface area to volume ratio. The increase in weight on the loose sand inside the 3DP box occurred during the initial stage of curing period was because of the adsorption mechanism of solvent present from the 3D printed part. There was a decrease in weight during the later stage which was because of the evaporation tendency of solvent from the entire box and loose sand.

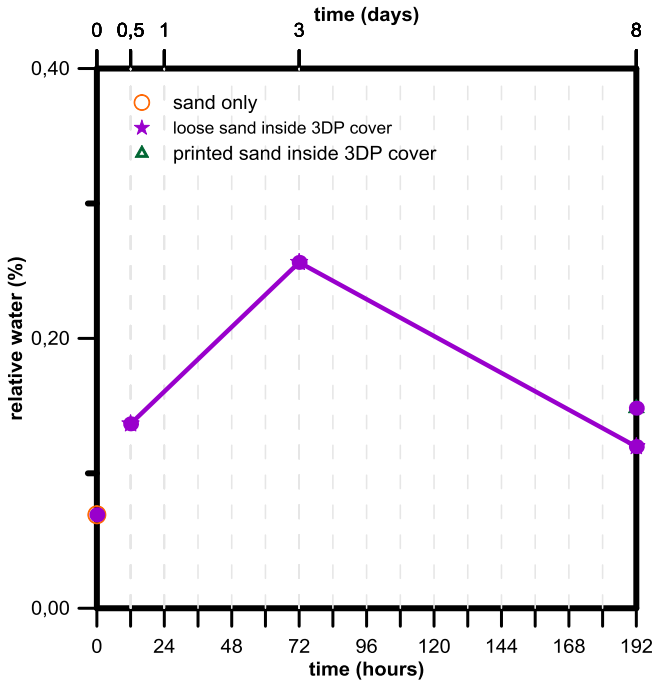


**Figure 15.** Relative water content over curing time

#### 3.1.5.2 Loss on Ignition

LOI results for both furan resin bonded 3D printed parts were provided, Fig.16. LOI values obtained for both set of parts were<1.6%. Both set of parts show that LOI decreased as the

ratio of time and relative water content. It is seen from the results that the LOI is much is lower for the 3DP box cured at room temperature and longer time, and this is because of the loose sand present within the 3DP box, which tends to adsorb the water present on the 3D printed sand mold. The result shows that the LOI is lower for the heat treated 3DP box than the one cured at room temperature. And this is because of two way curing, one is because of the initial curing by the loose sand present within the 3DP box, which tends to adsorb the water present from the 3D printed sand mold and the second one is due to the heat treatment at higher temperature leads to faster evaporation of water.

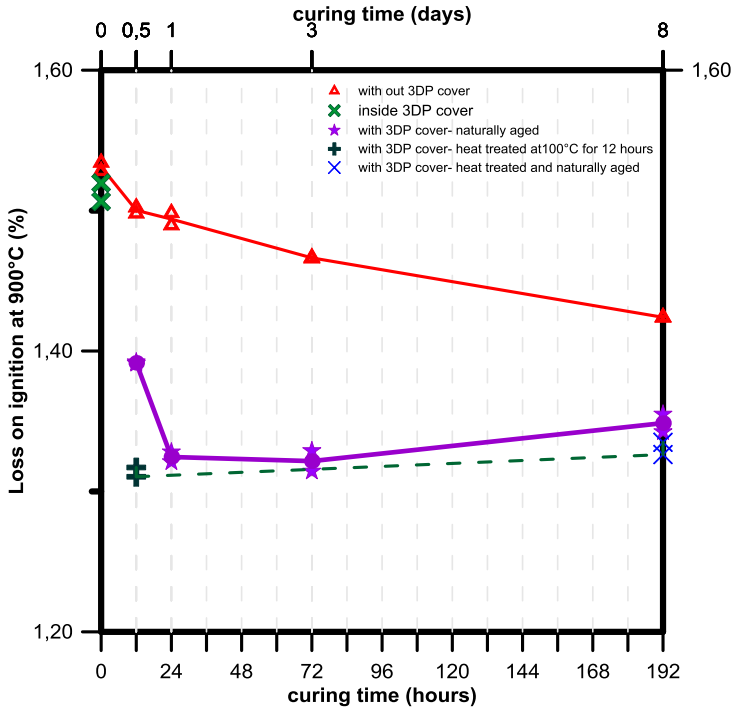


**Figure 16.** Loss on ignition over curing time

### 3.1.5.3 3PB Strength

3PB strength results for 3D printed parts were provided in Fig.17. At controlled room temperature, it is only the water which tends to evaporate gradually with time. At 100°C, since the boiling temperature of water is 100°C, here it is only the water which evaporates faster than at room temperature. So, curing up to 192 hours (imitate the transport time) at room and 100°C temperature was chosen, in order to remove sufficient amount of moisture from the 3DP specimen, also retaining adequate strength. It is identified that the three-point bending strength increases with increasing curing time at lower temperatures because of cross linked polymerization. The maximum 3PB strength achieved for both the specimens printed inside the 3DP box is nearly similar, which is great for the consideration and usage of 3DP

box for the transportation purpose, while undergoing heat treatment or curing while transportation.

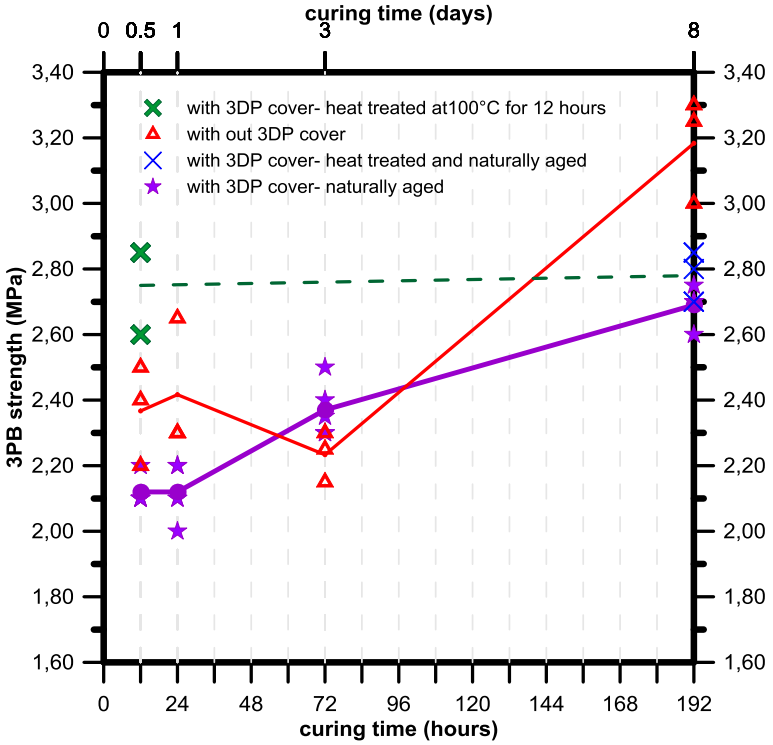


**Figure 17.** 3PB strength over curing time

Spreading of sand at higher speed by the recoater leads to non-uniform compaction of the sand bed and hence achieving less packing density due to high porosity. As the Furan Binder (FNB) is injected between the sand particles, these pores tend to get filled with the binder, hence reducing the pore size.

As the water tends to evaporate, the sand particles get tightly packed and hence increasing the 3PB strength of the 3DP specimen. When in room temperature, the evaporation is slower, hence a slow increase in 3PB strength. As the temperature is increased to 100°C, the water tends to evaporate more rapidly than at room temperature, hence achieving higher 3PB strength rapidly.

The main reason for the sudden increase in 3PB strength at lower temperatures in the presence of solvent (water and alcohol) tends to evaporate, and this leads to more volumetric reduction of resin bridges resulting in more 3PB strength. But for the 3DP box, water is adsorbed much faster by the loose sand present inside, which helps to control the rate of curing and hence slower rate of increase in 3PB strength.

Parts of a mold assembly printed along with the design of covered box helped the polymerization of furan resin to complete at its optimum. As the 3DP cover retains the acid which was mixed with sand before printing, the polymerization could continue until all monomer molecules were polymerized and the unbound sand particles around the bound particles helped the absorption of the byproduct, water, of this reaction and could have evaporated slowly through the porous media whereas in the case of printed parts kept outside may had been lost the activator, sulfonic acid, due to evaporation and hence the optimum reaction was not achieved and resulted in poor 3PB strength. The covered 3DP box did not only helped improving the strength of the printed parts but also a unique method to keep the parts of a certain assemblies together and ease the cleaning process of the job box.

The covered 3DP box also helped the safe storage and transport of these parts to another location with unique order number printed on it. The user can then break the 3DP cover and clean them before assembling these printed parts for casting to have the optimum dimensional tolerance of the mold.

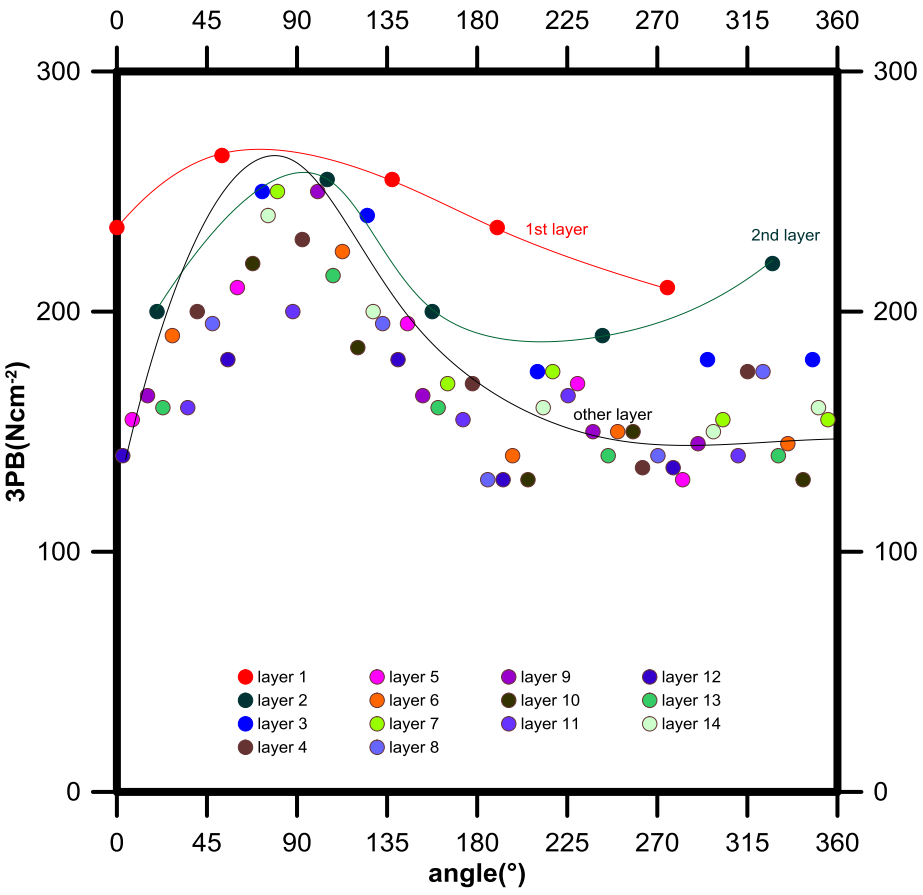


**Figure 18. 3PB strength over part printing position**

### 3.1.6 Conclusions

- ✓ The parts printed inside the 3DP box have similar 3PB strength but with reduced water content, which is an added advantage of curing while storage/transportation of 3DP molds from one place to another without causing any damage to the part due to the presence of loose sand bed around it.
- ✓ The 3DP box can be stored / transported directly after undergoing heat treatment, because this helps in removing maximum water content, and hence increasing the rate of polymerization, leading to achieving higher strength compared with the parts present inside non-heat treated 3DP box.
- ✓ Researchers can receive the part in most intact condition as possible due to the presence of the 3DP box around. Hence reduction of part cleaning issues by 3DP part suppliers hence increased rate of production.
- ✓ The desired part can be printed overnight and can be left inside the build platform (job-box), hence auto curing of part by adsorption mechanism by loose sand beside the 3D printed mold. This helps in reduction of heat treatment of 3D printed mold, which is more economical.
- ✓ The 3PB strength in y-orientation is more than double compared to others, Fig 18.

## 3.2 Effect of curing process parameters on 3DP sand mold

*This work has been published in the "International Journal of Advanced Manufacturing Technology" as:*

***Mitra, S., Rodríguez de Castro, A., El Mansori, M., 2018. The effect of ageing process on three-point bending strength and permeability of 3D printed sand molds. Int. J. Adv. Manuf. Technol. 97, 1241–1251. https://doi.org/10.1007/s00170-018-2024-8***

### 3.2.1 Introduction and Objective

The objective of the present work is to study the effects of curing parameters, i.e. curing time and temperature, on the strength and permeability of the 3DP sand molds. To do so, the aging mechanisms were experimentally investigated using a set of chemically bonded 3DP samples of the material used in casting applications. The evolution of the permeability and the three-

point bending strength of the samples was monitored over time and related to the amount of binder present in the 3DP mold. The amount of binder was characterized by means of Loss on ignition (LOI) experiments, the mechanical strength was measured through standard 3-point bending tests and the permeability was determined by measuring the air flow rate through the samples at a given pressure. The experimental results extended our understanding of the physics governing aging of the 3DP sand molds and provided rigorous criteria for the choice of the aging parameters.

### 3.2.2 Materials

The typical compositions of resin bonded sands used to produce casting molds and cores are 93-99% silica and 1-3% binder [52]. Silica sand is one of the most abundant materials on the earth's crust, and the commercially available standard sizes for mold production are 140 µm, 190 µm and 250 µm [68]. The average particle size distribution is shown below, Fig. 19, which was chosen for the investigated samples. The purpose of adding binder [54,55] is to give additional cohesion and strength to the powder, to ease the mold to retain its shape under a change in pressure, thermal expansion, and erosion when in contact with liquid metal.

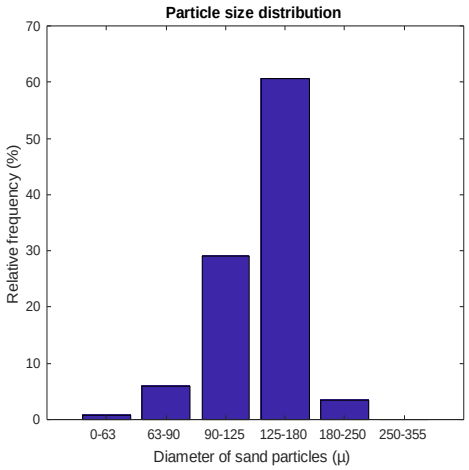


**Figure 19.** Grain size distribution

A Furan Binder (FNB) made up of an acid catalyst, furfuryl alcohol resin, urea and formaldehyde was used in the present experiments. Toluolsulfonic acid was used as catalyst to accelerate the generation a 3-dimensional chain network through acid-hardening reaction and polycondensation when added to the furan resin, leading to hardening of the binder. The FNB's condensation reaction produces water, which tends to slow down the cure rate (dehydration) [55].

### 3.2.3 Design of ageing mechanism experiment

A practical design of experiment was made, in order to determine the effect of ageing on the mechanical properties of the 3DP mold. According to the American Foundry Society standard dimensions, a rectangular bar of (172mm x 22.4mm x 22.4mm) and a cylinder of (Diameter 50mm, Height 50mm) was printed for the characterization of the mold. An interval of 2 hours was chosen in between each reading. Different curing temperatures were chosen for the ageing mechanism (Room temperature, 100°, 200°). A critical design of experiment was created in order to get the most accurate results. The printing process parameters were kept constant for all cases to get the nearest results for all the experiments performed.

First Job-box was printed, and numbers of samples were estimated as number of reading to be made with time as shown in Table II and were repeated with the same for second Job-Box. So, the first Job-Box was printed on Monday at 09:00 hrs with (18 bars and 18 cylinders). And the second Job-Box was printed on Wednesday with (12 bars and 12 cylinders) at 18:00 hrs and the reading was taken after curing it for 10 hrs in order to validate the results with the previous Job-Box. The same step was repeated for each temperature and the bending strength and permeability was determined.

### 3.2.4 Printing procedure and parameters

The specimens were first designed using Catia V5 [69], Fig. 20, and then converted into .stl format. Each sample was engraved with the specimen number to ease identification. The .stl file was transferred to NetFabb [70], which is a connected software for additive manufacturing and design. The Schematic design of a Job-Box in NetFabb is provided in Fig. 21. For the present work, the specimens were 3D-printed by means of the ExOne S-Print Furan [71] machine shown in Fig. 22, with a job box size of 800 × 500 × 400 $mm^3$.

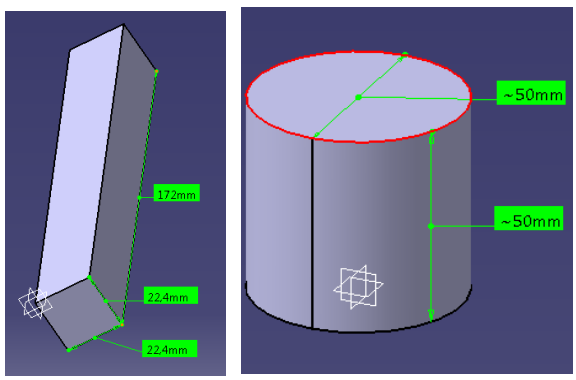


**Figure 20.** Schematic design of printed specimen on Catia

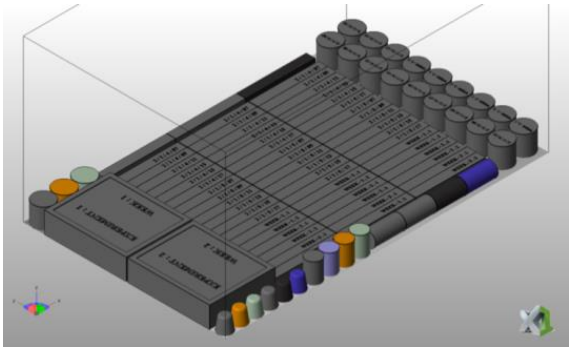

**Figure 21.** Schematic design of a Job-Box (NetFabb)

The printing process started by mixing sulfonic acid catalyst with 8 kg of silica sand particles inside a mixing chamber. Sand layers of 280-µm thickness were spread successively over the build platform (X-Y plane) and then a compacting force was applied over the sand bed by means of a re-coater. Then, the print head nozzle injected the liquid binding adhesive (furfuryl alcohol binder) on top of the sand layers to bind them. As the binder droplets are injected over the layer of acid activated sand bed, this facilitates the formation a thin coating of furan binder on each individual sand grain. When the surface of this binder coated sand grains crosslink with each other, there forms a nearly cylindrical binder bridge between the sand particles. This bridge is formed by capillary action shortly after the binder is applied and the respective strengthening mechanism occurs gradually over time. This makes the sand particles bond closer, experiencing surface tension and forming a strong binder-particle bridge. The 3DP sample is formed where the sand powder is bound to the liquid binding agent and unbounded sand remains surrounding the printed part. The entire process continues until the last slice of the sample is printed.

**Figure 22.** 3D sand printer used in the present experiments

The printed specimens were then taken out of the job box and de-powdered. During the process of de-powdering, the unbounded sand particles were removed using soft brushes and air-blown. The printing process parameters are listed in Table 1 and were chosen in agreement with preceding literature [67,72]. It is noted that spreading of sand at high speed by the recoater leads to non-uniform compaction of the sand bed and consequently lower packing density due to high porosity. In contrast, low values of recoating speed lead to high sand density, inducing greater flexural strength [22]. For this reason, 0.182 m/s (14% of the maximum achievable speed by the recoater-Sprint ExOne) were chosen. The print head voltage determines the volume of each furan droplet with the voltage set and was kept constant. Also, the printing resolution (furan drop spacing) was kept constant. The unbounded sand grains do not provide a good support for parts built higher up in the build volume, hence can lead specimens to sink into the excess powder during compaction [73–75]. Therefore the specimens were always printed over a thick sand layer of 1.4mm in the bottom of the job-box to neglect the sink issue and sub-layer displacements [73]. It is highlighted that quasi-identical binder contents were expected for all printed samples as the printing parameters were kept constant.

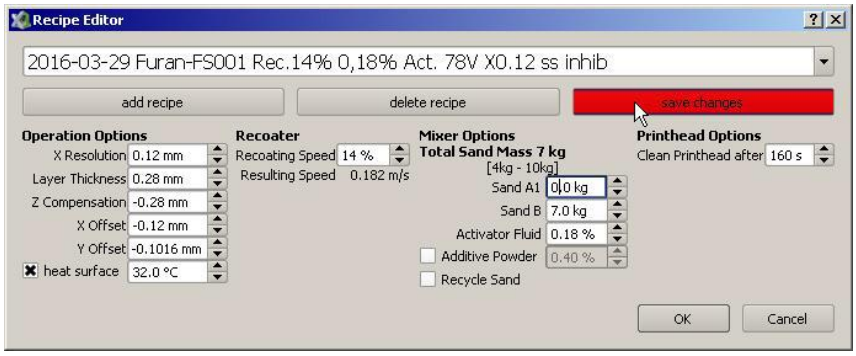


**Figure 23.** Printing recipe on ExOne 3D printer

**Figure 24.** 3D printed 3PB test bars and permeability specimens

**Table 3. Printing process parameters used with ExOne S-Print furan machine.**

| | |
|---|---|
| Average sand grain size | 140 µm |
| American Foundry Society (AFS) number | 97 |
| Recoating speed | 0.182 m/s (14%) |
| X Resolution | 120 µm |
| Y Resolution | 101.6 µm |
| Z-resolution/Layer thickness | 280 µm |
| Print head voltage | 78 V |
| Activator content(sulfonic acid) | 0.18% of the weight of sand |
| Infrared heating temperature | 32°C |

The specimens were printed inside a room with standard room conditions, at a temperature of 25 ± 1 °C and relative humidity of 40 ± 10%. 6 Job-Boxes (Fig 24) were printed. The process parameters were kept constant for printing all the job boxes. A total of 453 samples were printed: 324 bars with square section (172 x 22.4x 22.4 $mm^3$) for 3PB strength tests, 126 cylindrical specimens (diameter = 50mm, height = 50mm) for gas permeability tests and 3 cubic specimens for loss on ignition (LOI) tests. In order to have the standard error of the mean, 3 specimens were used each time for the 3PB test and 1 cylindrical specimen was measured 3 times for the permeability test. The specimens printed for the 3PB test and permeability tests were also used for the mass loss experiment, and for the calculations of the porosity of the specimens. Some of these samples are displayed in Fig. 24. The initial 3PB strength and permeability of the 3D printed specimens was measured after printing of the samples, obtaining 1.75 ± 0.5 MPa and 60 ± 7 GP, respectively. The procedures used to measure the mechanical strengths and the permeability of the samples are presented in sections 3.2.8 and 3.2.9, respectively.

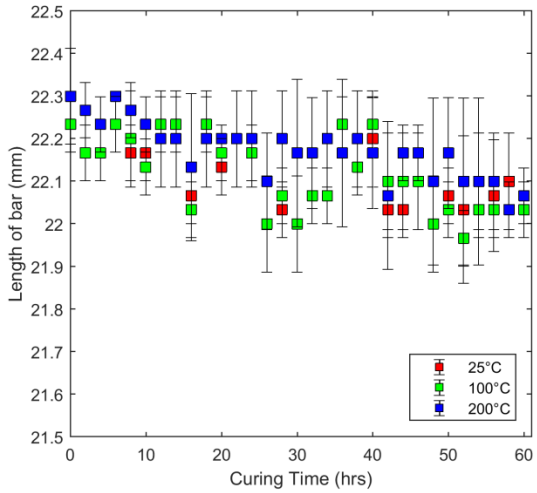


a. Precision on length of bars

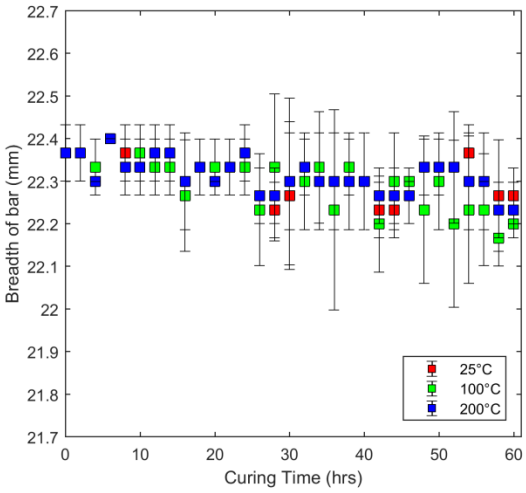


b. Precision on breadth of bars

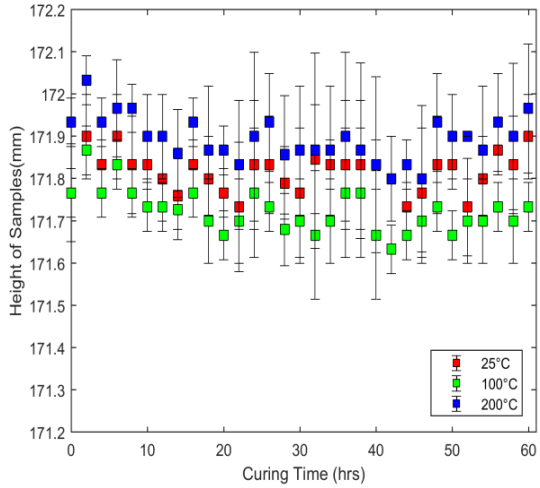


c. Precision on height of bars

**Figure 25.** Effects of curing temperature and time on the precision of the sand samples

The final dimensions of the 3D printed samples after curing at all temperatures and times are represented in the Fig. 25 as a histogram. It can be deduced that 90% of the sample lengths lie between 22 mm - 22.3 mm, 90% of the breadths lie between 22.2 mm - 22.4 mm, and 90% of the heights lie between 171.6 mm – 172 mm, which is close to the initial dimensions.

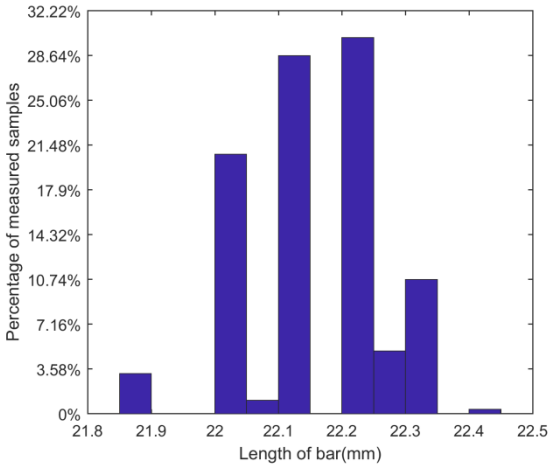


a. Precision on length of bars

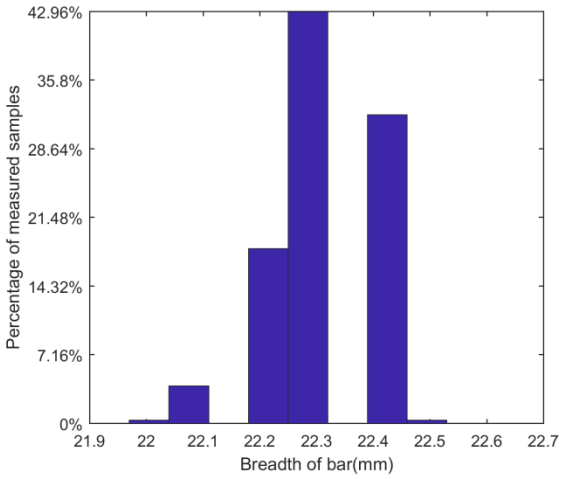


b. Precision on breadth of bars

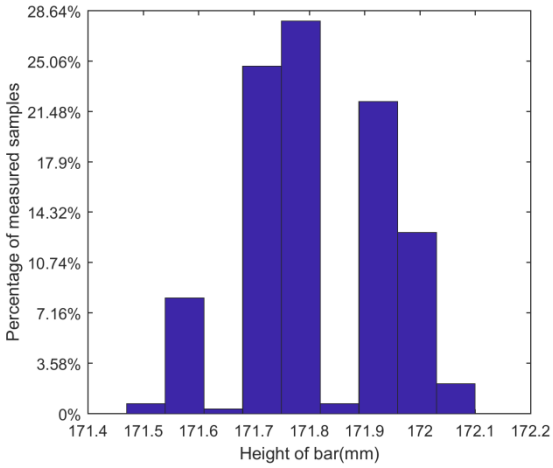


c. Precision on height of bars

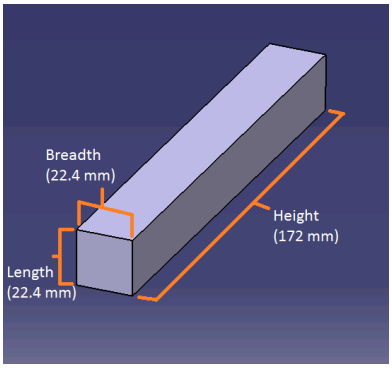


d. Dimension of bars with Catia

**Figure 26.** Precision of the 3D printed samples

### 3.2.5 Curing process

As mentioned earlier, the higher the amount of binder in a mold, the greater is its mechanical strength. However, higher amounts of binder lead to incomplete filling and gas defects. Therefore, it is necessary to understand the influence of curing time and temperatures on the amount of binder present in the sample and the resulting bending strength and permeability of the 3DP mold.

Since the boiling points at room conditions of water and furfuryl alcohol are 100°C and 180°C respectively, different curing temperatures were chosen to investigate the ageing mechanisms: 25º C, 100°C and 200°C. By doing so, the influence of the evaporation of each of these components on the 3PB strength and permeability of the 3DP mold could be evaluated.

The specimens were weighed every 12 h up to 60 h during storage at each curing temperature in order to assess the effect of mass loss rate during aging. Then, 3PB test and gas permeability tests were conducted at curing times ranging from 0 to 60 h. An interval of 2 hours was chosen in between measurements for the first 60 hours. After that, the specimens were tested once after every 7 days, and continued up to 54 days. The selected storage times were relevant for high-volume mold production and storage for a longer time. The initial strength of the 3D printed sand cores is important for manipulation of the mold after printing, and was tested 5 minutes after production. The results after 2 and 60 h are representative of the 3D printed mold/core properties at the beginning and end of a typical core usage in foundry practice, and the results from 60 h to 54 days are representative of the 3D printed mold/core properties during storage. All the bars for Three-Point bending (3PB) strength test, the cylindrical specimens for gas permeability test and the specimens for loss on ignition (LOI) test were cured.

### 3.2.6 Density and porosity

The porosity of the samples was evaluated through the oven-dry method [76]. The particle density was considered as being the density of $SiO_2$-quartz (2648 $kg.m^{-3}$), which constitutes 99.1% of the sand used by the printer. A laboratory precision balance, Fig. 26 was used to weight the printed specimens after drying in a hot-air oven at 105°C for 24 hours [44], and the bulk density of the 3DP specimen was calculated as the mass of sample per unit bulk volume. It is worth reminding that both the volume of solid and the volume of pores are taken into account for the calculation of bulk density. In contrast, the particle density is equal to the mass of sample per unit volume of silica sand particles. From the bulk density and particle density, the total porosity of the 3DP specimens was calculated as $\varepsilon = (1 - (\text{Bulk density})/(\text{Particle density})) \times 100$. The experimentally measured porosity values were close to 49% for all tested samples, with an estimated standard deviation of 0.2%. This porosity value roughly corresponds to the theoretical porosity of a simple cubic packing (~48%).

**Figure 27.** KERN Laboratory precision balance

### 3.2.7 Loss on Ignition (LOI) testing

Loss on Ignition is a widely used procedure to measure the amount of moisture, binder and impurities present in the sample through ignition at high temperatures. 3 3DP specimens were printed for this test, and the weight was close to 30g (initial mass) in all cases in agreement with previous works [31]. These specimens were then put into the ceramic crucibles. Before filling, the crucibles were pre-heated at 100°C in an oven to extract moisture and organic residues. After that, the 3DP specimens were put inside the crucibles and heated at 900°C for 30mins to burn-out and expel the binder and moisture. Then, the crucible was removed from the oven, and weight of the crucible was measured. The final mass is the weight of the burnt out specimen. LOI was then determined from Eq. (1):

$$\text{LOI} = \frac{\text{Initial mass} - \text{final mass}}{\text{Initial}} \times 100 \quad \% \qquad \textbf{Eq. 1}$$

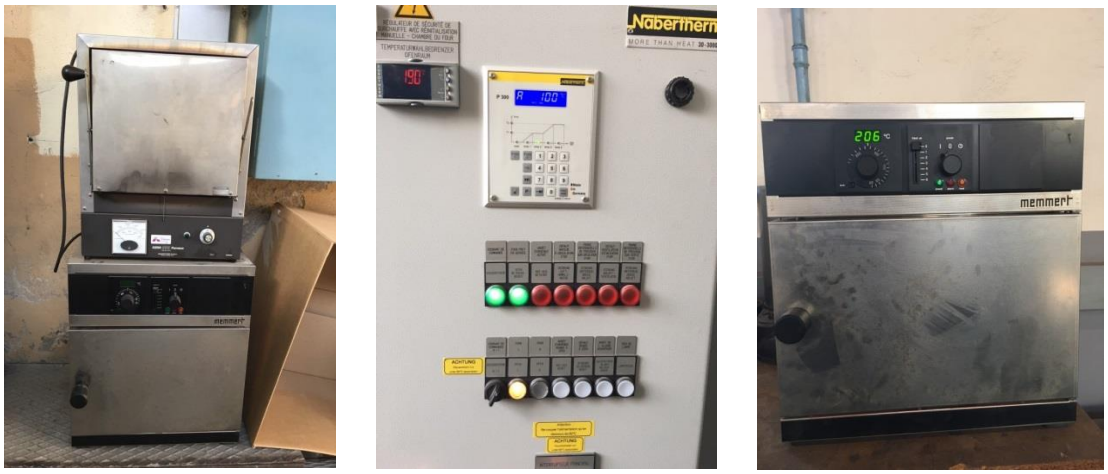


**Figure 28.** Ovens used for accelerated curing

Photos of the crucibles containing the tested samples at the different stages of the LOI tests are provided in Fig. 29. An average mass loss of 1.41%, with an estimated standard deviation of 0.02%, was measured by the LOI tests performed on the sand mold samples. The low variability observed in the measured mass loss values of the tested samples was an indicator of the high reproducibility of the binder dosage process.

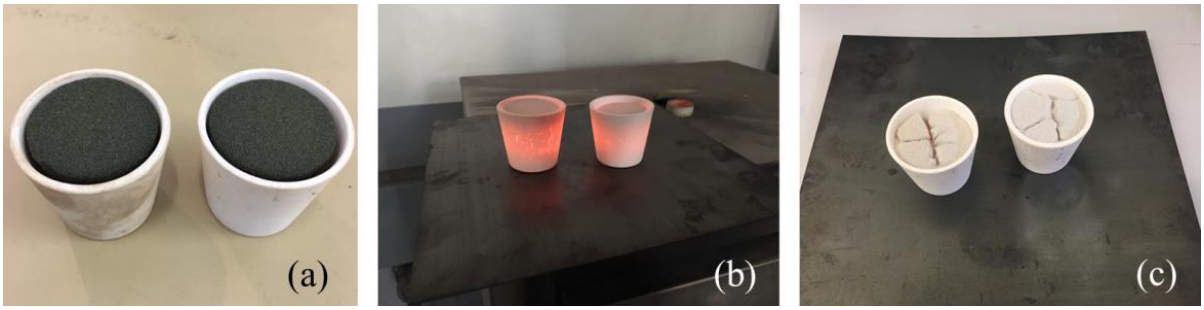


**Figure 29.** LOI test crucible with(a) powdered 3DP specimens, (b) immediately after taking out of the oven at 900 °C and (c) after cooling it to 150 °C, before measuring the mass loss

### 3.2.8 Three-point Bending test

The bending strength of the 3DP specimens was determined using a 3PB test, which is a destructive method commonly used for testing traditionally prepared sand molds. To determine the 3PB strength of the 3DP specimens, bars with a square section of length b = 172 mm, and width d = 22.4 mm were printed. 3PB tests were performed on the 3DP bar specimens using a universal strength test machine (Simpson-Electrical, Type: PFG, Serial No.3290, Item No.592-824-600, Year:2013) [77,78], shown in Fig. 30. This universal strength machine is widely used to measure the strength of resin bonded sand molds. The test fixture constitutes of two supporting pins, with a separation distance of l =150 mm. The load applied by the third pin was progressively increased at a rate of 0.1 MPa.$s^{-1}$ until the samples broke and the 3PB strength was determined. The measuring range of the machine covered up to 12.8 MPa, with an uncertainty of ±0.05 MPa. Also, the same specimens were weighed before the 3PB test to measure the evolution of mass loss over time during the aging process.

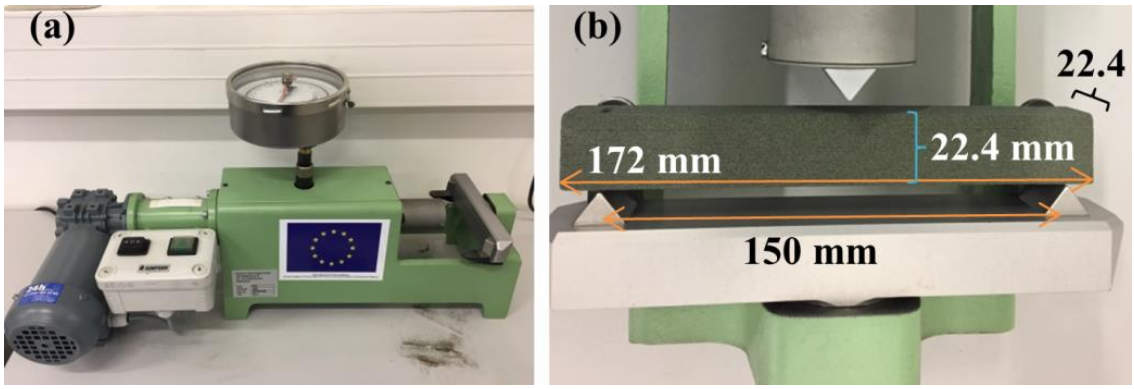


**Figure 30.** Universal strength machine for the 3PB test [78], (a) front view and (b) bar dimensions

### 3.2.9 Gas permeability test

A permeability measurement device (Simpson-Electrical, Type: PFG, Serial No.3290, Item No.592-824-600, Year:2013) [79] was used in the present experiments to measure the gas permeability of the 3DP sand mold samples. The standard orifice method was applied following the recommendations of the American Foundry Society (AFS). The gas permeability value (GP) gives the volume of air in $cm^3$ which passes through a cylinder, having a cross-sectional area of $1cm^2$ and a height of 1 cm, in 1 minute at a pressure of 100 mm SPWG (Static Pressure Water Gauge). The relationship for the calculation of GP is expressed by the following formula, Eq. 2:

$$GP = \frac{V \times h}{F \times p \times t} \qquad \textbf{Eq. 2}$$

where, V is the volume of air flowing through the tested sample, h is the height of the sample , F is the cross-sectional area of the sample, p is the pressure in mm Static Pressure Water Gauge (SPWG) and t is the passage time for 2000 $cm^3$ of air in minutes. In the present tests, the values V = 2000 $cm^3$, h = 5cm, F = 19.63 $cm^2$ and p = 100 mm SPWG = 980 Pa were used [79–81] and the resulting t was measured. The viscosity of the fluid (air) was taken as $1.8 \times 10^{-5}$ Pa sec. Cylindrical samples with a diameter of d = 50mm and length of l = 50mm were used in these tests. The flow rate was measured with the digital permeability meter (Simpson-Digital permeability meter) [79] shown in Fig. 30, which has a measuring range of 0-1000 GP. It should be noted that Eq. (5) does not provide k as defined by Eq. (1). Indeed, GP obtained from Eq. (5) is gas viscosity-dependent while k obtained from Eq. (2) does not depend on the physical properties of the injected fluid. However, GP is commonly used in

foundry industries, following the recommendations of the American foundry society (AFS). Consequently, the results of permeability measurements will be presented in terms of GP in this work.

**Figure 31.** Universal machine used for the gas permeability test[79]

### 3.2.10 Results

The ageing effect on weight loss, 3PB strength and permeability were experimentally investigated using the tests presented in the preceding section.

#### 3.2.10.1 Mass loss

The results in terms of mass loss as a function of curing time are presented in Fig. 32. It can be noted that, as expected, the total weight loss after curing was lower for 25°C and 100°C° than it was for 200°C. It was also observed that the evaporation rate increased with increasing curing times at 200°C. The amount of weight loss at 200°C was higher after 36 hours, due to the evaporation of both alcohol and water. Although the 3PB test were performed for all the specimens heat treated at 200°C, but it was not possible to measure the weight loss accurately after 36 hours due to loss of little sand particle while handling.

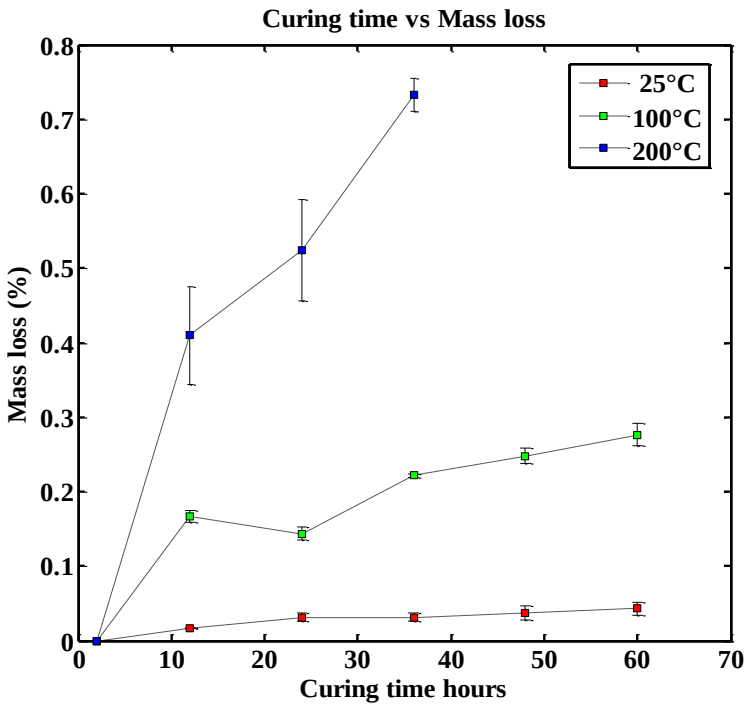


**Figure 32.** Critical effect of curing time and temperature on mass loss of specimens

### 3.2.10.2 3PB strength

The 3PB strength of the samples is presented in Fig. 33 as a function of the curing time for the three curing temperatures. From this figure, it can be deduced that bending strength remains approximately constant over time in the case of curing at 25ºC and 100ºC, apart from an initial increase in strength. However, a different tendency was observed when curing at 200ºC. Indeed, the bending strength decreased over time, roughly monotonically, for this curing temperature. Moreover, the values of 3PB obtained by ageing at 25ºC and 100ºC were very close and significantly greater than those obtained by ageing at 200ºC. It was noted that the measurements at 200ºC did not cover the full range of times up to 1296 h as the bending strengths were too low and did not fall within the working range of the apparatus for the further measurements.

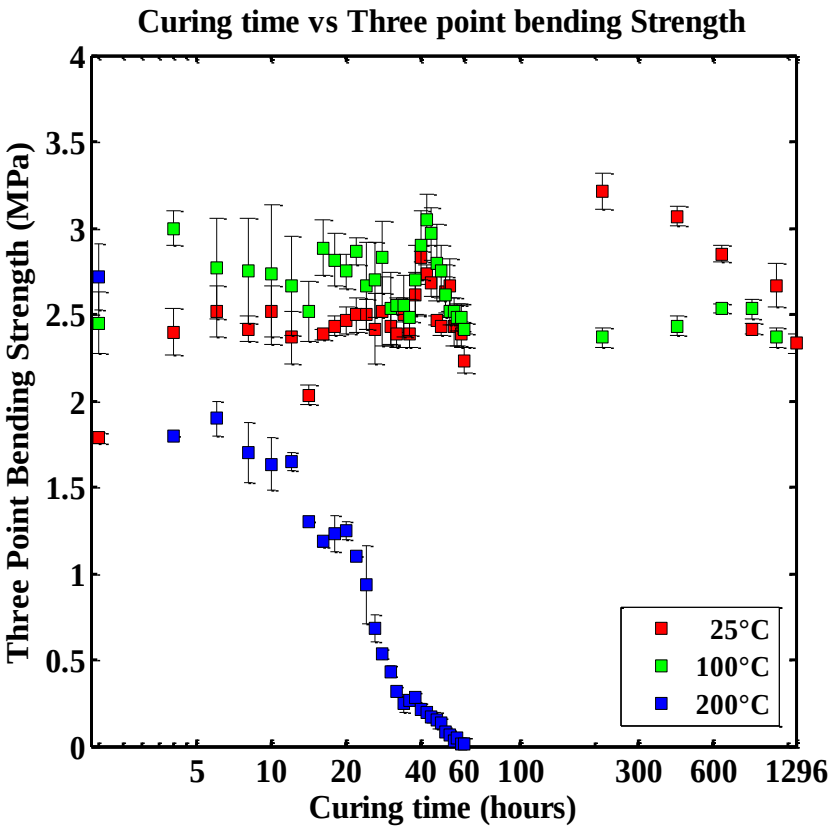


**Figure 33.** Critical effect of curing time and temperature on 3PB strength of specimens

### 3.2.10.3 Permeability

The permeability values of the mold samples measured at different curing times are presented in Fig. 34 for the three investigated curing temperatures. From this figure, the results showed that permeability remained approximately constant over time in the case of curing at 25ºC and 100ºC. However, a decrease in permeability over time was remarked when curing at 200ºC. Also, the permeability was shown to decrease with curing temperature, and the reasons will be discussed in section earlier.

The results in terms of mass loss as a function of 3PB strength and permeability were presented in Fig. 36 and 37. The mass loss at low temperatures may be explained by rapid evaporation of solvent. Moreover, a second stage occurs at high temperature when the resin bridge becomes brittle and breaks for prolonged heating at high temperatures, leading to loosening of powdered particles. Fig.9 shows that the 3PB strength was higher at 100°C as compared to the samples at 25°C, but decreased gradually at 200°C. However, permeability decreased with increased mass loss as can be observed in Fig.10. This is in contrast with the results obtained by previous researchers [24] and will be discussed in the following section.

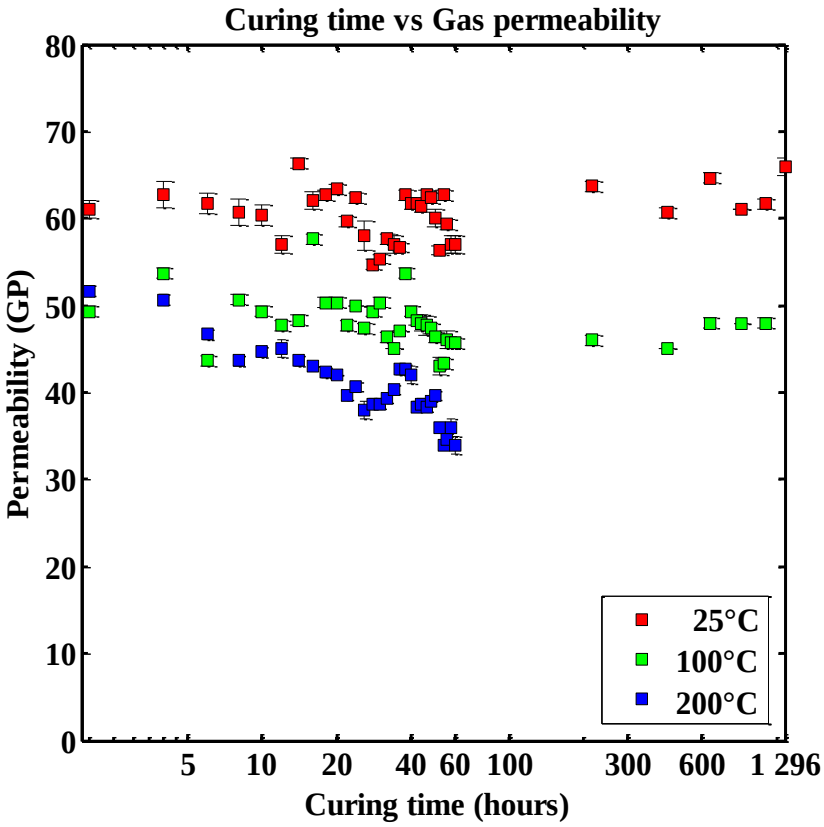


**Figure 34.** Permeability of the samples vs. curing time at different temperatures

### 3.2.11 Discussion

FNB binder is a simple two-part binder system made up of an acid catalyst and a reactive furan-type resin. The addition of an acid catalyst to a furan resin causes an exothermic polycondensation, which hardens the binder. The FNB's condensation reaction produces water, which tends to slow the cure rate (dehydration), Fig. 35. The bond producing reaction is the further polymerization of these chains with cross-linking.

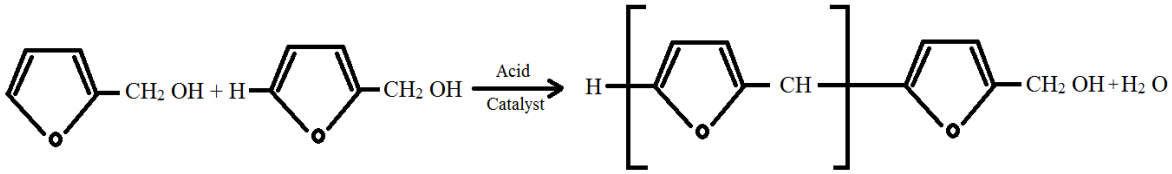


**Figure 35.** Furan binder chain reaction

The solvent present in the binder is volatile and evaporates during the ageing process, leading to shortening and hardening of the resin bridges. Only water experiences significant evaporation with time at 25º C. Also, water evaporates faster at 100°C than it does at 25º C (the boiling temperature of water is close to 100°C under the experimental conditions of our tests), which results in higher values of mass loss as reported in Fig. 31. On the other hand, the boiling temperature of furfuryl alcohol is 180°C, so it is the mixture of water and alcohol which experiences significant evaporation when curing at 200°C. The higher rate of evaporation at 200ºC leads to higher values of weight loss as shown in Fig. 32. The increase of evaporation rate with increasing curing time reported at 200ºC may be related to the increase in the area of the free surface of liquid (binder + water) with time. Indeed, the specific surface area of the liquid is expected to increase as it progressively evaporates, resulting in higher evaporation rates.

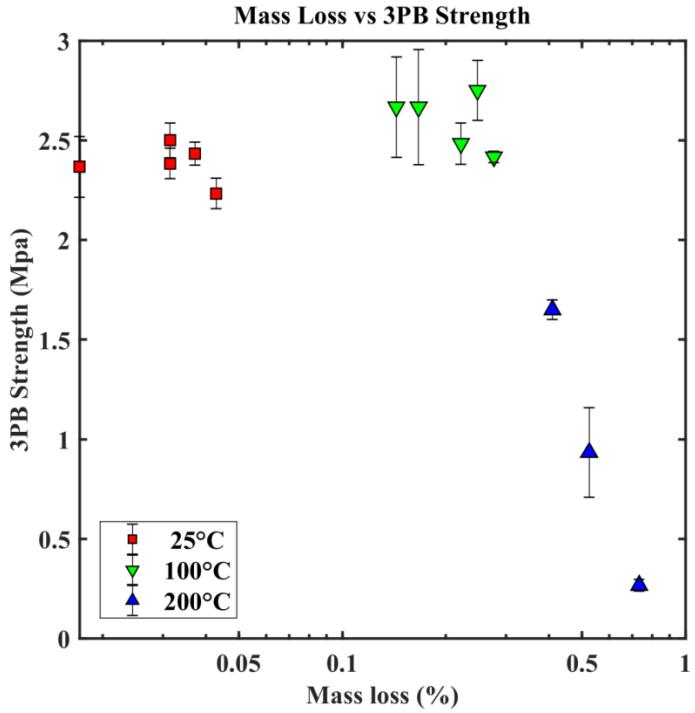


**Figure 36.** 3PB strength vs. mass loss for the three curing temperatures

It was observed in Fig. 33 that the 3PB strength experienced an initial increase before becoming constant with time after ~ 4h for 25ºC and 100ºC. This effect is generally associated with water being released during polycondensation occurring at the initial stages of curing, which leads to cross linked polymerization stemming from exothermic polycondensation [29]. This hardens the resin bridges between sand grains, providing greater

mechanical strength (3PB) to the 3DP specimen. Moreover, the polymer chain network is expected to break gradually at 200°C as the alcohol evaporates. This results in lower 3PB strength, of the 3DP specimens as presented in Fig. 33, in good agreement with the results of previous researchers [24].

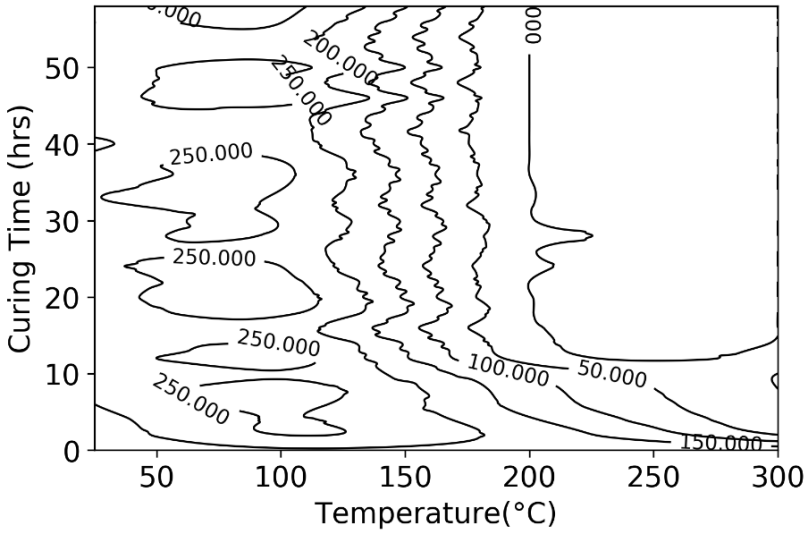


**Figure 37.** 3PB strength vs. curing time and temperatures

In the case of the present experiments, the furan system is a thermosetting resin (duroplast) which forms an insoluble infusible 3-dimensional polymer network chain through polymerization during curing stage [29]. The gradual increase in strength at lower temperatures (25°C, 100°C) may be related to the evaporation of the solvent, which causes shortening and hardening of resin bridges. This leads to both a gradual increase in 3PB strength and shrinkage of the mold [26]. The shrinkage of the mold samples during curing was also reported in previous works [26,82,83]. Therefore, an increase in ageing time causes more volumetric reduction of furan resin bridges, which results in more shrinkage and reduction of pore space between sand grains [26,27], thus leading to lower gas permeability values. This is consistent with the results presented in Fig. 34.

The FNB is injected between the sand particles, filling the interstices and reducing the effective pore size available for gas flow. This presence of binder layers that settle on the grain walls results in permeability reduction as predicted by Eq. (17). Consequently, as the binder evaporates, the effective pore size should increase leading to higher permeability values. However, shrinkage occurs simultaneously, so the sand particles should also become more tightly packed as they are dragged by the remaining binder. As a result, the variation in

permeability during binder evaporation is expected to be the combination of both effects. Given that Loss On Ignition is low (1.41%), the volume fraction of the pores occupied by binder should be also low. Therefore, shrinkage is expected to be the dominant mechanism which explains the reduction in permeability.

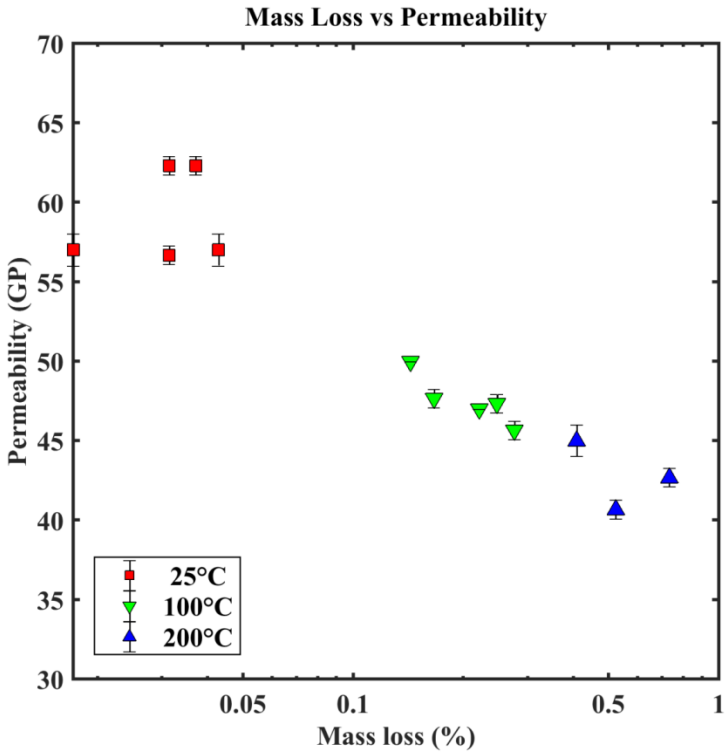


**Figure 38.** Permeability vs. mass loss for the three curing temperatures

Using Eq. (17), a permeability of 4.9 $\times 10^{-11}$ $m^2$ (or) 49 Darcy is predicted for a sand packing with porosity 0.49 and grain size of 140µm, which is close to the measured value k = 5.57$\times 10^{-11}$ $m^2$ (or) 56 Darcy provided by Eq. (2) for the present experiments. The slight difference between prediction and experiments may be explained by the presence of binder within the pores, which increases the effective $d_s$ in Eq. (17). Indeed, if the experimentally measured value of permeability value (k=56 Darcy) is used in Eq. (17), an effective grain diameter of ~ 155 µm is obtained. It is reminded that Eq. (17) provides accurate predictions in the case in which the volume fraction of binder (determined by LOI tests) is low.

The GP values obtained with the current technique are viscosity-dependent as can be deduced from comparison between Darcy equation (Eq. 5) and GP equation (Eq. 2). However, gas viscosity increases with temperature, thus generating greater pressure losses for the same flow rate at higher temperatures. Neither are other effects such as inertial pressure losses, fluid's

compressibility or slip on the wall taken into account by the permeability tests currently used in casting industry. Therefore, a new approach should be developed to obtain more accurate permeability values, which should improve the prediction of casting defects. Also, the three-point bending test can only be used for measuring the strength in a particular region of the 3DP specimen, so a different approach should be used to characterize the global strength of the samples.

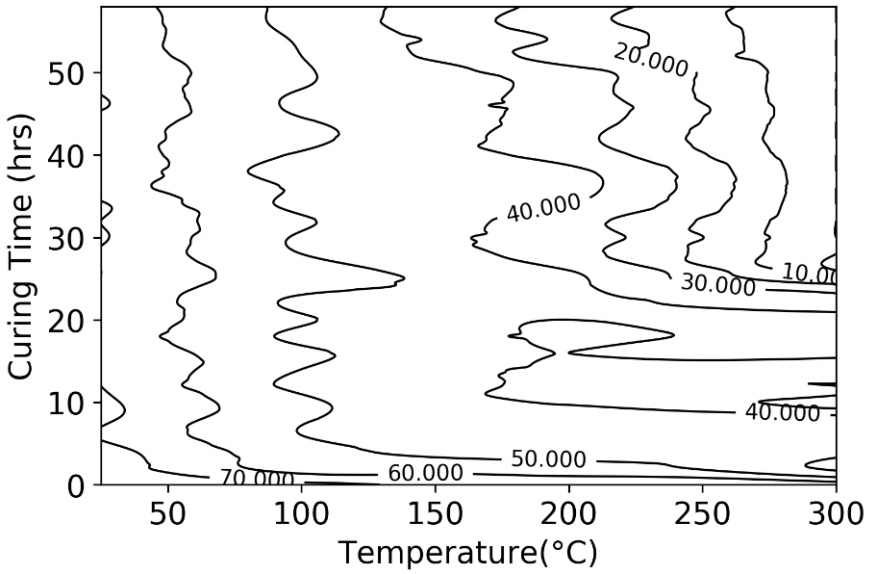


**Figure 39.** Permeability vs. curing time and temperatures

### 3.2.12 Conclusion

The effects of curing time and temperature on the permeability and 3PB strength of 3DP sand mold samples were experimentally evaluated. Both permeability and 3PB strength were shown to be altered by the curing process under certain conditions. Hardening of the binder and shrinkage of the mold arising from polycondensation reaction of the binder, which is a cross-linked, high-strength thermoset, may explain this. The following industrial implications are drawn:

- ✓ The printed molds can be stored at room temperature for a long time before being used, roughly preserving the initial values of 3PB strength and permeability.
- ✓ From the bulk density and the particle density values of the 3DP mold, the sand grains can be packed in a simple cubic structure, obtaining a porosity of 48%.
- ✓ Despite not taking into account the volume of binder in the pores, the prediction provided by Kozeny–Carman equation was in good agreement with experimental

permeability measurements obtained with a standard permeameter. This is explained by a low fraction of the pore volume being occupied by the binder, as deduced from the LOI tests.

- ✓ The permeability of the 3D printed specimen decreases with increasing temperature, which is potentially due to shrinkage of the 3DP sand mold.

## 3.3 Effect of Binder percent on 3DP sand mold

*This work has been published in the "Journal of Manufacturing Processes" as:*

***Mitra, S., Rodríguez de Castro, A., El Mansori, M., 2019. On the rapid manufacturing process of functional 3D printed sand molds. J. Manuf. Process 2019; 42:202-12. https://doi.org/10.1016/j.jmapro.2019.04.034***

### 3.3.1 Introduction and Objective

The improvement of three-dimensional (3D) printing technology has enabled the rapid manufacturing of sand molds for metal casting directly from computer models. Despite recent progress, it is still unclear how the microstructural characteristics of the resin-bonded sands, which are strongly altered by the presence of binder, affect both the mechanical and mass transport properties of the 3D Printed (3DP) sand molds. The objective of this work is to print functional sand molds and experimentally investigate the effects of binder content on the three-point bending strength and the permeability of 3DP sand molds at different curing conditions. To do so, several sets of samples were produced with a 3D printer using silica sand and three different mass fractions of furan resin binder. These 3DP samples were subsequently cured using different curing times and temperatures. Then, the pressure drop across the 3DP specimen was measured as a function of the injection flow rate in order to determine the permeability of the samples and quantify the inertial pressure drops. Also, the mechanical strength of the samples was characterized using traditional three-point bending strength measurements. Moreover, Loss-On-Ignition (LOI) tests were performed in order to monitor the mass loss during the curing stage and evaluate its effects on the variation of the investigated properties. The present results show that the mechanical strength of the printed molds is deeply dependent on the amount of binder and the aging process. In contrast, no significant effect of the amount of binder on the initial permeability of the samples before

curing was observed within the functional range of binder mass fraction (1.02 to 1.98%). Therefore, the mechanical strength of the sample can be optimized within the investigated range of binder contents without resulting in any significant decrease in permeability.

### 3.3.2 Materials

The raw materials used in the present experiments were quartz silica sand and a furfuryl-alcohol-based binder (furan resin) of density (1.1-1.2) g/cm³. The silica sand grains had regular spherical shape, with a mean diameter of 140 µm and a standard deviation of 25 µm, which corresponds to American Foundry Society (AFS) size number 97. The furan binder was a mixture of furfuryl alcohol (70-90 wt%), bisphenol A (5-15 wt%), resorcinol (1-10 wt%) and 3-aminopropyltriethoxysilane (0.1-0.2 wt%).

### 3.3.3 3D Printing stage

The specimens were first designed with Catia and was then transferred to the commercial software NetFabb$^{TM}$ [70], and were then converted to .stl format. The rectangular bar specimens for the 3 PB test were intitially designed with length of 172 mm, breadth of 22.4 mm and with height of 22.4mm. And the cylindrical specimens for the gas permeability test were designed with diameter of 30 mm and height or length of 75 mm. Then, the designed samples were fabricated by the help of ExOne S-Print Furan 3D printing machine [71], which has a job-box size of 800 × 500 × 400 mm$^3$. Job-box is defined as the place over which where the specimens were to be 3D printed. The process of 3D printing of specimens began by adding sulfonic acid (0.18 wt% of the sand) catalyst with 8 kg of silica sand grains inside the mixing chamber of the 3D printer. The sand-catalyst mixture was then subsequently transferred to the re-coater chamber. The 3D printing started by adding successive layers of sand grains over the build platform (job-box) and then a compacting force was applied over the spread sand powder bed by the help of a re-coater head. Then, the furfuryl alcohol binder was injected on top of these spread sand powder layers to bind them together, by means of a print head nozzle. A coating layer of furan binder was formed on top of each individual sand grain, as the droplets of furan resin binder (furfuryl alcohol) were dropped over the layer of sulfonic acid-activated silica powder sand bed. The surface of this furan resin-bonded sand grains crosslink with each other, forming a bridge of resin binder between the silica sand particles formed by capillarity and gravitational forces immediately after application of the binder. Then, and a hardening mechanism progressively occurs during curing, making the sand particles bond closer as a result of surface tension and forming a strong resin binder-

particle bridge. The process continued until the last slice of the sample was printed and the final two sand layers spread.

Previous experiments were performed to evaluate the effect of printing speed on the quality and part integrity [84]. It was concluded that an increasing printing speed would influence not only the dimensional accuracy but also the mechanical strength of the 3DP parts due to enhanced inertia forces. It is to be noted that a higher recoating speed also leads to non-uniform spreading of sand over the job-box and low compaction of sand bed, generating lower packing densities and high porosities. On the other hand, it is known that low recoating speed leads to high sand packing density, and consequently to greater flexural strength [22].

**Table 4. Printing process parameters used with ExOne S-Print furan machine**

| | |
|---|---|
| Average sand grain diameter | 140 µm |
| American Foundry Society (AFS) number | 97 |
| Recoating speed | 0.182 m/s (14%) |
| X Resolution | 80 µm, 120 µm and 140 µm |
| Y Resolution | 101.6 µm |
| Z-resolution/Layer thickness | 280 µm |
| Print head voltage | 78 V |
| Activator content(sulfonic acid) | 0.18% of the weight of sand |
| Infrared heating temperature | 32°C |

The recommended process parameters for minimal variation in 3PB strength and permeability along the job-box were selected according to Ref. [1,67,72] and are listed in Table 4. The recoating speed was kept constant throughout the printing process and only the printing resolution (furan drop spacing) was altered to achieve different binder percentages. It was highlighted in previous works that loose sand does not provide a good support for the 3D printed parts to build higher up in volume, and results in specimen sinking over the powder bed during compaction [73–75]. Therefore, the specimens were printed over a thick sand layer of 1.4 mm (around ten layers of sand) in order to avoid sinking, sub-layer displacements [73] and sticking of the resin-bonded sand to the job-box. A total of 150 (50 × 3 different binder content) cylindrical specimens were printed for permeability tests. Also, 90 (30 × 3 different binder content) rectangular bars were printed for the 3PB tests and (6 × 3 different binder content) 18 specimens were produced for loss on ignition (LOI) tests. The initial dimensions

of the 3D printed parts (bars) were measured using a Vernier caliper, with length, breadth and height of 22.3 ± 0.02 mm, 22.2 ± 0.02 mm and 171.9 ± 0.07 mm, respectively (the uncertainty corresponds to 95% confidence interval). The initial dimensions of the 3D printed parts (cylinders) were also measured using a Vernier caliper, with length of 74.9 ± 0.01 mm and diameter of 34.8 ± 0.02 mm with 95% confidence interval. The temperature of the printing room was 25 ± 3 °C and the relative humidity 40 ± 10%. After printing, the samples were then de-powdered, cleaned and taken out of the job-box.

To go further, scanning electron microscope (SEM) images were obtained using 3DP specimens of 5mm in diameter and height, to verify the furan resin bridges between sand particles. SEM images were obtained with a scanning electron microscope JEOL JSM-7001F. Micrographs of 3DP samples were obtained in low vacuum (0 - 40 Pa) with acceleration voltage of 5 kV at a 100 µm working distance for different magnifications. The scans were acquired and the obtained images were subsequently analyzed and processed using median filter with the open-source platform for image analysis Fiji-ImageJ [85], in order to differentiate between the sand particles, the pores and the furan resin bridges. Samples of SEM images are presented in Figure 40, showing the morphology of the furan resin bridges within a cross-section of the 3D printed sample.

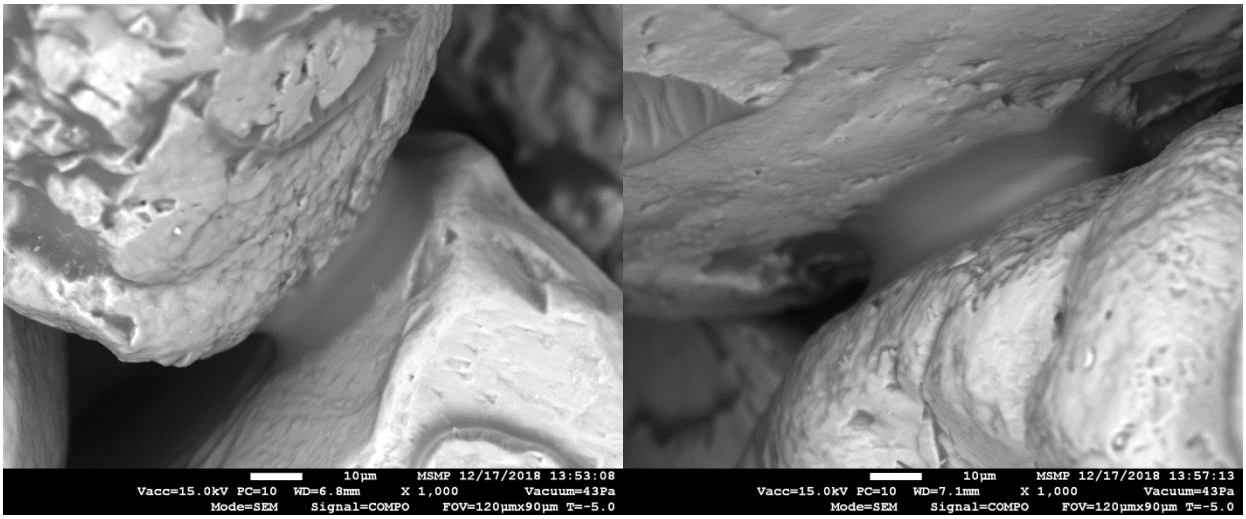


**Figure 40.** Scanning electron microscope (SEM) image of the 3DP sample, (a, b) zoom showing the resin bridges

### 3.3.4 Curing stages

Despite providing superior mechanical strength to the 3DP parts, high binder amounts can also generate a decrease in permeability, as the pores get filled with liquid. Also, more binder

leads to more off-gassing of the 3DP sand mold and the molds suffer from excessive moisture generated from polycondensation reaction (dehydration) after printing. Therefore, samples with usual mass fractions of binder require initial curing in order to remove excess moisture content which affects their 3PB strength and permeability. For this reason, oven curing was performed up to 60h at low temperatures to investigate its effect on the mechanical properties of the 3DP mold [1]. The binder percentage was measured after this initial curing stage by means of LOI test.

**Figure 41.** Samples heat treated inside oven for accelerated curing

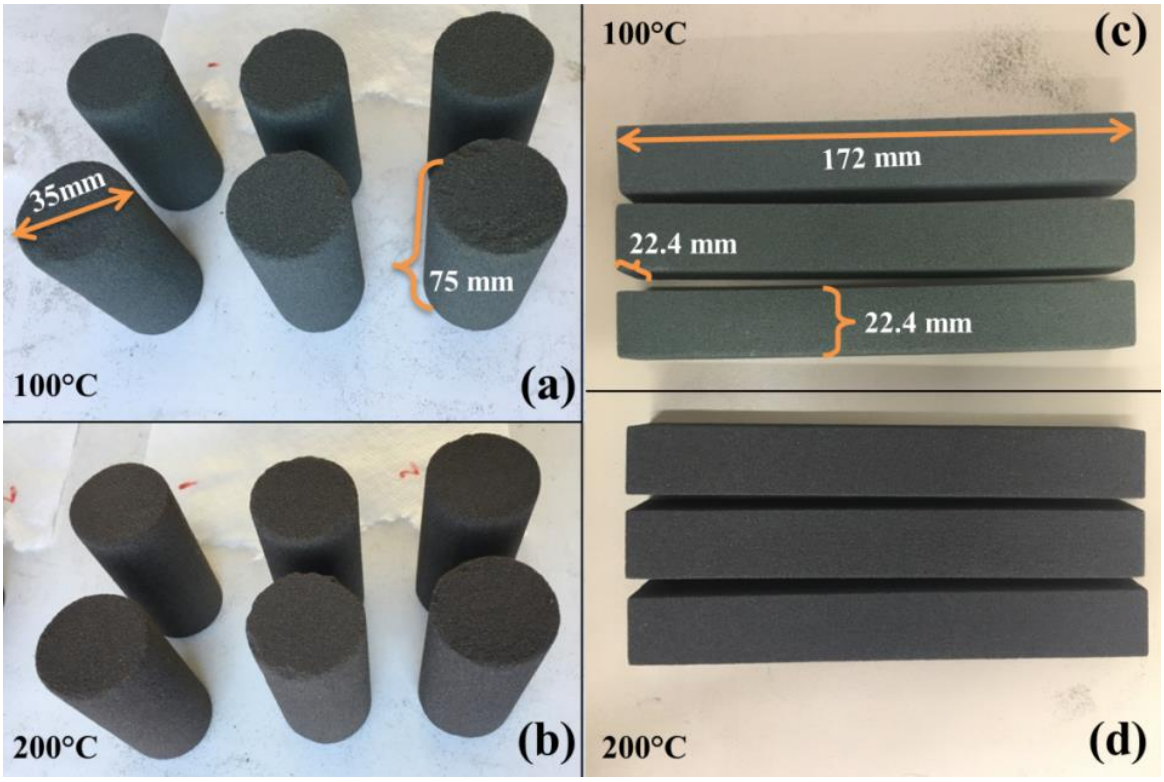


**Figure 42.** Heat-treated 3DP samples with 1.45% binder, (a,b) cylinders and (c,d) bars

After the pre-curing stage 25º C, 100°C and 200°C were chosen as curing temperatures to investigate the curing mechanisms. The choice of these temperatures is motivated by the boiling points at room conditions of water and furfuryl alcohol, which are 100°C and 180°C, respectively. Three curing times were considered: 0h, 2h and 14h. Here the 0h conditions, represents the initial conditions of the specimen after printing. As observed in the previous work [1], there is a rapid change in 3DP mold properties after 2h ageing and approach a constant value after 12h. Therefore, 0h, 2h and 14h were chosen for the experiments. Images oven, Fig. 40 and of a set of heat-treated specimens are shown in Fig. 42. One may note that the color of the samples evolves during curing due to the progressive evaporation of binder and water. The binder content, curing times and curing temperatures of the printed samples are listed in Table 5.

**Table 5. Experimental parameters**

| Parameters (Unit) | Category 1 | Category 2 | Category 3 |
|---|---|---|---|
| Binder (wt%) | 1.02±0.03 | 1.46±0.02 | 1.98±0.02 |
| Curing time (hours) | 2 and 14 | 2 and 14 | 2 and 14 |
| Curing temperature (°C) | 25, 100 and 200 | 25, 100 and 200 | 25, 100 and 200 |

### 3.3.5 Loss on Ignition tests

The Loss-On-Ignition (LOI) test is used to measure the amount of volatile materials present in a sample. In the case of the investigated 3DP sand samples, it was used to measure the mass of binder, i.e. the combined mass of water, resin, catalyst and volatile impurities. To do so, the initial mass of the printed specimens was first measured, obtaining values close to 30g (initial mass) in all cases. The specimens were then put into ceramic crucibles which had been pre-heated at 100°C for 1 h in an oven to extract moisture and organic residues. Once in the crucibles, the 3DP specimens were heated at 900°C for 45 min so as to burn-out and expel the binder and moisture. After that, the crucible was removed from the oven and the mass of the burnt-out specimen (final mass) was weighted. Images of the crucibles containing the tested samples at the different stages of the LOI tests are provided in Fig. 43. From the results of the LOI, the binder contents of the samples were determined using Eq. (3):

$$\text{Binder content} = \frac{\text{initial mass} - \text{final mass}}{\text{initial mass}} \times 100 \ \ \% \qquad \textbf{Eq. 3}$$

The remaining binder content at each stage of curing was calculated using this procedure, for all curing temperatures and initial binder contents. 6 repetitions were performed for each different binder specimens during the LOI test in order to estimate the experimental uncertainty of the measurements.

**Figure 43.** LOI test (a) 3DP samples, (b) immediately after taking out of the oven at 900 °C

### 3.3.6 Porosity measurements

The porosity of the samples was determined with the oven-dry method. The particle density was considered as being the density of $SiO_2$-quartz (2648 $kg.m^{-3}$), which constitutes 99.1% of the sand used by the printer. A laboratory precision balance was used to weight the printed specimens after drying in a hot-air oven at 105°C for 24 hours, and the bulk density of the 3DP specimen was calculated as the mass of sample per unit bulk volume. It is worth reminding that both the volume of solid and the volume of pores were taken into account for the calculation of bulk density. In contrast, the particle density was equal to the mass of sample per unit volume of silica sand particles. From the bulk density and particle density, the total porosity of the 3DP specimens was calculated as:

$$\text{Porosity} = 1 - \frac{\text{mass of the sample after LOI}}{\text{density of silica} \times \text{volume of the sample}} \qquad \textbf{Eq. 4}$$

The experimentally measured porosity values were close to 50% for all tested samples, with an estimated standard deviation of 0.2%. 6 repetitions were performed with 6 analogous specimens for each measurement in order to evaluate the uncertainty related to repeatability of the porosity tests.

### 3.3.7 Three-Point bending tests

The 3PB strength of 3DP specimens was determined through destructive tests, as commonly done with traditionally manufactured sand molds. The tests were performed using a universal strength test machine (Simpson-Electrical PFG type)[78]. The bars were fixed to the testing machine by means of two supporting pins separated 150 mm from each other. The load was applied by a third pin at the mid-length of the 3DP bar, with a load rate of 0.1 MPa.$s^{-1}$, until the specimens broke. The maximum load capacity of the machine was 12.8 MPa and the uncertainty of the pressure gauge was ±0.05 MPa. 4 repetitions were performed with 4 analogous specimens for each measurement in order to assess uncertainty.

### 3.3.8 Permeability tests

Permeability can be defined as the ability of gases to flow through a porous media driven by a pressure gradient and depends on the particle shape, the particle size distribution of the solids forming the bed and the packing structure (i.e. bed bulk porosity). In casting, the pressure gradient is generated by the melt-head pressure during filling of the mold with the liquid alloy and the shrinkage of the solidified alloy during cooling.

A standard approach to characterize the permeability of porous media (3DP mold) is to use Darcy's law (Equation 5), which relates the volumetric flow and the pressure gradient with properties of the fluid and porous materials.

$$Q = \frac{KA}{\mu L}\Delta P \qquad \textbf{Eq. 5}$$

Q : volumetric flow

A : cross-sectional area

μ : viscosity of the fluid

ΔP : pressure gradient

L : length

*K* : Darcian permeability coefficient

The Darcian permeability coefficient k quantifies the ability of the porous materials to transmit fluids. It will be possible to predict flow behavior of any liquid through the porous medium once thr Darcian permeability coefficient k can be measured or calculated.

If considering gas as a compressible fluid, the Darcian law (Equation 5) can be rewritten as,

$$Q = \frac{KA}{\mu L}\frac{(P_i^2 - P_o^2)}{2PL} \qquad \textbf{Eq. 6}$$

or

$$\frac{\mu}{K} \cdot v_s = \frac{P_i^2 - P_o^2}{2PL} \qquad \textbf{Eq. 7}$$

Pi : pressure at inlet

Po : pressure at outlet

P : pressure at which Q and μ were measured

$\frac{P_i^2 - P_o^2}{2PL}$ : pressure gradient

$v_s$ : velocity (Q/A)

The permeability value depends on various properties of the porous materials. The permeability values with the current technique are viscosity-dependent. However, gas viscosity increases with temperature, thus generating greater pressure losses for the same flow rate at higher temperatures. Past literatures showed that the permeability values obtained with compressible fluids may give diverse coefficient of permeability due to the consideration of inertial effects. The Darcian permeability coefficient k might generate extremely high values at low pressure, which is caused due to the consideration of fluid's compressibility or slip on the wall. This phenomenon is caused by "slippage" in the gas flow through pores, which was first identified by Klinkenberg. The effect of slippage depends on the size of gas molecule and the diameters of the pore. It is generally considered that the slip effect is higher when the permeability in porous media is lower. This effect is more prominent when pore diameter is close to the mean free path of gas molecules. At high pressures the Darcy's law is no longer

valid, because of the turbulent and inertial flow of the gas through the pores. Forchheimer's equation considered this inertial and turbulence effect of gas flow through pores. The provided equation is not a pure empirical formulation as it is a combination of an inertial term to the Darcy's equation. This Forchheimer's term is able to account for the non-linear behavior of the pressure difference vs volumetric flow rate.

Forchheimer's law for incompressible fluid flow in porous media:

$$\nabla P = \frac{\Delta P}{L} = \frac{\mu}{K}u + \frac{\rho F}{\sqrt{K}}u^2 = \frac{\mu}{K}u + \rho\beta u^2 = \frac{\mu}{K}\frac{Q_v}{S} + \rho\beta\left(\frac{Q_v}{S}\right)^2 \qquad \textbf{Eq. 8}$$

where $\nabla P = \frac{\Delta P}{L} = \frac{P_i - P_o}{L}$ is the pressure gradient, $\Delta P$ is the absolute value of the pressure drop over a porous medium of length L, $P_i$ is the absolute pressure at the inlet, $P_o$ is the absolute pressure at the outlet, $\mu$ is the dynamic shear viscosity of the injected fluid, K is the intrinsic permeability, $\rho$ is the fluid density, $\beta$ is the inertial coefficient, $u = Q_v/S$ is the average velocity, $Q_v$ is the volumetric flow rate and S is the cross-sectional area.

$Q_v$ is not constant when injecting compressible fluids, so Eq. (8) is commonly re-written in terms of mass flow rate $Q_m$:

$$\bar{\rho} S \nabla P = \frac{\mu}{K}Q_m + \frac{\beta}{S}Q_m^2 \qquad \textbf{Eq. 9}$$

where $\bar{\rho}$ is the average density of the fluid throughout the porous medium. If isothermal flow is assumed and the compressible fluid is considered to be an ideal gas, the following relationship can be used:

$$\frac{P}{\rho} = \frac{rT}{M} \qquad \textbf{Eq. 10}$$

where P is the absolute pressure, T is the absolute temperature, r is the universal gas constant ($\sim$ 8.31 J $Kg^{-1}$ $mol^{-1}$) and M is the molar mass of the gas ($\sim$ 28.96 g/mol for air). From Eq. (10), it can be deduced that $Q_m \sim 1.29\ Q_v$ when both $Q_m$ and $Q_v$ are given in SI units and $Q_v$ is

taken as the volumetric flow rate in standard conditions of pressure and temperature. Also, $\bar{\rho}$ can be calculated as:

$$\bar{\rho} = \frac{M}{rT}\overline{P} = \frac{M}{rT}\frac{(P_i - P_o)}{2} \qquad \textbf{Eq. 11}$$

with $\overline{P}$ being the average pressure of the gas throughout the sample.

The criteria for transition from Darcian to non-Darcian flow regimes are commonly given in terms of the non-dimensional Reynolds number Re. However, as discussed by researchers [86], the definition of Re in granular unconsolidated porous media as casting sand is controversial. This is due to the diverse characteristic lengths used in the definition of Re by different authors: average grain size, pore constriction size, square root of permeability, etc. The latter authors showed that the use of Forchheimer number $F_o$ is more suitable for establishing the transition between creeping and inertial flows. $F_o$ represents the ratio between inertial and viscous pressure drops and is defined from Eq. 3 as follows:

$$F_o = \frac{\Delta P_{inertial}}{\Delta P_{viscous}} = \frac{\Delta P_{total} - \Delta P_{viscous}}{\Delta P_{viscous}} = \frac{\Delta P_{total}}{\frac{\mu Q_m L}{K\bar{\rho}S}} - 1 \qquad \textbf{Eq. 12}$$

According to researchers [86], the transition to non-Darcian flow occurs at $F_o = 0.11$ (10% of inertial pressure drop), independently of the type of porous medium.

An apparent permeability $K_{app}$ can be defined as follows for every couple of $Q_m$-$\Delta P$ measurements:

$$K_{app} = \frac{\mu Q_m}{\bar{\rho} S \nabla P} \qquad \textbf{(Eq. 13)}$$

The preceding definition can be derived from Eq. 13, by using $\beta = 0$. Therefore, the inertial effects are not encompassed in $K_{app}$ and it is expected to markedly differ from K at moderate and high-pressure gradients. Standard permeability-characterization methods are based on the measurement of $K_{app}$.This explains that these methods are extremely inaccurate unless the flow rate used during the unique measurement is not meticulously selected, as will be shown in subsection 3.3.9.3. Indeed, $K_{app} \sim K$ only at low flow rates ($F_o < 1$).

The Darcy's law is valid only for low Reynolds number. The upper limit is at a value of Re between 1 and 10. Inertial effects can also become significant for flows in porous media with Reynolds numbers greater than about 1 to 10. The deviation from the Darcy's law will only be observed at a high Reynolds number. Previous works showed that the deviation from Darcy's law occurs at Re = (1~10), which cannot be termed as turbulent flow, but due to the inertial forces.

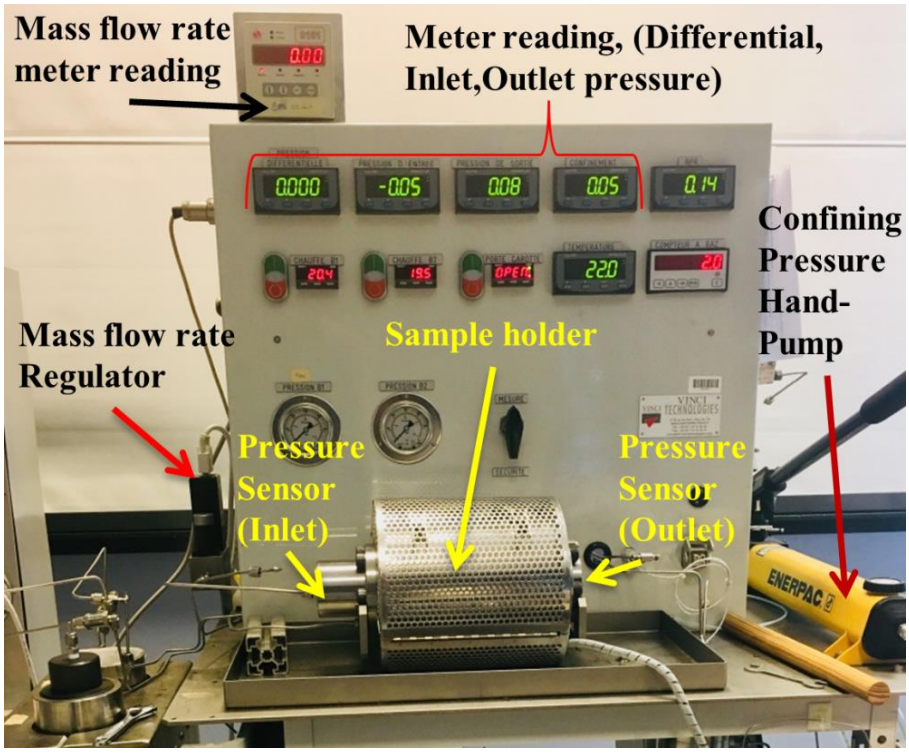


**Figure 44.** Perm-meter setup

The permeability of the printed samples was measured using the experimental setup shown in Fig. 44, (Vinci Technologies™ perm-meter [87]). The experimental procedure started by inserting the cylindrical 3DP sample into a Viton sleeve and mounting it in a Hassler-type core holder. After that, the core was confined with pressurized oil surrounding the sleeve in order to avoid lateral leaks during flow. This oil was provided by an auxiliary confining pump (Enerpac company). Then, air coming from a pressurized cylinder was continuously injected through the cores at controlled mass flow rate. A set of steeply increasing values of mass flow rate was imposed by means of two mass flow rate regulators (Brooks Instrument B.V, Accuracy: ± 0.7% of flow rate), with working ranges of 0 - 1 NL/min and 0 – 30 NL/min, respectively. The corresponding steady-state pressure drop ΔP between the inlet and the outlet of the core (L = 75 mm) was measured by a membrane-type differential pressure sensor

(DP15 Variable Reluctance Pressure Sensor, Validyne Engineering, Accuracy: ± 0.2% of flow rate). The outgoing air was released to atmospheric pressure, so $P_o$ was assumed to be 0.1 MPa and $P_i = P_o + \Delta P$. Each measurement was repeated four times in order to evaluate uncertainty related to the repeatability of the pressure. A total of 150 flow rate vs. pressure drop measurements were performed; covering the mass-flow-rate range from 0.01 Nl/min to 10 Nl/min. The temperature of the core-holder was maintained at 23.0±2 °C by using a temperature control subsystem consisting in an electric heating thermostat. The dynamic shear viscosity of air at this temperature was taken as $1.81\times10^{-5}$ Pa s. 4 repetitions were performed with 4 analogous specimens for each measurement in order to evaluate the uncertainty related to repeatability of the tests.

### 3.3.9 Results and discussion

The effects of binder content on mass loss, permeability and 3PB strength for uncured and cured samples were experimentally investigated from the results of the measurements presented in the preceding section.

#### 3.3.9.1 Evolution of binder content during curing as a function of the initial binder content

The mass loss during ageing, as measured by the LOI tests, are represented as a function of curing time and temperature in Figure 45 for the three different values of initial binder content. It is noted that loss of binder mass by evaporation was negligible at the room temperature of 25 °C, even after 14h of curing. This was expected given that 25 °C are far below the boiling temperatures of the water and alcohols present in the binder. In contrast, a significant decrease in the mass of binder is observed for the three initial values of binder content at both 100 °C and 200 °C. This decrease is more pronounced within the first two hours of curing.

It is reminded that the furan binder (FNB) is a mixture of furfuryl alcohol and acid catalyst [55]. FNB's condensation reaction produces water, which tends to slow down the rate of curing (dehydration) affecting the mechanical properties of the 3DP mold [32,54]. A closer look to Figure 45 reveals that the rate of mass loss when during curing at 200 °C is roughly similar to the one at 100 °C, leading to analogous values of remaining binder content after 2h and 12h in both cases. One may expect a higher evaporation rate at 200 °C, as this temperature is greater than the boiling temperature of both alcohol and water. However, it

must be borne in mind that water is released only after polycondensation, which is conditioned by the reaction of the acid catalyst with alcohol. Consequently, less water should be released at 200 °C as the polycondensation reaction is interrupted by the early evaporation of alcohol. Therefore, it can be concluded from Fig.45 that the mass of water being evaporated at 100 °C is equivalent to the sum of the masses of water and alcohol being evaporated at 200 °C.

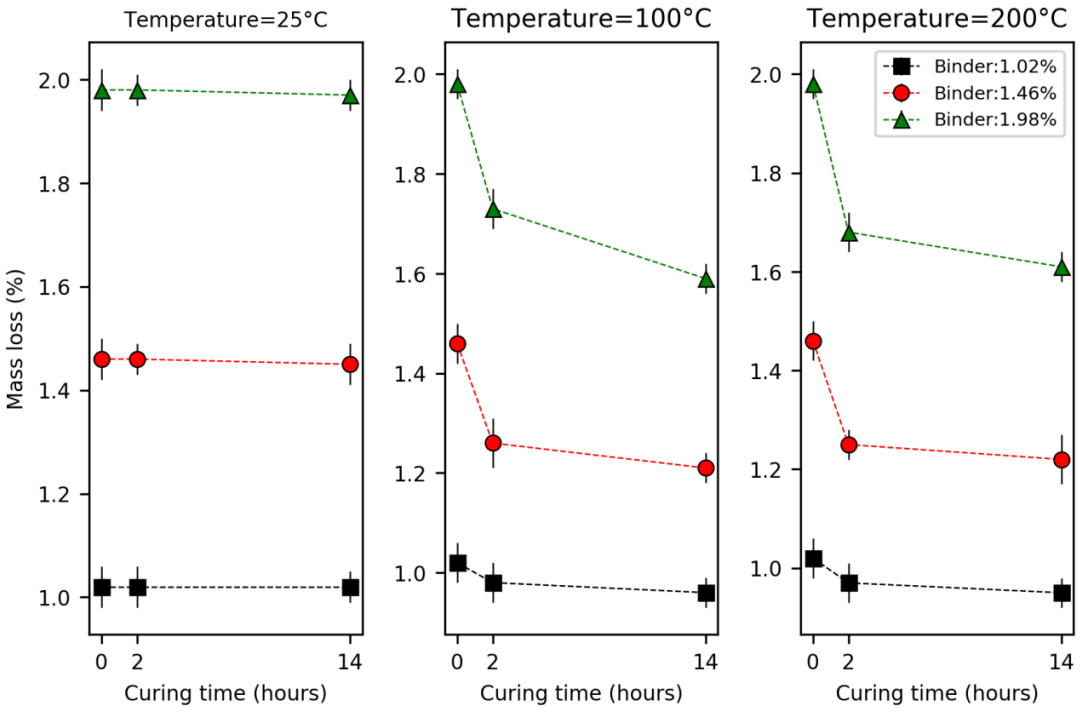


**Figure 45.** Mass loss as a function of curing time for three curing temperatures

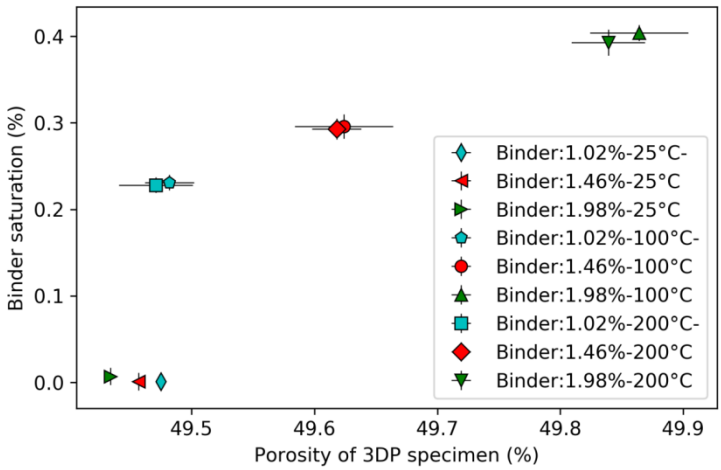


**Figure 46.** Binder saturation vs porosity of specimens

### 3.3.9.2 3PB strength as a function of the initial binder content for different curing conditions

The 3PB strength strength has a direct bearing on the strength of bonds between particles in the cured sample. The strength of intermolecular bonds in turn depends on the physical state of the furan resin binder and its interaction with the surrounding particles. In general, with curing of specimen, the resin binder material gets cured by polymerization, forming a network of substrate material (furan resin bridges) holding the loose particles together, and leading to a gradual rise in the 3PB strength of the sample. This is the trend in all the cases shown in Fig. 47 and Fig. 48; a rise in 3PB strength with increasing curing time and temperature of baking. As shown in Fig.48, at the same temperature, the retained 3PB strength increases with the increased resin content.

Figure 48 shows the 3PB strength test results of 3DP sand specimens in the uncured and cured conditions. It was found that 3PB strength increases with binder content for all curing times and temperatures. Moreover, 3PB strength increases when curing at 100 °C and decreases when cured at 200 °C for all binder contents. When curing at 100°C, the 3PB strength experienced an increase of 20% for 1.02% binder, 16.7% for 1.46% binder and 28% for 1.98% binder. However, when curing at 200 °C, the 3PB strength experienced a decrease of 41.6% for 1.02% binder, 40% for 1.46% binder and 22% for 1.98% binder.

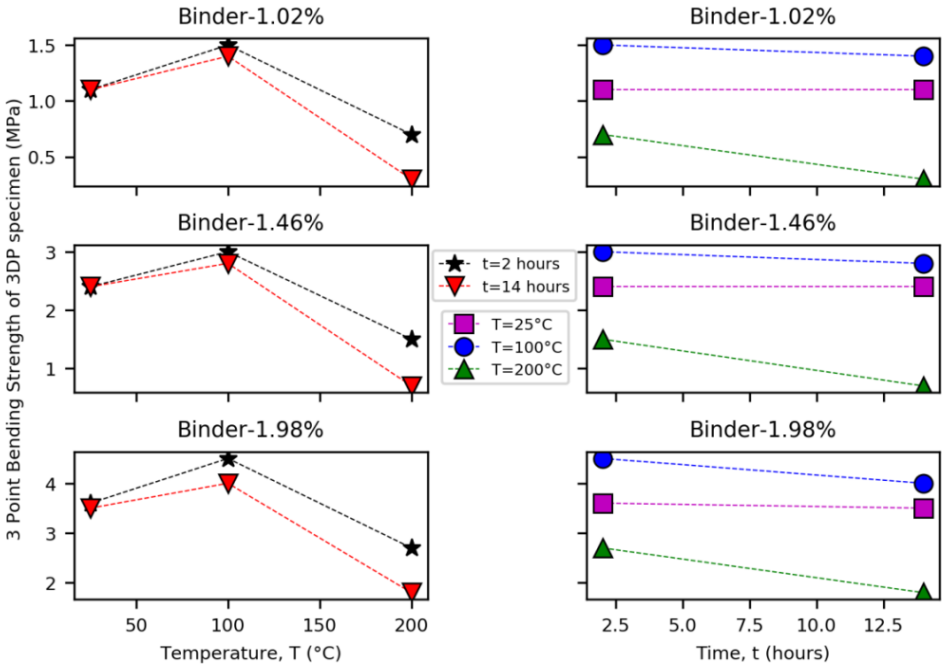


**Figure 47.** Variation of strength with binder, curing temperature and time

It is of crucial importance to manufacture 3DP sand molds meeting the requirements in terms of gas evolution during metal casting (low binder content) and optimum 3PB strength. In this regard, 3PB strength should be above 1.5 MPa so that the mold can resist the impact of liquid metal. Therefore, 1.46 wt% of sand can be selected as the optimum furan resin binder content to print 3DP molds for metal casting with the present technique. Indeed, when the initial furan resin binder content is 1.46 wt%, the 2 h and 14 h strengths are above 2 MPa, satisfying standard production requirement for casting melted alloy. It is also observed in Figure 6 that 3PB is unaltered by curing at 25 °C. The 3PB strength attains its maximum for all binder content when curing at 100 °C for 2 hours. The reason is that the low roasting temperature (100 °C) provides secondary hardening of furan resin bridges which increases the 3PB strength, while the resin bonding bridges of 3DP sand mold burn at high curing temperature (200 °C), resulting in reduced 3PB strength.

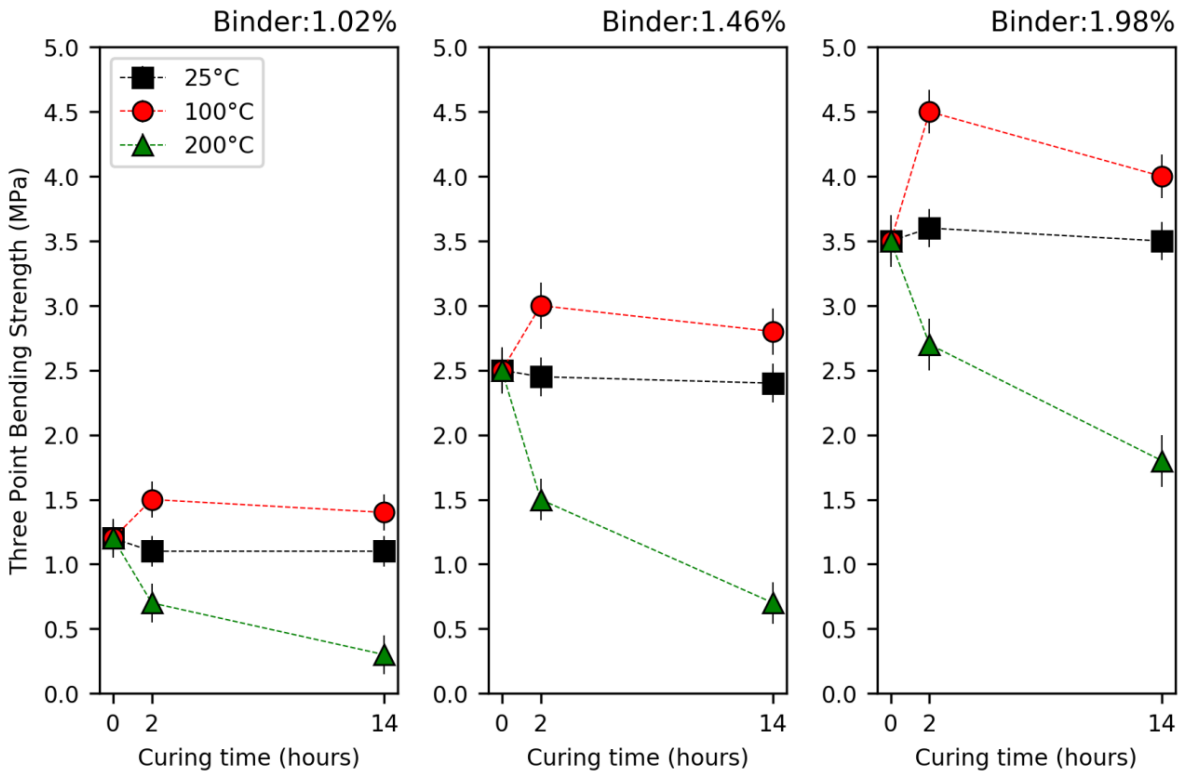


**Figure 48.** Effect of curing parameters on 3PB strength

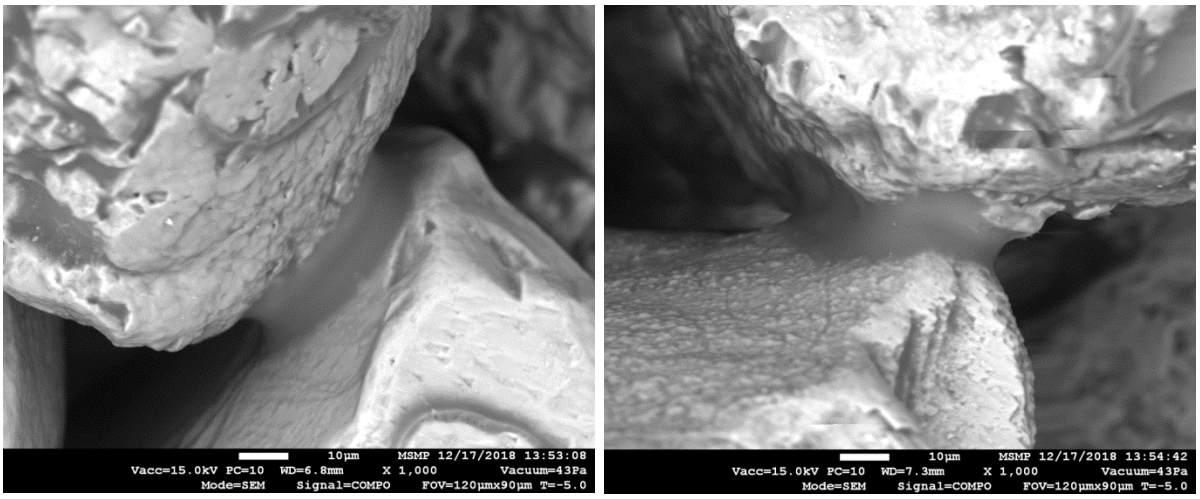


**Figure 49.** SEM image of 3DP specimen showing resin bridges between particles

The 3PB strength of 3DP sand mold has a direct influence on the strength of the furan resin bridge between sand grains in the sample (adhesion of binder between sand and cohesion of the furan resin binder), Fig. 48. This furan resin bridge is formed by capillary action after the binder is dropped by the print head (X-resolution) and strengthens gradually, Fig. 49. The intermolecular resin bond strength depends on the physical state of the binder and its interaction with the surrounding sand particles. When the 3DP specimen is cured, the furan resin binder hardens by polycondensation (polymerization and condensation), forming a network furan resin bridges which holds the sand particles together. The strength of the resin bridge greatly depends on the amount of the binder content. The volume of bridge corresponds to the printed furan binder content minus the evaporated solvent (mixture water and alcohol). This resin bridge strengthens gradually and affects the 3PB strength of the sample. The strength increases more rapidly at 100 °C (cured by heat treatment) than at 25 °C (cured at room temperature). However, this resin bridge hardening and strengthening mechanism has a limit, leading to reduced strength and loss of ductility hence cracking for prolonged heating at 100 °C or when heating at high temperature (200 °C), Fig. 51. These results facilitate the choice of the optimum binder content, curing time and temperature to obtain the functional values of 3PB strength.

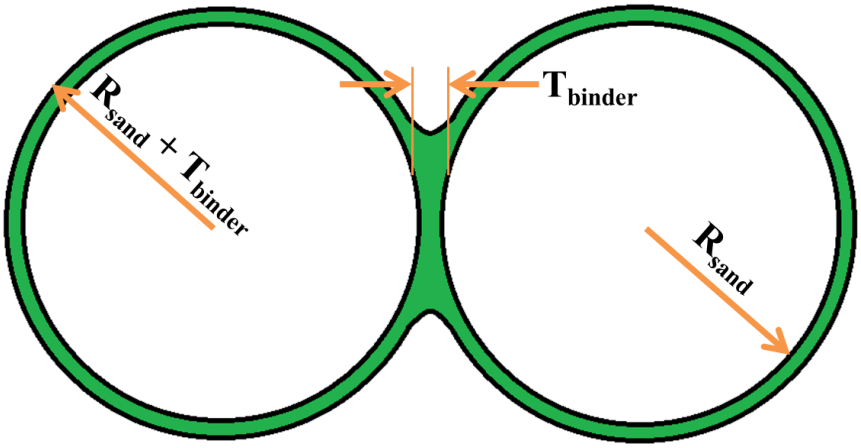


**Figure 50.** Resin bonding bridge of adjacent sand particles

The mechanical and the mass transport properties of the cohesive granular materials depend on their microscopic structure and their composition. A scheme of the resin-bonded bridges between sand particles with simple cubic compaction density is displayed in Figure 50, where $R_{sand}$ is the radius of the silica sand particle and $T_{binder}$ is the thickness of the furan resin bridge. Considering that the binder is evenly distributed over the sand particles, the thickness of the resin bridge is expected to increase when the binder content is increased. This leads to improved cohesion strength of the bonding bridges and higher 3PB strength, in agreement with the experimental results.

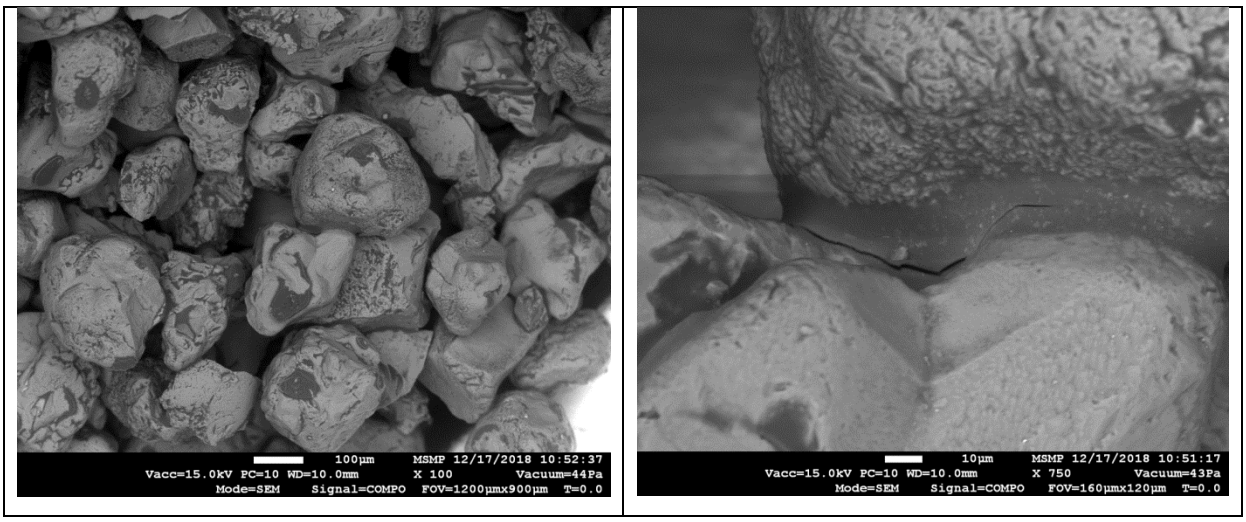

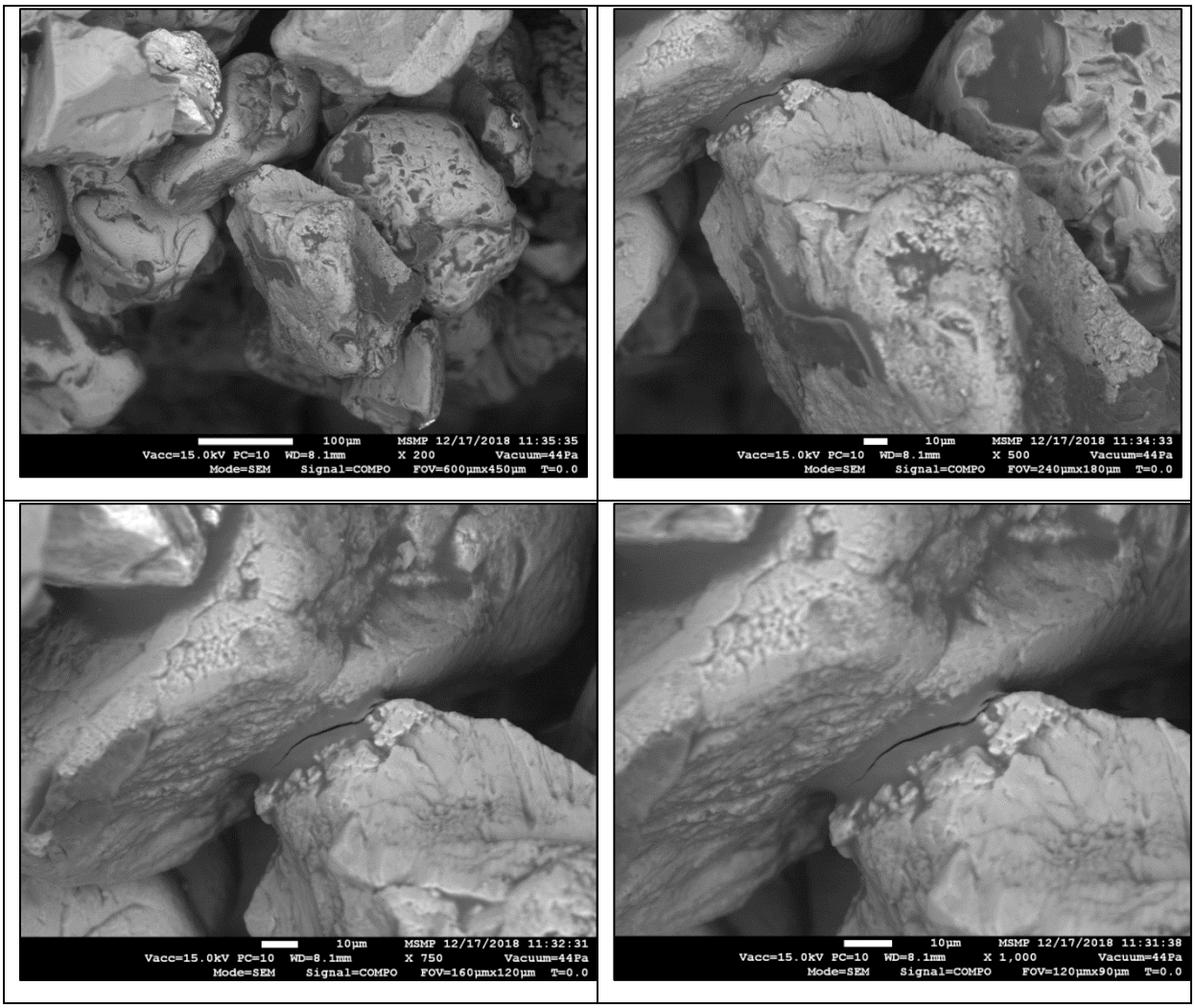


**Figure 51.** SEM image of 3DP specimen showing cracking of resin bridges at 200°C

### 3.3.9.3 Permeability as a function of the initial binder content for different curing conditions

The relationships between f ($= \bar{\rho}S\nabla P$) and $Q_m$ obtained during permeability measurements for uncured samples with different levels of initial binder content are shown in Figure 52. It is noted that f increases nonlinearly with increasing mass flow rate deviating from the linear relationship predicted by Darcy's law (Eq. 13 with $\beta = 0$). As explained in section 3.3.8, Darcy's law is only valid for creeping flow at low Reynolds numbers. Therefore, the non-linear behavior observed in Figure 8 reveals that the flow is no longer creeping at moderate and high mass flow rates and the inertial pressure losses are not negligible. The same figure shows that all f vs. $Q_m$ curves collapse for uncured samples, independently of the binder content. Therefore, similar values of permeability and similar inertial pressure drops are

expected for the three investigated binder contents when ageing is performed at room temperature (25 ºC). The f vs. $Q_m$ measurements for all the considered binder contents and curing conditions are represented in Figure 53, showing that the curves also collapse for all curing conditions in the case of 1.02% and 1.46% initial binder contents. Indeed, significant differences depending on the curing time and temperature were only observed for 1.98% initial binder content, which will be interpreted below in terms of permeability variation.

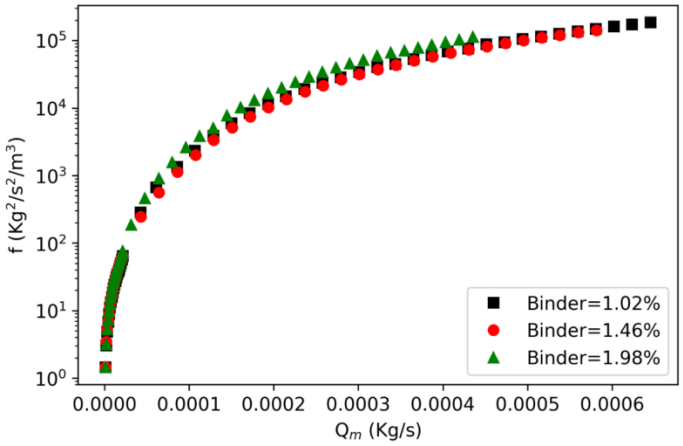


**Figure 52.** Effect of binder content on f vs. $Q_m$ rate for uncured samples at 25°C

$K_{app}$ was calculated using Eq. 13, as traditionally done with the standard permeability characterization methods, for different values of the injection flow rate. The experimentally obtained $Q_m$ vs. $K_{app}$ relationship for uncured samples with different binder contents is presented in Figure 54. These results show that $K_{app}$ is monotonically decreasing as $Q_m$ increases for all the specimens, which is explained by the inertial pressure drops which are not taken into account in the calculation of $K_{app}$. Moreover, it is observed that the $K_{app}$ tends to a constant value within the low flow rates region in which the flow is viscous-dominated and the inertial deviations are negligible. Therefore, $K_{app} \sim K$ at the lowest flow rates and K was considered to be equal to the plateau value.

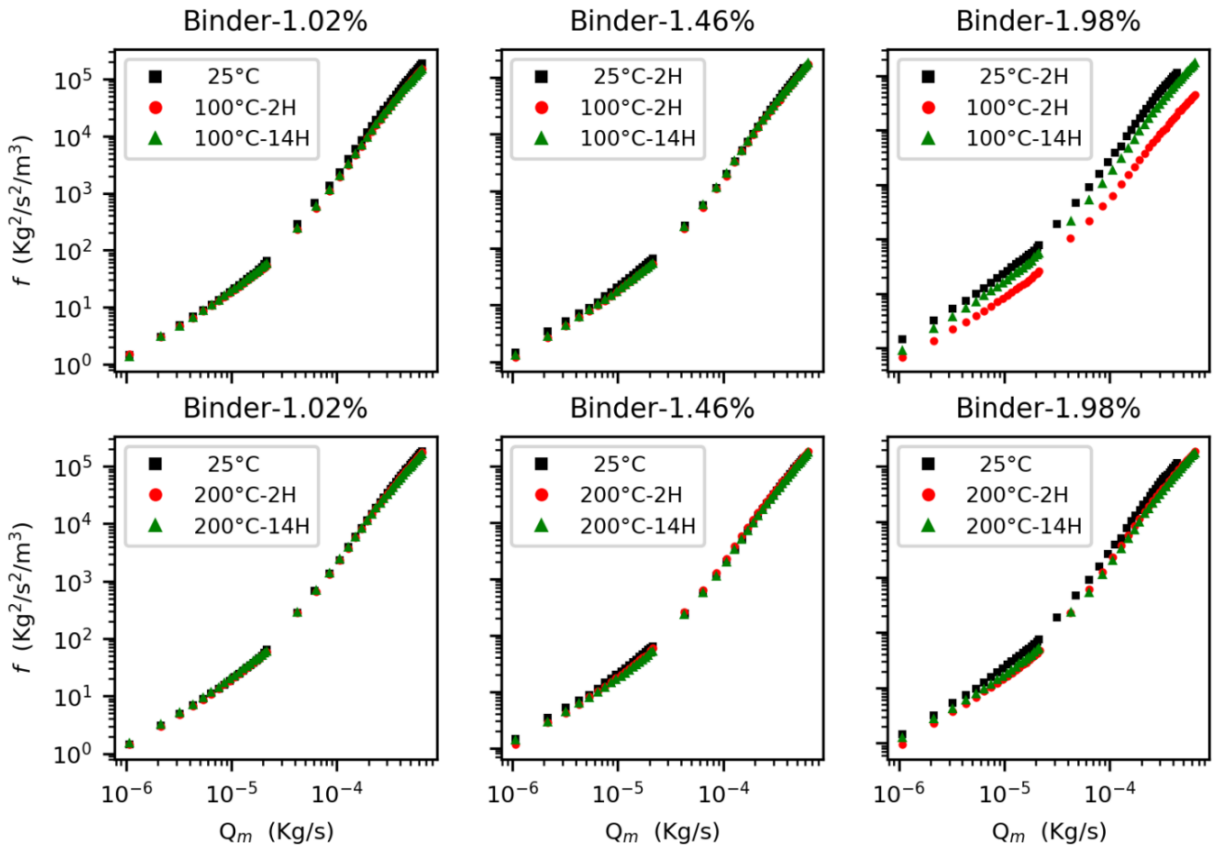


**Figure 53.** Effect of curing time on the relationship between f and $Q_m$ at different temperatures and binder contents

**Table 6. All results for 3PB strength and permeability**

| Curing Temperature (°C) | Curing Time (Hours) | Permeability, K ($m^2$) | 3 PB Strength (MPa) |
|---|---|---|---|
| | | | |
| **Binder = 0.98%** | | | |
| 25 | 2 | $1.34\times10^{-11}$ | 1.1 |
| 25 | 14 | $1.34\times10^{-11}$ | 1.1 |
| 100 | 2 | $1.38\times10^{-11}$ | 1.5 |
| 100 | 14 | $1.45\times10^{-11}$ | 1.4 |
| 200 | 2 | $1.33\times10^{-11}$ | 0.7 |
| 200 | 14 | $1.31\times10^{-11}$ | 0.3 |
| **Binder = 1.45%** | | | |
| 25 | 2 | $1.33\times10^{-11}$ | 2.4 |
| 25 | 14 | $1.33\times10^{-11}$ | 2.4 |

| | | | |
|---|---|---|---|
| 100 | 2 | $1.60\times10^{-11}$ | 3.0 |
| 100 | 14 | $1.51\times10^{-11}$ | 2.8 |
| 200 | 2 | $1.67\times10^{-11}$ | 1.5 |
| 200 | 14 | $1.51\times10^{-11}$ | 0.7 |
| **Binder = 1.96%** | | | |
| 25 | 2 | $1.33\times10^{-11}$ | 3.6 |
| 25 | 14 | $1.33\times10^{-11}$ | 3.5 |
| 100 | 2 | $2.87\times10^{-11}$ | 4.5 |
| 100 | 14 | $2.22\times10^{-11}$ | 4.0 |
| 200 | 2 | $2.04\times10^{-11}$ | 2.7 |
| 200 | 14 | $1.60\times10^{-11}$ | 1.8 |

Darcy's law (Eq. 13 with $\beta = 0$) was then fitted to the f vs. $Q_m$ measurements obtained during permeability tests, as illustrated in Figure 55a for the uncured 1.02% binder content sample. Similar results were observed for all considered curing conditions. From this figure, it can be deduced that the flow regime is creeping only at the lowest flow rates in which Darcy's law predictions are accurate. However, the deviations from Darcy's law become larger as $Q_m$ is increased due to additional inertial pressure drops. Therefore, it is confirmed that both creeping and inertial flow regimes were covered by the wide range of $Q_m$ imposed during the measurements. Furthermore, $F_o$ (Eq. 12) was also calculated as a function of $Q_m$ so as to quantify the relative importance of the inertial pressure drops, as presented in Figure 55b. The critical value of $F_o = 0.11$ (10% of inertial pressure drop) marking the transition from Darcian to non-Darcian flow occurs at $Q_m$ close to $3 \times 10^{-6}$ kg/s. Accordingly, for the given sample dimensions and experimental conditions, it can be concluded that flow rates close to $3 \times 10^{-6}$ kg/s must be used to characterize permeability in this type of casting sands. Non-dimensionalization of this criterion is challenging given the compressibility of the injected fluid and will not be addressed in the present work.

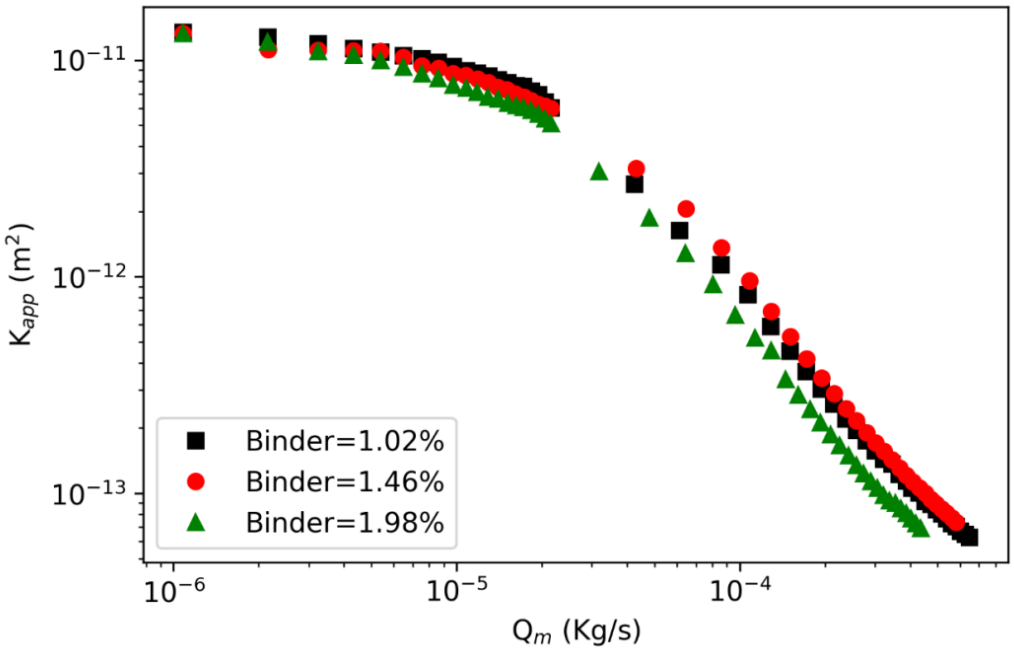


**Figure 54.** Relationship between apparent permeability and mass flow rate for uncured samples at 25°C

Following the procedure presented above, the permeability of the samples was calculated for all the investigated binder contents, curing times and temperatures. The results are presented in Figure 56 and 57. It can be observed that no significant evolution of K over time was obtained for the samples cured at 25 ºC. This was expected, given the low evaporation rate at room temperature in agreement with previous results [21] and the mass loss measurements presented in Fig. 45. Moreover, the permeability of these samples is very close for all binder contents. This may be explained by the combined effect of two mechanisms with opposed effects on permeability: 1) the generation of thicker resin bridges through polymerization at higher binder amounts tend to separate of the grains, which enhances porosity and permeability; and 2) higher binder amounts lead to a higher saturation of the interstices, resulting in a decrease in permeability. However, these mechanisms need further verification, for example through specifically dedicated X-ray micro computed tomography (µ-CT) experiments, which will not be presented here, and will be presented on section 4.

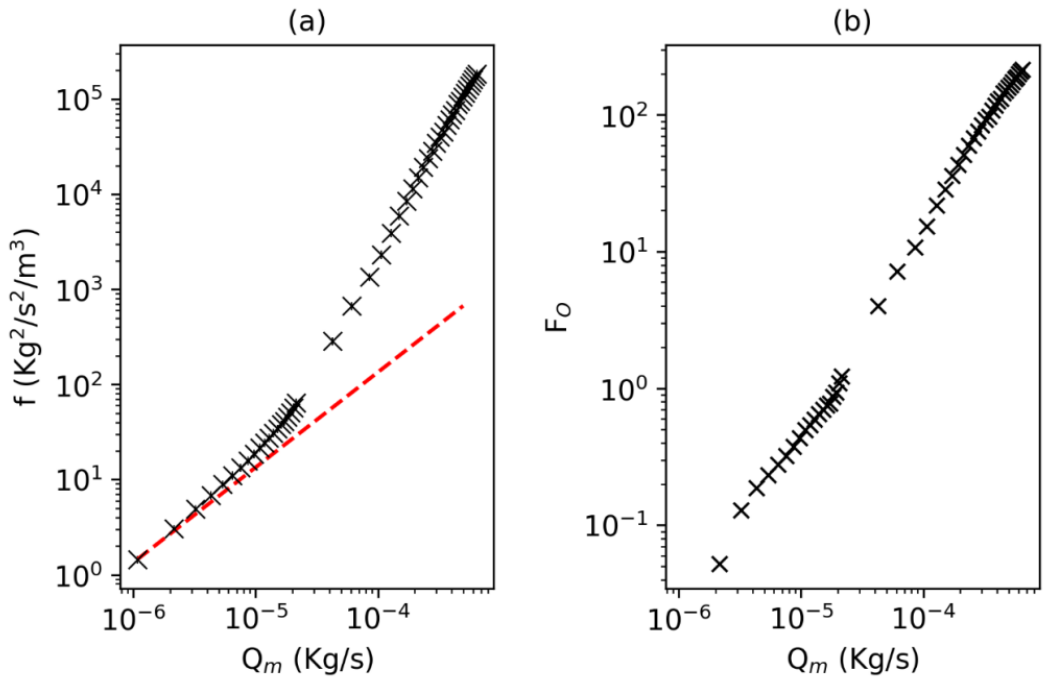


**Figure 55.** Evaluation of the inertial effects for uncured samples at 25°C and a binder content of 1.02%: (a) Darcy's law fit. Black symbols represent experimental measurements. The red dashed line represents Darcy's law fit; (b) Forchheimer number at different flow rates.

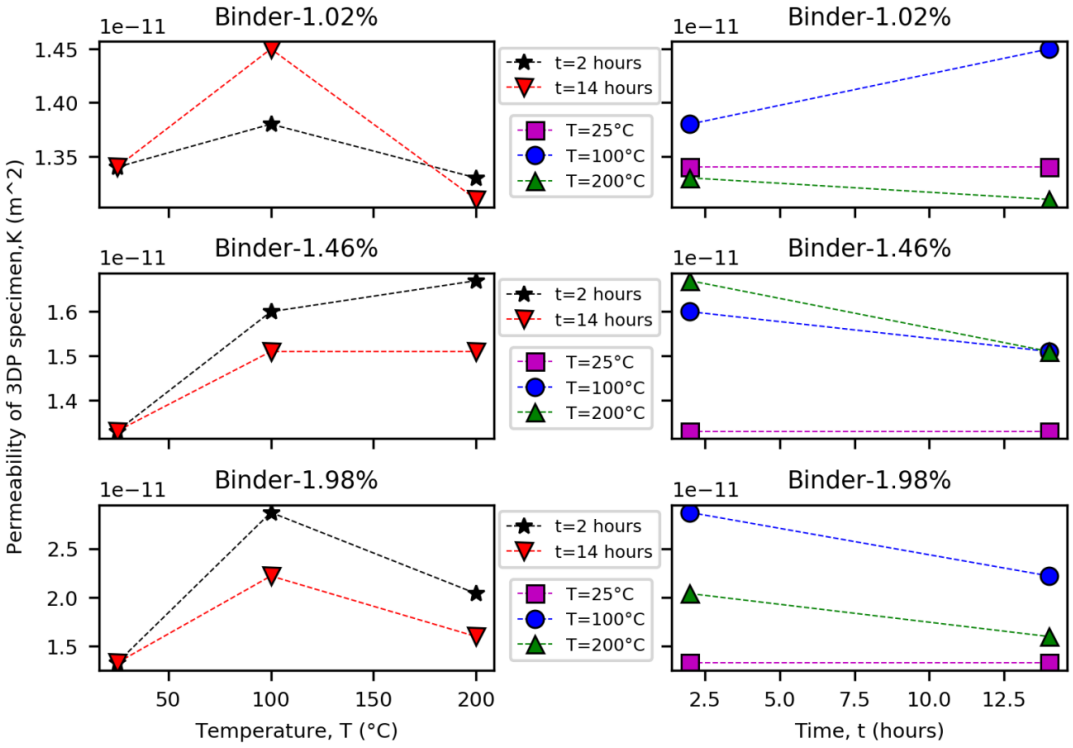


**Figure 56.** Variation of permeability with binder, curing temperature and time

It can also be observed in Fig. 57 that the permeability of the 1.02% binder content samples remains roughly constant throughout the 14h of curing at the three considered temperatures. This may be explained by the thinness of the liquid layer between the sand grains which produces only a very weak reduction in permeability. Also, the polymerization reaction (transformation of liquid binder into resin bridges) is expected to conclude earlier than for higher amounts of binder, so the liquid saturation is lower and the effects of remaining alcohol and water evaporation are minimum. A stronger effect of evaporation on permeability is observed at 1.46% and 1.98% binder contents, which is potentially due to the higher amount of remaining alcohol and water blocking air flow through the pores. Also, a decrease in permeability is observed after 14h of curing, which could be explained by the shrinkage effect produced by burning of the resin bridges [83]. The permeability attains its maximum in the case of the specimen with highest binder content when heat treated at 100°C for 2h. It is to be noted that higher amounts of binder would generate of more toxic gas.

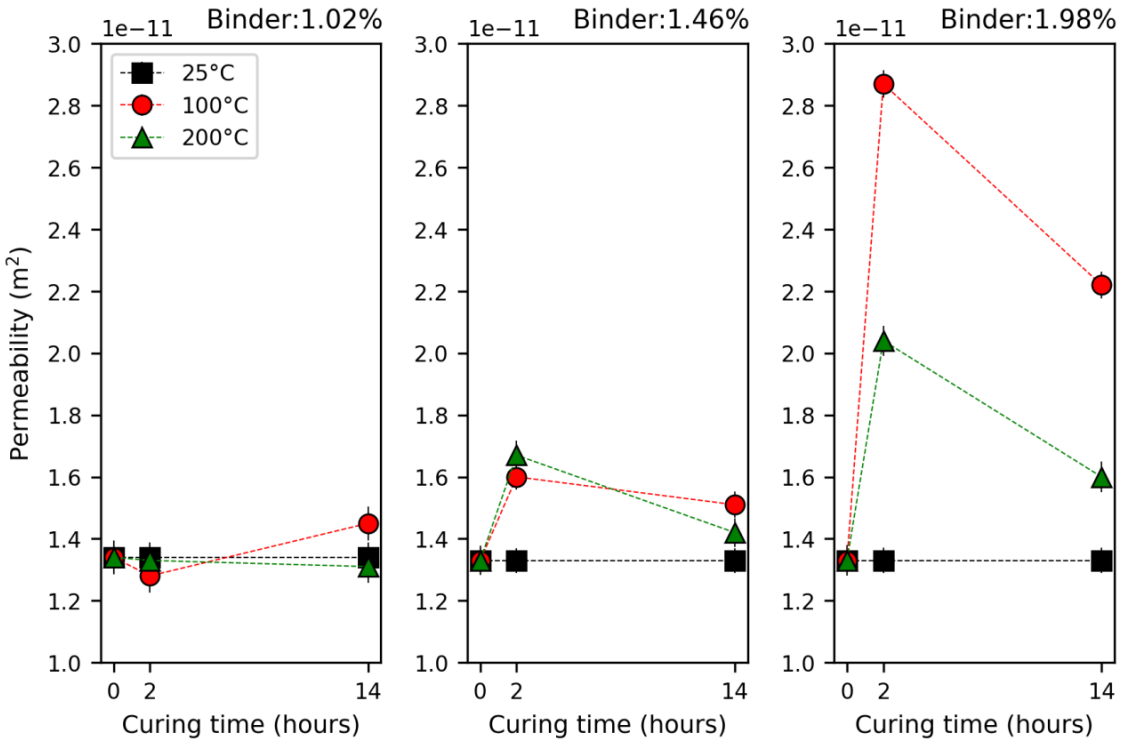


**Figure 57.** Variation of permeability with binder content, curing temperature and time

### 3.3.10 Conclusion

The quality of the parts produced by casting in 3DP molds is strongly conditioned by the careful choice of suitable binder content. Motivated by the vital role of this process parameter,

the effects of binder content on the permeability and the mechanical strength of 3DP sand molds has been experimentally evaluated for different curing times and temperatures. The following conclusions are drawn from the present work:

- ✓ Binder content has a profound influence on the 3PB strength of 3DP sand molds. Higher binder amounts lead to increased mechanical strengths. Moderate curing temperatures and times (100 ºC, 2h) are recommended in order to optimize 3PB (avoiding degradation of the resin bridges, excessive off-gassing and hot tearing).

- ✓ Mass-loss measurements performed during LOI tests allow the evaluation of liquid evaporation rates, which can be subsequently used in the analysis of the physical mechanisms governing the changes in permeability and 3PB strength during curing stage.

- ✓ The effect of binder content on permeability is not significant when curing at room temperature (25 ºC). However, liquid evaporation and binder shrinkage significantly affect permeability. Maximum permeability is attained at the same conditions as the optimum 3PB strength.

- ✓ The porosity of the 3DP sand molds is very high, leading to inertial-dominated flows at moderate values of air flow rate. Consequently, permeability measurements must be performed at sufficiently low injection flow rates in order to achieve creeping flow. Standard permeability characterization methods are not suitable for this material the large inertial pressure losses stemming from the higher permeability of the samples as compared to traditional casting sand.

The present experimental results facilitate the characterization of printing process parameters by quantifying the effects of binder content on the functionality of 3DP molds. These criteria are most valuable for the production of casting molds meeting the requirements of aerospace and automotive industries.

# 4. PERMEABILITY CHARACTERIZATION OF 3DP MOLDS USING X-RAY CT AND ADVANCED POROSITY MODELLING

In this chapter, X-Ray micro computed tomography (µ-CT), a non-destructive and non-intrusive technique was used for studying three-dimensional (3D) structure of materials by imaging representative samples. The µ-CT images allow extracting 3D shapes and structures which are used by models to estimate with a good precision the gas permeability of sand mold samples. Extensive numerical experiments were performed and we compare the results to other laboratory techniques and to theoretical data.

This chapter covers the theoretical background and the implementation of two modelling methods: The Lattice-Boltzmann method (LBM) for single-phase fluid flow simulation and a pore network modelling for pore and throat size distribution. Lattice Boltzmann method (LBM) is considered as the most widely used methods that can be applied to any complex porous geometry without simplifying it. Pore network models (PNM) are used to describe complex porous 3DP structures by a network of simplified geometrical components – termed as pore bodies and connected pore throats. The main result of this chapter is the demonstration of feasibility and applicability of LBM and PNM approaches in predicting the permeability of 3DP mold samples.

## 4.1 Introduction

Permeability is an important transport property of 3DP and mold structures, which is influenced by various printing parameters and by the pore characteristics at a micron scale. Finding or developing a method to measure gas permeability of 3D printed sand molds and understanding the impact of the structure of pores and grains is therefore highly important. A rapid measurement technique would allow quantified statistical analysis for these 3DP sand molds, which could help in more accurate macroscopic measurement of physical properties (i.e., local porosity, density, permeability, and strength) as required for casting simulations.

Several different techniques exist in characterizing porous samples at the micron scale. In material science, the scanning electron microscope (SEM) is a reference for surface imaging. X-ray micro computed tomography (µ-CT) is an extremely valuable tool by its ability to

generate 3D volumes of scanned samples. We used these two techniques in our studies since they answer very well to the characterization needs for our samples.

## 4.2 Scanning Electron Microscope (SEM): General functioning

Scanning electron microscopes use the interaction of an electron beam to the imaged samples. Depending on the instrument, the resolution ranges from less than 1 nm to 20 nm [88]. A beam is produced by an electron gun which is then focalized by condenser lens and further guided by objective lens which ensures the necessary displacement and focalization for a scanning mode. The sample which is placed on a holder is moved under the beam and scanned over a surface. The image is formed by collecting backscattered electrons which are converted to a gray level for a given scan position. A schematic representation of SEM is provided in Fig. 58.

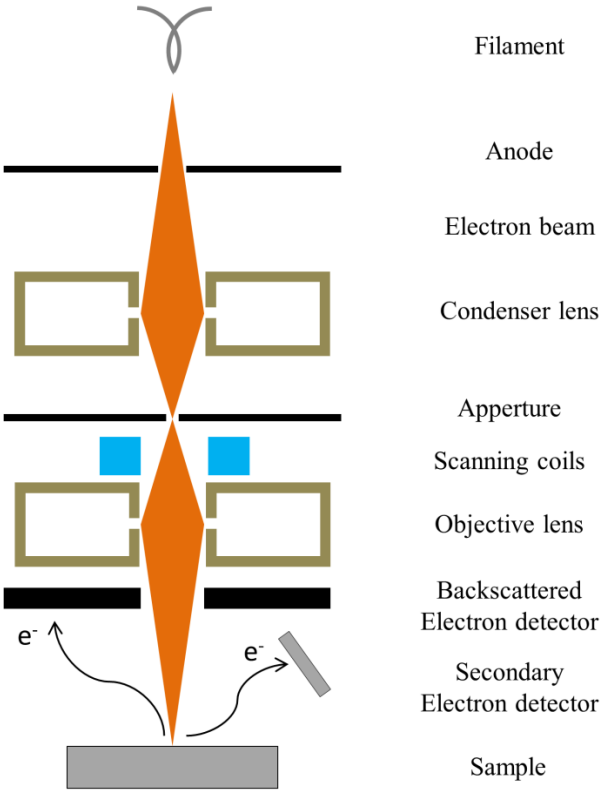


**Figure 58.** Schematic representation of SEM

In our work morphological characterizations were performed with a JEOL JSM-7001F scanning electron microscope (SEM) using secondary electrons for the surface topography and backscattered electrons for the chemical contrast (compo mode). SEM images were

obtained in low vacuum mode (44 Pa) with an acceleration voltage of 15 kV at a (6 - 10 mm) working distance for different magnifications.

### 4.3 Basic aspects in X-ray micro-computed tomography (X-ray µ-CT)

X-Ray tomography is a non-destructive imaging method having the roots in the medical field. In industrial and research applications it has three main uses: 3D characterization of samples, inspection of parts for various types of defects or morphology and for dimensional measurements. Computed tomography is a method to reconstruct a 3D volume from a set of projections acquired as radiographies. The typical setup consists of an X-ray source, a 2D detector (known also as "flat panel") and a turntable which is used to rotate the imaged sample (Fig. 59).

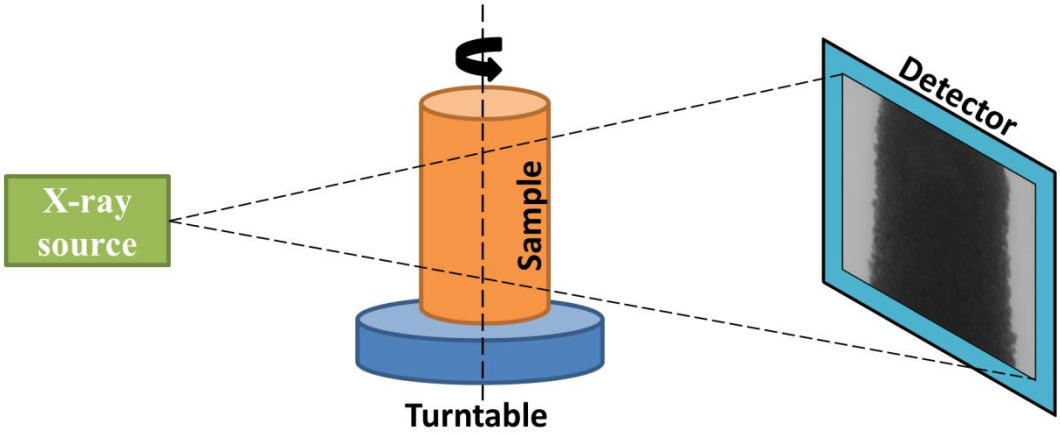


**Figure 59.** Schematic representation of principle of X-ray tomography

3D X-ray µ-CT provides accurate representation of the porous structures, with detailed grain size and pore size distribution, which allow to model numerical simulation of gas flow through the geometry. In the present study, the X-Ray µ-CT was used to reconstruct a 3D virtual representative model of a 3D printed sand mold, in order to evaluate the gas permeability of 3D printed sand mold using numerical simulation. The permeability values obtained with the computer simulation were then compared with theoretically calculated and experimentally measured permeability values.

The reconstruction process may use analytic or algebraic models. The gold standard in CT is the FDK algorithm [89,90] which is an analytic method with a direct inversion in a cone-beam configuration. Figure 60 and 61 presents the images on a 3DP sample, a projection and a reconstructed slice.

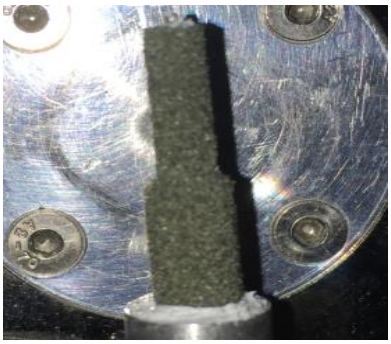

**Figure 60.** 3DP specimen

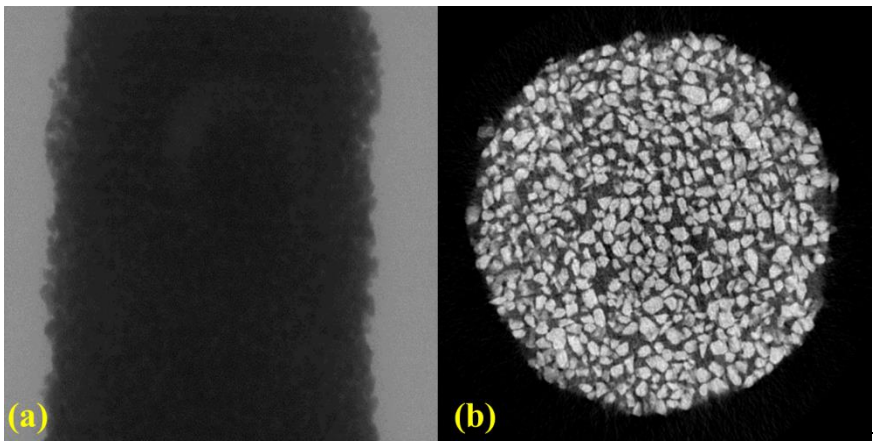


**Figure 61.** (a) The projection profile of attenuated X-ray radiography through a 3DP specimen received by the detector and (b) Reconstructed pixel data of 3DP specimen

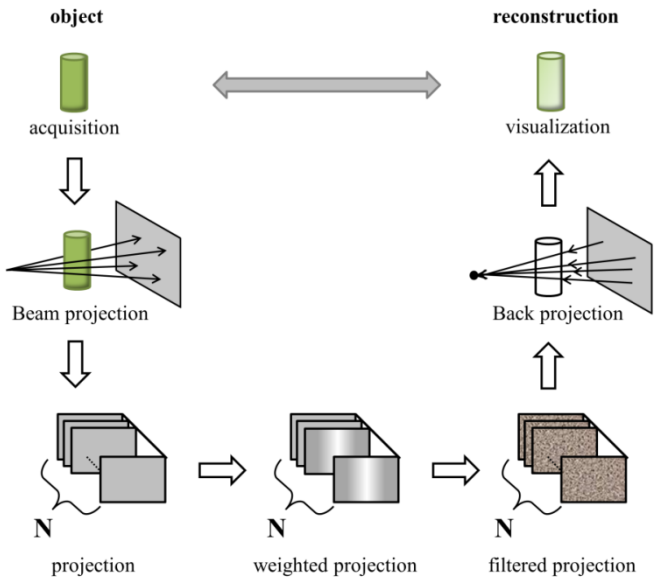


**Figure 62.** Main steps of 3D image reconstruction

Compared to the ideal case, the experimental setup with the acquisition parameters and the reconstruction algorithm may produce significant artefacts on the generated images. Various methods for reducing or correcting the artefacts exist and their use depends to a great extent on the sample and the acquisition parameters.

### 4.4 Processing reconstructed images

Reconstructed X-Ray computed tomographic images are filtered using a variance weighted mean filter to reduce the effect of background noise. Main steps involved 3D image reconstruction are 2D data acquisition, filtering processes, back projection process and 3D image visualization. A schematic representation of image acquisition to volumetric reconstruction is shown in Fig. 62. A 3DP specimen (porous media), consist of three phases with different absorption contrast, i.e. silica sand, binder and pores. For the present study two phase, most commonly solid (combination of silica sand and binder) is of more importance. For this reason the image is segmented into solid and everything else. From the set of trials a reasonable threshold value is selected, which separates the solid material (combination of silica sand and binder) from other phase (pores/void). Everything above that threshold value is then turned into white and everything below that is set to black. The resulting image has only two phases: solid (black) and void (white), Fig. 63.

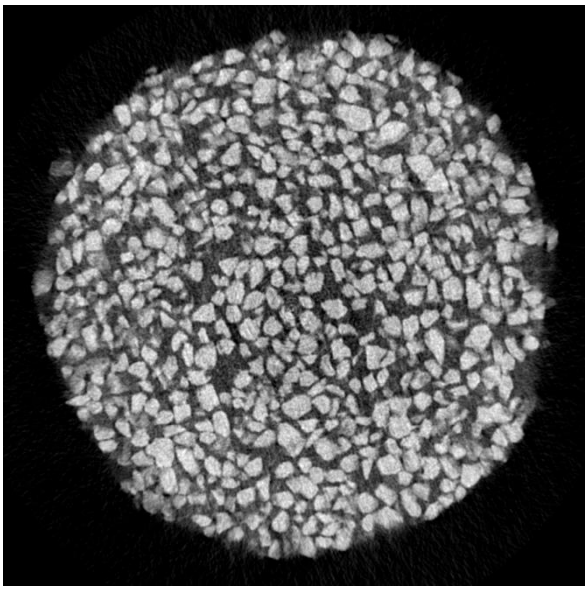

a. cropped stack

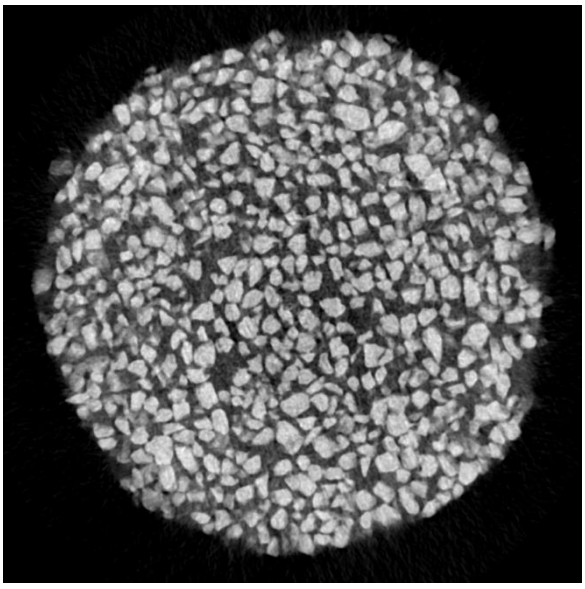

b. median filtered

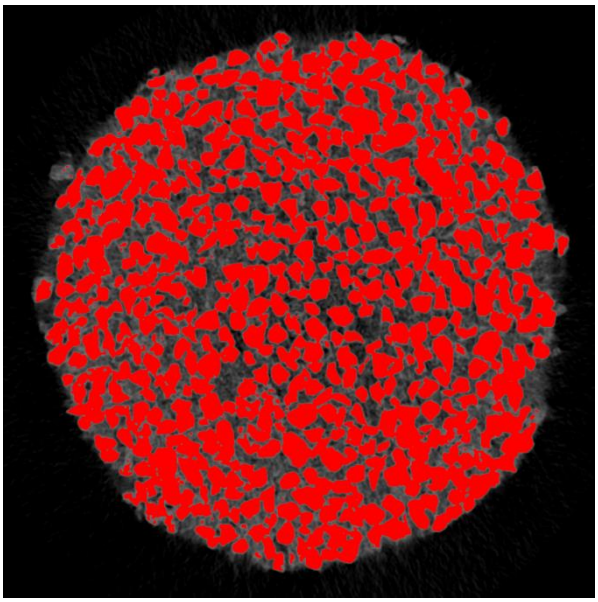

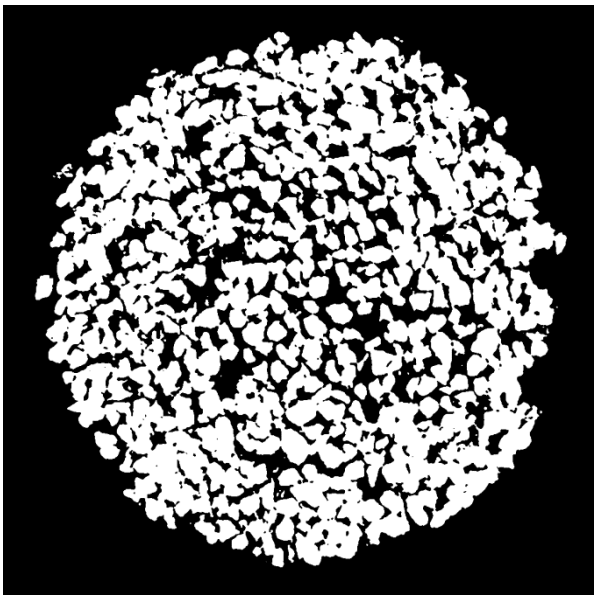

c. otsu's thresholding d. binary image

**Figure 63.** Steps of image processing with Fiji-ImageJ, (a) cropped stack; (b) using median filter; (c) otsu's thresholding; (d) binary image

In modern days, the most common noise removal filter used is the median filter. This kind of filter is a non-linear digital filtering method which removes any kind of noise from an image. This noise reduction is a characteristic pre-processing stage to improve the outcomes of later processing (e.g, edge detection on an X-ray image). This method is accepted widely as it preserved the initial edges while any noise from the image. A typical example of an effect of median filter is shown in figure below. In Fig. 64, the main effect of the median filter is shown by applying over a section of the 3DP specimen image. The image spatial resolution is 5.0 μm. A comparison of using filter and non-filtered segmentation is shown below.

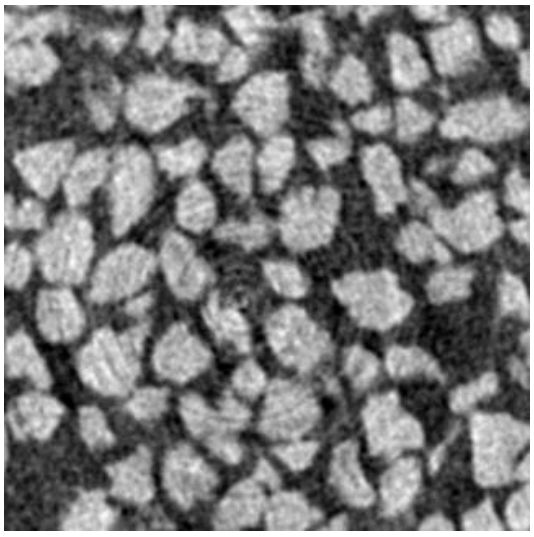

**(a)**

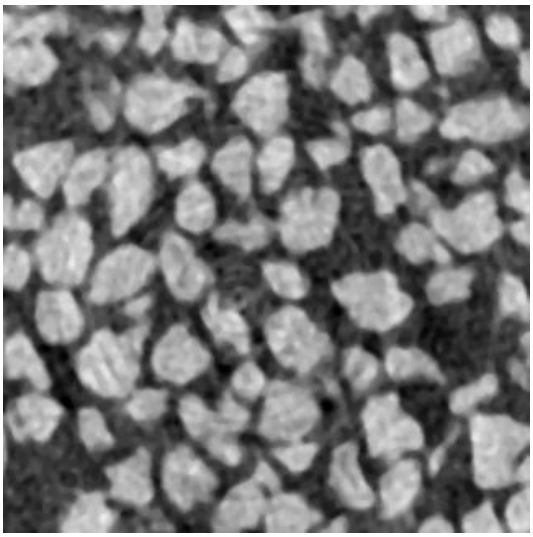

**(b)**

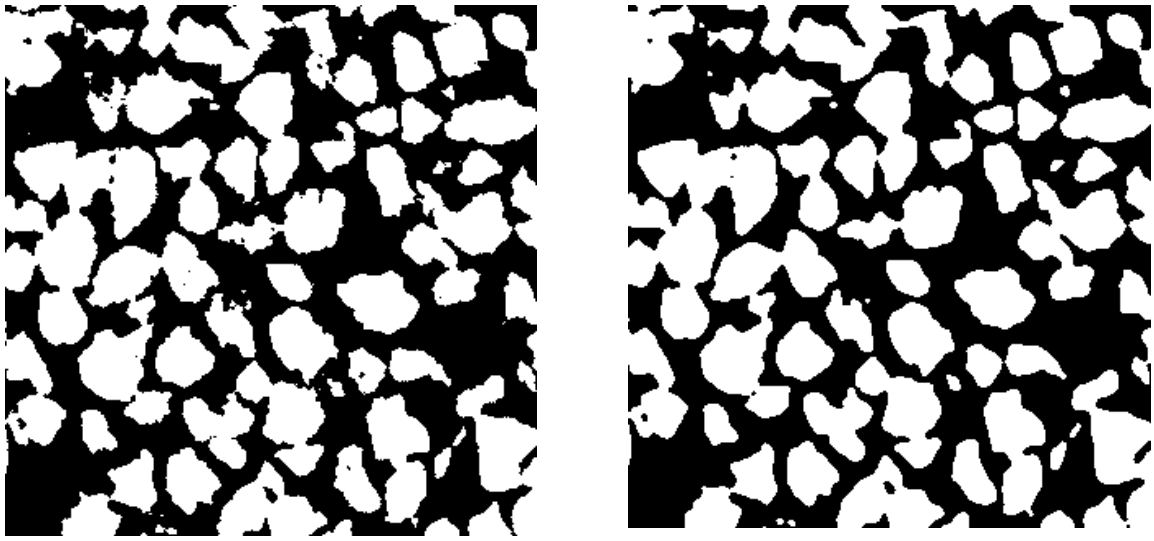

**(c)** **(d)**

**Figure 64.** (a) Cross section of raw image; (b) median filtered image of (a); (c) is binary image of (a); (d) is binary image of (b)

### 4.5 Experimental setup

In the present study, reconstructed 3D tomographic images of 3DP specimens were used to extract information on microstructural characteristics (grains, pores, porosity, tortuosity) and permeability through image analysis, PNM and LBM simulations. The X-ray μ-CT images were obtained at a facility of CEA LIST (NDT department). The X-ray equipment consists of a micro-focus X-ray generator, a flat panel detector, and a turn-table, situated in a large inspection cell which enables the addition of instrumentation for in-situ characterizations. The X-ray generator is a Viscom 225 kV (320 W) model with a micro-focus spot-size. The detector is a Perkin Elmer XRD0822 model having 1024 x 1024 pixels of 200x200 μm2 in size, and the acquisitions were performed in a classical setup with a rotating sample (360°) and static source and detector positions. The optimum scan settings for the specimens were determined, obtaining 100 kVp, 60 μA, and 1 second exposure time. For each CT scan, a number of 900 projections were acquired, with an integration time of 1 second. The total acquisition scan was about 30 minutes. The scan facility uses a temperature controlled inspection cell and therefore the impact of temperature variations is considered negligible. The magnification factor was set to 40, which gives a voxel size of 5 μm3 in the CT images. The reconstructions and preliminary analysis were performed by using VGSTUDIO MAXTM commercial software at a facility of CEA LIST (NDT department). The setup is shown in Fig. 65 as well as the sample holder and the details of specimens.

For the X-ray CT analysis, 10 small-grain and 10 big-grain cylindrical samples with different binder percentages were printed and named accordingly; (a) Small Grains with High Binder content (SGHB), (b) Small Grains with Low Binder content (SGLB), Big Grains with High Binder content (BGHB), Big Grains with Low Binder content (BGLB). Here small and big grains are 140 µm and 190 µm respectively. And low and high binders are 1% and 2% respectively  A set of 20 (5 × 2 different binder content × 2 different grain size) cylindrical specimens were printed for the experimental permeability measurements, with diameter of 50 mm and height of 50 mm.

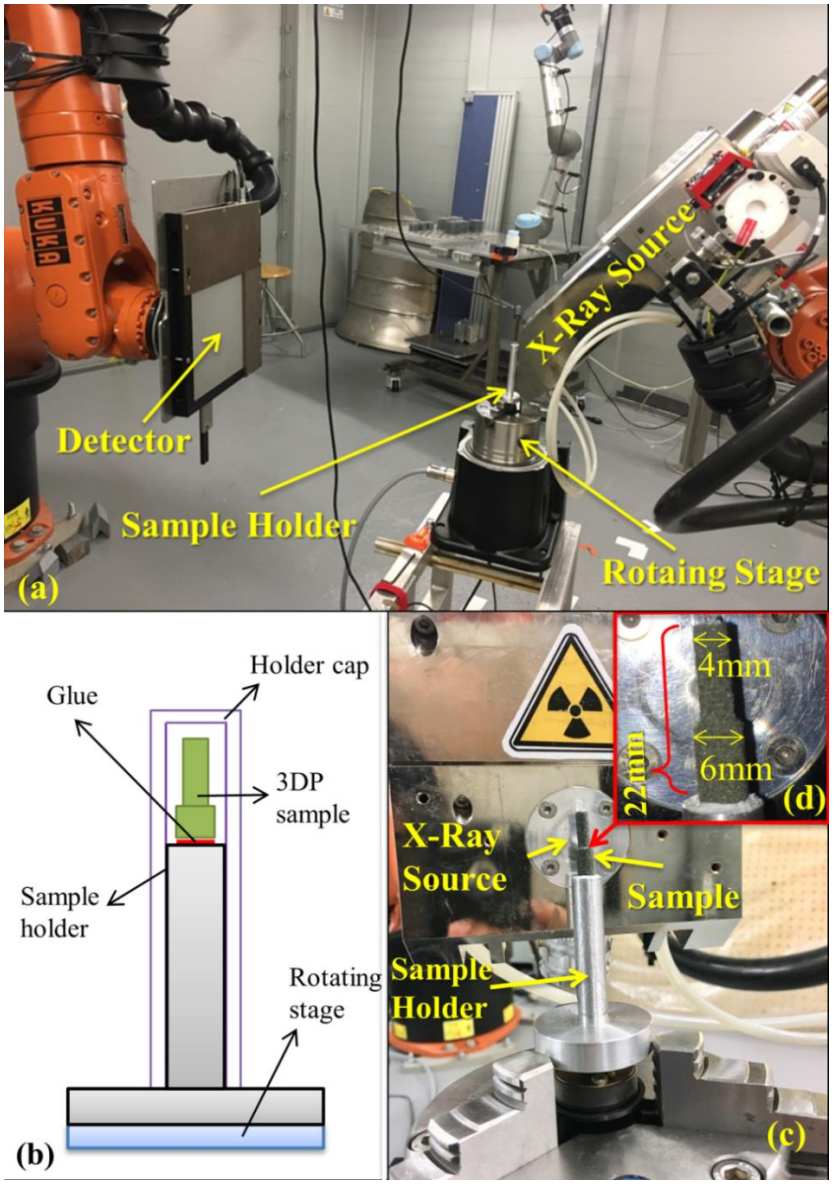


**Figure 65.** Different views and schemes of the experimental X-ray µ-CT setup showing: (a) the robotic X-ray inspection platform, (b) a schematic design of the sample holder (c) the sample holder and (d) a zoom-in view including the dimensions of the sample

The choice of the binder percentages was based on the recommended values for binder contents (0.9% - 2%) reported in previous research by [91]. The dimensions of the 3D printed parts for X-ray µ-CT tests were measured manually using Vernier caliper, with top height of 12 ± 0.02 mm, base height of 10 ± 0.02 mm, top diameter of 4 ± 0.02 mm and base diameter of 6 ± 0.02 mm, respectively (the uncertainty corresponds to 95% confidence interval), Fig. 65(d). The temperature of the 3D printing room was controlled at 25 ± 2 °C and the measured relative humidity of the room was 40 ± 10%. A detailed experimental investigation of the effects of mass transport improvement on mechanical strength of 3DP sand mold was presented in previous works by [1], [2] and [92].

## 4.6 Analysis of tomographic images of 3DP mold

### 4.6.1 Introduction

Characterization of mass transport properties through pore networks with complex geometry and connectivity, such as 3DP sand molds, is essential in order to assess the risks of incomplete filling and gas porosity in castings. The fundamental microstructural characteristics include grain size distribution, pore size distribution, throat (pore constriction) size distribution, pore-to-throat size ratio, pore connectivity, and tortuosity. These microscopic physical properties will control the macroscopic characteristics of the 3DP molds in terms of permeability and porosity governing the flow of liquid metal, and, more generally, the heat and mass transport within the 3DP sand mold. Therefore, knowledge of the relationships of 3DP process parameters and these microscopic characteristics is of vital importance to predict casting defects. On this subject, it was stated earlier by [67] that high reacoater speeds lead to lower grain packing densities in 3DP molds (porosity depends on recoating speed). It is also known that high levels of sand compaction reduce permeability due to the decrease in volume available for fluid flow and the increase in specific surface of the interstices. Pore Network Modelling (PNM) offers a simple demonstration of the complex pore structure and topology, but quiet more accurate than traditional bundle-of-capillaries model. In PNM the void phase is divided into a set of spherical pores connected by cylindrical throats. A complete review of PNM for porous geometries (pore network construction) has been studied elsewhere by [93]. [94] used PNM to extract the network of pores and the connected throats from a fibrous material to simulate two-phase flow. It was shown by [95]

and [96] that the permeability can be predicted using the throat size distributions with the modified Archie's law.

In the industrial foundry processes, numerical simulations of mold filling and casting solidification are employed in order to optimize the part designs, reduce the manufacturing costs and prevent defect generation. However, the lack of accurate estimations of key inputs, e.g., local porosity, density, permeability, and strength, limits the usefulness of the obtained numerical results. Therefore, it is crucial to develop a non-destructive method to properly characterize 3DP sand molds in order to predict the relationships between process parameters and the inputs to such simulations. Other non-destructive methods include the traditional permeability test in which air is injected to the 3D printed sample (although they need sampling of the mold). Also, Scanning Electron Microscope (SEM) imaging could be considered as a suitable non-destructive method, but only 2D microstructural information can be extracted. Although Mercury Intrusion Porosimetry (MIP) is by far the most popular method for characterizing the pore size distribution of porous materials with pores in the range of 500 μm to 3.5 nm as stated by [97], MIP experiments are not expected to work well on unconsolidated materials like 3D printed casting sands because the applied pressure damages the material and its void-structure. X-ray micro computed tomography (μ-CT) is a non-destructive and non-intrusive method as stated by [98], allowing the characterization of 3D printed sand mold specimens. On this regard, a complete review of X-ray μ-CT and its applications has been studied elsewhere by [99]. X-ray μ-CT has emerged as a powerful nondestructive technique (NDT) for the direct 3D characterization of complex porous geometries. [100] stated that the 3D images of the pore space, like those provided by X-ray μ-CT, can be used for direct computation of multiphase fluid flow and to reliably characterize permeability from the realistic digital images provided by this technique.

Different numerical methods exist for the simulation of creeping flow through porous media at the microscale, e.g., Finite Volume Method (FVM) and Lattice Boltzmann Method (LBM) [101,102]. [103] used FVM to model fluid flow through the real microstructure of a fibrous mat to predict the permeability and compared them to various analytical expressions. [104] used FVM to perform a direct numerical simulation of fluid flow in a fully saturated porous media for the prediction of permeability from μ-CT image. [105] idealized a geometrical introduced to characterize small volume of packed sand in pore-level computations using

YADE (Yet Another Development Engine) solver. In previous research by [106], it was proved that using LBM, to obtain permeability from a digital image is a reliable alternative to destructive traditional measurements. [107] presented a novel lattice Boltzmann scheme to simulate viscoelastic fluid flows, and stated that LBM results were found to be in good agreement with analytical and other numerical results. In this sense, some works were performed earlier by combining LBM and X-ray µ-CT for the calculation of permeability of volcanic pumices [96]. [108] characterized the local density of sand mold using industrial computed tomography, and found good agreement with the experimental density of sand mold. Some typical results were reported recently by [109] for the use of X-ray µ-CT to characterize the additively processed porous structure like 3DP sand mold. [110] used LBM to predict permeability from a computer-generated sphere packing, and to study the impact of sand compaction from the simulations. However, no other literature review exists tackling the particular case of permeability characterization of 3DP sand molds from µ-CT digital images using LBM and PNM.

The current work will describe an accurate and rigorous method to characterize the physical properties of such additively processed sand mold from the digital images provided by X-ray µ-CT. The first point of inquiry is, what is the real local permeability of 3D printed structure? To achieve that goal, a set of X-ray µ-CT experiments are first performed on additively processed silica samples with different silica grain sizes and binder percentage. The microstructural properties are secondly determined through the use of image analysis techniques and PNM. Then, LBM numerical simulations and analytical methods are used to predict the permeability of the samples, and the results are subsequently compared to experimental measurements provided by traditional techniques.

### 4.6.2 Grain Morphology: Grain Size Distribution (GSD) and Sphericity

#### 4.6.2.1 Analysis method

The sand grain shape and size plays an important role in the fabrication of 3DP sand mold, as they deeply impact the permeability of the sand molds, hence casting quality. The finer the silica grains, lower the permeability will be, similarly the coarse silica grains will lead to a higher permeability. Grains are generally categorized based on their shapes; rounded, sub-

angular and angular. Rounded grains lead to high permeability of sand mold, due to least contact with other grains during the sand compaction. However, these kinds of grain shape do not pack up to its maximum, hence lacks strength. Whereas sub-angular grains have low permeability with high strength values compared to the rounded grains. The angular grain provides higher strength to the 3DP mold, but with low permeability due to tight packing of grains. Therefore it was of great importance to characterize the grain size distribution along with their forms, as it directly affects the casting quality.

For the analysis of the silica grains size distribution, Morpholib - Distance Transform Watershed 3D algorithm by [111] included in ImageJ was applied to the thresholded images in order to separate touching objects (creating a border far from the center of the overlapping object). The watershed segmentation algorithm detects and separates pore bodies in 2D or 3D images. Then, the connected components are scrutinized using Analysis 3D – Labelling plugin by [112] from ImageJ. By using this algorithm, a new volume was generated in which all the particles were labeled. From the generated results, the equivalent diameter of each silica grain $d_g$ was calculated using Eq. (15):

$$\mathrm{d}_g = \sqrt[3]{6 \times \mathrm{volmarch}/\pi} \qquad \textbf{Eq. 14}$$

with $volmarch$ being the volume in marching cubes. Then, a result file in .xl format was generated by using the Analysis 3D – Parameter plugin by [112] listing several parameters: volume in pixel, volume in marching cubes, surface with marching cubes. A Granulometry-histogram plot was plotted using the total number of labeled particles as a function of particle diameter as obtained from Eq. 14. Then, the sphericity of the particles was computed using the following formula (nearly-spherical shapes approaching value 1):

$$\mathrm{sphericity} = 6 \times \mathrm{volmarch} \times \sqrt{\pi/\mathrm{surfacemarch}^3} \qquad \textbf{Eq. 15}$$

Where $surfacemarch$ is the surface with marching cubes as shown by [112]. Furthermore, the porosity of the 3DP specimen was calculated by dividing summation of resulting $volmarch$ values by the size of the reconstructed image multiplied by total number of slices. Also, standard Kozeny–Carman equation (bundle of cylindrical capillaries model) was used to

calculate permeability k from the obtained average grain diameter and pore space volume from the characterized µ-CT images by:

$$k = \frac{\varepsilon_{bed}^3 \, d_s^2}{180(1-\varepsilon_{bed})^2} \quad \textbf{Eq. 16}$$

where $\varepsilon_{bed}$ is the average bulk porosity of the µ-CT images of the 3DP specimen and $d_s$ is the average diameter of the silica grains.

To go further, the pore connectivity Z and the geometric tortuosity $\tau$ of the 3D printed sand mold specimens was also computed through an iterative-thinning algorithm (Median axis algorithm) by using Skeletonize 3D and Analyze Skeleton plugins from ImageJ by [113] for all the 3DP specimens (SGLB, SGHB, BGLB, and BGHB). The number of branches that originate from a junction (3, 4 and >4 branches) is termed as pore connectivity, and the ratio between the regular and the Euclidean length of such branches is termed as geometric tortuosity. A result window from the plugin displays the node-to-node distances ($d_i$), Euclidian distances ($d_{euclid}$), total number of junctions ($n_j$), total number of triple-branch junctions ($n_t$), total number of quadruple-branch junctions ($n_q$). Any junctions above that is a high-order junctions ($n_x$). It was shown earlier by [114], that the pore connectivity (Z) can be calculated from ($n_j$), ($n_t$), ($n_q$), and ($n_x$), using Eq. 17(a) and Eq. 17(b). Where, $n_t/n_j$, $n_q/n_j$, and $n_x/n_j$ provides the fraction of nodes connecting 3, 4 and >4 branches respectively.

From the resulting output image and data file, the geometric branch tortuosity ($\tau$) was calculated as being the ratio of the average Euclidean distances ($d_{euclid}$) between nodes over all node-to-node network distances ($d_i$) [113]. The average value of the geometric branch tortuosity was characterized by applying ImageJ- Skeleton plugin to the images of the all the specimens. τ was calculated as being the average of all node-to-node network distances over the Euclidean between those nodes, Eq. 18.

**Eq. 17**

$$Z = 3\frac{n_t}{n_j} + 4\frac{n_q}{n_j} + 5\frac{n_x}{n_j} \quad \text{(a)}$$

$$\frac{n_x}{n_j} = 1 - \frac{n_t}{n_j} - \frac{n_q}{n_j} \quad \text{(b)}$$

$$\tau = \frac{1}{n}\sum_{i=1}^{n}\frac{d_i}{d_{euclid}} \qquad \textbf{Eq. 18}$$

The results in terms of pore connectivity (Z) and tortuosity (τ) are provided in Table 7. It can be observed that most junctions have 3 branches, a significant number of junctions have 4 branches and only a few present 5 or more branches. An average pore connectivity value of Z ≈ 3 is obtained. In this regard, [109] showed in a previous work that the speed at which the recoater spreads the sand particles on the job box platform affects the pore-connectivity, hence affecting the permeability. It can be deduced from the results displayed in Table 7 that the size of the grain does not affect pore connectivity, in contrast to the case of recoating speed.

**Table 7. Results showing the pore connectivity and tortuosity**

| Sample | $n_t/n_j$ | $n_q/n_j$ | $n_x/n_j$ | Pore connectivity (Z) | Tortuosity (τ) |
|---|---|---|---|---|---|
| SGHB | 0.721 | 0.211 | 0.067 | 3.346 | 1.223 |
| SGLB | 0.703 | 0.243 | 0.052 | 3.348 | 1.221 |
| BGHB | 0.833 | 0.131 | 0.034 | 3.201 | 1.218 |
| BGLB | 0.773 | 0.176 | 0.049 | 3.275 | 1.225 |

The permeability of a 3DP sand mold depends on various influencing parameters, such as porosity, tortuosity and the diameter of pores and throats. Permeability is strongly related to the dimension of the pore constrictions (throats), as most pressure loss is generated in these regions. Previous research works [96] stated that the tortuosity ($\tau$), porosity ($\varepsilon$) can be directly correlated according to Archie's law ($\tau^2 = \varepsilon^{-m}$). In previous works a model was developed as shown in Eq. 19, to calculate k directly from the characteristic diameter of the throats $d_{throat}$ and Archie's law.

$$k = \frac{\varepsilon^m d_{throat}^2}{32} \qquad \textbf{Eq. 19}$$

The permeability was then calculated using the value of average throat size, and was then compared to the experimental and analytical permeability values.

#### 4.6.2.2 Results and discussion

It is to be noted that since the binder was associated to the solid phase in the CT images, an individual effect of the binder cannot be assessed and therefore the values for low binder and high binder were merged together for the assessment, Fig. 66, 67. The procedures presented earlier was applied to all the segmented X-ray µ-CT images in order to obtain the grain size and sphericity distributions of the silica particles. A normal distribution could be observed for the grain size distribution. The extracted silica grain diameter for small grain specimen varied from ~57 µm to ~331 µm, with a mean $d_g$ value of 171.98 µm and the extracted $d_g$ values for big grain specimen varied from ~61 µm to ~409 µm, with a mean grain diameter ($d_g$) of 208.05 µm. A more detailed report regarding the granulometry of the 3DP specimens is provided in Table 2, showing the values for high and lower binder contents. GSD has a profound effect on the permeability of the 3DP sand mold. It can be seen that for both small and bigger grains, there is a similar narrow distribution of grain sizes, hence provides good permeability for fabricated 3DP sand mold. Because sand grains with wide range has higher compaction leading to high density and low permeability compared to the narrow distribution.

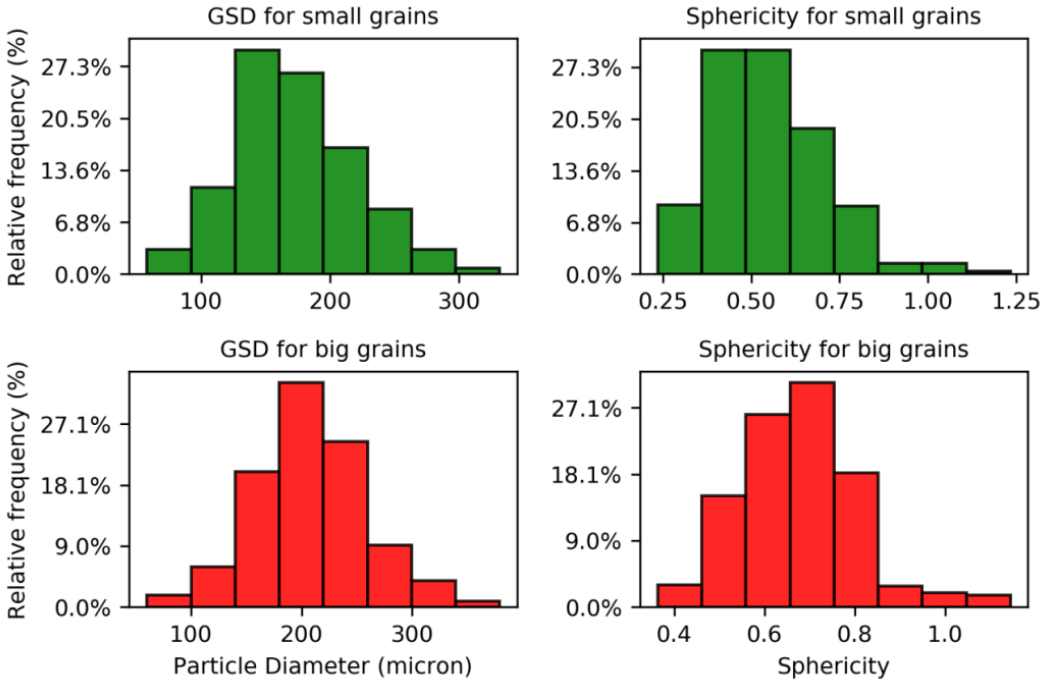


**Figure 66.** Grain size distributions and sphericity

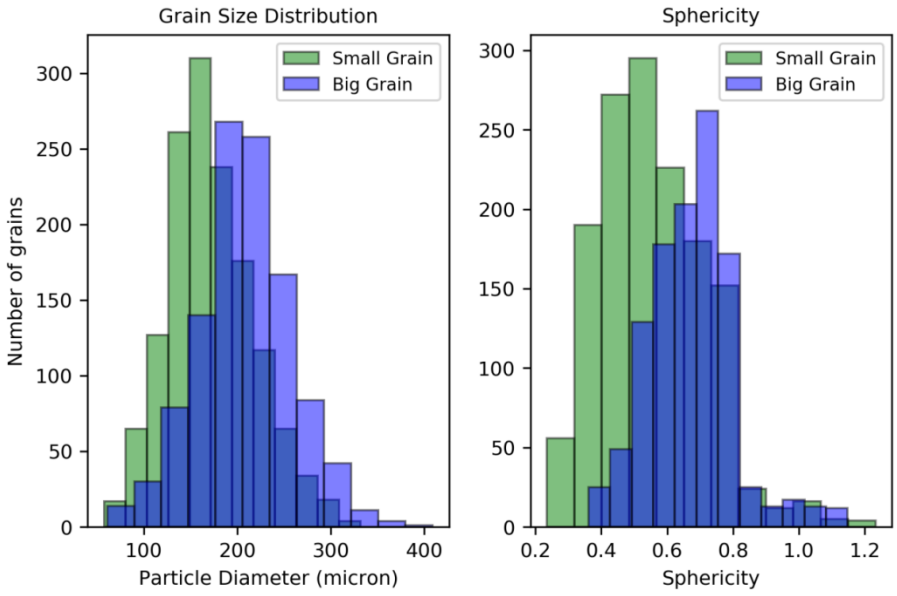


**Figure 67.** Combined (a) grain size distribution for small grains and big grains, and (b) sphericity distribution

Also, the sphericity measured from the X-ray µ-CT image provides the information about the particle shape, which affects grain packing density, hence varying porosity and permeability. We note the fact that grains with different shape might have identical sphericity values. The results in terms of sphericity are listed in Table 8. It is observed that the sphericity values of the bigger grain size specimens were higher than those of the small grain size specimens. Some examples of extracted grains from the big grain specimens are shown in Fig. 68. It can be noticed that the grains are far from being a perfect sphere, with an average sphericity value of ~0.6. As we discussed earlier the shape can be rounded, angular, sub angular, however in the present case, it can be observed that the grains are mostly sub angular. All the results of the sphericity of the specimens are shown as histogram in Fig. 66 and 67.

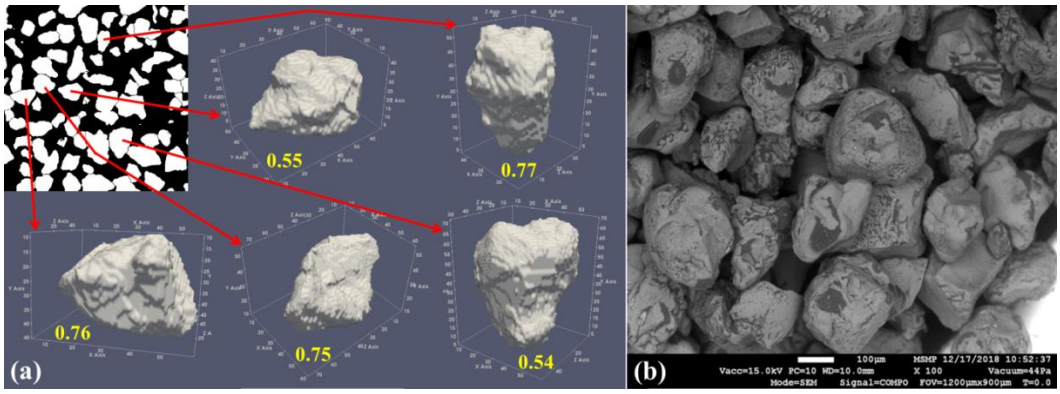


**Figure 68.** (a) Examples of silica grain with different sphericity number in the BG specimen. (b) SEM image of a 3DP specimen, showing the silica grains

**Table 8. Results from image analysis**

| Sample Type | Mean $d_g$ (µm) | Mean Sphericity | Mean porosity (%) | Permeability ($m^2$) | Permeability (Darcy) |
|---|---|---|---|---|---|
| *SGLB* | 154.07 | 0.56 | 50.97 | $6.593 \times 10^{-11}$ | 66.80 |
| *SGHB* | 156.85 | 0.55 | 49.37 | $6.182 \times 10^{-11}$ | 62.63 |
| *BGLB* | 210.11 | 0.66 | 48.48 | $1.003 \times 10^{-10}$ | 101.62 |
| *BGHB* | 207.04 | 0.67 | 49.35 | $1.077 \times 10^{-10}$ | 109.12 |

From the obtained granulometry, using the porosity and mean grain diameter, the permeability of the 3DP specimens were predicted with Kozeny-Carman equation (Eq. 16) as shown in Table 8. It is to be noted that since the binder was associated to the solid phase in the CT images, an individual effect of the binder cannot be assessed and therefore the values for low binder and high binder are very close.

### 4.6.3 Direct pore scale modelling

#### 4.6.3.1 Introduction

Direct pore scale characterizations are presently considered as a standard tool to measure the single-phase or one dimensional mass flow and transport properties of any complex porous geometry. Among all the existing characterization techniques, the Lattice Boltzmann method (LBM) is considered as the most widely used methods that can be applied to any complex porous geometry without simplifying it. Compared to other existing models for mass flow characterization, LBM do not require building any approximated models to measure the permeability of the porous geometry, which is an added advantage of the suggested method. The LBM is based on statistical (macroscopic) description of microscopic phenomena. It designates fluid motion in the geometry as collisions of imaginary particles, which are much bigger than the real fluid molecules. The imaginary particles are not real fluids but they exhibits similar behavior at a macroscopic scale.

In fact, the LBM have been shown to recover the Navier-Stokes equation at the macroscopic scale. Because the LBM describes macroscopic fluid flow by the collective behavior of many fictitious molecules but not by full molecular dynamics, it is referred to as a mesoscopic description of microscopic physics (Figure 68). The biggest advantage of the LBM comes

from its unique derivation (Figure 68). While other methods, such as network models, the finite-element method (FEM) and the finite-difference method (FDM), discretize the model and the governing equations (top-down approach), the Lattice-Boltzmann method recovers the governing equation from the rules in the discrete model (bottom-up approach). Since originated from the discrete lattice, we do not have to discretize the governing equation of the model; i.e. it is readily applied to any arbitrary discrete geometry.

#### 4.6.3.2 Lattice Boltzmann: Theory and Implementation

In this section we will be discussing about the mesoscopic lattice boltzmann methodology, and also we will be explaining the algorithm for solving fluid flow using lattice boltzmann methodology. A schematic representation of lattice Boltzmann equation has been provided below, Fig. 69, which takes information from the Navier-Stokes equation and converts into a physical lattice gas automata by performing some mathematical analysis using Boltzmann equation. The LBM method have advanced from lattice-gas (LG) models (cellular automatons), which is more spontaneous to understand. Therefore it can be observed that it is a coupling between engineering problem, mathematical problem and physical insight.

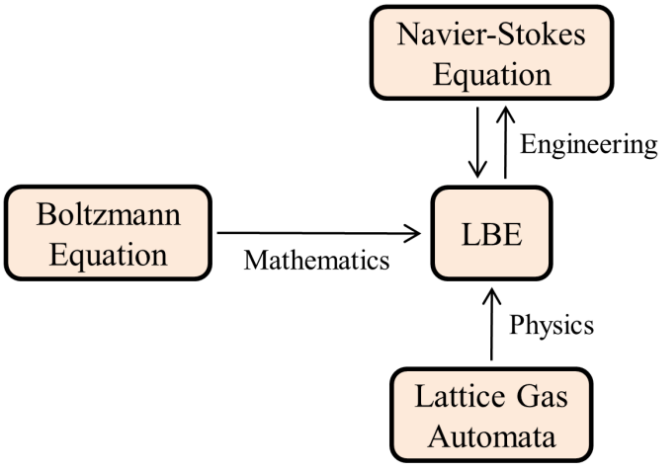


**Figure 69.** Govering equations with LBM

Before discussing theory behind the LBM, it is important to mention why this method is used for flow simulations in the porous materials. Actually, everything starts from the Navier-Stokes equations that govern the motion of fluids and are considered as the fundamental in fluid flow modeling. They can be interpreted as Newton's second law of motion for fluids

[115,116]. In a case of an incompressible Newtonian fluid, it is possible to write this as follows, Eq. 21. Therefore in the left hand side we are having unsteady and inertia term and in the right hand side we are having the pressure gradient term over viscous term.

$$\overbrace{\rho \cdot \left( \frac{\partial \mathrm{u}}{\partial t} + \mathrm{u}.\nabla \mathrm{u} \right)}^{\text{inertial forces}} = \underbrace{-\nabla p}_{\text{pressure gradient}} + \overbrace{\mu \cdot \nabla^2 \mathrm{u}}^{\text{viscous forces}} + \mathrm{F} \qquad \textbf{Eq. 20}$$

$$\frac{\partial \rho}{\partial t} + \nabla(\rho \cdot \mathrm{u}) = 0 \qquad \textbf{Eq. 21}$$

In lattice-gas (LG) models, the space is generally discretized by using regular lattice grids, on which the fluid particles can propagate along with the discretized velocities [117,118]. Now, let us focus on how the domain of the numerical simulation can be discretized in lattice Boltzmann methodology. For example, let us consider a rectangular domain as shown in Fig. 69. We will be discretizing the domain in small volumes or small lattices, because in LBM we consider that the domain is actually discretized in lattices. All the individual lattices are shown in the figure below. The discretization pattern is more or less similar to the finite volume or finite difference methodology. The only difference is that, in finite difference or finite volume methodology one can perform non-homogeneous discretization whereas in LBM allows only homogeneous discretization. Therefore as shown in figure, the rectangular domain has been divided into small uniform (homogenous discretization) volume or lattices. LBM has certain mechanism to carry forward the domain information, which is actually the information for the governing equation parameters (ρ, u in the provided equation). At each time step, the particles propagates (streaming operation) to its immediate neighboring lattice cell, depending on the velocity and its initial position, and then tend collide (collision operation) with each other, in such a way that the momentum is conserved. In lattice Boltzmann method, the moving fluid particles on the lattice grids are replaced by “packets” of moving particles, which is the particle velocity distribution [119]. This information can be perceived as a discretization of the behavior of a steady state ideal gas. One typical example of D2Q9 lattice structure has been shown below, and it can be observed that the (1) information generated in the lattice remains inside the lattice ($0^{th}$ direction), (2) along with 8 other possibilities (8 other direction apart from remain inside the lattice). Therefore for D2Q9, there exist 9 possible directions. The information about the directions is first captured before

streaming. Then after the collision, the information gets propagated depending on the streaming.

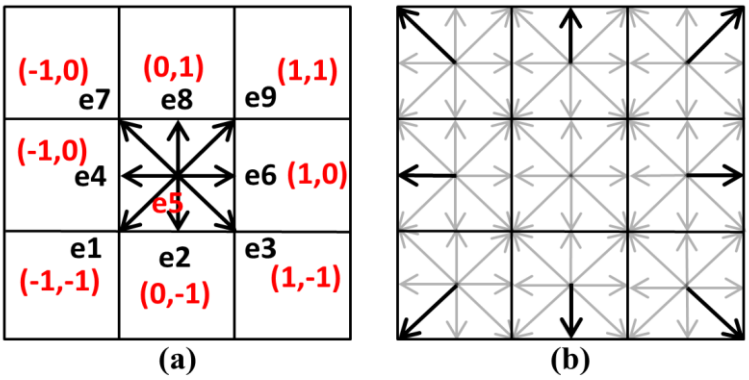


**Figure 70.** Streaming before and after propagation in lattice cells

A schematic representation of streaming before and after propagation is shown in Fig 70. It can be observed that after propagation, the left hand side horizontal direction has moved to the immediate left most lattice and similarly the right hand side horizontal direction has moved to the immediate right most lattice. The same repeats for all other lattice directions. Therefore, if information is generated in the center cell, it propagates to the immediate neighboring cell in the described pattern.

So these 2 steps are very important, first one being the collision and second one being the propagation of information based on the specified directions. It was stated that the LB method uses discretized Boltzmann equation of probability particle distribution that propagates and interacts on lattice with limited degrees of freedom (DOF) [120]. The particle distribution for each possible particle velocity vector is defined for each node on regular lattice.

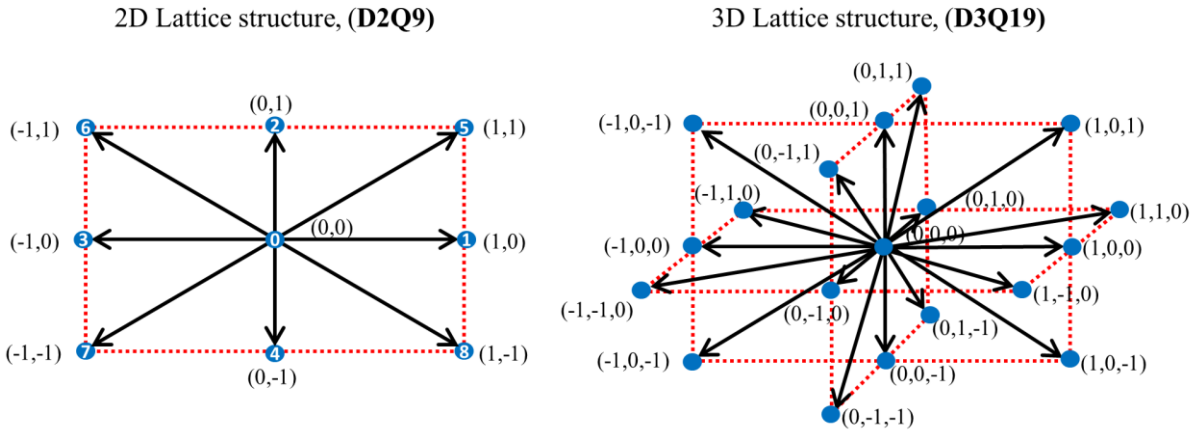


**Figure 71.** Diagram showing the velocity discretization in D2Q9 and D3Q19 lattice scheme

For a 2D lattice structure, we will be having a D2Q9 lattice scheme, as explained earlier. A complete schematic representation of lattice direction is shown in FIG. 71, along with 9 different marked directions (0 to 9).

First let us take $f_i$, which is actually is a probability function, whose summation will be giving 1 macroscopic variable, $\rho$. Therefore summation of $f_i$ for all different directions, depending on the chosen lattice structure we can write that it equals to $\rho$ . Therefore for D32Q9 lattice structure starting from $f_0$ to $f_8$, if we add all those $f_i$, we will be getting the macroscopic property $\rho$.

$$\rho = \sum_i f_i \qquad \textbf{Eq. 22}$$

In the similar way the lattice velocity ( $\mathbf{u}$ ) can be obtained using $\mathbf{e}_i$ and $f_i$. Where $\mathbf{e}_i$ is the lattice directional velocity.

$$\mathbf{u} = \sum_i \frac{f_i \mathbf{e}_i}{\rho} \qquad \textbf{Eq. 23}$$

Therefore for D2Q9 structure, the magnitudes for $0^{th}$ direction is having (0,0) velocity and the velocity magnitudes for all corresponding e's is shown in Figure 70(a). The velocity in terms of sine and cosine function for Zero$^{th}$, horizontal/vertical and for the corner components is shown below.

$$\mathbf{e}_i = \begin{cases} 0 & \text{for i = 0} \\ \left(\cos\left[(i-1)\pi/2\right], \sin\left[(i-1)\pi/2\right]\right)c & \text{for i = 1,2,3,4} \\ \sqrt{2}\left(\cos\left[(i-5)\pi/2+\pi/4\right], \sin\left[(i-5)\pi/2+\pi/4\right]\right)c & \text{for i = 5,6,7,8} \end{cases} \qquad \textbf{Eq. 24}$$

The weights for different directions are typically specified when defining the lattices. The usual weights we give for D2Q9 lattices are provided below.

$$w_i = \begin{cases} 4/9 & \text{for i = 0} \\ 1/9 & \text{for i = 1,2,3,4} \\ 1/36 & \text{for i = 5,6,7,8} \end{cases}$$ **Eq. 25**

In a similar way, for a 3D lattice structure, we will be having a D3Q19 lattice scheme. A complete schematic representation of lattice direction is shown in Fig. 70, along with different marked directions (0 to 18). Now after discretizing of this domain, the main task is to discretize the governing equations as explained earlier. The process of discretization involves some sort of collision, so we have to find out the probability density function for the collisions. Here the discretization function follows lattice Boltzmann discretization (lattice gas cellular automata formulation). In Finite volume method we use Taylor series expansion, whereas in case of lattice Boltzmann we use Boltzmann approximation.

The set of equations provided along with specific boundary conditions allows simulating fluid flow in the lattice Boltzmann framework. In the lattice structure, the density of fluid particles for each position of the cell is determined by:

$$\rho = \sum_i f_i(\mathrm{x},t) = \sum_i f_{i(\text{equilibrium})}(\mathrm{x},t)$$ **Eq. 26**

where $f_i(\mathrm{x},t)$ is the particle probability distribution function at location $X$ ( denotes the cell position, represented by the center of the cell) and time $t$ along the $i^{th}$ direction, and $f_{i(\text{equilibrium})}$ is the equilibrium probability distribution functions that depend on the macroscopic variables, density ρ, velocity u at position x and time t.

The velocity at each cell position is expressed by:

$$\rho \cdot \mathrm{u} = \sum_i \frac{f_i(\mathrm{x},t)}{c^2}\mathrm{e}_i = \sum_i \frac{f_{i(\text{equilibrium})}(\mathrm{x},t)}{c^2}\mathrm{e}_i$$ **Eq. 27**

Where, $\mathbf{e}_i$ represents the $i^{th}$ discrete local particle velocity (*i* from 0 to 19).

The D3Q19 discrete velocities as shown in Fig. 70 can also be written in a matrix form as:

$$E = \begin{bmatrix} 0 & 1 & -1 & 0 & 0 & 0 & 0 & 1 & -1 & 1 & -1 & 1 & -1 & 1 & -1 & 0 & 0 & 0 & 0 \\ 0 & 0 & 0 & 1 & -1 & 0 & 0 & 1 & -1 & -1 & 1 & 0 & 0 & 0 & 0 & 1 & -1 & 1 & -1 \\ 0 & 0 & 0 & 0 & 0 & 1 & -1 & 0 & 0 & 0 & 0 & 1 & -1 & -1 & 1 & 1 & -1 & -1 & 1 \end{bmatrix}$$

The velocity in each direction is commonly given by:

$$\mathrm{e}_i = \begin{cases} 0 & \text{for i = 0} \\ 1 \cdot c & \text{for i = 1,....,6} \\ \sqrt{2} \cdot c & \text{for i = 7,....,18} \end{cases} \qquad \textbf{Eq. 28}$$

Where, $c = \delta_x / \delta_t$ is the characteristic lattice velocity as defined by the lattice grid spacing $\delta_x$ and at the time step $\delta_t$.

For each time step, the particles at all nodes propagates (streaming, Fig. 70) to the immediate neighboring nodes along the corresponding directions according to their volocities as explained earlier, then colliding (relaxed by a collision step) and forming new particle probability distributions [119]. The change of the density distributions before and after collisions is usually computed using single relaxation time approximation. Therefore, for LBM computer simulation, there occurs two operations at each time step ($\delta_t$), namely the streaming operation (propagation) and collision operation. The propagation or the streaming operation is expressed by:

$$f^{'}(\mathrm{x} + \mathrm{e}_i \delta_t, t + \delta_t) = f_i(\mathrm{x}, t) \qquad \textbf{Eq. 29}$$

The simplest case takes place when the collision operator is defined as the Bhatnagar-Gross-Krook (BGK) operator; however, correctly modeling the effect of viscosity requires two-relaxation time models [121]. It was shown earlier by researchers that the Navier–Stokes equations can be recuperated from the LB scheme in the incompressible limit [122]. The collision operator always depends on the present value of present particle distribution function and the equilibrium value. The collision operation is expressed by:

$$f_i(\mathrm{x} + \mathrm{e}_i \delta_t, t + \delta_t) = f^{'}(\mathrm{x} + \mathrm{e}_i \delta_t, t + \delta_t) - \frac{\left[ f_i(\mathrm{x}, t) - f_{i(\text{equilibrium})}(\mathrm{x}, t) \right]}{\tau} \qquad \textbf{Eq. 30}$$

Where, the parameter $\tau$ is the dimensionless relaxation time and $f_{i(\text{equilibrium})}$ are the equilibrium distribution functions that depend on the macroscopic variables, density ρ and velocity u at position x and time t.

$$\Omega(f_i)_{(\text{BGK})} = -\frac{\left(f_i(\mathrm{x},t) - f_{i(\text{equilibrium})}(\mathrm{x},t)\right)}{\tau} \qquad \textbf{Eq. 31}$$

The BGK collision operation scheme is a very simple in form, but there is a linear increase of permeability with increase in relaxation frequencies, which can be unphysical in nature. However, this unphysical effect is removed when $\tau = 1$ is used. BGK collision operator allows in avoiding complicated collision models by using single relaxation time for the computation, e.g. the multiple relaxation time models.

The two operations (streaming and collision) can be combined as expressed below:

$$f_i(\overbrace{\mathrm{x} + \mathrm{e}_i\delta_t}^{\text{after propagation}}, \underbrace{t + \delta_t}_{\text{next time step}}) - f_i(\mathrm{x},t) = -\frac{\left[f_i(\mathrm{x},t) - f_{i(\text{equilibrium})}(\mathrm{x},t)\right]}{\tau} = \Omega(f_i(\mathrm{x},t)) \qquad \textbf{Eq. 32}$$

The equilibrium distribution $f_{i(\text{equilibrium})}$ in Equation 33 resembles to a steady state to which the particle distribution functions tend to a specific ideal macroscopic state. This was derived from a Maxwellian distribution function and can be expressed in terms of macroscopic flow parameters $(\rho \cdot \mathrm{u})$ under a low-Mach assumption to ensure fluid incompressibility.

For the D3Q19 model, the equilibrium functions are:

$$f_{i(\text{eq})}(\mathrm{x},t) = f_{i(\text{equilibrium})}(\rho,\mathrm{u}) = \rho w_i\left(1 + \frac{3}{c^2}(\mathrm{e}_i.\mathrm{u}) + \frac{9}{2c^4}(\mathrm{e}_i.\mathrm{u})^2 - \frac{3}{2c^2}\mathrm{u}^2\right) \qquad \textbf{Eq. 33}$$

The weighting factor given by:

$$w_i = \begin{cases} 1/3 & \text{for i = 0} \\ 1/18 & \text{for i = 1,....,6} \\ 1/36 & \text{for i = 7,....,18} \end{cases} \qquad \textbf{Eq. 34}$$

The fluid pressure field $p$ is directly related to the density of the flouid as $p = c_s^2 \rho$, where $c_s$ is known as the speed of sound provided in terms of the lattice speed $C$ , and can be expressed as $c_s = c/\sqrt{3}$.

Here the relaxation time $\tau$ is actually dependent on the fluid property. For example for the momentum equation the $\tau$ will be dependent on viscosity, and for an energy equation the will be dependent on the thermal conductivity (this won't be discussed here). The relaxation time $\tau$ is directly related to the kinematic viscosity of the fluid for the present case, given by:

$$\nu = \frac{\delta_t . c^2}{3}\left(\tau - \frac{1}{2}\right) = \frac{\delta_x^2}{3\delta_t}\left(\tau - \frac{1}{2}\right) \qquad \textbf{Eq. 35}$$

From Equation 35 it is clear that in order to provide numerical stability and by having positive viscosity value, the relaxation time should be greater than 0.5 ( $\tau > 0.5$ ) should take place.

#### 4.6.3.3 Calculation of permeability using LBM

In general, permeability can be calculated according to the empirical Darcy's law, which for a

Single-phase 1D flow is defined as follows:

$$k = \frac{\mu \cdot \langle u \rangle}{\frac{\partial p}{\partial x}} \qquad \textbf{Eq. 36}$$

Where $\langle u \rangle$ is the velocity, $\mu$ is the viscosity of fluid and $\frac{\partial p}{\partial x}$ is the pressure gradient.

Application of the Darcy's law, or continuum modeling, becomes possible after averaging macroscopic parameters obtained from the direct pore-scale simulations. It is worth noting that the use of Equation 37 requires adherence of several important assumptions about fluid flow in porous media. In particular, having a laminar (i.e. slow, low- Reynolds flow), single-phase and 1D horizontal flow. Flow laminarity means that it is possible to neglect inertial forces compared with viscous ones. Assuming also absence of external forces, the following expression is obtained:

$$-\nabla p + \mu \cdot \nabla^2 \mathrm{u} = 0 \qquad \textbf{Eq. 37}$$

Furthermore, an additional source term must be added to Equation 38. From mechanical point of view, this term is a drag force due to the viscous friction of fluid with solid walls. Taking this fact into account and using an averaged value for velocity, one may write a new expression as follows:

$$-\nabla p + \mu \cdot \nabla^2 \langle \mathrm{u} \rangle - \frac{\mu}{k} \cdot \langle \mathrm{u} \rangle = 0 \qquad \textbf{Eq. 38}$$

In most cases, the viscous term $\mu \cdot \nabla^2 \langle \mathrm{u} \rangle$ is considered negligible compared with $\frac{\mu}{k} \cdot \langle \mathrm{u} \rangle$.

Considering this, one may obtain simple Darcy's law:

$$-\nabla p - \frac{\mu}{k} \cdot \langle \mathrm{u} \rangle = 0 \quad \text{or} \quad \langle \mathrm{u} \rangle = -\frac{k}{\mu} \cdot \nabla p \qquad \textbf{Eq. 39}$$

#### 4.6.3.4 Implementation of LBM to predict permeability of 3DP sand mold

A volume of 367×367×367 voxel (corresponding to 1835×1835×1835 $\mu m^3$) was cropped from the original reconstructed image with voxels of $5^3$ $\mu m^3$. The cropped image was then binarized using the procedure presented in subsection 2.2.1. The porosity was then computed by dividing the number of pore space voxels (white) by the total volume of the image stack.

The volume of the image being used as input to numerical simulations must be large enough to produce a representative and statistically meaningful value of permeability for the 3DP sand mold. While too big volumes would require a powerful and parallel computer clusters, the Representative Volume Element (RVE) must lead to statistically meaningful results while reducing computation time. Therefore, four different sizes of representative were selected from the original cropped binary image: 200×200×200 voxel, 150×150×150 voxels 100×100×100 voxels and 50×50×50 voxels, as shown in Fig. 72, corresponding to 1000×1000×1000 $\mu m^3$, 750×750×750 $\mu m^3$, 500×500×500 $\mu m^3$, and 250×250×250 $\mu m^3$ volumes, respectively. These 4 cropped segmented stacks were then used as inputs to the LBM numerical simulations performed with Lattice-Boltzmann Method (LBM) solver PALABOS in order to determine the RVE for permeability calculation. The entire process was repeated for all the binder content-grain size combinations.

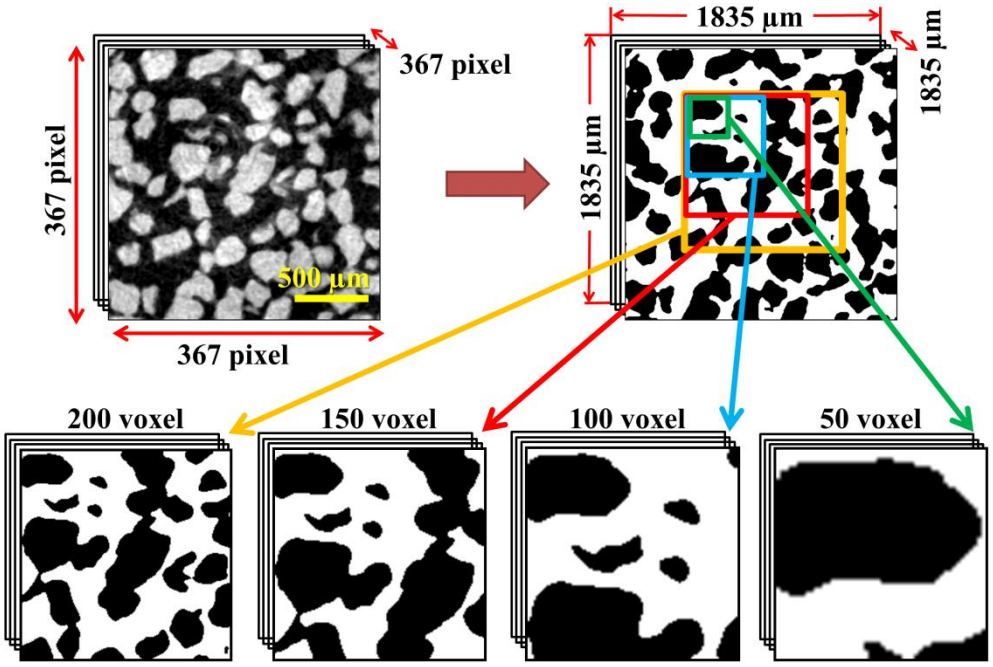


**Figure 72.** Images of different dimensions used to determine the Representative Volume Element (RVE) of the BGLB specimen. Pores are displayed in white and silica sand grains in black on the binary image.

In the present work, it was possible to perform the numerical simulation of single-phase gas flow through the 3DP samples using the open source Lattice-Boltzmann Method (LBM) software PALABOS (Parallel Lattice Boltzmann Solver). LBM is highly reliable and has been applied extensively [123]. [124] used LBM to predict the permeability of a random array of spheres and clay soil, and found that the predicted permeability is consistent with the experimentally measured values. [125] studied the numerical simulations of mass transport through 3D tomographic images of Fontainebleau sandstone, and found that the LBM simulations were similar as compared to the finite difference calculations and with the laboratory experimental measurements. Typically, the lattice grid is just used as the voxel grid of the 3D image obtained from an X-ray µ-CT scan. Therefore, no complicated meshing procedures have to be executed. Solid boundaries are typically handled with a simple bounce-back condition (as explained earlier in theory section), which means that a packet of imaginary fluid particles which strikes or collides a solid wall node during streaming or propagation at a certain time step are usually “bounced back” to the node in the pore space from where they have generated [126]. It was studied and verified earlier that X-ray micro computed tomography (µ-CT) along with LBM can be used for modeling the fluid flow phenomena through complex porous geometries to study the permeability

[96,118,124,125,127]. [96] combined X-ray µ-CT and LBM solver PALABOS to perform numerical simulations of gas flow through volcanic pumices, and validated the method by comparing the resulting data with the experimentally obtained values. Hence for the present numerical simulation, LBM was used to predict the permeability of the additively processed sand mold. In between the interfaces of pore space and silica sand grains, a bounce back boundary condition was applied. In PALABOS-LBM numerical simulation, D3Q19 [128] lattice scheme is proposed. D3Q19 lattice describes the fluid flow in three dimensions with 19 possible velocity vector directions, along with the zero velocity [102,128].

For the numerical simulation of mass transport through the 3D tomographic image of 3DP specimen, a bounce-back boundary condition (no-slip boundary condition) was applied in between the interfaces of pore space and silica sand grains. In PALABOS-LBM numerical simulation, a D3Q19 lattice scheme is proposed as demonstrated earlier by [128]. D3Q19 lattice describes the fluid flow in three dimensions with 19 possible velocity vector directions, along with the zero velocity as shown by [128] and [102]. A standard Bhatnagar Gross-Krook (BGK) collision operator was applied to the D3Q19 lattice scheme. A constant pressure gradient (∇P) was applied through the porous medium, and the initial velocity within the interstices was set to zero. The imposed values of ∇P were low enough to ensure creeping flow regime (Darcy flow). Non-slip boundary conditions were applied to the lateral walls of the geometry shown in Fig. 73. Permeability (k) was then calculated on the non-dimensional lattice unit system from the obtained pressure and velocity maps using the traditional Darcy's equation,

$$-\frac{dP}{dz} = \frac{\mu}{\mathrm{k}} v \qquad \textbf{Eq. 40}$$

where dP/dz is the pressure gradient along the main flow z-direction, µ is the dynamic viscosity, $v$ is Darcy velocity and k is the permeability of the 3DP mold. The calculation methodology used by PALABOS to measure the permeability of porous media involves in solving a modified version of the actual Darcy's equation. Here, *Q/A* is denoted by the term $v$, which is the mean fluid velocity through the porous media or as stated earlier as Darcy's velocity. Q is the flow rate of fluid through a sample of cross section area A.

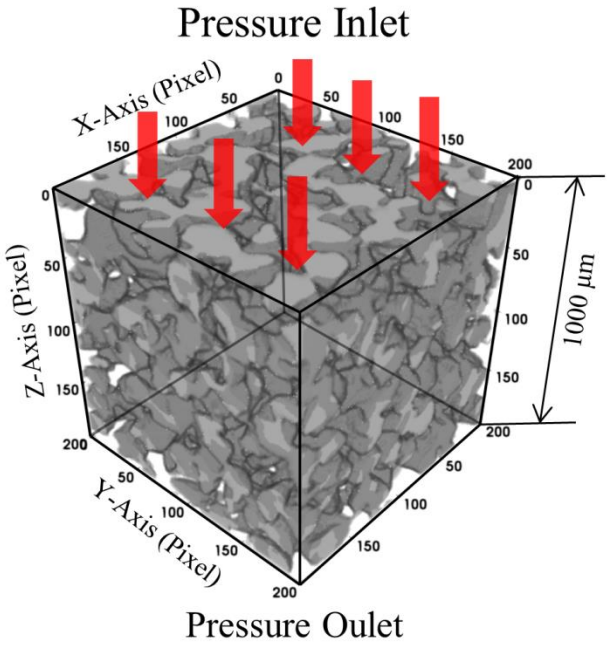


**Figure 73.** Representative volume element (RVE), for BGLB specimen

For the numerical simulation, it is necessary for the 8 bit grayscale binary image to be converted into a DAT-file to ensure the software is capable to read the entire porous 3D printed geometry (along with distinguished pores and grains). The DAT-file conversion procedure along with the code for MATLAB was used from the tutorial as provided in the PALABOS website. The purpose of the code is to distinguish the different interfaces as present on the µ-CT binarised greyscale image. The code helps in separating the grains from the pores, by creating a boundary in between the pores and the grains on the image. The resulting converted DAT-file is a combination of 0's, 1's and 2's, where 0's represents the color in 'dark blue' (pore space volume), 1's represents the color in 'light blue' (interface between the pore space and the silica sand grains) and 2's represents the color in 'yellow' (silica sand grains). The visualization of the converted DAT-file is provided in the figure below, Fig. 74. This conversion methodology reduces the need to convert the image stack into a larger mesh file for simulation, which is an added advantage over other available commercial expensive software's. Hence with LBM, the pixel size of the µ-CT binary image is same as the number of lattice cell (1 lattice cell = 1 pixel). Following the conversion the resulting DAT-file was transferred to the directory of PALABOS for the numerical simulation of gas permeability. Then a constant pressure was imposed through the inlet towards the outlet of the porous complex geometry and at the initial stage the fluid being set to zero. The time-dependent fluid flow (stationary pressure driven) then continued to flow through the

pore space due to the imposed pressure gradient (Grad P). In PALABOS, the steady state for laminar flow is reached only when the standard deviation of mean energy tends to reach a constant state. As stated earlier, the Darcy's law requires many assumptions and in order to make sure the flow reached a steady state (laminar), the simulation was run using different magnitudes of pressure difference; $5\times10^{-4}$, $5\times10^{-5}$ and $5\times10^{-6}$. It has to be made sure that the flow remained constant for different low flow rate, hence reaching laminar flow regime. The PALABOS software then runs the simulations and calculates the permeability (k) of the porous geometry in non-dimensional lattice units (l.u), which was later converted to physical units by multiplying the generated value with the squared spatial resolution of the original µ-CT image (5 micron per pixel).

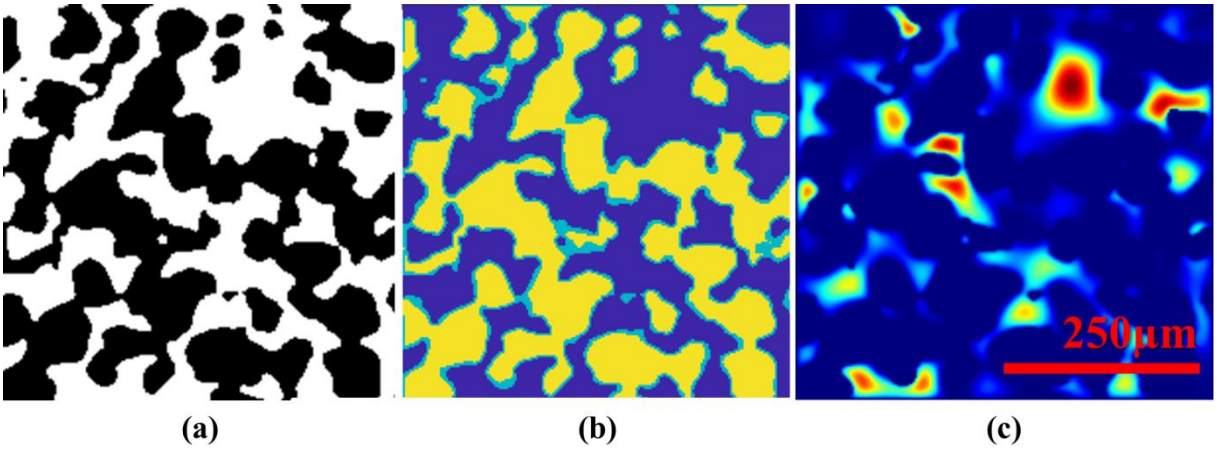


**Figure 74.** Visualization of steps in conversion of a µ-CT image for velocity distribution simulation in the case of the SGHB specimen (200 voxels): (a) 2D slice of the binary volume and (b) converted image for simulation with pore space (dark blue pixel), grains (yellow pixel) and grain boundary interface (light blue pixel) where the bounce-back boundary condition is implemented. (c) Simulated velocity distribution through a cross-section.

#### 4.6.3.5 Experimental approach: Local porosity and permeability

A detailed review of experimental characterization for density, porosity and permeability method has been explained earlier and also was published recently [1,2], so this section contains only a short description of the method. The weight of the 3D printed specimens was measured using a laboratory precision balance and the density of specimen was calculated as the mass of specimen per unit volume. The experimentally measured bulk density of the 3D printed sand specimen was 1.3 g/cm$^3$. The particle density is the density of quartz silica sand with 2.6 g/cm$^3$. From the measured bulk density of 3DP specimen and silica particle density, the porosity of the 3DP specimen was calculated as,

$$Porosity\ (\%)\ =\ 1-\frac{Density_{bulk}}{Density_{silica}} \qquad \textbf{Eq. 41}$$

The experimentally measured porosity values were close to 49-50% for all tested samples, with an estimated standard deviation of 0.2%. Also, the permeability of the 3DP sand mold samples was determined with a permeameter device (Simpson-Electrical, Type: PFG, Serial No.3290, Item No.592-824-600), following the recommendations of the American Foundry Society (AFS) and the same procedure presented in previous works by [72] and [67]. The initial dimensions of the 3D printed parts (cylinders) for permeability characterization were measured using a Vernier caliper, with length of 49.8 ± 0.01 mm and diameter of 49.9 ± 0.02 mm with 95% confidence interval. The gas permeability value gives the volume of air in $cm^3$ which passes through a cylinder, having a cross-sectional area of $1cm^2$ and a height of 1 cm, in 1 minute at a pressure of 100 mm SPWG (Static Pressure Water Gauge). The relationship for the calculation of GP is expressed by the following formula:

$$GP = \frac{V \times h}{F \times p \times t} \qquad \textbf{Eq. 42}$$

Where $V$ is the volume of air, $h$ is the height of the 3DP specimen, $F$ is the cross-sectional area of the 3DP specimen, $p$ is the pressure in mm Static Pressure Water Gauge (SPWG) and $t$ is the passage time for 2000 $cm^3$ of air in minutes. An average permeability value of $5.57 \times 10^{-11}$ $m^2$ or 56.43 Darcy was measured for the small grain (SG) specimens, and $9.02 \times 10^{-11}$ $m^2$ or 91.39 Darcy for the big grain (BG) specimens.

#### 4.6.3.6 Results and discussion

The steady-state velocity maps provided by the LBM simulations introduced in subsection 2.3., throughout the simulated specimens were represented using PARAVIEW software as shown in Fig. 75. It can be deduced from this figure that the velocity distribution is not uniform throughout the porous media, as expected due to the varying cross section dimensions of the interstices. The ratio between pressure difference (ΔP) and volumetric flow rate was constant for all the tested values of ΔP, confirming creeping regime. Different image sizes ($50^3$ voxel, $100^3$ voxel, $150^3$ voxel and $200^3$ voxel) were used in the simulations for the computation of k. Table 9 provides the permeability values for all the specimens as provided by LBM solver PALABOS by using the modified Darcy's equation (Eq. 41) as stated earlier section. Indeed, from Fig. 76, it can be observed that the permeability value for 50 voxel image is lower than that of 100 voxel, 150 voxel and 200 voxel image stack for all the 3DP

specimens. The permeability values approached a plateau value when the size of the RVE was greater than 100 voxels. Therefore, it is suggested to use an input volume of 500 $\mu m^3$, which corresponds to the size of 3 - 4 equivalent layers (3×190 µm or 4×140 µm) of silica grains for 3DP specimens with average grain diameter of 140 µm and 190 µm. Bigger image sizes would lead to higher simulation times without any significant improvement in accuracy.

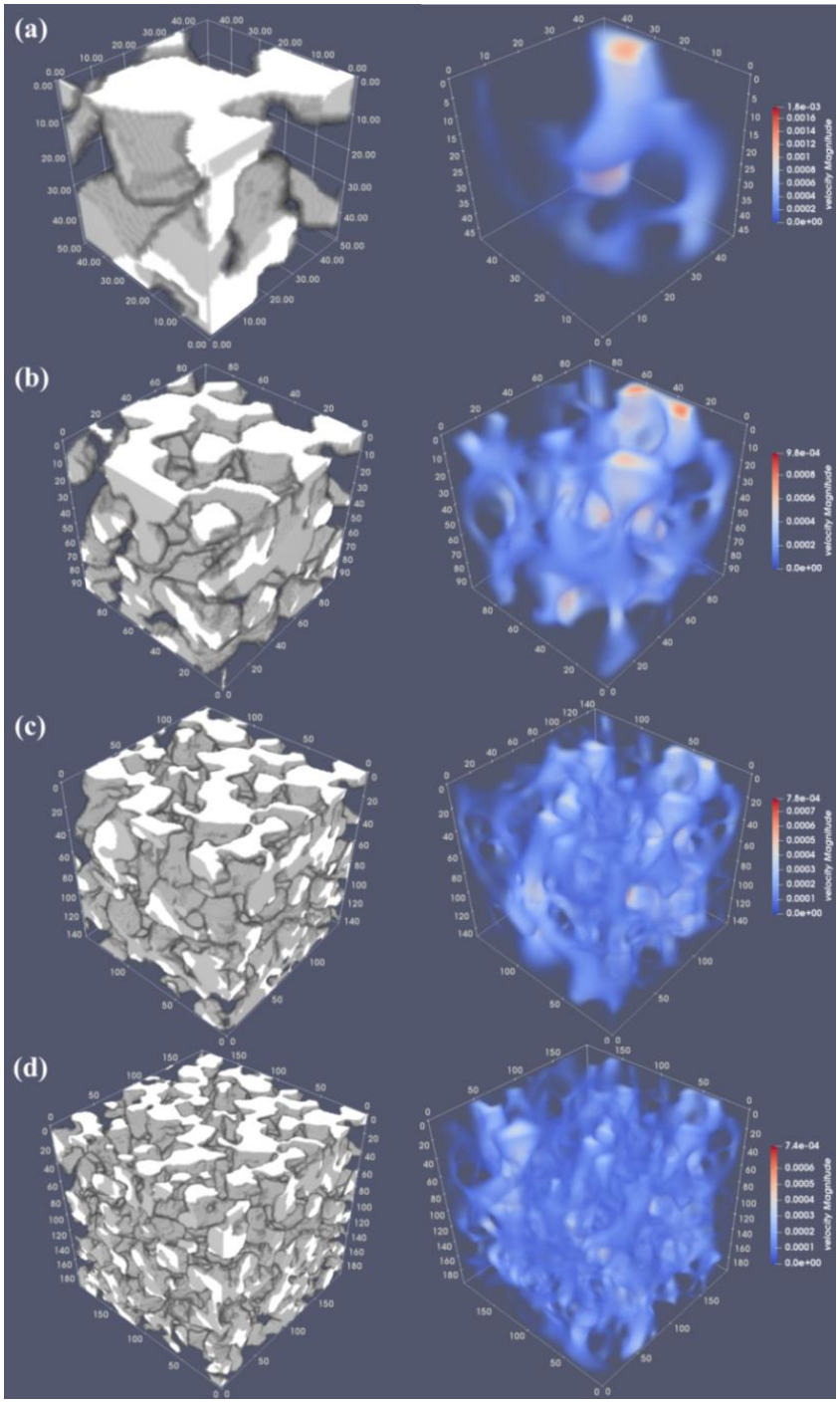


**Figure 75.** Velocity map in lattice units through specimens of, (a) 50, (b) 100, (c) 150, and (d) 200 voxel. (Warmer colors represent higher velocity)

**Table 9. Results from permeability simulation**

| Image Size (voxel) | Porosity (%) | Permeability ($m^2$) | Permeability (darcy) |
|---|---|---|---|
| ***Small Grain Low Binder (SGLB)*** | | | |
| 50 | 51 | $4.431 \times 10^{-11}$ | 44.89 |
| 100 | 50 | $4.844 \times 10^{-11}$ | 49.08 |
| 150 | 51 | $5.215 \times 10^{-11}$ | 52.84 |
| 200 | 52 | $4.842 \times 10^{-11}$ | 49.06 |
| ***Small Grain High Binder (SGHB)*** | | | |
| 50 | 49 | $4.403 \times 10^{-11}$ | 44.61 |
| 100 | 51 | $5.475 \times 10^{-11}$ | 55.47 |
| 150 | 50 | $5.077 \times 10^{-11}$ | 51.44 |
| 200 | 53 | $5.166 \times 10^{-11}$ | 52.34 |
| ***Big Grain Low Binder (BGLB)*** | | | |
| 50 | 49 | $3.889 \times 10^{-11}$ | 39.41 |
| 100 | 51 | $8.801 \times 10^{-11}$ | 89.17 |
| 150 | 49 | $8.788 \times 10^{-11}$ | 89.04 |
| 200 | 52 | $9.092 \times 10^{-11}$ | 92.12 |
| ***Big Grain High Binder (BGHB)*** | | | |
| 50 | 49 | $4.171 \times 10^{-11}$ | 42.26 |
| 100 | 52 | $9.157 \times 10^{-11}$ | 92.78 |
| 150 | 53 | $9.027 \times 10^{-11}$ | 91.46 |
| 200 | 53 | $9.189 \times 10^{-11}$ | 93.11 |

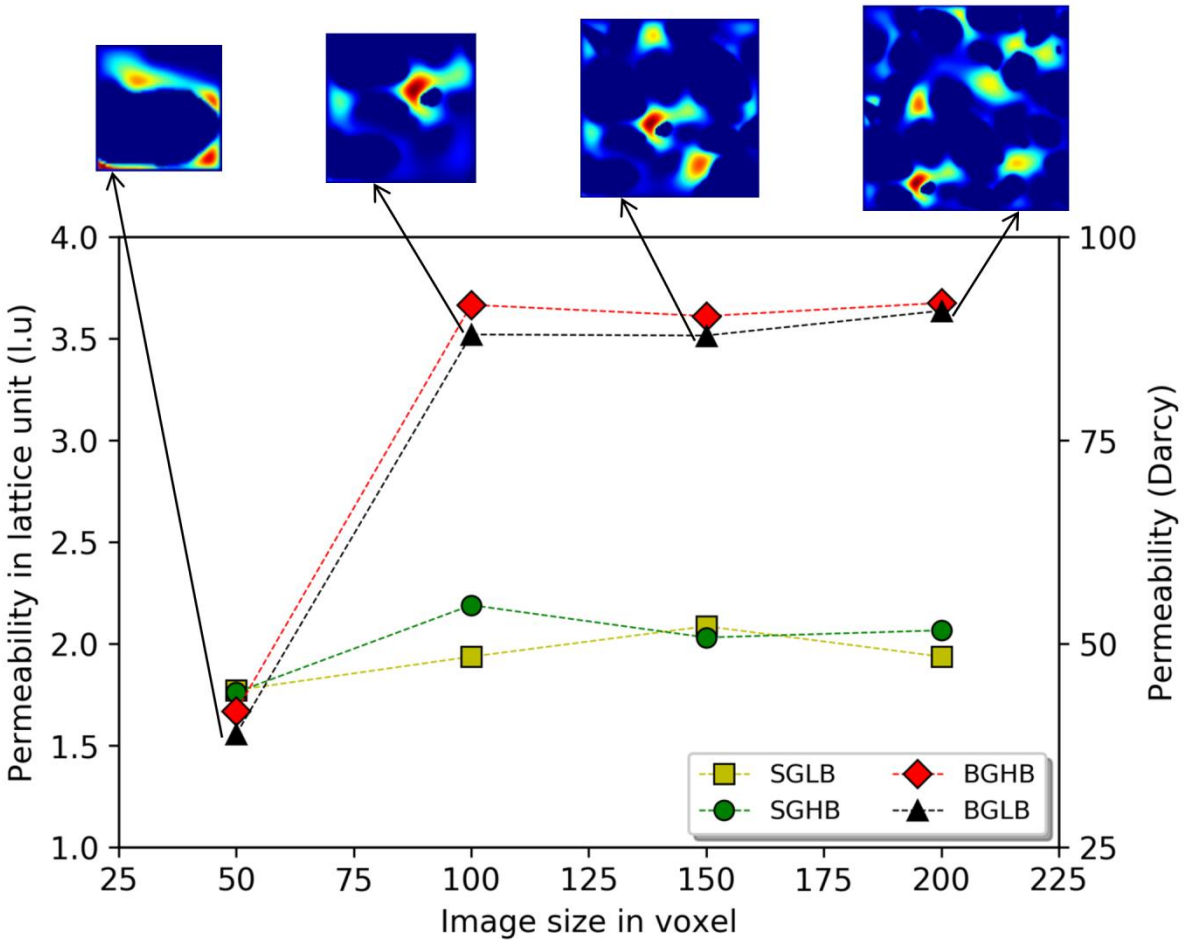


**Figure 76.** Effect of input geometry volume on the computed value of permeability

The computed results of permeability for 3DP specimen through PALABOS with different grain and binder percent samples can be compared with the predicted analytical results and image analysis results. The agreement is good between the analytical method, the image analysis and the experimental results for all the 3DP specimens (SGLB, SGHB, BGLB and BGHB). The permeability calculations obtained with PALABOS are in good co-relation with the experimental measurements performed with the 3DP specimen. Although it is of worth mentioning that an analytical permeability of $4.925 \times 10^{-11}$ $m^2$ (or) 49.9 Darcy was predicted with Kozeny-Carmen equation (Eq 16), using the average grain size of 140 micron (as provided by the ExOne sand provider) and measured porosity of 49.2 %. And also a permeability of $9.071 \times 10^{-11}$ $m^2$ (or) 91.9 Darcy was predicted with the average grain size of 190 micron (as provided by the ExOne sand provider) and measured porosity of 49.5 %. A deviation of permeability could be observed compared to analytical permeability value as the prediction of Kozeny-Carmen is based on the particles being a perfect sphere (the equation uses the mean diameter, ds), whereas in the present scenario the particle is close to being a

perfect sphere (average sphericity = 0.65). The analytically predicted permeability value using Kozeny-Carmen equation worked as a reference for the permeability measurements. It can be observed from the table that, it is possible to predict the absolute permeability of 3DP sand mold using the non-destructive LBM simulation and is a very strong method for mass flow simulation in complex 3D printed sand mold.

### 4.6.4 Pore scale modelling with pore network models

#### 4.6.4.1 Introduction

A porous medium is a type of matter composed of a solid matrix containing void spaces that can be discretized as individual pores. Gas or fluids can flow through the connected porosity of these materials, e.g. air through chemically-bonded casting sand, or be contained within the interstices of the solid matrix, e.g. liquid binder. Pore network model (PNM) are a mechanistic model that uses an idealization of the complex pore structure of the porous medium. Pore network models (PNM) is generally used to describe complex porous structures by a network of simplified geometrical components – termed as pore bodies and connected pore throats. Pore throats are termed as the narrow constrictions that connect pores together. It is typically attained by demonstrating the pore structure by pore elements having preferably simple geometrical shapes and sizes. The purpose of the PNM is to distribute the void (pore space) phase into many networks of circular pores connected by cylindrical throats. Several attempts to extract pore network from 3D µ-CT images have been tried earlier, although it was only possible to simulate fluid flow through the porous medium on regular lattice of tubes with random radii using network concept. After that, pore size distribution (PSD) theory was used to match coordination numbers of the extracted pore and throat networks for regular lattice patterns. PNM is of foremost interest for many domain of application, and several theories have arose on this subject. PNM delivers a more accurate detail of the in any complex porous material, whereas with lattice networks it is not suitable to determine preciously the complex pore-scale morphology and topology of such structures. Therefore, PNM with extracted pores and throats is a widely accepted method in characterization of any complex porous structures, as it could provide realistic pores along with their connected throats directly from a 3D image. PNM provides more details of the pore-scale multiphase flows in the porous material [129–131]. PNM is an effective alternative used to characterize or predict macroscopic properties from fundamental pore-scale behavior of processes and phenomena based on geometric volume averaging. A complete review of pore network modelling of

porous media (pore network construction) have been studied elsewhere [93], where the experimental methods for pore space determination, including direct imaging from X-ray μ-CT, mercury intrusion porosimetry (MIP) [97] were summarized. PNM has been proven to be a reliable alternative as it could help in studying the complex geometry which is not possible experimentally. The best possible way to predict the mass transport properties of a complex porous specimen would be with the extraction of 3D porous network by direct image characterization. PNM is non-unique representation of void space, and different network extraction algorithm consists in different assumptions, which confound significantly as compared by earlier [132].

Typically, extraction of pore and throat includes different segmentation of continuous void spaces into distinct network elements and defining the most important geometrical properties for each section, e.g. the area, volumes and lengths of pores and throats, etc. [132]. There exits several different approaches to classify PNM extraction; however, the most common one used are Medial axis algorithm and maximal balls algorithms, which are discussed in more details below.

The *Medial Axis Algorithm* extraction method converts the void space images into a medial axis which was the compact illustration of the void space acts as a topological skeleton (topology-central methods). The topological central skeleton is generally constructed alongside the center of the void channels by utilizing a thinning algorithm, which deletes the pore space until a line with denoting centers of the void space is obtained. Thinning algorithm occurs only in the largest pores and happens while this erosion does not affect the topology of the void structure. Fig. 77 demonstrates a typical example of medial axis network extraction processing of the void space for the porous geometries. It is shown that the pores are positioned near the skeleton branch whereas the throat connects the resulting pores. The medial axis algorithm method tends to conserve the topology of the void space mathematically; however it is difficult, to identify voids or pores definitely. As they are very much sensitive to minor defects in the resulting input void space which might lead to substantial over-segmentation of voids or pores. Preprocessing and post-processing of the 3D images could help in avoiding such problem [132,133]. Medial axis algorithm might detect the inter pore connectivity of void spaces but could miss out in identifying few pores.

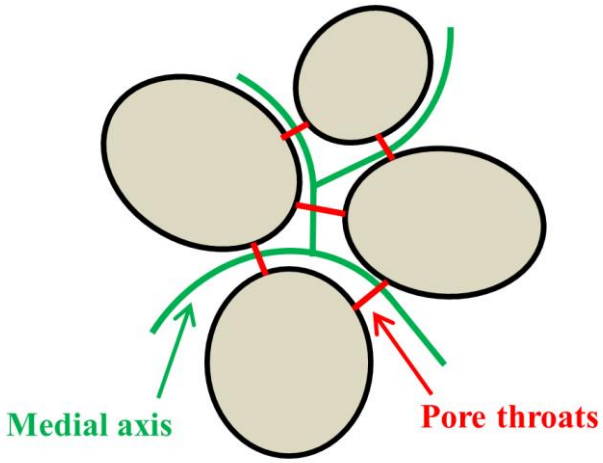


**Figure 77.** Pores and throats identified by medial axis algorithm

The *Maximum ball algorithm* constructs the largest spheres centered on each pore poxel which fits in the void space. Pore and throat diameter are well-characterized as the diameter of the largest sphere that can be inscribed in a pore space and a throat, respectively. The concept of maximal ball algorithm has been suggested in earlier research works, where it has been implemented to extract pore network of any porous geometry, whereas the study on 3D printed sand mold was not studied anywhere else. The modelling of pore network of a porous medial with maximum ball algorithm starts by extracting the maximal balls (largest pore size) which are technically the largest inscribed spheres being centered on each pore space (void) voxel touching just the boundary of the particle (silica grains for the present case). The maximal ball (MB) algorithm is a well-established method and has been widely used for the studying the morphology of any porous geometry (porous media). The main purpose of the algorithm is to extract the network of pore space (spherical pores) and throats (cylindrical pores) from volumetric µ-CT image data. After that the spheres which are situated totally inside other spheres were removed, which allows reducing the difficulties and complexity of the resulting number of maximum balls (pores). It was then possible to group them into a single family chain network (pores and throats), where pore represents the common ancestors of each cluster and throat is determined as a child of parents with different common ancestors, and was used to define the pore space's topology as described by a research work done previously, Fig. 78.

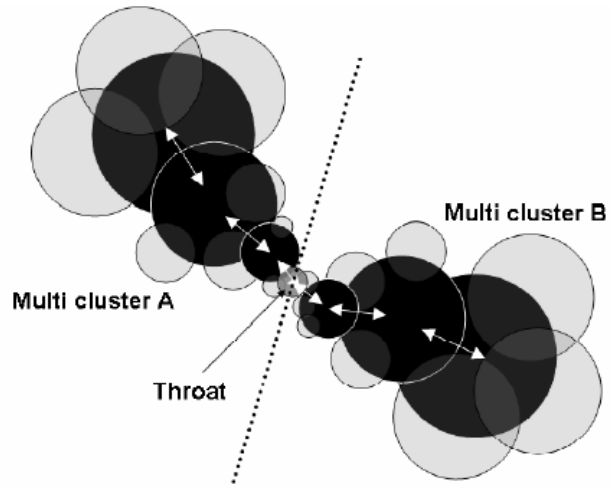


**Figure 78.** The clustering of overlapping maximal balls into families, where white arrows indicate the pore–throat chain [133]

#### 4.6.4.2 Chord Length distribution

As described earlier, the microstructural characterization of complex porous 3DP sand molds is of great importance, as it affects the permeability of the porous media. Chord length distribution (CLD) is generally defined by the intersection of lines with 2 phase interface, which is solid and void for the present case. Therefore for the 3DP specimens, the CLD is used to reconstruct the macro-pore spaces. Here the CLD of 3DP specimen was obtained by generating chords over the void spaces (pores) rather than the solid phases (silica grains). This could help in understanding the pore space distribution in a given direction within the 3DP sand mold. It was possible to obtain more information about anisotropy of the 3D printed material by observing at the distributions of applied chords lengths in each of the principle directions.

In this study, we used a reconstructed image of 3DP sand specimen to extract their CLD. The porosity of the reconstructed image is 49%. The porosity was measured as a fraction of pore voxel in the reconstructed volumetric image of 3DP specimen. With CLD, the complex pore structure of a 3DP sand mold can be represented by a connected chord lengths (pore spaces). Fig. 79 gives the visual comparison of the reconstructed image and a micro-CT image of 3DP specimen. The CLD was performed over all X-ray tomography images of the 3DP specimens (SGLB, SGHB, BGLB and BGHB) were performed over a µ-CT image size of $200^3$ voxel with a resolution of 5 µm per voxel, by using the apply_chords function python code as provided by PMEAL-Porespy. The code helped in reconstructing voids or solid phase by generating intersection of lines with a defined spacing in between them. It is to be noted that

in all the images, the chords connected to the edge have been detached and displayed as cumulative frequency distribution for all axis on Fig. 80-83.

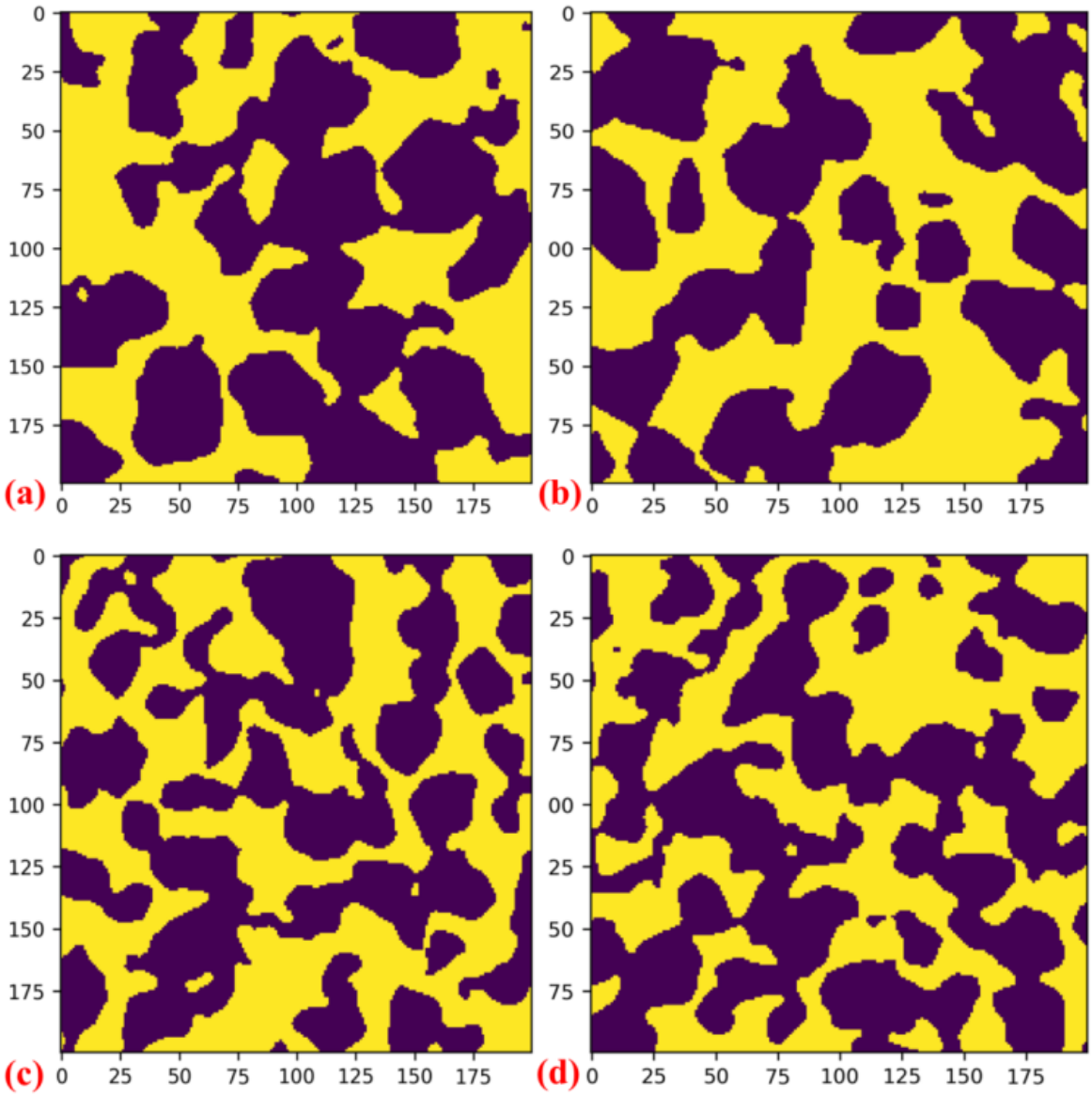


**Figure 79.** Binary images of the 3DP specimens (SGLB, SGHB, BGLB and BGHB)

The pore-size distributions (PSDs) in terms of pore diameter were extracted from the generated pore network and are represented as a cumulative distribution function, Fig 79-82. The extracted chord lengths for SGLB specimen varied from ~2 pixel to ~50 pixel, and the extracted chord length for SGHB specimen varied from ~2 pixel to ~50 pixel. Similarly, the extracted chord length for BGLB specimen varied from ~2 pixel to ~70 pixel and the

extracted chord length for BGHB specimen varied from ~2 pixel to ~70 pixel. It is to be noted that 1 pixel corresponds to ~5 µm (spatial resolution). All the extracted chord lengths along with their respective cumulative distribution function are provided below.

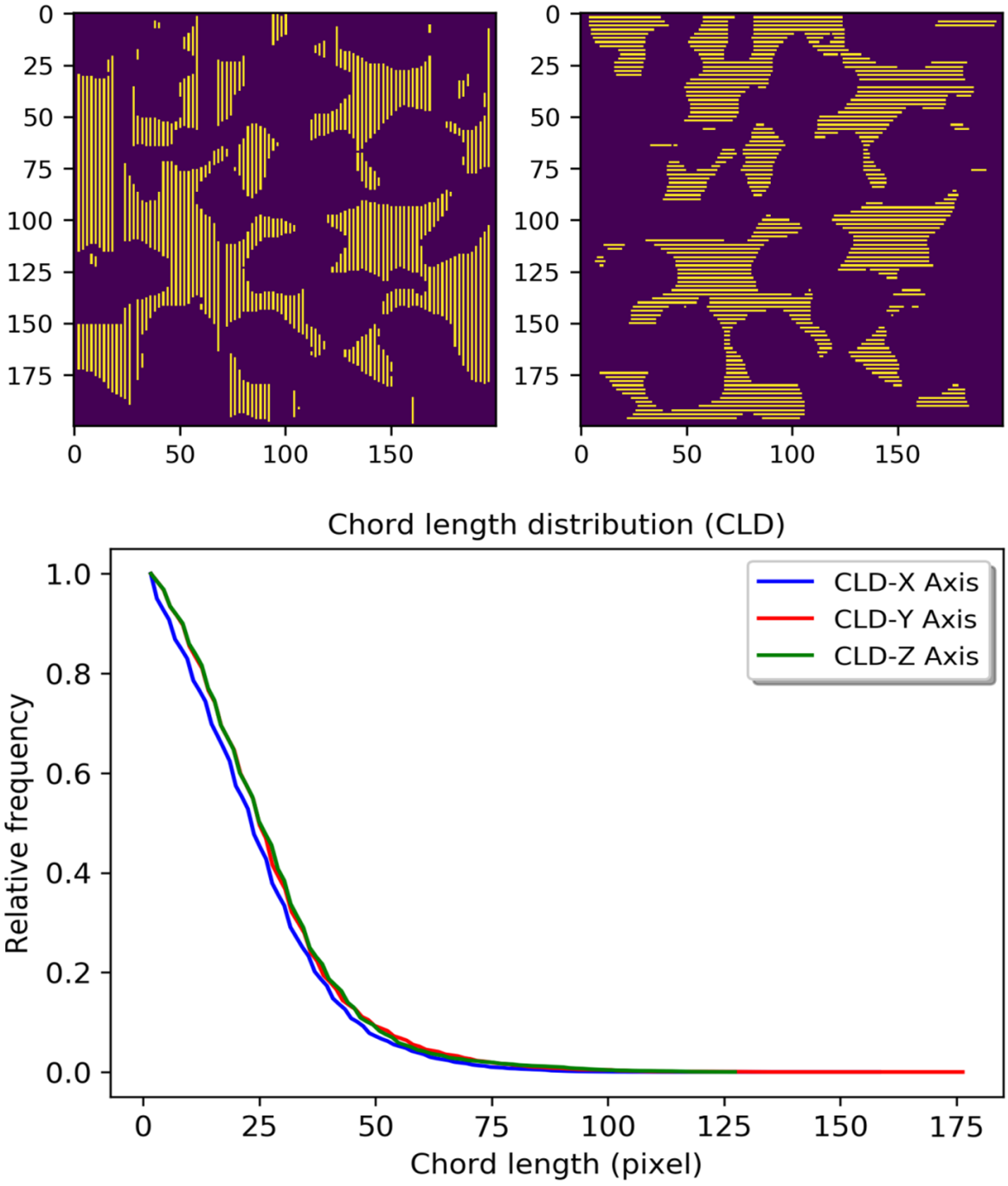


**Figure 80**. CLD for BGLB specimen

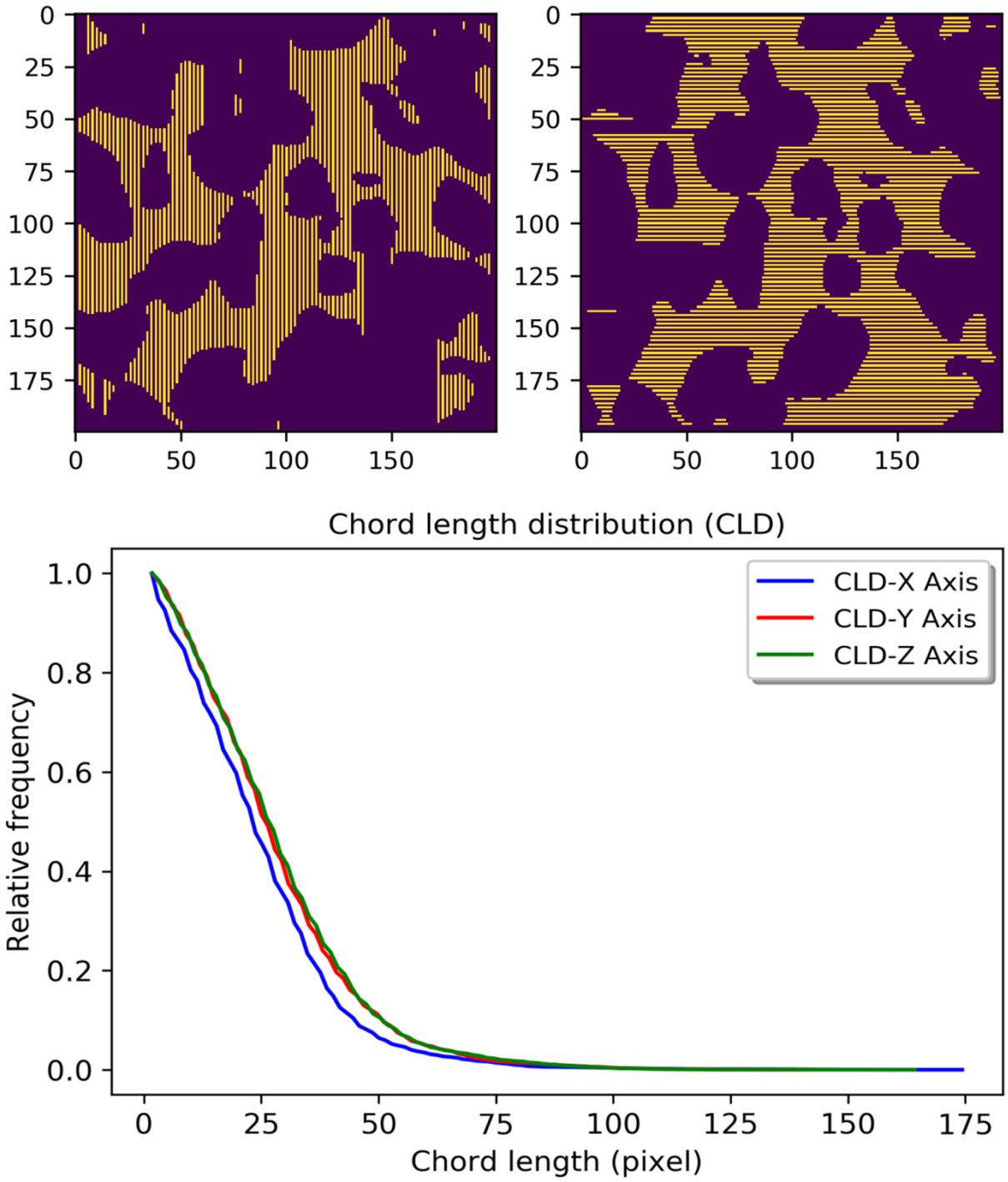


**Figure 81. CLD for BGHB specimen**

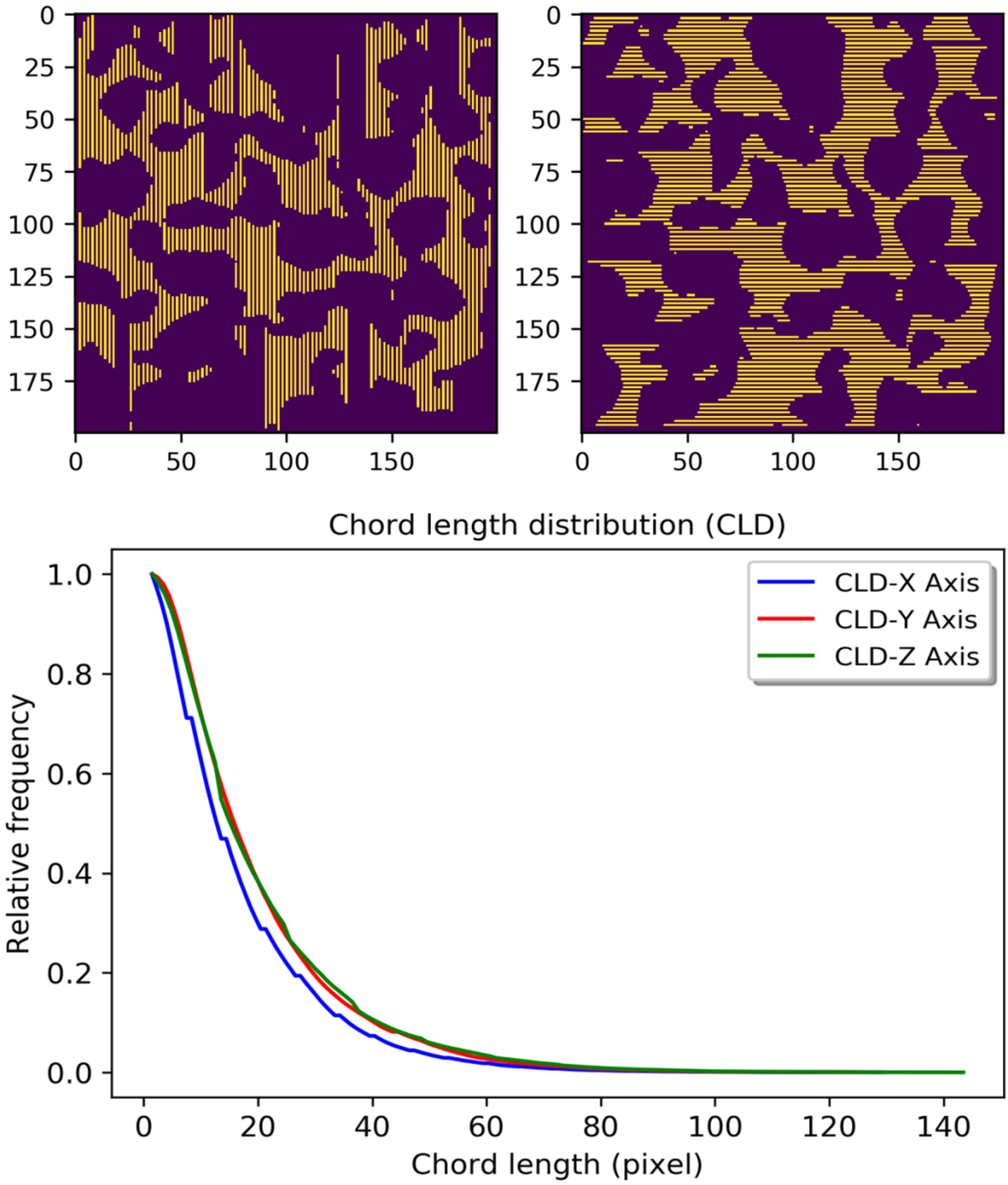


**Figure 82.** CLD for SGLB specimen

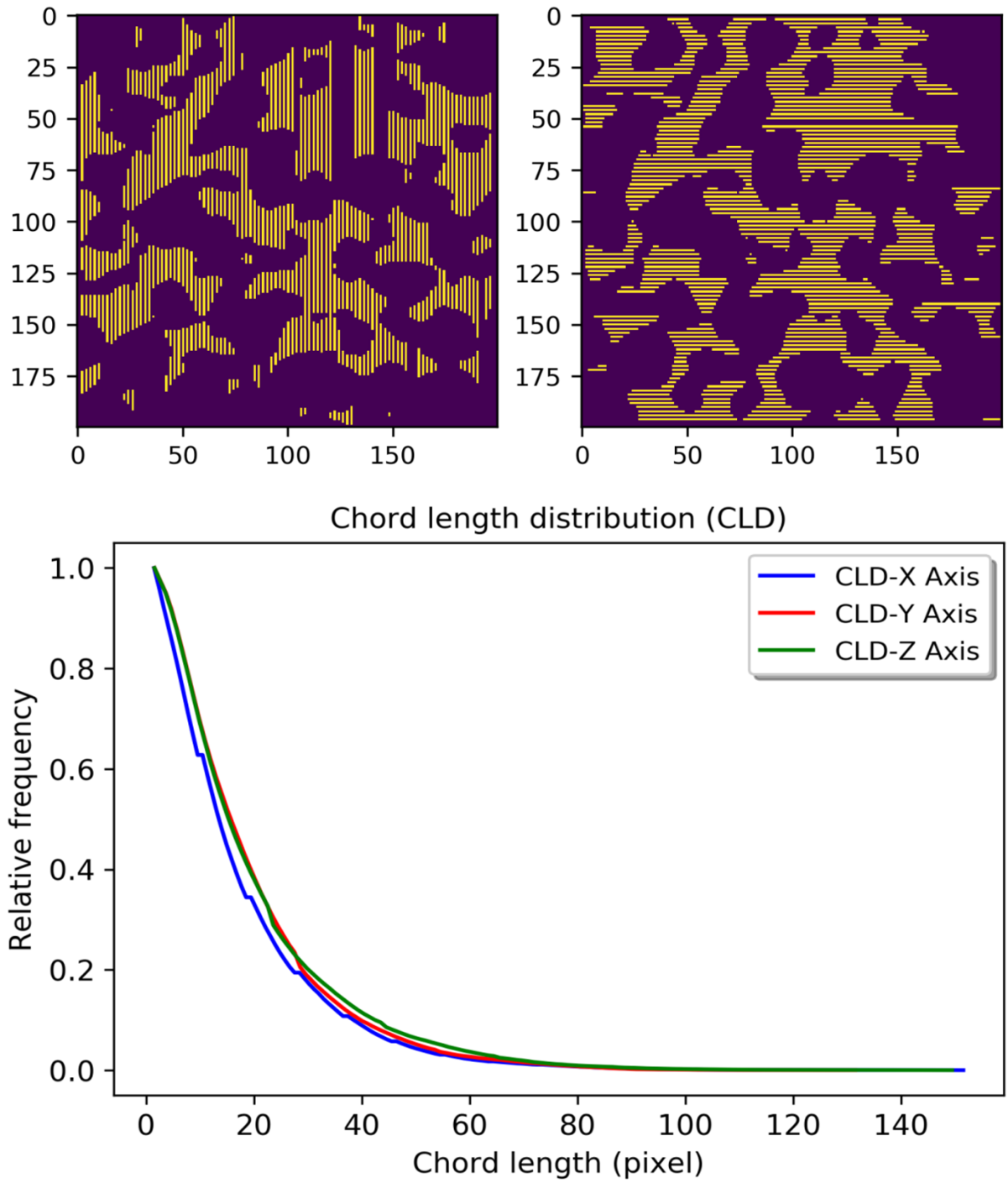


**Figure 83.** CLD for SGHB specimen

#### 4.6.4.3 Pore network extraction from µ-CT images: pore and throat size distributions

In this study, we used a reconstructed image of 3DP sand specimen to extract their pore networks. The porosity of the reconstructed image is 49%. Fig. 84 give the visual comparison of the reconstructed image and a micro-CT image of 3DP specimen.

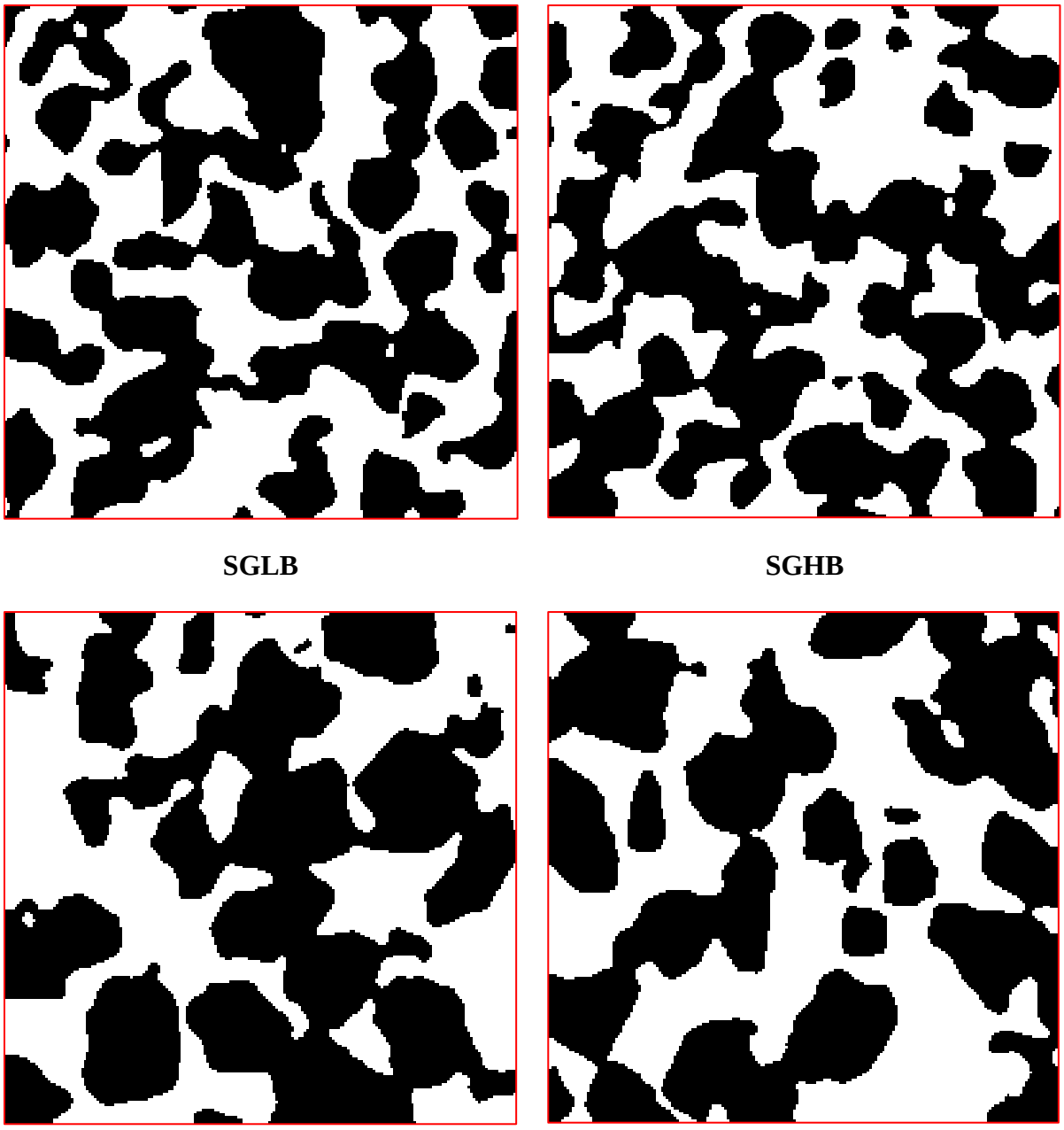


**Figure 84.** ALL specimens used for the pore network extraction

A PNM approach was followed in order to characterize the dimensions of the pore bodies and constrictions of the 3DP molds, by using the images displayed in Figure 84 as inputs. In the present work, the pores and the throat networks were then extracted from the obtained X-ray μ-CT of the 3DP specimens using the SNOW and GETNET algorithm as shown earlier [134]. This algorithm was previously implemented on various porous medium ranging from fibrous mats to sandstone, for the extraction of pore and throat sizes, and predicting permeability values. The SubNetwork of the Oversegmented Watershed (SNOW) open-source algorithm

[134] was used in the current investigation the extract the pore-network from the X-ray µ-CT images. The extracted pore and throat diameters correspond to the diameter of the largest spheres that can be inscribed in a pore body and a constriction, respectively.

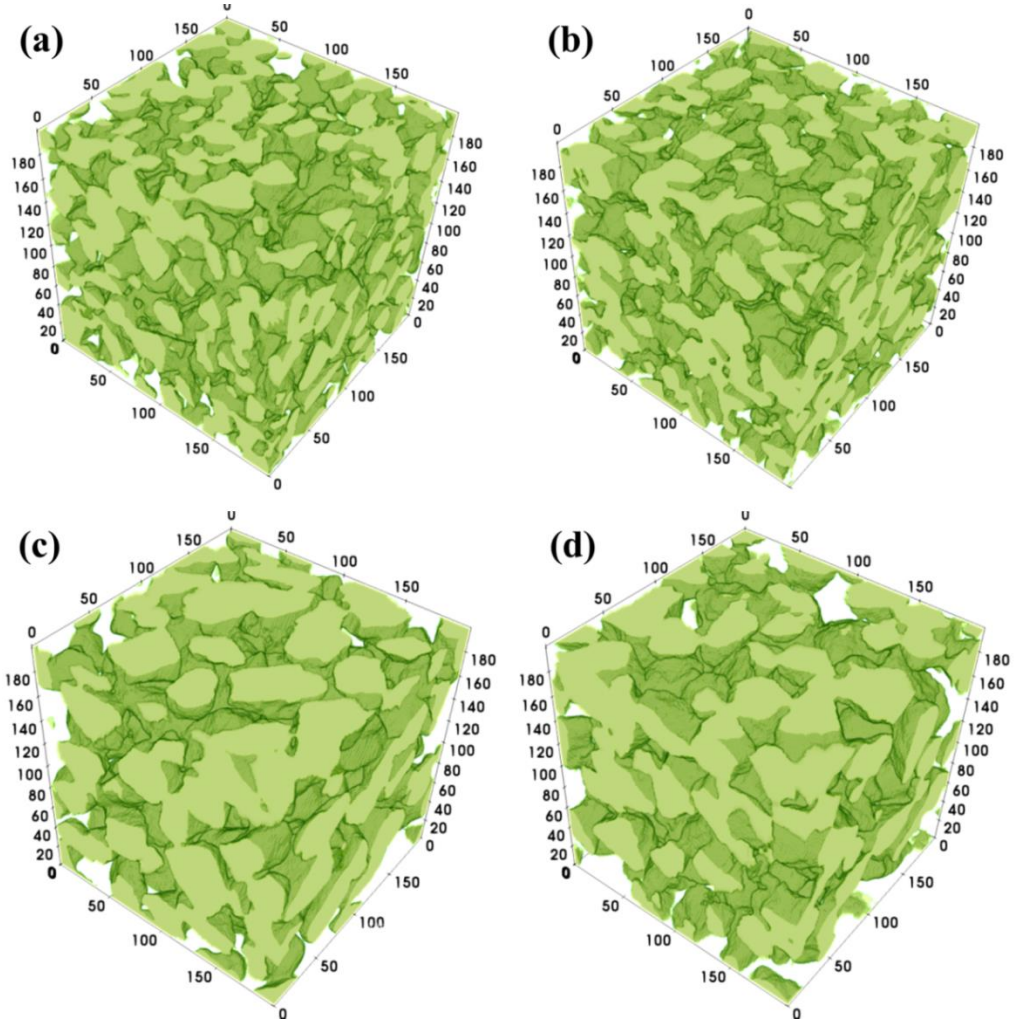


**Figure 85.** X-ray µ-CT image for all specimens used for PNM

The method for pore network extraction starts by using GETNET.py code [134], which extracts a conventional pore network from the provided µ-CT image of voxel size size $200^3$. As stated earlier the GETNET.py code [134] works in 4 steps, first it extracts the distance map of the pore space (distance transform), secondly a filter was used on the distance map to smoothen the image and to remove the saddles and the plateaus, thirdly merging the peaks that's are too near to each other and finally assigning the void voxel to the appropriate pores using a marker-based watershed algorithm. Recently, reserchers have used the code to extract the pore and throat network of a sandy porous structure [135]. Similarly, for the present extraction, the X-ray µ-CT image of 3DP specimen was first thresholded and then converted into an 8-bit file. Then, using the SNOW algorithm in PYTHON, the X-ray µ-CT image is

imported for further characterization. This import class then extracts all the information of the provided µ-CT image, such as pore and throat sizes, their locations and their network connectivity. All pore and throat properties are stored in Numpy arrays, which can be easily accessible at later stage for generating the network.

Permeability is strongly related to the dimension of the pore constrictions (throats), as most pressure loss is generated in these regions. It was also studied in detail the impact of morphology on flow law parameters in metallic foams [136]. On the other hand, researchers showed that the tortuosity ($\tau$), porosity ($\varepsilon$) can be directly correlated according to Archie's law ($\tau^2 = \varepsilon^{-m}$) [95,96]. They also developed a model to calculate k directly from the characteristic diameter of the throats ($d_{throat}$) and Archie's law:

$$k = \frac{\varepsilon^{m} d_{throat}^{2}}{32} \qquad \textbf{Eq. 43}$$

The permeability was calculated by using the average throat size provided by the network model.

#### 4.6.4.4 Results and discussion

PNM provides a reasonable prediction of mass transport properties at pore scale, and offers the flexibility of characterizing macroscopic properties relationship of 3DP sand mold with pore structure. With PNM, the complex pore structure of a 3DP sand mold can be represented by a network of pores (pore spaces) and connected throats (narrow paths that connect pores) with simplified geometries. A pore network modelling aims at better representation of pore and throat interconnectivity in a porous medium like 3DP sand mold. All the pore network extractions for different specimens (SGLB, SGHB, BGLB, BGHB) were performed over a µ-CT image size of $200^3$ voxel with a resolution of 5 µm per voxel and are represented in Fig. 86.

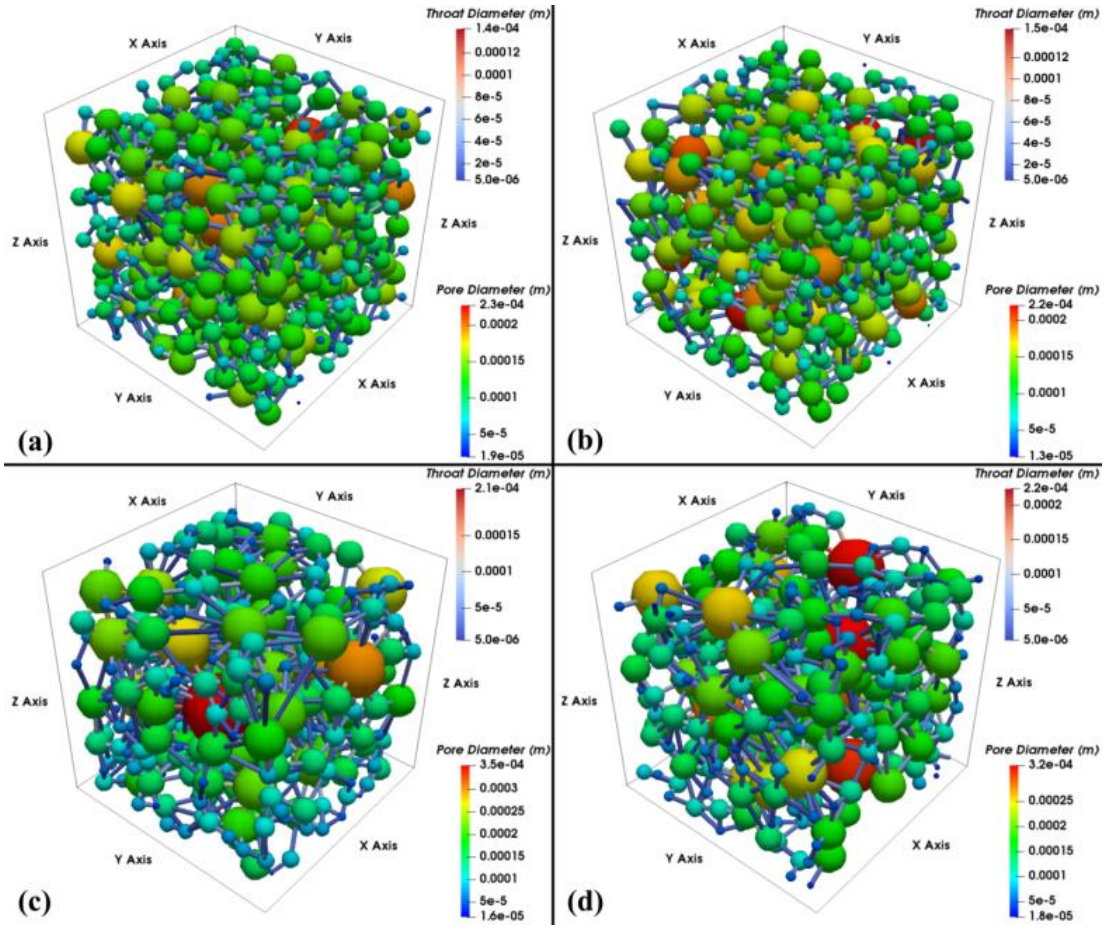


**Figure 86.** Extracted pore network for (a) SGLB, (b) SGHB, (c) BGLB and (d) BGHB specimens

The pore-size distributions (PSDs) in terms of pore diameter were extracted from the generated pore network and are represented as a histogram, Fig 87 and Fig. 88. The extracted pore diameter for SGLB specimen varied from ~19 µm to ~226 µm, with a mean pore diameter of 105.84 µm and the extracted pore diameter for SGHB specimen varied from ~14 µm to ~220 µm, with a mean pore diameter of 108.05 µm. Similarly, the extracted pore dimeter for BGLB specimen varied from ~16 µm to ~350 µm, with a mean pore diameter of 108.07 µm and the extracted pore dimeter for BGHB specimen varied from ~18 µm to ~320 µm, with a mean pore diameter of 108.31 µm. Although previous work by [137] showed that the grain size and pore radius are functionally interdependent, it can be observed that the average pore diameters are very similar for all the specimens (both SG and BG) in the currently investigated samples. However, careful observation of Fig. 88 shows that the standard deviation of the PSD is considerably higher for the big sand grains samples (± 55.9 µm for BGLB and ± 56.1 µm for BGHB) as compared to the small sand grains samples (± 37.3 µm for SGLB and ± 38.7 µm for SGHB). Consequently, the size of the biggest pores in the big grain samples is much higher than for the small grain samples, even if the average

pore size is close in both cases. This can be also observed in the red-colored pores of Fig. 86 (approximately 350 micrometers of big grains and 230 for small grains) and in the PSDs provided in Fig 87 and Fig. 88.

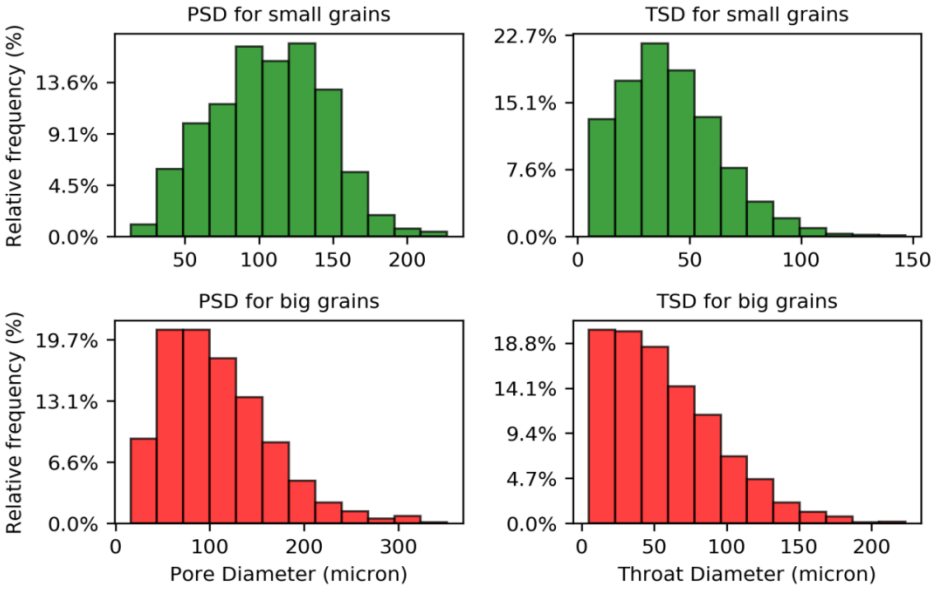


**Figure 87.** Pore and throat size distribution

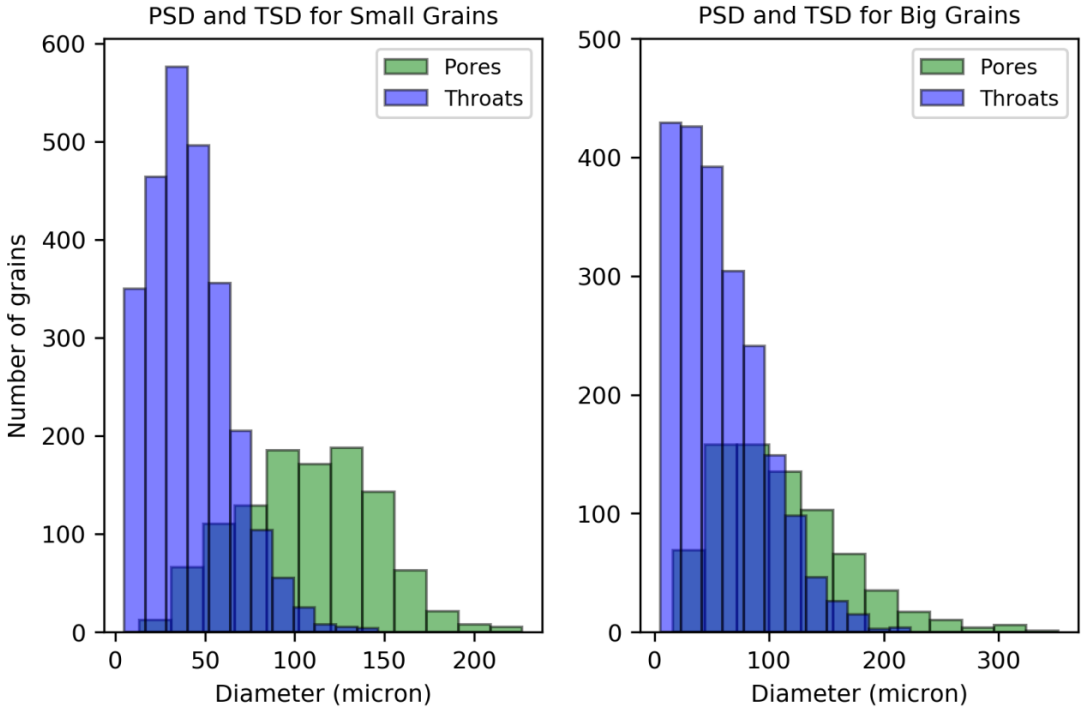


**Figure 88.** Combined (high binder +low binder) pore size and throat size distribution for (a) small grains and (b) big grains

The throat-size distributions (TSDs) in diameter were also extracted from the generated throat network and were then represented as a cumulative histogram with the throat diameter, Fig 87 and Fig. 88. The extracted throat dimeter for SGLB specimen varied from ~5 µm to ~140 µm, with a mean throat diameter of 38.66 µm and the extracted throat dimeter for SGHB specimen varied from ~5 µm to ~146 µm, with a mean throat diameter of 44.43 µm. Similarly, the extracted throat dimeter for BGLB specimen varied from ~5 µm to ~214 µm, with a mean throat diameter of 56.92 µm and the extracted throat dimeter for BGHB specimen varied from ~5 µm to ~220 µm, with a mean throat diameter of 58.42 µm. Peak values appear at low pore sizes indicate the microstructure is complex in nature and the structural detail is preserved. It can be observed for big grain specimens that the throats and pores overlap with each other, which suggests that some small pores exist, of similar size as the throats. Moreover, the distribution of throat size for all the specimens shows a right-skewed distribution, with a large portion of the small throats (peak throat size smaller than average), which construct minor flow paths.

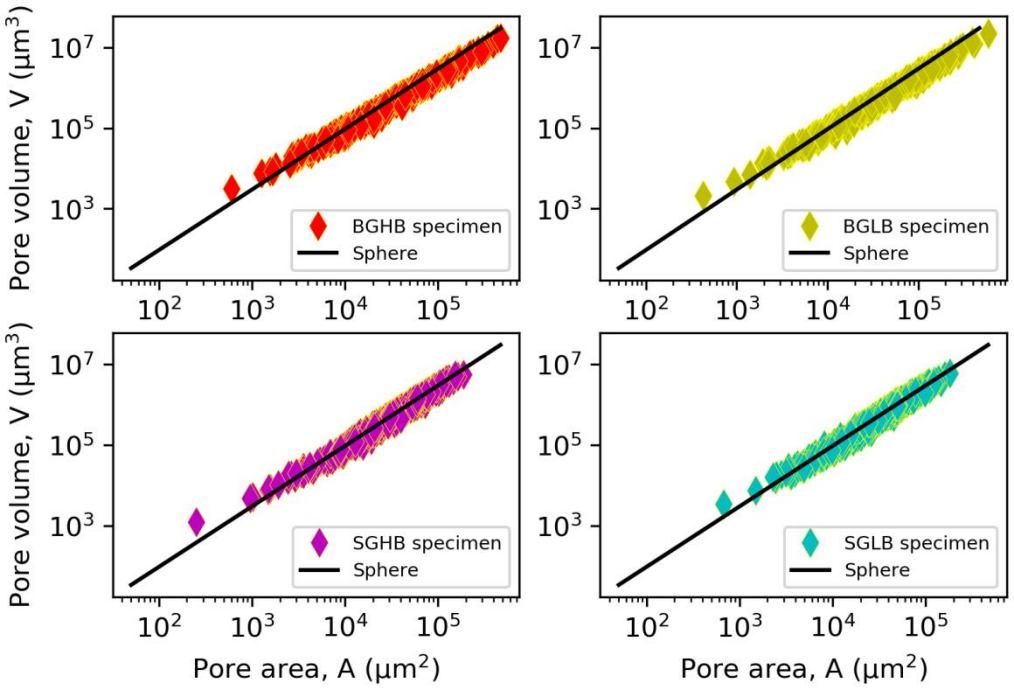


**Figure 89.** Relationship between surface area and volume of all pores in all three samples

A typical relationship of representing a relationship between the surface area of pores and the volume of the pores for all the 3DP specimens has been provided, Fig. 89. For the comparison, surface area ($4\pi r^2$) to volume ($\frac{4}{3}\pi r^3$) of spheres have also been plotted, with *r* being radius of regular sphere. As seen from the plot, for the provided volume of pores of

3DP specimens, the surface area of pores for most of the pores is more or less large than for a sphere. Such resulting values are expected because the sphere is the shape with minimal surface area for a given volume, and as explained and demonstrated in the earlier section of sphericity, that the pores are nearly spherical in nature.

From the obtained average equivalent throat diameter, permeability was calculated using the equation described in the previous section, Eq. 19, and the results are presented in Table 10. The calculated permeability values fit well with the one obtained with theoretical, experimental and numerical analysis with deviation of less than 10%, showing that the pore network models constructed in this work are accurate and reliable. It can be observed from the results that no significant differences in terms of permeability (k) were obtained for small grain samples with different binder content along with big grain samples with different binder content, as the furan resin binder was only associated to the solid phase in the µ-CT images. An individual effect of the binder over pore network structure cannot be assessed and therefore the values for pore and throat diameter for samples with low binder and high binder are very close.

**Table 10. Results from pore network modelling**

| Sample Type | Mean Pore Diameter (µm) | Mean Throat Diameter (µm) | Permeability ($m^2$) | Permeability (Darcy) |
|---|---|---|---|---|
| *SGLB* | 105.84 | 38.66 | $3.138 \times 10^{-11}$ | 31.79 |
| *SGHB* | 108.05 | 44.43 | $4.144 \times 10^{-11}$ | 41.98 |
| *BGLB* | 108.07 | 56.92 | $6.915 \times 10^{-11}$ | 70.06 |
| *BGHB* | 108.31 | 58.42 | $7.165 \times 10^{-11}$ | 72.59 |

Permeability, porosity, tortuosity grain size distribution, pore size distribution, average pore diameter, throat size distribution and average throat diameter are essential inputs when predicting gas flow in 3DP molds. It is to be noted that complex porous media like 3DP sand mold have anisotropic properties (mechanical and mass transport) due to variation in printing process parameters. For the present study, only the variation of furan resin binder droplet resolution on silica sand powder bed is studied (different binder percentage) along with different silica grain size, as this affects the properties of complex porous resin bonded 3DP mold with the recoater speed. PNM is advantageous on the prediction of the flow permeability of such complex porous structure like 3DP sand mold directly from the extracted throat size distribution from X-Ray µ-CT digital images. The predicted permeability values

using PNM is found to be in good agreement. This would help the foundry industry to accurately measure the mass transport properties as required as an input for numerical simulations (solidification and filling), to study the effect of printing process parameters (printing speed, binder percentage, grain size, etc.) and thermal degradation of furan resin binder during metal casting. Therefore, the present approaches of merging permeability measurements on 3DP sand mold specimens with direct extraction of pore and throat network structure using for X-ray µ-CT helped in exploring and better understanding the pore structure and its role on mass transport phenomenon. It also helped us in developing and validating more reliable predictive models for mass transport parameters, which are promising for performing accurate risk assessments of toxic contaminants produced during metal casting in foundry industry.

The drainage curve for all the 3DP specimens obtained from the mercury porosimetry simulation is presented in the figure below, Fig. 90 and Fig. 91. The presented drainage curve compares the phase saturation for all the simulated 3DP specimens. It can be observed for all the specimens that there is a deviation for phase saturation which can be due to late filling of pores. As shown with the curves, for all specimens printed (SGLB, SGHB, BGLB, and BGHB) the capillary pressure curve does not fits well, since the pore size distribution and throat size distribution are not similar for both the specimens, and here the drainage curve is totally dependent on the pore connectivity and pore size distribution. It can be also observed from the curve that, there is shift of curve towards the right for SGLB specimen as compared to SGHB specimen. The shift towards the right is due to the presence of lower porosity region in SGLB samples, as lower phase saturation is obtained with small pores filled at the similar capillary pressure.

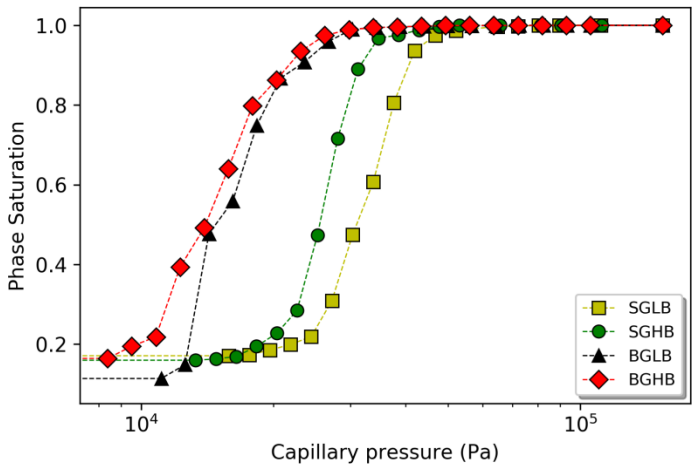


**Figure 90.** Drainage curve

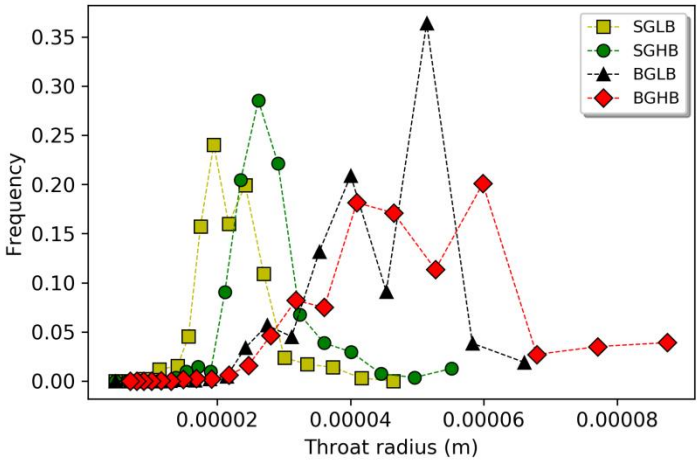


**Figure 91.** Throat distribution

The mercury intrusion capillary pressure values obtained from the simulation were then directly converted to corresponding pore size (mean largest entrance to pores) by using the Washburn equation as explained earlier. However, it is to be noted that the mercury porosimetry measurements does not definitively provides the actual pore size, however the it determines the biggest connection (throat) or the biggest entrance to the pores of the porous geometry. Hence the throat size or pore size obtained with this method will definitely be much smaller compared to the results obtained with analysis of X-ray µ-CT image analysis. It can be concluded from the Fig. 90 and Fig. 91 that, the bigger pores are obtained with bigger grains, as expected. And also, it can be observed for SGLB and BGLB (low binder specimens) leads to smaller pores as compared to SGHB and BGHB respectively. This may be explained due to the presence of binder (not observed with the current X-ray experiments), which proves the reason for the increase in the separation (pore space) between grains. All the results obtained from the mercury porosimetry method have been presented with Table. 11.

**Table 11.** Results from MIP

| Sample Type | Mean Entry Size (µm) |
|---|---|
| *SGLB* | 21.714 |
| *SGHB* | 27.284 |
| *BGLB* | 43.359 |
| *BGHB* | 48.597 |

## 4.7 Model efficiency

One of the challenges in foundry is the lack of methods for proper non-destructive characterization of the local permeability of the 3DP sand mold. The X-ray µCT technique overcomes this challenge and allows a non-destructive visualization and characterization of internal volume and the external surface of a sand mold. This paper, for the first time, fully characterizes the intrinsic physical parameters of 3DP sand mold including grain structure, porosity, pore connectivity, tortuosity, pore size distribution, throat size distribution and local density. Table. 12 shows the cumulative results of permeability as obtained by different methods (from traditional experiment, from GSD, from LBM and from PNM). The permeability value using the GSD method overpredicts the permeability value as obtained with the traditional experiments. Indeed, the permeability value from GSD using Kozeny-Carman equation is based on the particles being a perfect sphere (the equation uses the mean particle diameter, $d_s$), whereas in the present scenario the particle is close to being a perfect sphere (average sphericity = 0.65). However, the permeability value obtained with GSD using Kozeny-Carman equation can still be considered as a reference for other models.

Moreover, the permeability values yielded by LBM simulations were found to be close to the results provided by traditional tests. Nevertheless, LBM requires much computational power for larger µ-CT images, hence this method can be time consuming. Therefore, it was crucial to identify the optimum RVE not only to predict reliable permeability values but also to reduce simulation times. An alternative approach to predict permeability from pore-network modelling (PNM) is proposed. Pores are the relatively wide portions of the interstices and throats are the relatively narrow portions that separate the pore bodies. The pores and throats space of a 3D printed sand mold can be extracted from the segmented 3D µ-CT image. As can be observed from Table 12, significant differences are reported in some cases between the results of traditional experiments and PNM, while the agreement is better between traditional tests and GSD and LBM. Nevertheless, as compared to LBM simulations, PNM require less computational power due to the simplifications of the void-space geometry and topology when constructing the pore network model. The computational time needed for the extraction of the pore and throat network on a computer with Intel Xeon processor and 16 GB of memory is in the order of minutes, whereas using LBM computation takes hours. This allows the computation of permeability over larger sampling volumes. However, it should be noted that the computational time can be significantly reduced by using a more powerful and expensive supercomputer. [138] showed that for unconsolidated porous media where pore

throats are much smaller than pore bodies, the viscous dissipation can be considered as being localized only in pore throats. This approximation is quite acceptable in many cases, since the pore body-to-pore throat radius is generally quite large, varying from values around 3 for random monosized sphere packs, to around 5 for random packs of sharp-edged grains with a narrow size distribution. However, in the case of the highly-porous 3DP sand molds investigated in the present work, the pore-to-throat size ratios range from ~1.7 to ~2.7 (Table 5). Therefore, the PNM-based estimation obtained with Eq. 19, in which viscous dissipation is assumed to be localized only in pore throats, is not expected to be highly accurate, but is still useful to provide a lower permeability bound. Hence, PNM approach can be a reasonable alternative to the traditional experimental, LBM and GSD methods as it takes into account of the microstructural features of the 3DP sand mold and can also easily deal with any kind of complex geometry.

**Table 12.** Permeability measured with different methods

| **Sample** | **Traditional experiment (Darcy)** | **GSD (Darcy)** | **LBM using 100 voxel (Darcy)** | **PNM (Darcy)** |
|---|---|---|---|---|
| SGLB | 56.4 | 66.8 | 49 | 31.79 |
| SGHB | 58.9 | 62.6 | 55.4 | 41.98 |
| BGLB | 91.3 | 101.6 | 89.1 | 70.06 |
| BGHB | 93.2 | 109.1 | 92.7 | 72.59 |

Permeability, porosity, tortuosity grain size distribution, pore size distribution, average pore diameter, throat size distribution, and average throat diameter are essential inputs when predicting gas flow in 3DP molds. It is to be noted that complex porous media like 3DP sand mold have anisotropic properties (mechanical and mass transport) due to variation in printing process parameters. For the present study, only the variation of furan resin binder droplet resolution on silica sand powder bed is studied (different binder percentage) along with different silica grain size, as this affects the properties of complex porous resin bonded 3DP mold with the recoater speed. The present modeling approaches are advantageous on the prediction of the flow permeability of such complex porous structure like 3DP sand mold directly from the from X-Ray µ-CT digital images. This would help the foundry industry to accurately measure the mass transport properties as required as an input for numerical simulations (solidification and filling), to study the effect of printing process parameters (printing speed, binder percentage, grain size, etc.) and thermal degradation of furan resin

binder during metal casting. Therefore, the present approaches of merging permeability measurements on 3DP sand mold specimens with extraction of throat and pore network structure using for X-ray µ-CT helped in exploring and better understanding the pore construction and its pivotal role on mass flow phenomenon. It also helped us in developing and validating reliable models for non-destructive prediction of gas permeability, which are favorable for carrying out precise risk assessments of harmful toxic pollutants produced during metal casting in foundry industry.

## 4.8 Conclussion

Permeability is one of the most important factors affecting the generation of gas defects during metal casting, so it is of major importance to characterize it. In this work, the advantage of the application of X-ray µ-CT (NDT), Pore Network Modelling methods and Lattice Boltzmann Method in exploring the mass transport properties of additively processed silica sand mold was demonstrated. X-ray µ-CT images were used to compute the porosity, pore size, throat size and the permeability of the 3D printed specimens for different binder contents and grain sizes, using analytical and numerical methods. The permeability predicted in the steady-state was compared with experimental and analytical measurements for layered silica grain arrangement. A major advantage of using X-ray CT characterization is the non-destructive nature of the tests. The computed permeability can be used as input to numerical simulations of metal casting allowing the prediction of macroscopic defects. The following scientific and industrial implications are drawn from the present work:

- The permeability values predicted with LBM from X-ray µ-CT image of 3DP specimen are in good agreement with the traditional experimental measurements.

- The proposed non-destructive X-ray µ-CT technique is an effective and reliable alternative to traditional laboratory experiments for permeability characterization of additively processed sand molds. The good agreement between the analytical model, traditional experimental estimations and the proposed method based on CT data validates this approach.

- An RVE of 100×100×100 voxel corresponding to 500×500×500 $\mu m^3$ is suggested for a faster and reliable permeability simulation.

- ❖ The characterization of the 3D printed specimen was performed by using available open-source software such as ImageJ, Palabos, and OpenPNM and therefore the proposed approach may be used in a broad range of academic or research applications.

- ❖ The permeability value predicted using pore network modeling can be a reasonable alternative as it takes into account of the microstructural features of the 3DP sand mold.

The present findings represent a step forward towards improved prediction of mass transport properties of the 3DP sand molds. However, further characterization of permeability of such additively processed sand mold should be performed with varying average grain diameter, to check the convergence of the present model. Also samples printed with other printing process parameters should be studied.

# 5. MELT INTERACTION WITH 3DP MOLD SURFACE

In this chapter, we test the printing process parameters presented in Chapter 3 and 4 to study the erosion phenomena that occurs at the liquid metal and 3DP sand mold interface during the metal casting. The chapter covers an evaluation of erosion resistance of the 3DP sand molds with different binder percentage. Experiments were designed to investigate the 3D printed molds in terms of mold erosion related to metal casting to select the process parameters to print molds not only with good mechanical properties but also to minimize the mold erosion during metal casting. A method for determination of the erosion resistance of sand molds has been established, based on the volume of the erosion-deformed surface. The volume of the eroded surface was measured using modern reverse engineering technique.

## 5.1 Introduction

The course of castings forming is usually examined from thermodynamic or chemical reaction viewpoint in the liquid metal-mold interface during solidification, starting from the pouring temperature to the ambient room temperature. During this period a remarkable heat exchange occurs in between the liquid metal and 3DP sand mold, followed by a significant influence on the 3DP sand mold properties. The courses of mutual effect between the liquid metal and the 3DP sand molding material are significant in casting processes which are more complex in nature. The by-products of such inter-reactions are set to occur on the either sides, the side of metal casting as well as over the side of the 3DP sand mold. Several properties of metal casting and their dimensional accuracy or surface properties were usually determined from contact of surfaces in liquid metal and 3DP sand mold. Such processes give rise to several casting defects (holes, cracks, etc), hence affecting the properties of casting. Re-shaping or tooling of casting can be really expensive. Therefore, it was applicable to study the mechanism of 3DP sand mold destruction using heavier metal (cast iron) to observe the maximum possible defects. The destruction of 3DP sand mold surface will be primarily due to erosion. The advancement in 3D printing technology has enabled the rapid manufacturing of complex sand molds for metal casting directly from design data. In principle, when liquid metal gets transferred into a 3DP sand mold by the action of gravity casting, it causes turbulence, hydrostatic pressure and binder burnout (local destruction of bonds) resulting in sand particles getting detached from the mold surface which affects the surface finish of the part due to mold erosion. The erosion tendency of 3D printed mold mainly depends on the amount of binder, printing speed (packing density), grain size and kinetic energy of the melt.

Low binder amount with low sand packing density may lead to less gas emission from binder burnout during metal casting but causes slag inclusions during liquid metal filling due to the deposition of eroded material on the raw casting surface. However, high binder amount with high packing density might lead to high mold strength and less mold erosion but may give rise to excessive gas generation during casting operations. Experiments were designed to investigate the 3D printed molds in terms of mold erosion related to metal casting to select the process parameters to print molds not only with good mechanical properties but also to minimize the mold erosion during casting. A hypothesis was taken into consideration that the high mold erosion will occur for the parts with low binder content and in the places when the mold is directly hit by the melt and along the route of the flow. This can be explained due to lose packing of sand and burning of resin bridges during filling. Recommendations are also proposed to attain predefined mold properties and minimize erosion wear during metal casting.

## 5.2 Experimental design and Methodology

In order to study the sand mold erosion, a pilot mold was 3D printed. The benchmark mold design part along with the gating system geometry were adopted from past research work [139]. The design of the 3DP mold is a modified version of previously designed mold [139], which was used by researchers to study the mold erosion with cast iron using traditional silica sand mold. A schematic deign of the mold is shown in Fig. 92. The mold erosion will be studied on Test Sab printed with two different binder percent (1% and 2%). The low binder (1%) sample has been named as LB and high binder (2%) sample has been termed as HB in order to facilitate the study and comparison. The choice of binder has been explained in earlier experiments. The testing slabs were printed individually for each testing measurement following the same principle as described in the earlier sections. Each rectangular test slab has a dimension of 170 × 50 mm and a thickness of 22.4 mm. The volume of the slab was 190400 $mm^3$. The chosen thickness of 22.4 mm corresponds to the thickness of bar specimens traditionally used for 3-point bending strength test and flexion test. The testing specimens were printed 24 hours before the casting. The weight of the casting over the pouring basin was fixed, and the kinetic energy of the liquid metal was calculated by the height of pouring (sprue height) of 200 mm. The top end of the sprue had a radius of 5.5 mm and the down sprue had a radius of 4 mm. The end of sprue and testing slab was fixed at 30 mm. The average pouring time for all the experiment varied from 55 – 60 seconds.

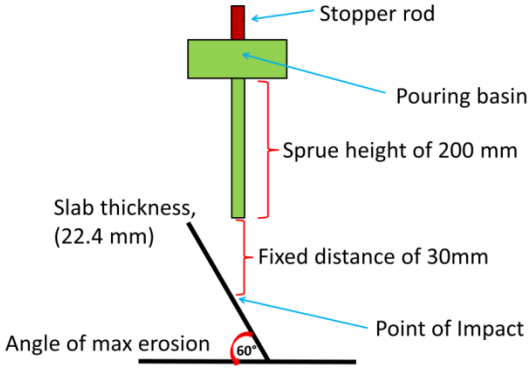


**Figure 92.** Comparison of permeability for different methods

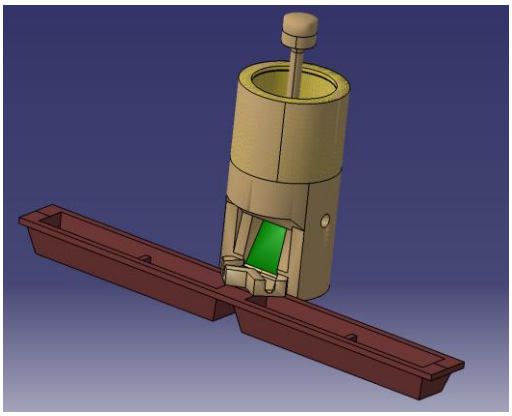

**Figure 93.** Schematic design of mold erosion experiment

The 3DP mold is made from Silica sand quartz, with average grain size of 140 micron. The binder was furfuryl-alcohol-based binder (furan resin) of density (1.1-1.2) g/cm³. The furan binder was a mixture of furfuryl alcohol (70-90 wt%), bisphenol A (5-15 wt%), resorcinol (1-10 wt%) and 3-aminopropyltriethoxysilane (0.1-0.2 wt%). In order to characterize the erosion of mold under the force of gravity, a casting test experiment has been carried out with the molten metal. The recommended casting 3DP sand mold model and design are shown in Fig. 93. The liquid metal was poured into the pouring basin of the casting 3DP mold rapidly at ~1,370 ℃ (as noted on thermocouples during experiment), as shown in the Fig. 94d. The density (ρ) of cast iron was 7850 $kgm^{-3}$. Once the pouring basin is filled, the stopper rod is removed in order to have a steady flow through the sprue. The average time of emptying of pouring basin was 55-62 secs for all the tests. A thermocouple was positioned (TC3) not on the surface of the interaction but just behind the testing slab, to monitor the heat transfer rate during the metal interaction with the mold. All the steps in the casting experiment have been

shown below, Fig. 94. And the temperature of the mold and metal during the casting is shown in Fig.95.

**Figure 94.** Steps involved, (a) 3D printing of sand mold, (b) melting iron, (c) casting process and (d) eroded molded with the respective positioning of thermocouples.

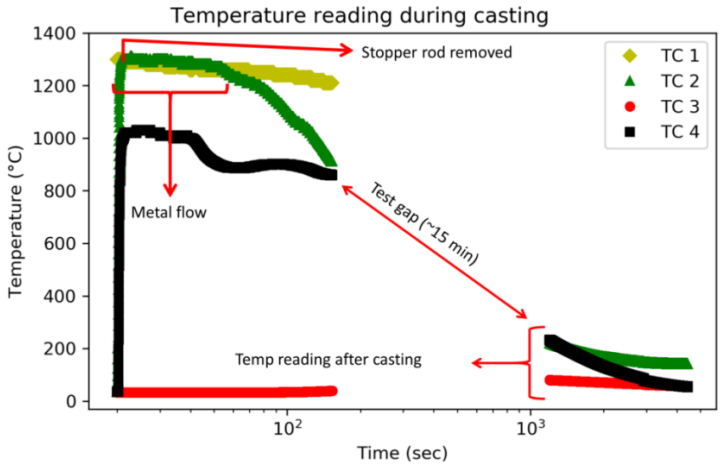


**Figure 95.** Temperature as noted during casting by thermocouples

In order to determine the deformation of the testing slabs from the interaction of melt, modern reverse engineering method was implemented, where CAD model of a total testing slab is created by means of 3D laser scanning. A literature review of reverse engineering will be not provided as this is not the point of focus for the thesis. The volumetric measurements were performed not only at the metal-mold interaction point, but also along the path on which the metal flowed. The reverse engineering method was chosen to characterize the volume and depth of erosion in a non-destructive manner. 3D laser scanning was performed on the tested slabs using the ROMER Absolute Arm RA 7520 SI with Integrated Scanner along with the inspection software to generate data set. The eroded slab specimen was placed on the table, as shown in Fig. 96, during the entire laser scanning process.

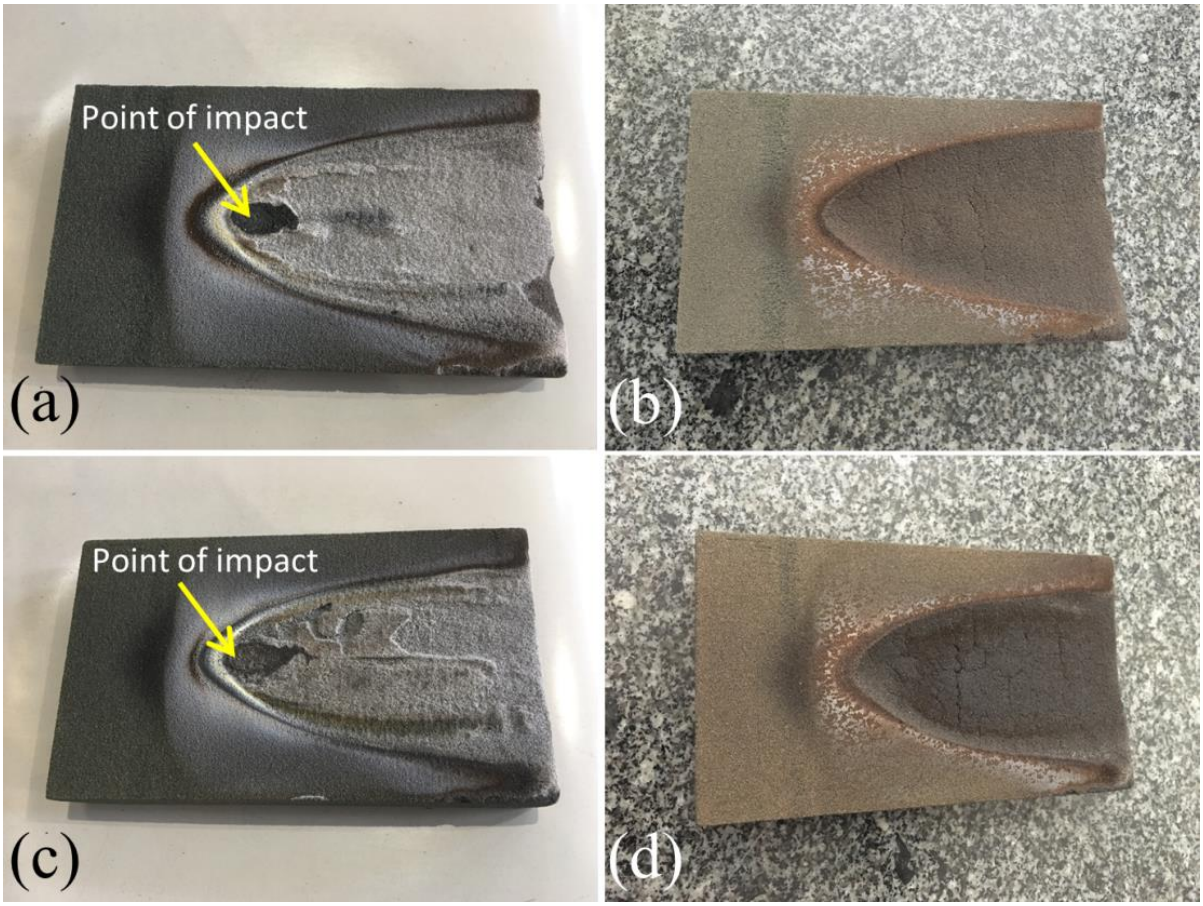


**Figure 96.** Tested slabs as used to study the melt interaction with 3DP sand mold. (a) LB specimen, (b) cleaned LB specimen, (c) HB specimen and (d) cleaned HB specimen

In order to produce the complete geometry of the object, individual scans from different angles were merged in to a single cloud point data set. The scanning was repeated until all the obtained scans were correctly associated and merged together to form a single data set. By

using the mentioned procedure, a point cloud data in .IGS file format was obtained, as shown in Fig. 100b and Fig 100b. The obtained .IGS file was imported into Catia V5 software, on which a CAD model of the eroded slabs was constructed. The resulting CAD model from point cloud data is shown in Fig. 100c Fig. 100c. To analyse the volume of the eroded part, the cloud date was first converted into mesh in Catia-Generative Shape Design mode. The eroded part of the slab was converted into a surface in Catia-Quick Surface Reconstruction mode. Few volumetric operations (Pad, Pocket) were performed in Catia-Mechanical Part Design mode and the resulting eroded volume and deforming depth was measured for the scanned LB and HB slab specimens. The difference in volume between the tested slab as 3D printed and the eroded test slab gave the volume of mold erosion.

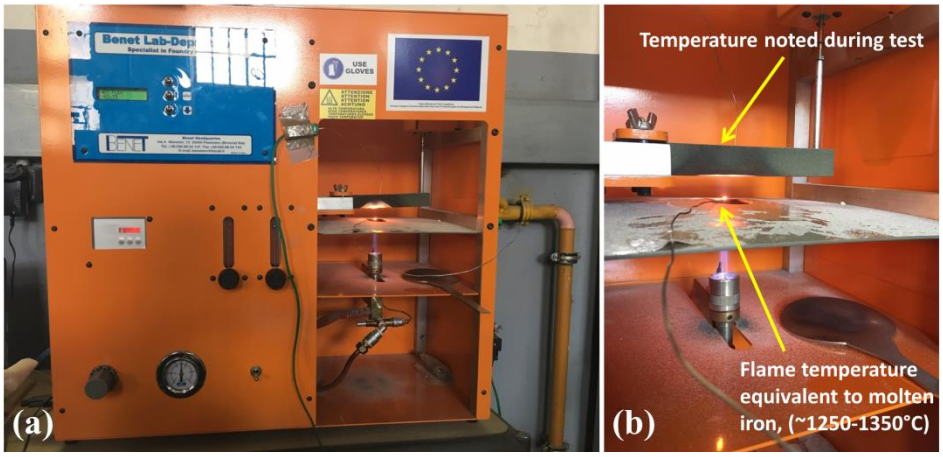


**Figure 97.** (a) Thermal deformation testing machine, and (b) zoomed view

In order to compare and validate the mold erosion results with traditional mechanical testing equipment's in foundry, a Thermal Deformation Test (TDT) was performed over 3DP bars with 2 different binder percent (1% and 2%). The machine used for the test was Hot Deformation Tester "HOT FLEX" manufactured by BENETLAB SRL (Com. No. 59/2014; S/N. 08/2014), Fig 97a. Each rectangular bar for the test has a dimension of 172 × 22.4 mm and a thickness of 22.4 mm. To operate the TDT machine, electrical power is switched on and the flame temperature was adjusted to simulate a specific liquid metal temperature, for the present case a temperature of 1350°C for cast iron was specified. The computer and data acquisition system are turned on to monitor and plot graphs for time (in seconds) versus temperature (in degree Celsius) along with distortion versus time plot. The experiment was focused mainly over the temperature of the specimen. The duration of test was chosen to be of

60 secs, after which the flame was turned off. The selected time of 60 secs corresponds to the time of cast iron flow time (55-60 secs) over the 3DP test slabs as used earlier for the mold erosion test. The maximum burnt depth will be compared for both type of binder specimens. The temperature of bars was not noted for the surface of the interaction of flame-mold but just behind the testing slab, to monitor the heat transfer rate during the metal interaction with the mold.

### 5.3 Results and discussion

Thermocouple readings in the mold were collected in real time, as soon as the molten metal was poured in the 3DP mold. The readings indicate the temperate rise in the molds during pouring, Fig. 95. The temperature rise of the cast iron at the pouring basin and sprue end are plotted as shown in Fig. 95 and it is clear that the maximum temperature of the casting attained was found to be ~1350-1400 °C. The readings from the thermocouples are used for plotting the Time vs Temperature graph, Fig. 95. Fig. 98 shows the change in temperature behind the testing slabs, and it can be observe that during the interaction with metal (first 60 secs) no heat is been transmitted and the temperature tends to rise only after the pouring. This will be explained from Fig. 99 that the critical changes mainly occurred only over the top 3 area, and with minimal or no changes on the fourth marked area.

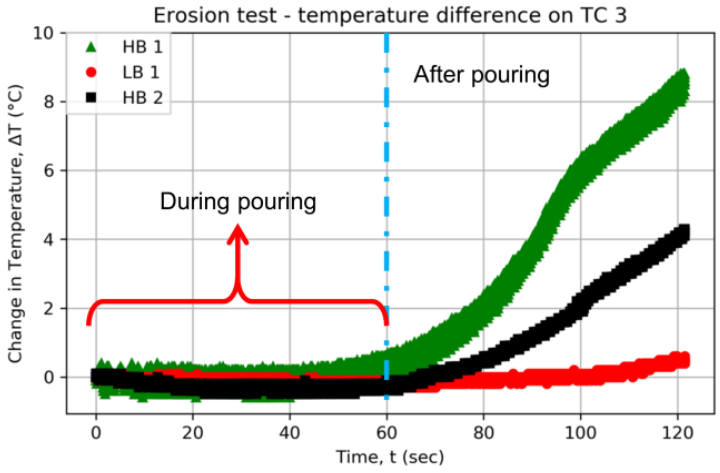


**Figure 98.** Temperature noted on the back part of testing slab during casting

The pouring temperature of liquid cast iron varied within a temperature range 1350–1400 °C, whereas the initial temperature of the 3DP sand mold and its surfaces was 28 - 32°C. During the cooling period, the resin bonded layer where the liquid metal is in contact to mold is decomposed. Such thermal decomposition of furan binder is generally followed by the

emission of toxic gaseous yields. These toxic gases affect the process of oxidation, where metal penetrates/interacts into the 3DP sand mold, hence formation of silicate in the zone of contact of liquid metal–sand mold. By just monitoring visually, it is obvious that reaction between the liquid cast iron over the 3DP sand mold surface have occurred, which burnt the resin bridges, hence formation dark layered surface, as shown in Fig. 99c, area 1.

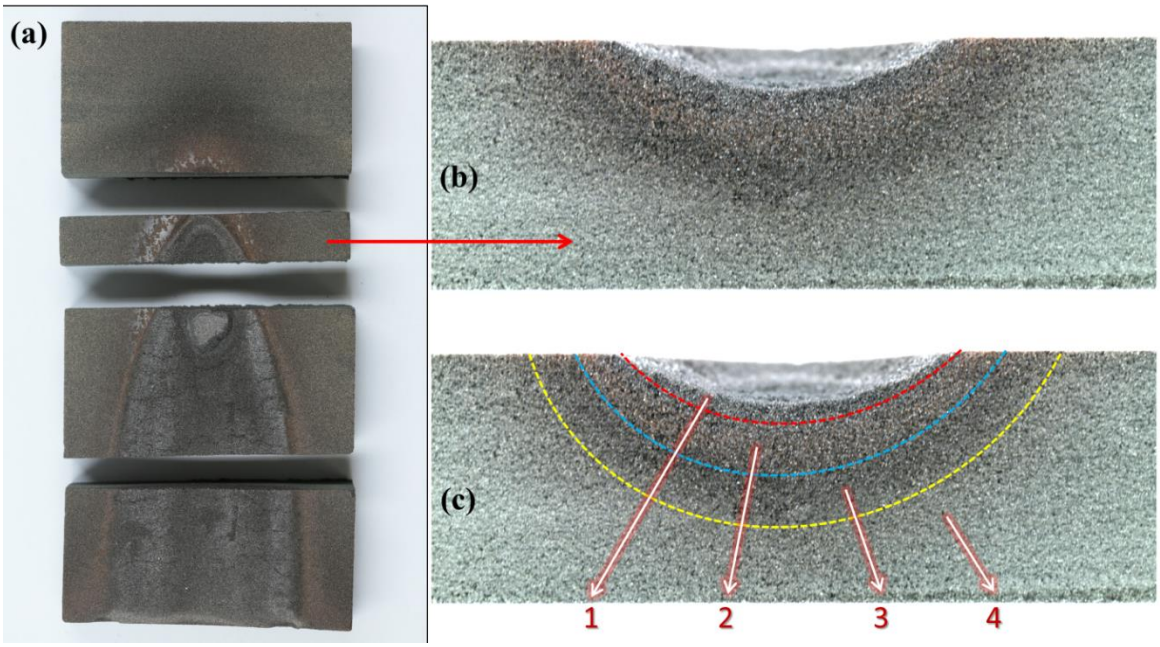


**Figure 99.** Cut section of the testing slabs, (a,b) zoomed view of the side section of interaction

The critical changes mainly occurred only over the top 3 area, and with minimal or no changes on the fourth marked area, as shown in the Fig. 99. The first affected area (marker 1) is highly dark in color which is the zone of direct interaction of the liquid cast iron to the 3DP mold surface. Significant changes occurred only on the first layer. The changes in silica quartz grains are the result of significant thermal reaction and the totally burnt resin (binder burns out at 400 °C from the heat of the liquid metal. In this area, the liquid cast iron interacted directly with 3DP mold material instantly after pouring; hence intensive reactions of liquid phase occur with the surface of the 3DP mold surface. The contact of such intense amount of heat causes reaction on entire surface of 3DP mold, hence maximum burnt resin bridges leading to growth of reaction layer at the beginning of the metal casting. The second most affected area (marker 2) is little lighter in color, which occurred due to the resulting allotropic changes of quartz. Here the light-colored zone is due to the change of α-quartz into the β-quartz. The third light dark area (marker 3) is the region in which only minor changes

might have occurred. And the following fourth area (marker 4) is a layer where no changes have occurred with unchanged properties and compound.

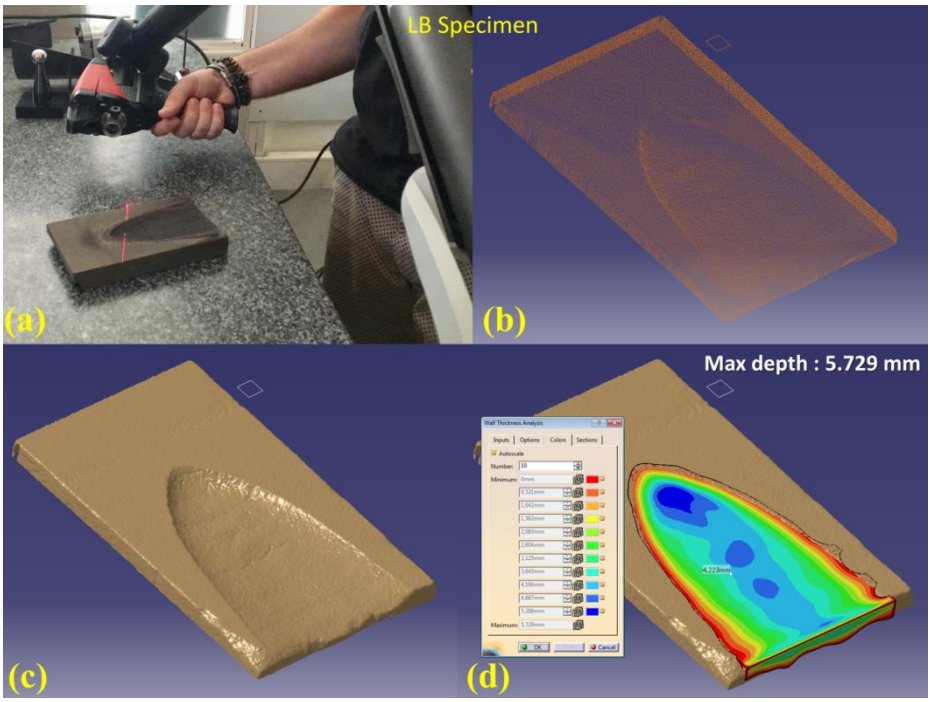


**Figure 100. For** LB specimen, (a) laser scanning of testing slabs, (b) cloud data points from scanned data, (c) meshing of cloud data, (d) surface generation and measuring deformation

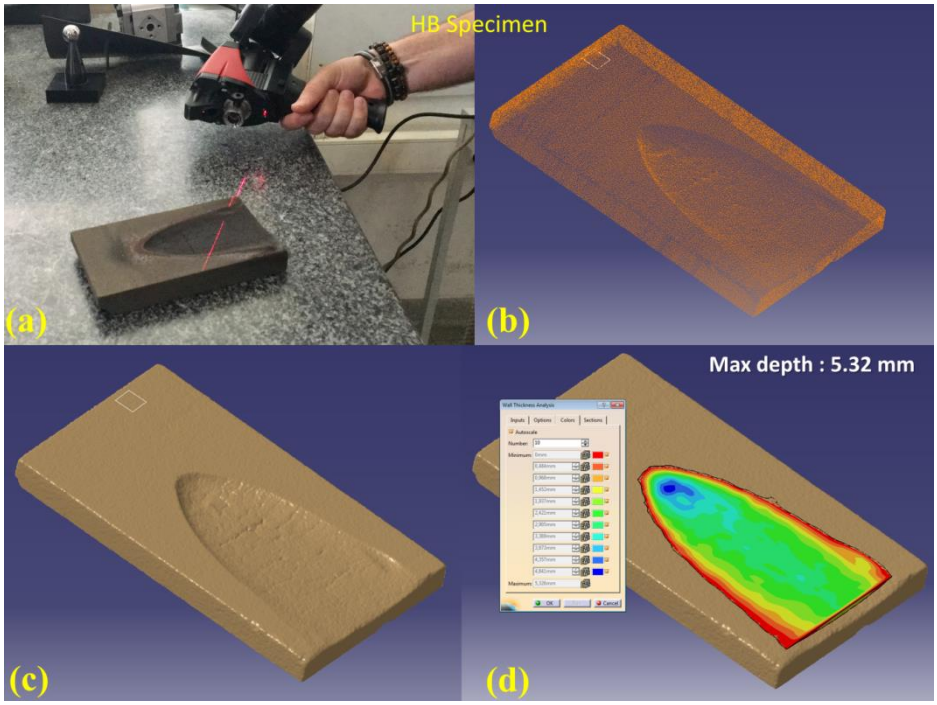


**Figure 101.** For HB specimen, (a) laser scanning of testing slabs, (b) cloud data points from scanned data, (c) meshing of cloud data, (d) surface generation and measuring deformation

The eroded volume and the maximum depth at the point of interaction were measured on Catia V5. The results have been listed on Table. 13. It can be observed visually and well from the result table that maximum volumetric erosion has occurred for the 3DP mold specimen printed with low binder. LB specimen eroded with 11% of the total volume of the slab (190400 $mm^3$) and the HB specimen eroded with 7.31%. And it also can be observed that high mold erosion occurs not only where the mold is directly hit by liquid metal, but also along the path of the metal flow. 3DP sand mold with low binder percent (~1%) have low resistance to erosion. This occurs mainly due to the low amount of binder present in between the interstices of the silica sand grains for the LB specimen.

The binder burn out temperature for furan binder is 400 °C, and at the direct interaction point for liquid metal and mold, there generates high concentration of energy (thermal and kinetic), which tends to burn the low amount of binder present in between the interstices of the silica sand grains, hence easy destruction of grain-binder bridge, leading to more detachment of particles. Whereas as observed and explained earlier in Section 3.3 the strength of 3DP mold has a direct bearing on the strength of bonds between particles. The strength of intermolecular bonds in turn depends on the physical state of the furan resin binder and its interaction with the surrounding particles. Reducing the amount of binder percent definitely reduced the resistance to mold erosion and compared to high binder percent.

With low amount of binder, the resin binder bridges are not well connected, leading to smaller cross section of resin bridges, Fig. 49. However, the erosion is less significant when the sand mold had high binder content, this occurs mainly due to the high amount of binder present in between the interstices of the silica sand grains for the HB specimen, hence less grain detachment. 3DP mold with furan binder are mostly used nowadays because of their numerous advantages, one of them being high resistance to mold erosion. But still it requires a careful selection of printing parameters, by controlling the amount of furan in 3D printing the sand mold, in addition to curing of the printed mold. The present work can help the foundry industries in selecting optimum parameters to print mold not only with good properties but also reducing its effect on the casting. The link between these structural characteristics of 3D printed molds with the influence the 3DP processing will allow in defining the functional rules for the design of sand molds as required for casting.

**Table 13. Results from laser scanned specimens**

| Specimen | Volume Eroded ($mm^3$) | Maximum depth size (mm) |
|---|---|---|
| Low Binder (LB) | 21249.976 | 5.72 |
| High Binder (HB) | 13931.315 | 5.32 |

Several batches of samples were tested using the TDT machine. 7 LB specimens along with 7 HB specimens were tested. It can be observed from Fig. 103, that the temperature of the 3DP mold printed with low binder percent reached higher temperature as compared to the high binder specimen. This can be explained due to the phenomenon of mold erosion and burn out of resin. The binder burn out temperature for furan binder is 400 °C, and at the direct interaction point for flame and mold, there generates high concentration of thermal energy which tends to burn the low amount of binder present in between the interstices of the silica sand grains, hence easy destruction of grain-binder bridge, leading to more detachment of particles and more indent depth and presented in Table. 14.

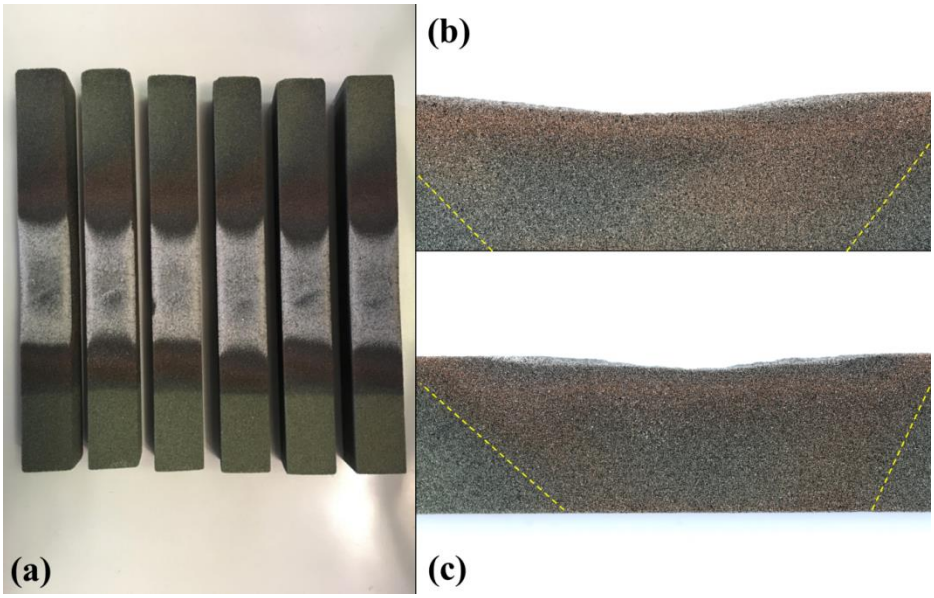


**Figure 102.** Bar specimens used form thermal deformation testing, (b) zoomed view of LB specimen, and (d) zoomed view of HB specimen

It was explained earlier in Section 3.3 that the mechanical properties of 3DP mold has a direct relation on the strength of bonds between silica grain particles. The strength of intermolecular bonds in turn depends on the physical state of the furan resin binder and its interaction with the surrounding particles. Reducing the amount of binder percent definitely reduced the resistance to mold erosion as seen from burnt depth thickness on Table. 14. It can be observed

from Fig. 102b and 102c that the heat has been transferred until the end of sample. This explains the difference between mold erosion due to liquid metal (weight, density, etc.) and mold erosion due to just thermal effect hence the heat got transferred until the end of the specimens, Fig. 102, as compared to the mold erosion due to casting of cast iron.

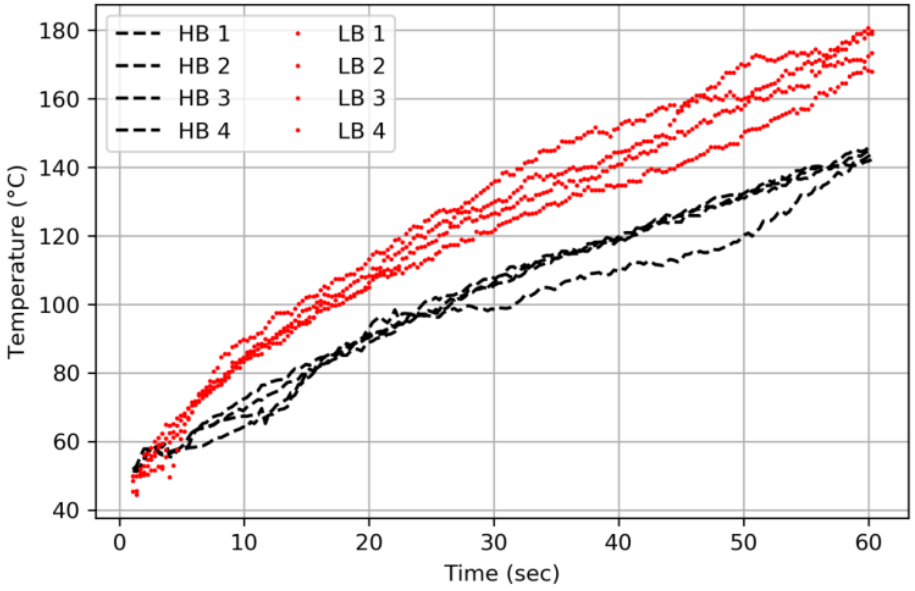


**Figure 103.** Temperature as noted for the HB and LB specimens

**Table 14. Results from thermal deformation test**

| No | Burnt depth (mm) | Mean burnt depth (mm) |
|---|---|---|
| Low binder (LB) specimen | | |
| 1 | 3.55 | 3.605 |
| 2 | 3.54 | |
| 3 | 3.62 | |
| 4 | 3.71 | |
| High Binder (HB) Specimen | | |
| 1 | 2.46 | 2.331 |
| 2 | 2.37 | |
| 3 | 2.31 | |
| 4 | 2.2 | |

## 5.4 Conclusion

The quality of the parts produced by casting in 3DP molds is directly related to the binder content. Motivated by the vital role of this process parameter, the effects of binder content on the volumetric erosion of 3DP sand molds during casting has been experimentally evaluated. The following conclusions are drawn from the present work:

- High mold erosion occurs not only where the mold is directly impacted by liquid cast iron, but also along the path of the flow.
- Binder percent of 3DP mold has a high influence on the volumetric erosion of 3DP sand molds. Higher binder amounts lead to increased resistance to erosion as compared to low binder percent.

The present findings represent a step forward towards improved characterization of mold erosion properties of the 3DP sand molds. However further characterization of such additively processed sand mold should be performed with varying average grain diameter, to check the convergence of the present hypothesis. Also samples printed with other printing process parameters should be studied.

# 6. CONCLUSIONS AND FUTURE PERSPECTIVES

## 6.1 Summary

This chapter summarizes the contributions, conclusions presented and discussed throughout this work as well as some hints for prospective future works.

The recent developed additive manufacturing technique used for printing sand molds in alloy casting processes is almost unique. The parts of the mold assembly can be manufactured by precisely controlling the printing process parameters, and the toxic gas producible materials within the printed mold. A functional mold can be manufactured with the required gas permeability, mold strength, and hence ensure a high success rate of quality casting with an optimized design for weight reduction. It overcomes many of the limitations of the traditional mold design with a very limited number of parts in the mold assembly. It has not been possible to find large references dealing closely with this innovative additive manufacturing production method.

This doctoral work dealt with an experimental investigation of the mechanisms governing the mechanical and microstructural response of 3DP mold to the variation of different printing process parameters. Also, an innovative approach combining x-ray tomography and advanced image analysis tools was employed to extract information at different scales, including micro-scale, i.e., the scale of sand grains. The quantitative analysis of the behavior of 3DP mold offered valuable three-dimensional (3D) data set against which theoretical and numerical approaches were tested.

## 6.2 Conclusion

To conclude, this PhD project dealt with the mastery of the additive manufacturing of sand molds around the following four themes:

- *Physical understanding* of additive processes with identification of process parameters of the 3D printer, and the mechanical characteristics of the 3DP mold.
- *Methods for characterizing* the 3DP mold (mechanical and mass transport properties), to establish the limits and specifications of the printing process parameters.
- *Non-Destructive characterization* of 3DP sand mold using X-Ray CT, to extract information at different scales, including micro-scale, i.e., the scale of sand grains.
- *Volumetric erosion* of 3DP mold during metal casting.

First, a bibliographic study was conducted in order to understand the basis of the additive manufacturing technique. The control parameters were identified, together with qualitative evaluation of their influence on the quality of the 3DP mold. This study showed that variations of printing process parameters, such as build orientation, recoating speed and binder saturation, are significant for the strength and permeability of the 3DP sand mold.

A first set of characterization experiments was performed to establish the limits and specifications of the printing process parameters and the effects of aging on the permeability and mechanical strength of 3D printed sand mold. The present permeability ($k$) and 3PB strength experimental results about this type of 3DP models are state of the art and had not been previously published. For this reason, it was essential to develop a fluid flow permeameter, which allowed testing a unidirectional fluid flow through the 3DP sand mold to measure the mass transport properties under different curing conditions. These were then studied in detail and compared with the results obtained from X-Ray CT images in order to understand the physical mechanisms governing permeability variation during the curing stage of the 3DP sand molds. In order to improve the design of the functional mold to limit casting defects, we have listed the existing rules in the literature. The continuity of the work consisted of successive iterations between X-Ray CT and experiments, allowing the determination of the influence of process parameters on the mold properties and also identified a lack of knowledge of curing effects and binder percent on the functionality of 3D printed molds.

## 6.3 Perspectives

The influence of other existing printing process parameters (powder type, grain size, printing speed, activator content, binder type, printing layer thickness (Z-axis), etc.) is also an important scope and must be studied in detail. It would be interesting to repeat similar model tests with a 3DP molds with different printing process parameters as explained above. The X-ray CT imaging tools used in this PhD work could not reveal the influence of the binder on the observed grain kinematics, and resin-bridge interface. It would be interesting to explore and compare the behavior of the silica sand grain and resin bridge interface during both tension and compression phases during mechanical characterization tests. The present findings represent a step forward towards improved prediction of mass transport properties of the 3DP sand molds. However further characterization of permeability of such additively processed sand mold should be performed with varying printing process parameters, to check

the convergence of the present model. Also for more accurate prediction of permeability a different approach could be considered, e.g., in-situ X-ray CT analysis by flooding small 3DP specimens with a gas having a high X-ray attenuation coefficient, to be able to detect the existence of isolated pores in that do not contribute to gas flow throughout the sample.

# 7. BIBLIOGRAPHY


[1] Mitra S, Rodríguez de Castro A, El Mansori M. The effect of ageing process on three-point bending strength and permeability of 3D printed sand molds. Int J Adv Manuf Technol 2018;97:1241–51. doi:10.1007/s00170-018-2024-8.

[2] Mitra S, Rodríguez de Castro A, El Mansori M. On the rapid manufacturing process of functional 3D printed sand molds. J Manuf Process 2019;42:202–12. doi:10.1016/j.jmapro.2019.04.034.

[3] Mitra S, EL Mansori M, Rodríguez de Castro A, Costin M. Study of the evolution of transport properties induced by additive processing sand mold using X-ray computed tomography. J Mater Process Technol 2020;277:116495. doi:10.1016/j.jmatprotec.2019.116495.

[4] Gutowski T. Casting 2.810 n.d.

[5] Sachs EM, Haggerty S, Michael J, Williams PA. Three-Dimensional Printing Techniques, 1993.

[6] Sachs E, Cima M, Cornie J, Brancazio D, Bredt J, Curodeau A, et al. Three-Dimensional Printing: The Physics and Implications of Additive Manufacturing. CIRP Ann - Manuf Technol 1993;42:257–60. doi:10.1016/S0007-8506(07)62438-X.

[7] Bredt JF, Anderson T. Method of three dimensional printing, 1999.

[8] Sachs E, Cima M, Cornie J. Three-Dimensional Printing: Rapid Tooling and Prototypes Directly from a CAD Model. CIRP Ann 1990;39:201–4. doi:10.1016/S0007-8506(07)61035-X.

[9] Sachs E, Cima M, Cornie J. Three-dimensional printing: rapid tooling and prototypes directly form a CAD model. CIRP Ann - Manuf Technol 1990;39:201–4. doi:http://dx.doi.org/10.1016/S0007-8506(07)61035-X.

[10] Sachs EM, Haggerty JS, Cima MJ, Williams PA. Three-dimensional printing techniques 1993.

[11] Patent US, Haggerty S, Michael J, Williams PA. Three-Dimensional Printing Techniques-United States Patent. 1993.

[12] Williams CB. Design and development of layer-based additive manufacturing process for realization of metal parts of designed mesostructure 2008:421.

[13] Almaghariz ES, Conner BP, Lenner L, Gullapalli R, Manogharan GP, Lamoncha B, et al. Quantifying the role of part design complexity in using 3d sand printing for molds and cores. Int J Met 2016;10:240–52. doi:10.1007/s40962-016-0027-5.

[14] Almaghariz ES. Determining When to Use 3D Sand Printing : Quantifying the Role of Complexity By Eyad S . Almaghariz A thesis Submitted in Partial Fulfillment of the Requirements for the Degree of Master of Science in the 2015.

[15] Conner BP, Manogharan GP, Martof AN, Rodomsky LM, Rodomsky CM, Jordan DC, et al. Making sense of 3-D printing: Creating a map of additive manufacturing products and services. Addit Manuf 2014;1:64–76. doi:10.1016/j.addma.2014.08.005.

[16] Low ZX, Chua YT, Ray BM, Mattia D, Metcalfe IS, Patterson DA. Perspective on 3D printing of separation membranes and comparison to related unconventional fabrication techniques. J Memb Sci 2017;523:596–613. doi:10.1016/j.memsci.2016.10.006.

[17] Shepler J, Chapman S. ExOne - A Case Study in Optimizing Casting Design Using 3 D Printing. 2017.

[18] Motoyama Y, Inoue Y, Saito G, Yoshida M. A verification of the thermal stress analysis, including the furan sand mold, used to predict the thermal stress in castings. J Mater Process Technol 2013;213:2270–7. doi:10.1016/j.jmatprotec.2013.06.024.

[19] Marumoto N, Kashimura H, Yoshida K, Toyoda T, Okane T, Yoshida M. Dynamic measurements of the load on gray cast iron castings and contraction of castings during cooling in furan sand molds. J Mater Process Technol 2016;237:48–54. doi:10.1016/j.jmatprotec.2016.05.012.

[20] Nastac L, Jia S, Nastac MN, Wood R. Numerical modeling of the gas evolution in furan binder-silica sand mold castings. Int J Cast Met Res 2016;29:194–201. doi:10.1080/13640461.2015.1125983.

[21] Tiedje N, Crepaz R, Eggert T, Bey N. Emission of organic compounds from mould and

core binders used for casting iron, aluminium and bronze in sand moulds. J Environ Sci Health A Tox Hazard Subst Environ Eng 2010;45:1866–76. doi:10.1080/10934529.2010.520595.

[22] Bobby SS. A Preliminary Investigation of Gypsum Bonded Moulds By Three Dimensional Printing. IJRET Int J Res Eng Technol 2014;03:501–7.

[23] Frascati J. Effects of Position, Orientation, and Infiltrating Material on Three Dimensional Printing Models. Dep Mech Mater Aerosp Eng 2007;degree of. doi:10.1017/CBO9781107415324.004.

[24] Mckenna N, Singamneni S, Diegel O, Singh D, Neitzert T, George JS, et al. Direct Metal casting through 3D printing : A critical analysis of the mould characteristics. 9th Glob Congr Manuf Manag 2008:12–4.

[25] Snelling D, Williams CB, Druschitz AP. A Comparison of Binder Burnout and Mechanical Characteristics of Printed and Chemically Bonded Sand Molds. SFF Symp 2014:197–209.

[26] Khandelwal H, Ravi B. Effect of Binder Composition on the Shrinkage of Chemically Bonded Sand Cores. Mater Manuf Process 2015;30:1465–70. doi:10.1080/10426914.2014.994779.

[27] Khandelwal H, Ravi B. Effect of molding parameters on chemically bonded sand mold properties. J Manuf Process 2016;22:127–33. doi:10.1016/j.jmapro.2016.03.007.

[28] Meisel N a., Williams CB, Druschitz A. Lightweight Metal Cellular Structures via Indirect 3D Printing and Casting. Solid Free Fabr Symp 2012:162–76.

[29] Renhe H, Hongmei G, Yaoji T, Qingyun L. Curing mechanism of furan resin modified with different agents and their thermal strength. China Foundry 2011;8:161–5.

[30] Gill SS, Kaplas M. Efficacy of powder-based three-dimensional printing (3DP) technologies for rapid casting of light alloys. Int J Adv Manuf Technol 2011;52:53–64. doi:10.1007/s00170-010-2716-1.

[31] Günther D, Mögele F. Additive Manufacturing of Casting Tools Using Powder-Binder-Jetting Technology. New Trends 3D Print., InTech; 2016. doi:10.5772/62532.

[32] Zeitsch KJJ. The Chemistry and Technology of Furfural and its Many By Products. vol. 13. 2001. doi:10.1016/S1385-8947(00)00182-0.

[33] Nassar a. R, Reutzel EW. A proposed digital thread for additive manufacturing. Solid Free Fabr 2013:19–43.

[34] Pratt MJ. Introduction to {ISO} 10303—the {STEP} {Standard} for {Product} {Data} {Exchange}. J Comput Inf Sci Eng 2001;1:102–3. doi:10.1115/1.1354995.

[35] International A. INTERNATIONAL STANDARD ISO / ASTM 2013;2013.

[36] Kumar V, Dutta D. An assessment of data formats for layered manufacturing. Adv Eng Softw 1997;28:151–64. doi:10.1016/S0965-9978(96)00050-6.

[37] Marsan A, Kumar V, Dutta D, Pratt M. An assessment of data requirements and data transfer formats for layered manufacturing. NIST, US Dep … 1998.

[38] Sachs EM, Cima MJ, Caradonna MA, Grau J, Serdy JG, Saxton PC, et al. Jetting layers of powder and the formation of fine powder beds thereby, 2003.

[39] Fuller SB, Wilhelm EJ, Jacobson JM. Ink-jet printed nanoparticle microelectromechanical systems. J Microelectromechanical Syst 2002;11:54–60. doi:10.1109/84.982863.

[40] Heinzl J, Hertz CH. Ink-Jet Printing. Adv Electron Electron Phys 1985;65:91–171. doi:10.1016/S0065-2539(08)60877-X.

[41] Le HP. Progress and trends in ink-jet printing technology. J Imaging Sci Technol 1998;42:49–62. doi:citeulike-article-id:3979011.

[42] Sachs EM. Powder dispensing apparatus using vibration, 2000.

[43] Harwood CF. Powder segregation due to vibration. Powder Technol 1977;16:51–7. doi:10.1016/0032-5910(77)85020-1.

[44] Cumberland, D. J and Crawford RJ. The packing of particle. Amsterdam : Elsevier; 1987.

[45] Kwan AKH, Fung WWS. Packing density measurement and modelling of fine aggregate and mortar. Cem Concr Compos 2009;31:349–57.

doi:10.1016/j.cemconcomp.2009.03.006.

[46] Stovall T, de Larrard F, Buil M. Linear packing density model of grain mixtures. Powder Technol 1986;48:1–12. doi:10.1016/0032-5910(86)80058-4.

[47] C.C. Mounfield S.F. Edwards. A model for the packing of irregularly shaped grains. Phys A Stat Mech Its Appl 1994;210:301–16. doi:10.1016/0378-4371(94)90078-7.

[48] Barksdale RD, Kemp MA, Sheffield WJ, Hubbard JL. Measurement of aggregate shape, surface area, and roughness. Transp Res Rec 1991:107–106.

[49] Tay BY, Evans JRG, Edirisinghe MJ. Solid freeform fabrication of ceramics. Int Mater Rev 2003;48:341–70. doi:10.1179/095066003225010263.

[50] Ederer I, Günther D. Device and method for 3d printing methods, with accelerated execution, 2015.

[51] Yao AWL, Tseng YC. A robust process optimization for a powder type rapid prototyper. Rapid Prototyp J 2002;8:180–9. doi:10.1108/13552540210431004.

[52] Gardziella A, Pilato LA, Knop A. Phenolic resins: chemistry, applications, standardization, safety and ecology. Springer Science & Business Media.; 2013.

[53] Hussein NIS, Ayof MN, Sokri NIM. Mechanical Properties and Loss on Ignition of Phenolic and Furan Resin Bonded Sand Casting. Int J Mining, Metall Mech Eng 2013;1:223–7.

[54] Quaker T, Company O. Catalyst composition and method for curing furan-based foundry binders-US 4451577 A 1984.

[55] Holtzer M, Dańko R. Molds and Cores Systems in Foundry 2015:27–43. doi:10.1007/978-3-319-14583-9.

[56] József Tamás Svidró, Judit Tóth, Attila Diószegi, David Stevenson. Heat absorption capacity and binder degradation characteristics of 3D printed cores investigated by inverse fourier thermal analysis. Int J Met 2016;10:276–88. doi:10.1007/s40962-016-0043-5.

[57] Hoyt D. Learning from the Past can help Insure Success in the Future. AFS Sand Cast. Conf., Indianapolis, IN: 2012.

[58] Fred P. Schleg. Technology of Metalcasting. Schaumburg, IL: American Foundry Society; 2003.

[59] Kaddhour G, Ando E, Salager S, Bésuelle P. Application of X-ray Tomography to the Characterisation of Grain-Scale Mechanisms in Sand 2013:195–200.

[60] Cil MB, Alshibli K, Kenesei P, Lienert U. Combined high-energy synchrotron X-ray diffraction and computed tomography to characterize constitutive behavior of silica sand. Nucl Instruments Methods Phys Res Sect B Beam Interact with Mater Atoms 2014;324:11–6. doi:10.1016/j.nimb.2013.08.043.

[61] Mukunoki T, Miyata Y, Mikami K, Shiota E. X-ray CT analysis of pore structure in sand. Solid Earth 2016;7:929–42. doi:10.5194/se-7-929-2016.

[62] Aloe M, Lefebvre D, Sholapurwalla A. Advanced casting simulations. Simulation n.d.:1–14.

[63] Shepel S V., Paolucci S. Numerical simulation of filling and solidification of permanent mold castings. Appl Therm Eng 2002;22:229–48. doi:10.1016/S1359-4311(01)00068-0.

[64] Jolly MR, Lo HSH, Turan M, Campbell J. Use of simulation tools in the practical development of a method for manufacture of cast iron camshafts. Model Cast Weld Adv Solidif Process (MCWASP IX), Aachen, Ger 2000:311–8.

[65] Simulation-of-Flow-Pattern-and-Temperature-Profile-in-the-Shot-Sleeve-of-a-High-Pressure-Die-Casting-Process.pdf n.d.

[66] Liu F, Yang L, Huang Y, Jiang P, Li G, Jiang W, et al. Performance of resin bonded sand for magnesium alloy casting. J Manuf Process 2017;30:313–9. doi:10.1016/j.jmapro.2017.10.002.

[67] Sivarupan T, ElMansori M, Coniglio N. 3D Printing Process Parameters and Properties of Additively Manufactured Sand Mold for Rapid Casting : Strength and Permeability. Addit Manuf 2017:(under review).

[68] ExOne. ExOne: Digital Part Materialization 2017.

[69] Dassault Systèmes. Catia V5 2017.

[70] Autodesk Inc. Netfabb® 2017.

[71] ExOne. S-Print ™ Furan. 2014.

[72] Coniglio N, Sivarupan T, El Mansori M. Investigation of process parameter effect on anisotropic properties of 3D printed sand molds. Int J Adv Manuf Technol 2017:1–11. doi:10.1007/s00170-017-0861-5.

[73] Lee JJ, Sachs E, Cima M. Layer position accuracy in powder based rapid prototyping. Rapid Prototyp J 1995;1:24–37. doi:10.1108/13552549510104447.

[74] Dimitrov D, Beer N. Developing capability profile for the three dimensional printing process. R D J 2006;22:17–25.

[75] D.M. Dimitrov, N. de Beer. IMPROVEMENTS IN THE CAPABILITY PROFILE OF 3-D PRINTING: AN UPDATE. South African J Ind Eng 2014;25:1–12. doi:10.11842/wst.2014.02.015.

[76] C. O. Willits's. Methods for Determination of Moisture-Oven Drying. Anal Chem 1951:1058–1062. doi:10.1021/ac60056a003.

[77] Simpson Technologies Corporation. SIMPSON Sand Testing machines for Molding and Core Sands DESIGNED 2008.

[78] Simpson. SIMPSON Universal Strength Machine PFG. vol. 41. 2008.

[79] Simpson. Simpson Permeability Meter PDU-D. vol. 41. 2002.

[80] DISA Industrie AG. Testing instruments and accessories to determine the permeability of moulding and core sands 2017.

[81] Georges Fischer société anonyme. Permeametre type PDU 2017.

[82] Bobrowski A, Grabowska B. The impact of temperature on furan resin and binder structure. Metall Foundry Eng 2012;38:73–80.

[83] Lowe K E, Showman R E. Dimensional Changes in Chemically Bonded Molds and Cores. Trans Am Foundry Soc 2011;119:251–60.

[84] Miyanaji H, Momenzadeh N, Yang L. Effect of printing speed on quality of printed parts in Binder Jetting Process. Addit Manuf 2018;20:1–10.

doi:10.1016/j.addma.2017.12.008.

[85] Schindelin J, Arganda-Carreras I, Frise E, Kaynig V, Longair M, Pietzsch T, et al. Fiji: An open-source platform for biological-image analysis. Nat Methods 2012;9:676–82. doi:10.1038/nmeth.2019.

[86] Zeng Z, Grigg R. A Criterion for Non-Darcy Flow in Porous Media. Transp Porous Media 2006;63:57–69. doi:10.1007/s11242-005-2720-3.

[87] Vinci Technologies. BENCH TOP PERMEAMETER SYSTEM n.d.

[88] Wikipedia. Scanning electron microscope n.d. https://en.wikipedia.org/wiki/Scanning_electron_microscope (accessed September 10, 2019).

[89] Feldkamp L a, Davis LC, Kress JW. Practical cone-beam algorithm. J Opt Soc Am A 1984;1:612. doi:10.1364/JOSAA.1.000612.

[90] Wikipedia. Cone beam computed tomography n.d. https://en.wikipedia.org/wiki/Cone_beam_computed_tomography#cite_note-16 (accessed September 10, 2019).

[91] Hawaldar N, Zhang J. A comparative study of fabrication of sand casting mold using additive manufacturing and conventional process. Int J Adv Manuf Technol 2018;97:1037–45. doi:10.1007/s00170-018-2020-z.

[92] Ramezani Dana H, El Mansori M. Etude du comportement mécanique d'une structure poreuse obtenue par impression 3D au sable. 24ème Congrès Français de Mécanique, 2019.

[93] Xiong Q, Baychev TG, Jivkov AP. Review of pore network modelling of porous media: Experimental characterisations, network constructions and applications to reactive transport. J Contam Hydrol 2016;192:101–17. doi:10.1016/j.jconhyd.2016.07.002.

[94] Huang X, He Y, Zhou W, Deng D, Zhao Y. Pore network modeling of fibrous porous media of uniform and gradient porosity. Powder Technol 2019;343:350–61. doi:10.1016/j.powtec.2018.11.022.

[95] Degruyter W, Bachmann O, Burgisser A. Controls on magma permeability in the volcanic conduit during the climactic phase of the Kos Plateau Tuff eruption (Aegean Arc). Bull Volcanol 2009;72:63–74. doi:10.1007/s00445-009-0302-x.

[96] Degruyter W, Burgisser A, Bachmann O, Malaspinas O. Synchrotron X-ray microtomography and lattice Boltzmann simulations of gas flow through volcanic pumices. Geosphere 2010;6:470–81. doi:10.1130/GES00555.1.

[97] Giesche H. Mercury porosimetry: A general (practical) overview. Part Part Syst Charact 2006;23:9–19. doi:10.1002/ppsc.200601009.

[98] FLANNERY BP, DECKMAN HW, ROBERGE WG, D'AMICO KL. Three-Dimensional X-ray Microtomography. Science (80- ) 1987;237:1439–44. doi:10.1126/science.237.4821.1439.

[99] De Chiffre L, Carmignato S, Kruth JP, Schmitt R, Weckenmann A. Industrial applications of computed tomography. CIRP Ann - Manuf Technol 2014;63:655–77. doi:10.1016/j.cirp.2014.05.011.

[100] Hazlett RD. Simulation of capillary-dominated displacements in microtomographic images of reservoir rocks. Transp Porous Media 1995;20:21–35. doi:10.1007/BF00616924.

[101] Rodríguez de Castro A, Radilla G. Non-Darcian flow of shear-thinning fluids through packed beads: Experiments and predictions using Forchheimer's law and Ergun's equation. Adv Water Resour 2017;100:35–47. doi:10.1016/j.advwatres.2016.12.009.

[102] Ding WT, Xu WJ. Study on the multiphase fluid-solid interaction in granular materials based on an LBM-DEM coupled method. Powder Technol 2018;335:301–14. doi:10.1016/j.powtec.2018.05.006.

[103] Jaganathan S, Vahedi Tafreshi H, Pourdeyhimi B. A realistic approach for modeling permeability of fibrous media: 3-D imaging coupled with CFD simulation. Chem Eng Sci 2008;63:244–52. doi:10.1016/j.ces.2007.09.020.

[104] Soulaine C. Direct numerical simulation in fully saturated porous media. StanfordEdu 2015:1–27.

[105] Thabet A, Straatman AG. The development and numerical modelling of a

Representative Elemental Volume for packed sand. Chem Eng Sci 2018;187:117–26. doi:10.1016/j.ces.2018.04.054.

[106] Boek ES, Venturoli M. Lattice-Boltzmann studies of fluid flow in porous media with realistic rock geometries. Comput Math with Appl 2010;59:2305–14. doi:10.1016/j.camwa.2009.08.063.

[107] Malaspinas O, Fiétier N, Deville M. Lattice Boltzmann method for the simulation of viscoelastic fluid flows. J Nonnewton Fluid Mech 2010;165:1637–53. doi:10.1016/j.jnnfm.2010.09.001.

[108] Kadauw A. Characterization of the parameters of sand moulds in compaction process by use of the industrial computer tomography (ICT). Arch Metall Mater 2014;59:1097–101. doi:10.2478/amm-2014-0189.

[109] Sivarupan T, El Mansori M, Daly K, Mavrogordato MN, Pierron F. Characterisation of 3D printed sand moulds using micro-focus X-ray computed tomography. Rapid Prototyp J 2018. doi:10.1108/RPJ-04-2018-0091.

[110] Anbar S, Thompson KE, Tyagi M. The Impact of Compaction and Sand Migration on Permeability and Non-Darcy Coefficient from Pore-Scale Simulations. Transp Porous Media 2019;127:247–67. doi:10.1007/s11242-018-1190-3.

[111] Legland D, Arganda-Carreras I, Andrey P. MorphoLibJ: Integrated library and plugins for mathematical morphology with ImageJ. Bioinformatics 2016;32:3532–4. doi:10.1093/bioinformatics/btw413.

[112] Boulos V, Fristot V, Houzet D, Salvo L, Lhuissier P. Investigating performance variations of an optimized GPU-ported granulometry algorithm To cite this version : Investigating performance variations of an optimized GPU-ported granulometry algorithm. Des Archit Signal Image Process (DASIP), 2012 Conf on, Oct 2012, Karlsruhe, Ger 2013:1–6.

[113] Ignacio Arganda-Carreras, Rodrigo Fernandez-Gonzalez, Arrate Munoz-Barrutia, Carlos Ortiz-De-Solorzano. 3D reconstruction of histological sections: Application to mammary gland tissue. Microsc Res Tech 2010;73:1019–29.

[114] Hormann K, Baranau V, Hlushkou D, Höltzel A, Tallarek U. Topological analysis of

non-granular, disordered porous media: Determination of pore connectivity, pore coordination, and geometric tortuosity in physically reconstructed silica monoliths. New J Chem 2016;40:4187–99. doi:10.1039/c5nj02814k.

[115] Comsol. Multiphysics Cyclopedia- Navier-Stokes Equations n.d. https://www.comsol.com/multiphysics/navier-stokes-equations (accessed July 10, 2019).

[116] Mandzhieva R. Introduction to digital core analysis : 3D reconstruction , numerical flow simulations and pore network modeling. Thesis 2017:138.

[117] Higuera FJ, Succi S, Benzi R. Lattice gas dynamics with enhanced collisions. Epl 1989;9:345–9. doi:10.1209/0295-5075/9/4/008.

[118] Sukop MC, Thorne DT. Lattice Boltzmann Modeling. Berlin, Heidelberg: Springer Berlin Heidelberg; 2006. doi:10.1007/978-3-540-27982-2.

[119] Meakin P, Tartakovsky AM. Modeling and Simulation of Pore-Scale Multiphase Fluid Flow and Reactive. Transport 2009;47:1–47. doi:10.1029/2008RG000263.1.INTRODUCTION.

[120] Ramstad T, Øren P-E, Bakke S. Simulation of Two-Phase Flow in Reservoir Rocks Using a Lattice Boltzmann Method. SPE J 2010;15:917–27. doi:10.2118/124617-pa.

[121] Talon L, Bauer D, Gland N, Youssef S, Auradou H, Ginzburg I. Assessment of the two relaxation time Lattice-Boltzmann scheme to simulate Stokes flow in porous media. Water Resour Res 2012;48:1–13. doi:10.1029/2011WR011385.

[122] Thijssen J. Computational Physics. Cambridge: Cambridge University Press; 2007. doi:10.1017/CBO9781139171397.

[123] Chopard B, Dupuis A, Masselot A, Luthi P. Cellular Automata and Lattice Boltzmann techniques: an approach to model and simulate complex systems. Adv Complex Syst 2002;05:101–2. doi:10.1142/S0219525902000560.

[124] Heijs AWJ, Lowe CP. Numerical evaluation of the permeability and the Kozeny constant for two types of porous media. Phys Rev E 1995;51:4346–52. doi:10.1103/PhysRevE.51.4346.

[125] Ferrol B, Rothman DH. Lattice-Boltzmann simulations of flow through Fontainebleau sandstone. Transp Porous Media 1995;20:3–20. doi:10.1007/BF00616923.

[126] Llewellin EW. LBflow: An extensible lattice Boltzmann framework for the simulation of geophysical flows. Part I: theory and implementation. Comput Geosci 2010;36:115–22. doi:10.1016/j.cageo.2009.08.004.

[127] Auzerais FM, Dunsmuir J, Ferréol BB, Martys N, Olson J, Ramakrishnan TS, et al. Transport in sandstone: A study based on three dimensional microtomography. Geophys Res Lett 1996;23:705–8. doi:10.1029/96GL00776.

[128] Hecht M, Harting J. Implementation of on-site velocity boundary conditions for D3Q19 lattice Boltzmann 2008:1–14. doi:10.1088/1742-5468/2010/01/P01018.

[129] Blunt MJ, Jackson MD, Piri M, Valvatne PH. Detailed physics , predictive capabilities and upscaling for pore-scale models of multiphase flow 2001;25:1069–89.

[130] Blunt MJ, Bijeljic B, Dong H, Gharbi O, Iglauer S, Mostaghimi P, et al. Pore-scale imaging and modelling. Adv Water Resour 2013;51:197–216. doi:10.1016/j.advwatres.2012.03.003.

[131] Luo G, Ji Y, Wang CY, Sinha PK. Modeling liquid water transport in gas diffusion layers by topologically equivalent pore network. Electrochim Acta 2010;55:5332–41. doi:10.1016/j.electacta.2010.04.078.

[132] Bultreys T, De Boever W, Cnudde V. Imaging and image-based fluid transport modeling at the pore scale in geological materials: A practical introduction to the current state-of-the-art. Earth-Science Rev 2016;155:93–128. doi:10.1016/j.earscirev.2016.02.001.

[133] Dong H. Micro-Ct Imaging and Pore Network Extraction a Dissertation Submitted To the Department of Earth Science and Engineering of Imperial College Lodon in Partial Fulfilment of the Requirements for the Degree of 2007:1–213.

[134] Gostick JT. Versatile and efficient pore network extraction method using marker-based watershed segmentation. Phys Rev E 2017;96:1–15. doi:10.1103/PhysRevE.96.023307.

[135] Rodríguez de Castro A, Agnaou M. Numerical Investigation of the Apparent Viscosity Dependence on Darcy Velocity During the Flow of Shear-Thinning Fluids in Porous

Media. Transp Porous Media 2019. doi:10.1007/s11242-019-01279-x.

[136] Bonnet JP, Topin F, Tadrist L. Flow laws in metal foams: Compressibility and pore size effects. Transp Porous Media 2008;73:233–54. doi:10.1007/s11242-007-9169-5.

[137] Glover PWJ, Walker E. Grain-size to effective pore-size transformation derived from electrokinetic theory. Geophysics 2009;74. doi:10.1190/1.3033217.

[138] Chauveteau G, Nabzar L, El Attar Y, Jacquin C. Pore Structure and Hydrodynamics. SCA Conf. Pap. Number 9607, 1996.

[139] Mocek J, Zych J, Chojecki A. Study of erosion phenomena in sand moulds poured with cast iron. Int J Cast Met Res 2004;17:47–50. doi:10.1179/136404604225020542.

# 8. Annex : Terminology

**Pixel**

In digital imaging, a pixel, pel, or picture element is one raster element from an image. A pixel consists of one single color or gray value and represents a particular distance in the image. Pixels are usually squares, so they have the same dimensions in horizontal axis or row (x coordinate) and vertical axis (y coordinate), termed as the pixel size.

**Voxel**

As described earlier that a pixel is one element in a 2D image, similarly one element in a 3D image is termed as voxel, or volume element, which can also be described as a 3D pixel.

**Three dimensional images (3D images)**

A stack or pile of 2D images represents a 3D volume. These 3D datasets have a pixel size in x and y directions, with an additional spacing between the images in z direction. However, this spacing between images in z direction does not always necessarily have the same pixel size.

**Spatial resolution**

This spatial resolution (or resolving power) is defined as the smallest distance between two features in a sample, for which these features are seen as separate objects. The local and global contrast in the image play an important role in the estimation and therefore different interpretations may arise.

HESAM UNIVERSITÉ

Arts Sciences et Technologies et Métiers

2019-ENAM-0043

École doctorale n° 432 : Sciences des Métiers de l'ingénieur

# Doctorat

# T H È S E

**pour obtenir le grade de docteur délivré par**

## l'École Nationale Supérieure d'Arts et Métiers

**Spécialité " Mécanique-matériaux "**

*présentée et soutenue publiquement par*

**Saptarshee MITRA**

le 15 novembre 2019

# Caractérisation expérimentale et numérique des propriétés fonctionnelles des moules sables produits par fabrication additive (procédé d'impression 3D par projection de liant) en fonderie rapid

Directeur de thèse : **Mohamed EL MANSORI**
Co-encadrement de la thèse : **Antonio RODRÍGUEZ DE CASTRO**
Co-encadrement de la thèse : **Marius COSTIN**

**Jury**

| | |
|---|---|
| **M. Michel BELLET**, Professeur des Universités, CEMEF, Mines ParisTech | Président |
| **M. Liam BLUNT**, Professeur des Universités, CPT, University of Huddersfield, England | Rapporteur |
| **M. Jean-Yves HASCOET**, Professeur des Universités, GeM, Ecole Centrale Nantes | Rapporteur |
| **M. Ismail LAZOGLU**, Professeur des Universités, MARC, Koc University, Turkey | Examinateur |
| **M. Mohamed EL MANSORI**, Professeur des Universités, MSMP-EA-7350, Arts et Métiers ParisTech | Examinateur |
| **M. Antonio RODRÍGUEZ DE CASTRO**, Maître de Conférences, Arts et Métiers ParisTech | Examinateur |
| **M. Marius COSTIN**, Researcher in NDT, Institute List – CEA Saclay | Examinateur |

T H È S E

**Arts et Métiers - Campus de Aix-en-Provence**
**Laboratoire MSMP (EA-7350)**

# 1. Introduction générale

La coulée hybride est une technique avancée de fabrication de moules additifs, dans laquelle la conception du modèle informatique est intégrée à l'impression 3D afin de fabriquer des moules en sable pour produire des moulages. Cela offre aux entreprises de fonderie une excellente occasion de repenser les approches de coulée des métaux traditionnelles ou anciennes et de concevoir des pièces à forme complexe à l'aide de modèles informatiques. Dans la coulée hybride, les moules sont fabriqués sans aucun outil additif et de manière totalement automatisée en utilisant la méthode de construction par couches. L'imprimante 3D génère des couches superposées successives jusqu'à la fabrication du moule complet. Les nombreux avantages offerts par ce procédé de coulée innovant comprennent une réduction considérable du temps de fabrication des moules et une amélioration de la qualité des pièces moulées en métal. En outre, l'absence de coûts d'outillage rend ce procédé particulièrement économique et permet de repenser une géométrie complexe qui ne peut être fabriquée avec du coulage en sable traditionnel. Les imprimantes 3D sont généralement plus rapides, plus faciles à utiliser et moins chères que d'autres technologies complémentaires. Il est également possible de fabriquer des moules en sable de fonderie pour des pièces extrêmement petites et très minces. Les industries de fonderie modernes utilisent progressivement cette technologie de coulée hybride, car elle permet d'obtenir un bon état de surface avec le moulage au sable. La résine à base de furanne est l'un des liants les plus populaires utilisés pour maintenir ensemble les particules de grains dans la fabrication de moules 3DP. Les quantités et les proportions de liant au furanne peuvent influer de manière significative sur les propriétés du moule imprimé en 3D, ce qui altère la qualité de la coulée. Avec l'importance croissante de la coulée hybride, il est nécessaire d'étudier et d'optimiser les paramètres du processus d'impression 3D, qui affectent les propriétés du moule et ont un impact majeur sur la qualité de la coulée.

Le présent projet de thèse porte sur la modélisation de la technologie 3DP afin de produire des moules fonctionnels pour la coulée des métaux en termes de résistance mécanique et de perméabilité. Cela devrait aider l'industrie aérospatiale / automobile à choisir les paramètres de processus optimaux permettant de minimiser les défauts de moulage. La plate-forme de moulage en sable à basse pression (LPSC) du laboratoire de mécanique, traitement des surfaces et des matériaux (MSMP) a été utilisée pour résoudre ces problèmes de manière expérimentale. En particulier, la machine 3DP ExOne a fourni des résultats précieux pour

l’étude de l’effet des paramètres du procédé 3DP (par exemple, la quantité de liant / résolution X des gouttelettes de résine furanique, la vitesse de la tête d’injection et le compactage du moule) sur les fonctionnalités des moules. Le présent travail étudie l'effet du temps et de la température de vieillissement sur les propriétés du 3DP pour de différents contenus de liant, ce qui facilitera la sélection du pourcentage de liant optimal pour un produit de coulée donné. De plus, le CEA LIST dispose de plusieurs appareils d’imagerie à rayons X qui ont été utilisés pour inspecter les moules 3DP afin de détecter des défauts ou d’autres anomalies. Un scanner de tomographie à haute résolution assistée par ordinateur a été utilisé pour caractériser des petits échantillons, ce qui a permis d'extraire des informations structurelles (c'est-à-dire la taille des grains et leur distribution, les porosités du moule, etc.). Le lien entre les propriétés structurelles des moules imprimés et l’influence des paramètres du procédé a permis de définir les règles fonctionnelles pour la conception des moules en sable.

Les travaux de recherche suivants ont été menés:

- ✓ Comprendre les effets des paramètres de processus utilisés lors de l'impression 3D sur la fonctionnalité des moules (principalement le contenu du liant, la vitesse du système d’injection du revêtement et la taille des grains de sable) et choisir une méthode expérimentale rigoureuse pour caractériser les propriétés de résistance mécanique et de transport de masse du moule imprimé en 3D.
- ✓ Caractériser la résistance mécanique et la perméabilité des pièces 3DP produites dans de différentes conditions de vieillissement, afin d'améliorer la compréhension des mécanismes contrôlant la phase de vieillissement.
- ✓ Caractérisation du comportement des moules 3DP par analyse d'images volumétriques non destructives (tomographie à rayons X). Calcul de la perméabilité à partir de simulations numériques effectuées sur les images numériques 3D obtenues et comparaison aux résultats expérimentaux.
- ✓ Étudier les processus impliqués lors de l’interaction de la matière en fusion avec le moule en sable 3DP et mesurer l’érosion volumétrique de l’humidité au moyen de techniques de rétroingénierie.

# 2. Etat de l'art

Ce chapitre commence par une revue bibliographique de la coulée en sable en fonderie, axée sur la technique traditionnelle. Ensuite, la technologie de fabrication additive et son utilisation en fonderie pour l'impression de moules en sable pour la coulée des métaux sont introduites. Enfin, les bases théoriques et physiques de la technologie de projection de liant en poudre sous-jacente aux développements du moulage en sable sont résumées.

## 2.1. Processus de coulée

Le processus de moulage est l'une des premières méthodes de façonnage du métal de l'histoire de la civilisation. Les données archéologiques indiquent que l'origine du processus de coulée remonte à environ 5000 ans. Ces procédés consistent à verser un métal en fusion dans un moule (sable ou métallique), avec une cavité de la forme à fabriquer, et à le laisser se solidifier dans le moule. Une fois solidifié, l'objet métallique souhaité est retiré du moule, soit en cassant le moule en sable jetable, soit en le séparant lorsqu'un moule métallique réutilisable est utilisé. L'objet solidifié s'appelle brut de fonderie, Fig. 1. La coulée en sable est le procédé de coulée du métal le plus largement utilisé dans l'industrie, et presque tous les alliages peuvent être coulés dans des moules en sable. La taille des moulages en sable varie de très petite à extrêmement grande. Les blocs moteurs, les bases de machines-outils, les culasses, les corps de pompes et les soupapes sont des exemples remarquables d'articles fabriqués dans l'industrie moderne par des procédés de coulée en sable.

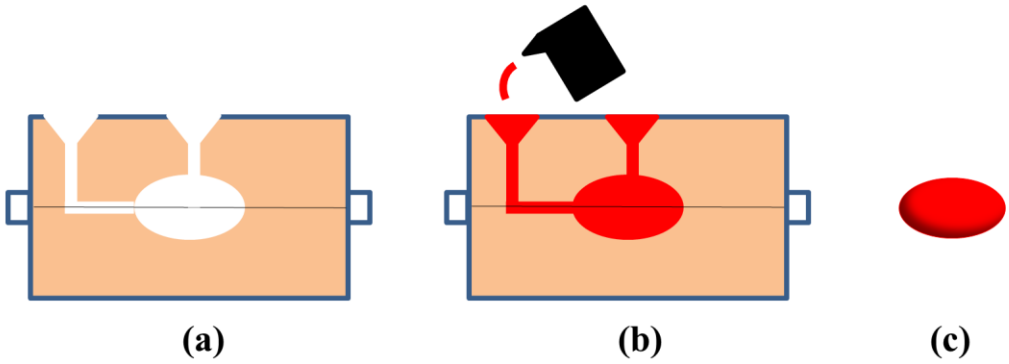


**Figure 1.** Processus traditionnel de moulage en sable; (a) moules assemblés, (b) coulage du métal liquide et (c) coulée finale solidifiée sans le système de remplissage.

La clé d'un projet de moulage de métal solide et réussi est un mélange systématique d'expérience et de science de l'ingénierie. Les principales étapes du processus de conception sont énumérées ci-dessous.

i. *Conception de la pièce à couler*

   Identifier le but de la coulée, la forme, la taille, les tolérances (fabrication), en tenant compte des modifications dimensionnelles au cours des processus de coulée.

ii. *Sélection du matériau pour la pièce à mouler*

   Propriétés mécaniques et physiques du matériau, y compris la coulabilité, les propriétés thermiques et les propriétés d'écoulement du fluide.

iii. *Conception et production des modèles pour les moules et les noyaux*

   Conception du système de portail et du canal de la colonne montante, basée sur les concepts de mécanique des fluides et de transfert de chaleur.

iv. *Sélection du processus de coulée*

   Type de moule (sable ou moule métallique), taille et rugosité du moule, perméabilité du moule (pour les moules en sable) et coût de production.

v. *Post-traitement de la coulée*

   Usinage soustractif, traitement thermique, soudage.

vi. *Contrôle de la qualité des pièces moulées*

   Propriétés mécaniques et physiques, essais destructifs ou non destructifs.

Au stade de la conception du système, la simulation du remplissage et de la solidification de la pièce proposée est extrêmement utile. De nos jours, les ordinateurs modernes sont généralement combinés à de puissants logiciels pour donner un aperçu du remplissage du moule et illustrer le chemin de la solidification. De telles simulations sont essentielles pour réduire le délai entre la conception et les prototypes, en évitant une approche par essais et erreurs pour la conception du système de remplissage. Bien qu'il existe de nombreuses solutions possibles pour les géométries de fonderie avec la méthode de coulée traditionnelle, les coûts d'investissement élevés engendrés pour les pièces complexes font de la technologie d'impression 3D une excellente alternative pour les industries de fonderie et une occasion de repenser les anciennes approches de coulée en utilisant des modèles informatiques. La technologie de prototypage rapide (RP), également appelée fabrication par couches ou

fabrication additive, connaît une croissance et une évolution rapides, et les moules en sable imprimés en 3D se sont révélés être un moyen efficace de prototyper et de fabriquer rapidement des moules en sable pour la coulée du métal. En conséquence, l'impression 3D de moules complexes pour la coulée des métaux est actuellement utilisée par différentes sociétés telles que ExOne, 3D Systems et Viridis3D.

### 2.2. Technologie d'impression 3D dans les applications de moulage

La fabrication additive, plus couramment appelée impression tridimensionnelle (3DP), a été inventée au MIT en tant que technique de prototypage rapide permettant de créer des couches en trois dimensions directement à partir du modèle de conception informatique. Des imprimantes au sable 3D à l'échelle commerciale ont été inventées au MIT (Massachusetts Institute of Technology) pour créer des pièces en trois dimensions (3D) directement à partir d'un modèle de conception informatique. Dans les processus 3DP, les modèles de conception CAO 3D sont découpées en tranches pour imprimer une couche de matériau granulaire sur une couche de liant dans un moule. AM (« *Additive Manufacturing* ») est défini comme le processus de jonction de particules à partir de données de conception 3D pour former un objet couche par couche, contrairement à la fabrication soustractive. L'impression tridimensionnelle (3DP) de moules en sable utilisant la technologie de jet de liant permet de surmonter les difficultés rencontrées dans le procédé de production traditionnel, par exemple; limitations en termes de complexité et de taille de pièce, de temps de production et de coût (qui dépendent de la quantité et de la complexité de la pièce, optimisation de la conception de pièce / liberté de conception pour tout alliage coulable.

Aujourd'hui, 3DP (impression 3D) est devenu la méthode standard pour la production de moules et de noyaux dans l'industrie de la fonderie, avec des applications dans divers domaines, tels que les aéronefs, les automobiles et le médical. Ce processus de prototypage rapide a été largement accepté en raison de son potentiel considérable de réduction des coûts de fabrication de composants très complexes. Parmi tous les processus rapides d'outillage et de fabrication, 3DP est particulièrement indiqué pour une intégration rapide dans les industries existantes, car il peut produire des moules en sable complexes et de haute qualité avec les propriétés requises pour de meilleures solutions de coulée dans un court délai. De plus, l'utilisation de la technique de projection de liant pour la production de conceptions de pièces optimisées permet de réduire le poids jusqu'à 33% par rapport au processus de fabrication de moules en sable traditionnel ou même à toute autre technique d'impression 3D.

La technologie 3DP basée sur la fabrication par couches produit des pièces poreuses en liant des particules individuelles, ce qui génère des moules perméables qui conviennent à la coulée des métaux malgré une résistance mécanique réduite. Cette perméabilité facilite l'évacuation des gaz depuis l'empreinte du moule. En plus, il faut souligner que les moules présentant des niveaux de résistance mécanique excessivement élevés peuvent provoquer une déchirure à chaud et une contrainte résiduelle élevée, ce qui ne convient pas à la coulée. Dans le cas des moules de fonderie, les céramiques sont utilisées comme matériaux particulaires pour assurer la réfractarité, et un liant liquide est utilisé pour assurer la cohésion entre les particules.

Qualitativement, le liant liquide forme des ponts capillaires entre les grains de sable, comme le montre schématiquement la Fig. 2, et la courbure de l'interface liquide génère une pression capillaire qui provoque une attraction entre les grains et une rigidité élevée des pièces imprimées en 3D. Cela génère un réseau de grains de sable reliés par des ponts de résine, ce qui permet d'imprimer un moule complexe pour la coulée du métal.

Les interstices entre les grains de sable dans les pièces imprimées en 3D permettent l'évacuation de l'air lors du remplissage du moule ainsi que l'écoulement des gaz générés lors du remplissage et de la solidification de l'alliage. Ces gaz seront évacués plus ou moins rapidement en fonction de la perméabilité du sable. Une bonne perméabilité du moule réduit les défauts de coulée formés par le piégeage des poches de gaz au sein de l'alliage liquide et améliore par la suite la capacité de remplissage. Cependant, une perméabilité élevée peut conduire à un défaut de pénétration du métal en raison du grand espacement entre les grains de sable (abreuvage).

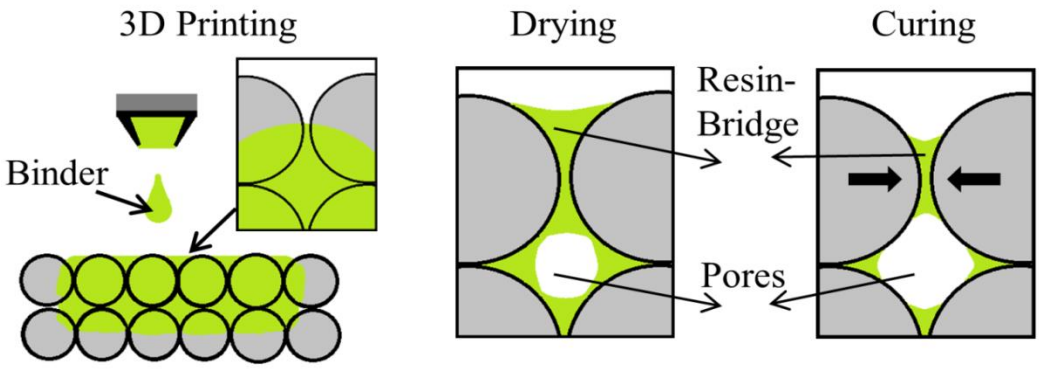


**Figure 2.** Représentation schématique du liant particulaire et de la résine

La résistance à la flexion du moule est fonction de la taille du grain, du taux de liant présent dans le moule et du compactage au sable. En effet, le liant liquide bloque l'écoulement de gaz

à travers le sable, ce qui entraîne une plus grande accumulation de gaz lors de la coulée de l'alliage et, par conséquent, des défauts de gaz. Ainsi, un fort taux de liant augmente la résistance à la flexion et le retrait, mais génère un excès de gaz pendant les opérations de coulée et un risque de remplissage incomplet. Par conséquent, il est indispensable d'évaluer les propriétés mécaniques et fonctionnelles du moule en sable imprimé en 3D en fonction des paramètres de fabrication.

Parmi les divers liants existants, les liants à base de furanne organique sont couramment utilisés dans les fonderies utilisant la technique de fabrication additive de moules en sable pour couler des alliages légers. L'avantage principal du liant furanique est qu'il durcit à la température ambiante et possède une bonne résistance mécanique. La réaction de condensation du liant furanne produit de l'eau, ce qui a tendance à ralentir la vitesse de vieillissement et affecte donc la résistance à la flexion et la perméabilité en 3 points. L'augmentation de la durée de vieillissement de la pièce 3DP entraîne l'évaporation d'une plus grande quantité d'eau de l'échantillon.

### 2.3. Processus de Powder Binder Jetting (PBJ)

Dans cette section, un aperçu du processus de Powder Binder Jetting (PBJ) est fourni. La fabrication additive de sable utilise la technologie de PBJ, qui consiste en plusieurs étapes qui sont répétées en continu pour fabriquer un composant 3D. Comparée à d'autres techniques de fabrication additive, la technologie PBJ présente l'avantage particulier de ne pas dégager de chaleur pendant le processus d'impression, ce qui n'entraîne aucune contrainte résiduelle induite. Il est considéré comme la méthode standard pour la production de moules et de noyaux 3DP. Le processus PBJ a la capacité de fabriquer des composants 3DP volumineux et est souvent plus économique que toute autre technologie de fabrication additive existante. Parmi tous les processus, le processus PBJ est aussi considéré comme le plus évolutif. Cela a un impact sur les tailles possibles des composants et les performances du système. La Fig. 3 montre une représentation schématique de certaines étapes clés du processus.

En PBJ, un modèle CAO de la pièce désirée est d'abord créé. À partir de la conception de la pièce CAO, les images sont traitées en tranches, puis converties en différents formats, tels que STL ou le fichier de fabrication additive récemment développé, AMF. Alors que le fichier STL traditionnel ne traite que de la géométrie, le fichier AMF permet la modification de matériaux et de textures. Le nouveau format de fichier ASTM AMF est un développement massif pour le traitement des images 3D pour la fabrication additive et remplacera la plupart

des autres formats disponibles. Contrairement au format de fichier STL prédécesseur, le format de fichier AMF prend en charge la couleur, les textures, les matériaux et les réseaux.

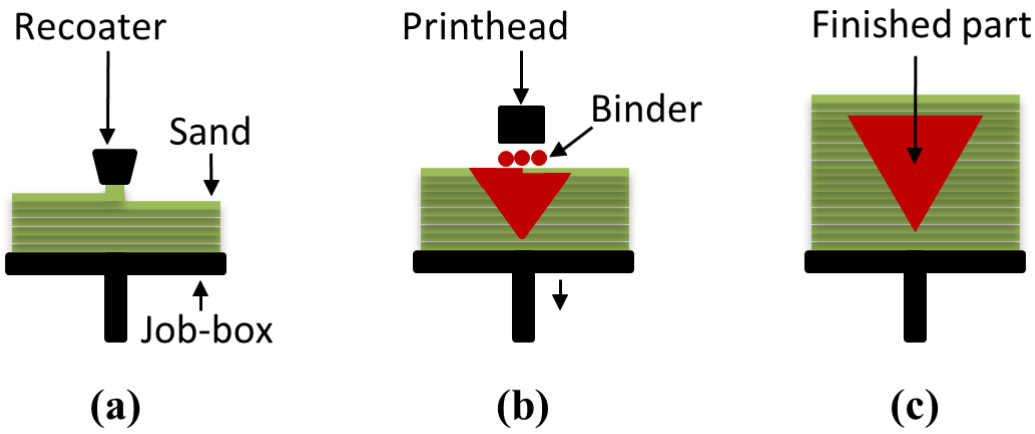


**Figure 3.** Représentation schématique d'une imprimante 3D: (a) abaissement de la plate-forme de construction, stratification avec du matériel et (b) processus d'impression à l'aide d'un liant, (c) pièce finale

Le processus PBJ comprend les étapes suivantes:

1. Le sable est répandu sur la plate-forme de construction à l'aide d'un rouleau automatisé (« *recoater* » ou système d'injection par couches).
2. Le lit de sable est ensuite appliqué avec une force de compactage à l'aide du « *recoater* ».
3. La buse d'impression injecte l'adhésif liant les liquides au sommet du lit de sable, dans la direction X et Y.
4. Liaison des grains de sable en assurant la cohésion lors du séchage et du vieillissement .
5. La plate-forme de construction est abaissée en fonction de l'épaisseur de couche requise dans la direction Z.
6. L'objet est formé lorsque la poudre de sable est liée au liant liquide.
7. Le sable non lié reste dans une position entourant l'objet imprimé.
8. L'ensemble du processus est répété jusqu'à ce que l'objet requis soit imprimé.

# 3. Expériences de laboratoire

Dans ce chapitre, trois séries d'expériences différentes ont été réalisées pour étudier les propriétés fonctionnelles du moule 3DP. Tout d'abord, les bases de la méthode de caractérisation seront présentées avec la procédure de fabrication du moule 3DP. La conception des expériences sera également présentée dans le but de déterminer les propriétés (mécanique et transport de masse) d'un moule en sable 3DP fabriqué de manière additive dans une plage donnée de paramètres de processus d'impression.

## 3.1. Expériences 1 :

L'objectif du présent travail est d'étudier les effets des paramètres de vieillissement, c'est-à-dire le temps et la température de vieillissement, sur la résistance et la perméabilité des moules en sable 3DP. Pour ce faire, les mécanismes de vieillissement ont été étudiés expérimentalement en utilisant un ensemble d'échantillons 3DP à prise chimique du matériau utilisé dans les applications de moulage. L'évolution de la perméabilité et de la résistance à la flexion en trois points des échantillons a été suivie dans le temps et mise en relation avec la quantité de liant présente dans le moule 3DP. La quantité de liant a été caractérisée par des expériences du type « Loss on Ignition (LOI) », la résistance mécanique a été mesurée par des tests de flexion standard à 3 points (3PB) et la perméabilité a été déterminée en mesurant le débit d'air à travers les échantillons à une pression donnée. Les résultats expérimentaux ont élargi notre compréhension de la physique régissant le vieillissement des moules en sable 3DP et fourni des critères rigoureux pour le choix des paramètres de vieillissement.

### 3.1.1 Méthodes expérimentales

Les éprouvettes ont été imprimées dans une chambre avec conditions ambiantes étaient normales, à une température de 25 ± 1 °C et à une humidité relative de 40 ± 10 %. 6 ensembles d'échantillons « *job boxes* » ont été imprimés. Les paramètres de processus ont été maintenus constants pour l'impression de toutes les *job box*. Un total de 453 échantillons ont été imprimés: 324 bars de section carrée (172 x 22,4 x 22,4 $mm^3$) pour les essais de résistance 3PB, 126 éprouvettes cylindriques (diamètre = 50 mm, hauteur = 50 mm) pour les essais de perméabilité aux gaz et 3 éprouvettes cubiques pour LOI tests. Pour obtenir l'erreur type de la moyenne, 3 échantillons ont été utilisés à chaque fois pour l'essai 3PB et 1 échantillon cylindrique a été mesuré 3 fois pour l'essai de perméabilité. Les spécimens imprimés pour le test 3PB et les tests de perméabilité ont également été utilisés pour l'expérience de perte de

masse et pour le calcul de la porosité des spécimens. Certains de ces échantillons sont représentés sur la Fig. 4. La résistance et la perméabilité initiales de 3PB des échantillons de 3DP ont été mesurées après l'impression des échantillons, obtenant 1,75 ± 0,5 MPa et 60 ± 7 GP, respectivement.

**Figure 4.** Spécimens imprimés en 3D pour des expériences

### 3.1.2 Résultats

Les résultats en termes de perte de masse en fonction du temps de vieillissement sont présentés à la Fig. 5. On peut observer que, comme prévu, la perte de poids totale après vieillissement était inférieure pour 25 °C et 100 °C par rapport à 200 °C. Il a également été observé que la vitesse d'évaporation augmentait avec les temps de vieillissement à 200 °C. La perte de poids à 200 °C était plus importante après 36 heures, en raison de l'évaporation d'alcool et d'eau.

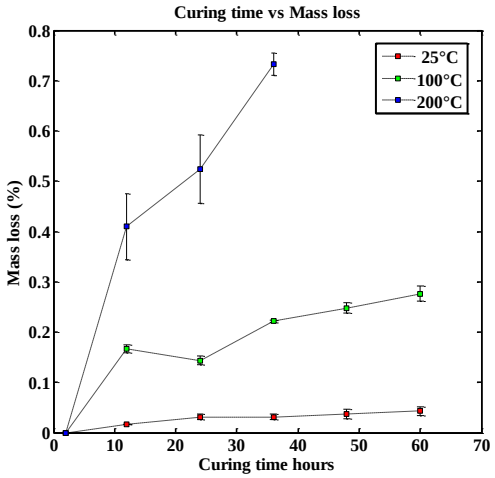


**Figure 5.** Effet critique du temps de vieillissement et de la température sur la perte de masse des échantillons

La résistance 3PB des échantillons est présentée à la figure 6 en fonction du temps de vieillissement pour les trois températures de vieillissement. On peut déduire de cette figure que la résistance à la flexion reste à peu près constante dans le temps dans le cas du

vieillissement à 25 °C et à 100 °C, mis à part une augmentation initiale de la résistance. Cependant, une tendance différente a été observée lors du vieillissement à 200 °C. Les valeurs de perméabilité des échantillons de moule mesurées à différents temps de vieillissement sont présentées à la figure 6 pour les trois températures étudiées. D'après cette figure, les résultats ont montré que la perméabilité restait à peu près constante dans le temps dans le cas d'un vieillissement à 25 °C et à 100 °C. Cependant, une diminution de la perméabilité dans le temps a été observée lors du vieillissement à 200 °C.

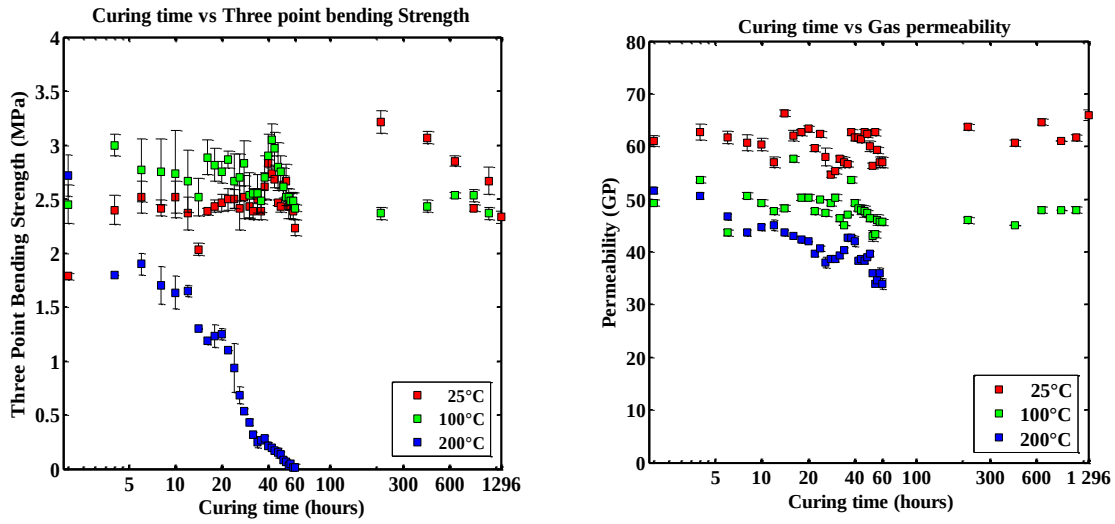


**Figure 6.** Effet critique du temps de vieillissement et de la température sur le 3PB et la perméabilité des échantillons

Les résultats en termes de perte de masse en fonction de la résistance 3PB et de la perméabilité, ont été présentés aux Fig. 7. Le solvant présent dans le liant est volatil et s'évapore au cours du processus de vieillissement, ce qui entraîne un raccourcissement et un vieillissement des ponts de résine. Seule l'eau présente une évaporation significative avec le temps à 25 °C. De plus, l'eau s'évapore plus rapidement à 100 °C qu'à 25 °C (la température d'ébullition de l'eau est proche de 100 °C dans les conditions expérimentales de nos tests), ce qui a pour conséquence des valeurs plus élevées de perte de masse, comme indiqué dans la figure 5. D'autre part, la température d'ébullition de l'alcool furfurylique est de 180 °C; il s'agit donc du mélange d'eau et d'alcool qui subit une évaporation significative lors du séchage à 200 °C. Le taux d'évaporation plus élevé à 200 °C conduit à des valeurs plus élevées de perte de poids, comme le montre la Fig. 5.

Il a été observé sur la figure 6 que la force de 3PB a connu une augmentation initiale avant de devenir constante avec le temps après ~ 4h pour 25 °C et 100 °C. Cet effet est généralement associé à la libération d'eau au cours des premières étapes du vieillissement lors de la polycondensation, ce qui conduit à une polymérisation réticulée résultant d'une polycondensation exothermique. Cela durcit les ponts de résine entre les grains de sable, procurant une plus grande résistance mécanique (3PB) à l'échantillon 3DP. De plus, le réseau de chaînes de polymères devrait se rompre progressivement à 200 °C, à mesure que l'alcool s'évapore. Il en résulte une résistance plus faible en 3PB des spécimens 3DP, telle que présentée à la Fig. 6.

Par conséquent, une augmentation du temps de vieillissement entraîne une réduction plus volumétrique des ponts en résine furanne, ce qui entraîne un rétrécissement plus important et une réduction de l'espace poreux entre les grains de sable. Cela entraîne à son tour une diminution des valeurs de perméabilité aux gaz, ce qui est cohérent avec les résultats présentés dans la Fig. 6. Par conséquent, au fur et mesure que le liant s'évapore, la taille effective des pores devrait augmenter, ce qui entraînerait des valeurs de perméabilité plus élevées. Cependant, le rétrécissement se produit simultanément, de sorte que les particules de sable devraient également devenir plus serrées lorsqu'elles sont entraînées par le liant restant. En conséquence, la variation de la perméabilité pendant l'évaporation du liant devrait être la combinaison des deux effets. Étant donné que la perte au feu est faible (1,41%), la fraction volumique des pores occupés par le liant devrait être également faible. Par conséquent, le rétrécissement devrait être le mécanisme dominant qui explique la réduction de la perméabilité.

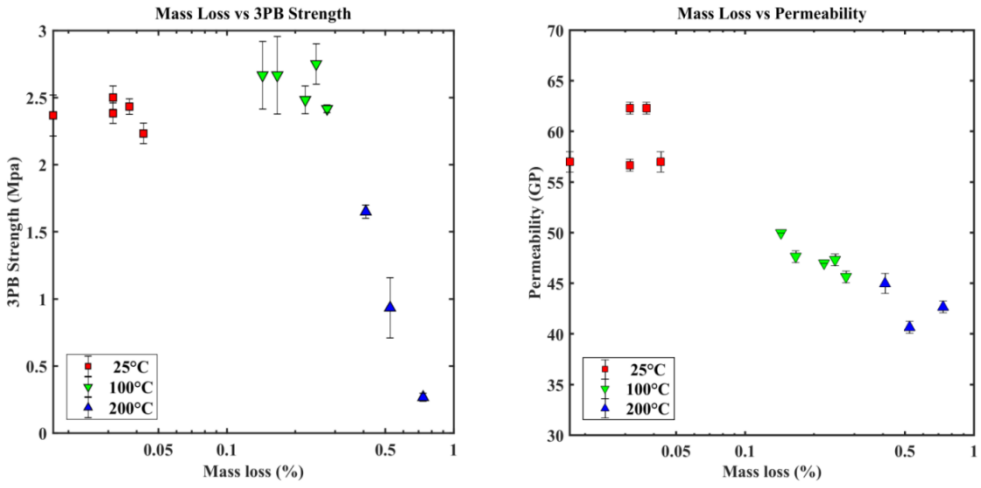


**Figure 7.** Perte de masse Vs 3PB et Permeability

### 3.1.3 Conclusion

Les effets du temps de vieillissement et de la température sur la perméabilité et la résistance 3PB des échantillons de moules en sable 3DP ont été évalués de manière expérimentale. Le processus de vieillissement a montré que la perméabilité et la résistance du 3PB étaient altérées dans certaines conditions. Le vieillissement du liant et le retrait du moule résultant de la réaction de polycondensation du liant, qui est un thermodurcisseur réticulé à haute résistance, peuvent expliquer cette situation. Les implications industrielles suivantes en sont tirées :

- ✓ Les moules imprimés peuvent être conservés à la température ambiante pendant une longue période avant d'être utilisés, en conservant à peu près les valeurs initiales de résistance et de perméabilité 3PB.
- ✓ À partir de la densité apparente et des valeurs de densité de particules du moule 3DP, les grains de sable peuvent être emballés dans une structure cubique simple, obtenant une porosité de 48%.
- ✓ Bien que le volume de liant dans les pores n'ait pas été pris en compte, la prévision fournie par l'équation de Kozeny-Carman était en bon accord avec les mesures expérimentales de perméabilité obtenues avec un perméamètre standard. Ceci s'explique par le fait qu'une faible fraction du volume des pores est occupée par le liant, comme déduit des tests de LOI.
- ✓ La perméabilité de l'éprouvette imprimée en 3D diminue avec l'augmentation de la température, ce qui est potentiellement dû au retrait du moule en sable 3DP.

## 3.2. Expériences 2 :

L'amélioration de la technologie d'impression tridimensionnelle (3D) a permis la fabrication rapide de moules en sable pour la coulée du métal directement à partir de modèles informatiques. Malgré les progrès récents, on ne sait toujours pas comment les caractéristiques microstructurales des sables liés à la résine, qui sont fortement modifiées par la présence de liant, affectent à la fois les propriétés mécaniques et de transport de masse des moules à sable 3D Printed (3DP). L'objectif de ce travail est d'imprimer des moules en sable fonctionnels et d'étudier de manière expérimentale les effets du contenu du liant sur la résistance à la flexion en trois points et la perméabilité des moules à sable 3DP dans différentes conditions de vieillissement.

### 3.1.4 Méthodes expérimentales

Pour ce faire, plusieurs séries d'échantillons ont été produites avec une imprimante 3D utilisant du sable de silice et trois fractions de masse différentes de liant à base de résine furanne. Ces échantillons 3DP ont ensuite été durcis en utilisant de différentes durées et températures de vieillissement. Ensuite, la chute de pression à travers le spécimen 3DP a été mesurée en fonction du débit d'injection afin de déterminer la perméabilité des échantillons et de quantifier les pertes de charge inertielles. En outre, la résistance mécanique des échantillons a été caractérisée à l'aide de mesures classiques de la résistance à la flexion en trois points et des tests LOI ont été réalisés afin de surveiller la perte de masse pendant la phase de vieillissement et d'évaluer ses effets sur la variation des propriétés étudiées.

**Tableau 1.** Paramètres expérimentaux

| Parameters (Unit) | Category 1 | Category 2 | Category 3 |
|---|---|---|---|
| Binder (wt%) | 1.02±0.03 | 1.46±0.02 | 1.98±0.02 |
| Curing time (hours) | 2 and 14 | 2 and 14 | 2 and 14 |
| Curing temperature (°C) | 25, 100 and 200 | 25, 100 and 200 | 25, 100 and 200 |

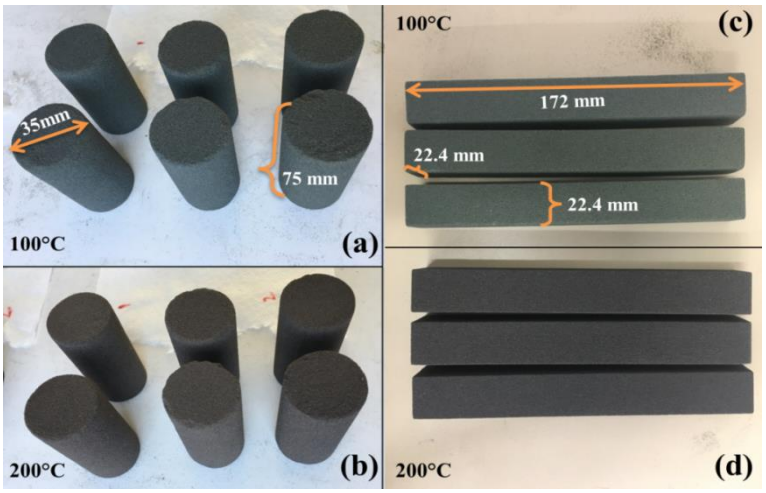


**Figure 8.** Échantillons 3DP traités thermiquement avec un liant à 1,45%, des cylindres (a, b) et des barres (c, d)

### 3.1.5 Résultats

Les pertes de masse au cours du vieillissement, telles que mesurées par les tests LOI, sont représentées en fonction du temps de vieillissement et de la température sur la figure 9 pour les trois valeurs différentes du taux de liant initial. Il est à noter que la perte de masse de liant par évaporation était négligeable à la température ambiante de 25 °C, même après 14h de

vieillissement  Cela était prévisible étant donné que les 25 °C sont très inférieurs aux températures d'ébullition de l'eau et des alcools présents dans le liant. En revanche, une diminution significative de la masse de liant est observée pour les trois valeurs initiales de la teneur en liant à la fois à 100 °C et à 200 °C. Cette diminution est plus prononcée dans les deux premières heures de vieillissement.

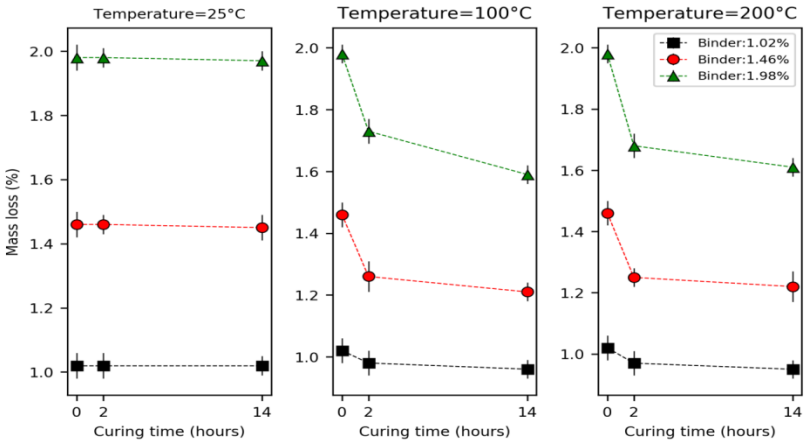


**Figure 9.** Perte de masse en fonction du temps de vieillissement pour trois températures de vieillissement

La figure 10 montre les résultats des tests de résistance 3PB de spécimens de sable 3DP dans des conditions sanas vieillissement et avec vieillissement. Il a été constaté que la résistance de 3PB augmente avec la teneur en liant pour toutes les durées et températures de vieillissement. De plus, la résistance du 3PB augmente lors du vieillissement à 100 °C et diminue quand il est durci à 200 °C pour tous les contenus de liant. Lors du vieillissement à 100 °C, la résistance du 3PB a connu une augmentation de 20% pour le liant à 1,02%, de 16,7% pour le liant à 1,46% et de 28% pour le liant à 1,98%. Cependant, lors du vieillissement à 200 °C, la résistance du 3PB a diminué de 41,6% pour un liant à 1,02%, de 40% pour un liant à 1,46% et de 22% pour un liant à 1,98%. La résistance augmente plus rapidement à 100 °C (polymérisation par traitement thermique) qu'à 25 °C (polymérisation à la température ambiante). Cependant, ce mécanisme de vieillissement et de renforcement du pont de résine a une limite, ce qui conduit à une résistance réduite et à une perte de ductilité, d'où une fissuration pour un chauffage prolongé à 100 °C ou lors d'un chauffage à haute température (200 °C), Fig. 11. Ces résultats facilitent le choix de la teneur optimale en liant, du temps de vieillissement et de la température pour obtenir les valeurs fonctionnelles de la résistance 3PB.

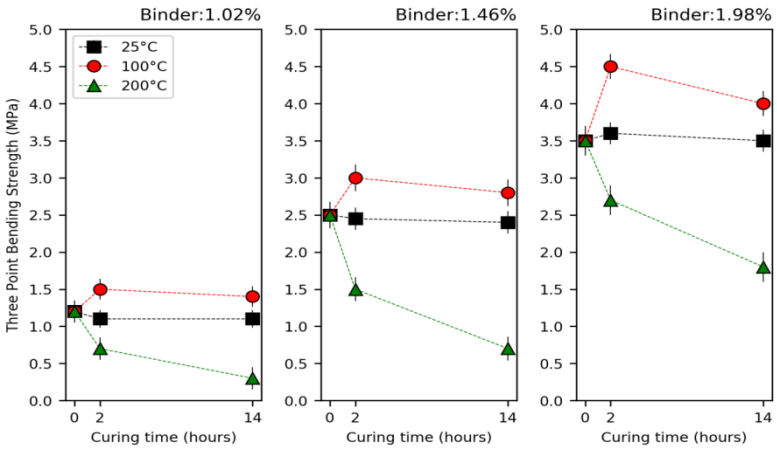


**Figure 10.** Variation de la résistance avec le liant, la température de vieillissement et le temps

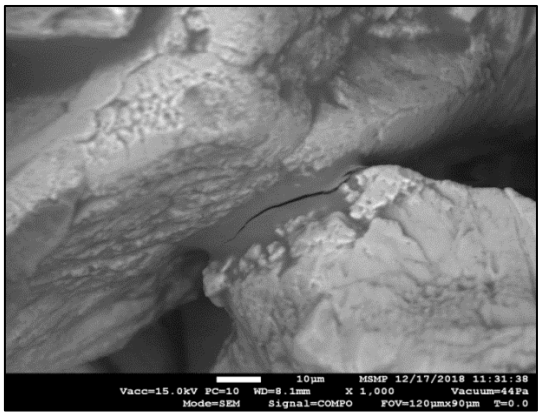


**Figure 11.** Image au MEB d'un spécimen 3DP montrant la fissuration des ponts de résine à 200 °C

On peut également observer sur la figure 12 que la perméabilité des échantillons contenant 1,02% de liant reste à peu près constante tout au long des 14 heures de vieillissement aux trois températures considérées. Cela peut s'expliquer par la minceur de la couche liquide entre les grains de sable qui ne produit qu'une très faible réduction de la perméabilité. De plus, la réaction de polymérisation (transformation du liant liquide en ponts de résine) devrait se terminer plus tôt que pour des quantités plus élevées de liant, puisque la saturation en liquide est inférieure et les effets de l'évaporation d'alcool et d'eau restante sont minimaux. Un effet plus important de l'évaporation sur la perméabilité est observé à des teneurs en liant de 1,46% et 1,98%, ce qui est potentiellement dû à la quantité plus élevée d'alcool restant et au flux d'air bloquant l'eau à travers les pores. De plus, une diminution de la perméabilité est observée après 14h de vieillissement  ce qui pourrait s'expliquer par l'effet de retrait produit par la

combustion des ponts de résine. La perméabilité atteint son maximum dans le cas de l'échantillon avec le plus fort taux de liant traité thermiquement à 100 °C pendant 2h.

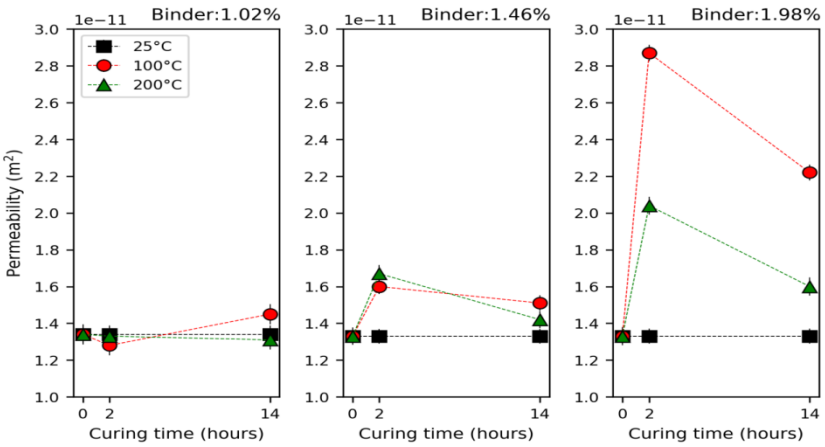


**Figure 12.** Variation de la perméabilité avec le taux de liant, la température et le temps de vieillissement

### 3.1.6 Conclusion

- ✓ Content La teneur en liant a une influence profonde sur la résistance 3PB des moules en sable 3DP. Des quantités plus élevées de liant entraînent une augmentation des résistances mécaniques. Des températures et des temps de vieillissement modérés (100 ºC, 2h) sont recommandés afin d'optimiser le 3PB (éviter la dégradation des ponts de résine, les dégagements gazeux excessifs et les criques à chaud).
- ✓ Les mesures de perte de masse effectuées lors des tests LOI permettent d'évaluer les taux d'évaporation des liquides, qui peuvent ensuite être utilisés dans l'analyse des mécanismes physiques régissant les modifications de la perméabilité et de la résistance à la flexion au cours de la phase de vieillissement.
- ✓ L'effet du taux de liant sur la perméabilité n'est pas significatif lors du vieillissement à la température ambiante (25 ºC). Cependant, l'évaporation du liquide et le retrait du liant affectent de manière significative la perméabilité. La perméabilité maximale est atteinte dans les mêmes conditions que la résistance à la flexion optimale.
- ✓ La porosité des moules en sable 3DP est très élevée, ce qui entraîne des écoulements inertiels à des valeurs de débit d'air modérés. Par conséquent, les mesures de perméabilité doivent être effectuées à des débits d'injection suffisamment faibles pour obtenir un écoulement rampant.

# 4. Expériences de Microtomographie 3D

Dans ce chapitre, la micro-tomodensitométrie à rayons X (µ-CT), une technique non destructive et non intrusive, a été utilisée pour étudier la structure tridimensionnelle (3D) de matériaux en imaginant des échantillons représentatifs. Les images µ-CT permettent d'extraire des formes et des structures 3D utilisées par les modèles pour estimer avec une bonne précision la perméabilité aux gaz d'échantillons de moules en sable. Des expériences numériques approfondies ont été effectuées et nous avons comparé les résultats à d'autres techniques de laboratoire et à des données théoriques.

Ce chapitre traite du contexte théorique et de la mise en œuvre de deux méthodes de modélisation : la méthode de Lattice-Boltzmann (LBM) pour la simulation de l'écoulement monophasique du gaz et une modélisation du réseau de pores pour la distribution de la taille des pores et des constrictions. La méthode Lattice Boltzmann (LBM) est considérée comme la méthode la plus largement utilisée pouvant s'appliquer à toute géométrie poreuse complexe sans la simplifier. Les modèles de réseau de pores (PNM) sont utilisés pour décrire des structures 3DP poreuses complexes par un réseau de composants géométriques simplifiés, appelés corps de pores et constrictions de pores connectées. Le principal résultat de ce chapitre est la démonstration de la faisabilité et de l'applicabilité des approches LBM et PNM pour la prévision de la perméabilité des échantillons de moisissures 3DP.

La caractérisation des propriétés de transport de masse à travers des réseaux de pores à géométrie et connectivité complexes, tels que les moules en sable 3DP, est essentielle pour évaluer les risques de remplissage incomplet et de porosité des gaz dans les moulages. Les caractéristiques microstructurales fondamentales incluent la distribution granulométrique, la distribution granulométrique, la distribution de la taille des constrictions des pores, le rapport entre taille de pore et taille de constriction, la connectivité des pores et la tortuosité. Ces propriétés physiques microscopiques contrôlent les caractéristiques macroscopiques des moules 3DP en termes de perméabilité et de porosité régissant l'écoulement du métal liquide et, plus généralement, le transport de chaleur et de masse dans le moule en sable 3DP. Par conséquent, la connaissance des relations entre les paramètres de processus 3DP et ces caractéristiques microscopiques est d'une importance vitale pour prédire les défauts de coulée.

Le µ-CT 3D à rayons X fournit une représentation précise des structures poreuses, avec une granulométrie détaillée et une distribution de la taille des pores, ce qui permet de modéliser la simulation numérique de l'écoulement de gaz à travers la géométrie. Dans la présente étude, le rayon X-Ray µ-CT a été utilisé pour reconstruire un modèle représentatif virtuel 3D d'un moule en sable imprimé en 3D, afin d'évaluer la perméabilité aux gaz du moule en sable imprimé en 3D à l'aide d'une simulation numérique. Les valeurs de perméabilité obtenues avec la simulation informatique ont ensuite été comparées aux valeurs de perméabilité calculées théoriquement et mesurées expérimentalement.

Le processus de reconstruction peut utiliser des modèles analytiques ou numériques. La norme de référence en tomographie par ordinateur est l'algorithme FDK, qui est une méthode analytique avec une inversion directe dans une configuration en faisceau conique. Les figure 13 présentent les images sur un échantillon 3DP, une projection et une tranche reconstruite.

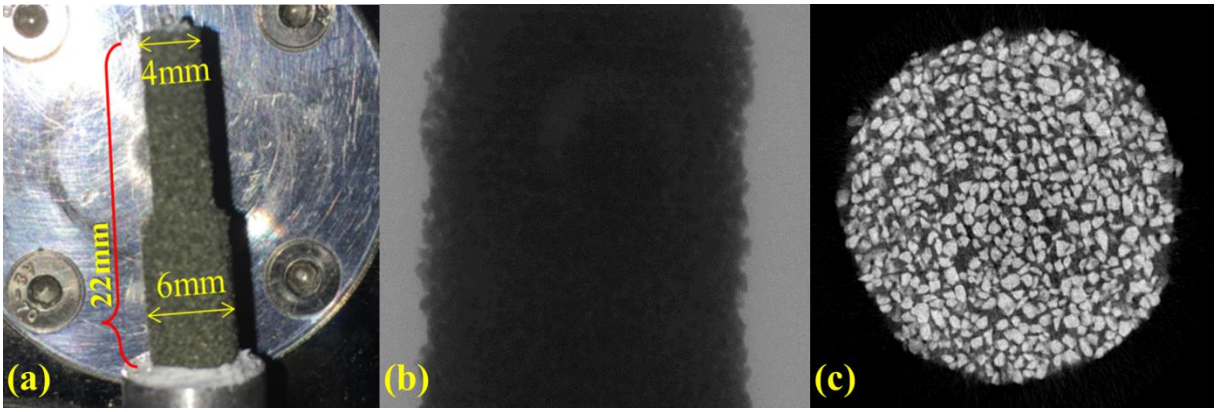


**Figure 13.** (a) Le profil de projection de la radiographie aux rayons X atténuée à travers un échantillon 3DP reçu par le détecteur et (b) les données de pixels reconstruits de l'échantillon 3DP.

**Tableau 2.** Spécimens 3DP utilisés pour l'analyse

| **Échantillon** | **Taux de liant (wt%)** | **Taille de grain moyenne (µm)** |
|---|---|---|
| Petits Grains avec Fort taux de Liant (SGHB) | ~2 | 140 |
| Petits Grains avec Faible taux de Liant (SGLB) | ~1 | 140 |
| Grands Grains avec Fort taux de Liant (BGHB) | ~2 | 190 |
| Grands Grains avec Faible taux de Liant (BGLB) | ~1 | 190 |

### 4.1. Modélisation à l'échelle des grains

Il convient de noter que, comme le liant est associé à la phase solide dans les images de tomodensitométrie, l'effet individuel du liant ne peut pas être évalué et, par conséquent, les valeurs de faible taux de liant et de fort taux de liant ont été fusionnées pour l'évaluation (figure 14). Les procédures présentées précédemment ont été appliquées à toutes les images µ-CT segmentées aux rayons X afin d'obtenir la distribution granulométrique et sphérique des particules de silice. Une distribution normale a pu être observée pour la distribution granulométrique. Le diamètre des grains de silice extraits pour les échantillons de petits grains variait de ~ 57 µm à ~ 331 µm, avec une valeur de $d_g$ moyenne de 171,98 µm et les valeurs de $d_g$ extraites pour les échantillons de gros grains étaient comprises entre ~ 61 µm et ~ 409 µm, avec un grain moyen diamètre ($d_g$) de 208,05 µm. Un rapport plus détaillé concernant la granulométrie des échantillons 3DP est fourni dans le Tableau 3, montrant les valeurs pour les teneurs en liant élevé et faible. La distribution de taille des grains a un effet profond sur la perméabilité du moule en sable 3DP. On peut constater que, pour les petits et les gros grains, il existe une distribution similaire des tailles de grains, ce qui permet une bonne perméabilité au moule en sable 3DP fabriqué. En effet, les grains de sable présentant une large gamme de tailles ont un compactage plus élevé conduisant à une densité élevée et une faible perméabilité par rapport à des distributions étroites

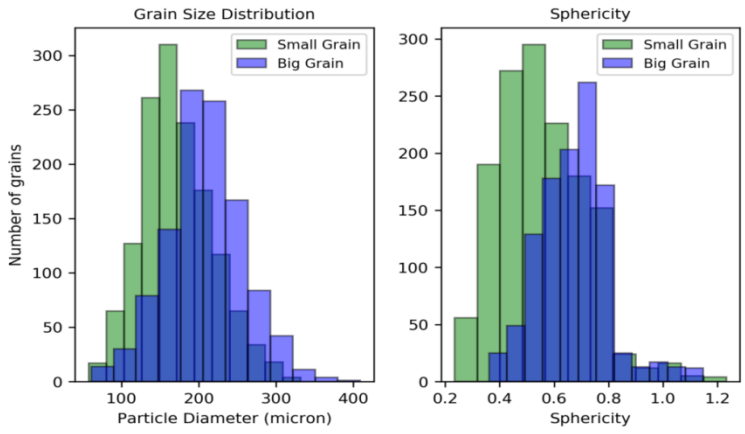


**Figure 14.** Combinaison (a) de la taille des grains pour les petits grains et les gros grains, et (b) la distribution de la sphéricité

En outre, la sphéricité mesurée à partir de l'image µ-CT aux rayons X fournit des informations sur la forme de la particule, qui affecte la densité de tassement du grain, d'où une porosité et une perméabilité variables. Il ne faut pas oublier le fait que des grains de formes différentes

peuvent avoir des valeurs de sphéricité identiques. Les résultats en termes de sphéricité sont répertoriés dans le Tableau 3. Il a été observé que les valeurs de sphéricité des spécimens de taille de grain plus grande étaient supérieures à celles des spécimens de taille de grain réduite. La Fig. 15 présente quelques exemples de grains extraits de spécimens à gros grains. On peut remarquer que les grains sont loin d'être une sphère parfaite, avec une valeur de sphéricité moyenne d'environ 0,6. Comme nous l'avons vu précédemment, la forme peut être arrondie, angulaire, sous-angulaire. Cependant, dans le cas présent, on peut observer que les grains sont essentiellement sous-angulaires. Tous les résultats de la sphéricité des spécimens sont présentés sous forme d'histogramme aux Fig. 14. À partir de la granulométrie obtenue, en utilisant la porosité et le diamètre moyen des grains, la perméabilité des spécimens 3DP a été prédite à l'aide de l'équation de Kozeny-Carman.

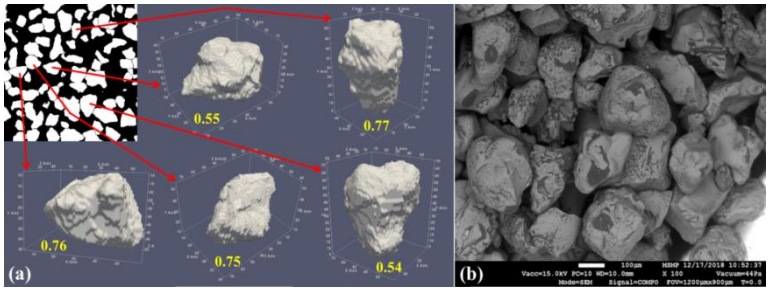


**Figure 15.** (a) Exemples de grains de silice avec un nombre de sphéricité différent dans le spécimen BG. (b) Image au MEB d'un spécimen 3DP montrant les grains de silice

**Tableau 3.** Résultats de l'analyse d'images

| Échantillon | Taille de grain moyenne (µm) | Sphéricité moyenne | Porosité moyenne (%) | Perméabilité ($m^2$) | Perméabilité (Darcy) |
|---|---|---|---|---|---|
| *SGLB* | 154.07 | 0.56 | 50.97 | $6.593 \times 10^{-11}$ | 66.80 |
| *SGHB* | 156.85 | 0.55 | 49.37 | $6.182 \times 10^{-11}$ | 62.63 |
| *BGLB* | 210.11 | 0.66 | 48.48 | $1.003 \times 10^{-10}$ | 101.62 |
| *BGHB* | 207.04 | 0.67 | 49.35 | $1.077 \times 10^{-10}$ | 109.12 |

### 4.2. Modélisation à l'échelle des pores

Dans le présent travail, il a été possible de simuler numériquement l'écoulement monophasique de gaz à travers des échantillons 3DP en utilisant le logiciel open source PALABOS Lattice-Boltzmann Method (LBM) (Parallel Lattice Boltzmann Solver). La géométrie utilisée dans les simulations a été obtenue directement à partir d'un scanner à

rayons X µ-CT. Par conséquent, aucune procédure de maillage compliquée ne doit être effectuée. Il a déjà été étudié et vérifié que la micro-CT (µ-CT) ainsi que le LBM pouvaient être utilisés pour modéliser les phénomènes d'écoulement de fluides à travers des géométries poreuses complexes afin de caractériser leur perméabilité. Dans la simulation numérique PALABOS-LBM, le schéma de réseau D3Q19 est proposé. Le réseau D3Q19 décrit un écoulement de fluide en trois dimensions avec 19 directions possibles du vecteur vitesse, comme Un opérateur de collision standard de Bhatnagar Gross-Krook (BGK) a été appliqué au schéma de réseau D3Q19 avec un gradient de pression constant (P). à travers le milieu poreux et la vitesse initiale dans les interstices a été réglée à zéro. Les valeurs imposées de ∇P étaient suffisamment basses pour assurer un régime d'écoulement rampant (flux de Darcy). Des conditions aux limites antidérapantes ont été appliquées aux parois latérales de la géométrie illustrée à la Fig. 16. La perméabilité (k) a ensuite été calculée sur le système d'unité de réseau non dimensionnel à partir des cartes de pression et de vitesse obtenues à l'aide de l'équation de Darcy traditionnelle :

$$k = \frac{\mu v}{\nabla P}$$

Ici, $\mu$ est la viscosité et $v$ est la vitesse de Darcy (débit total divisé par la surface de la section transversale). La valeur résultante de $k$ en unités de réseau non dimensionnelles a été convertie en unités SI en la multipliant par le carré de la résolution spatiale de l'image µ-CT.

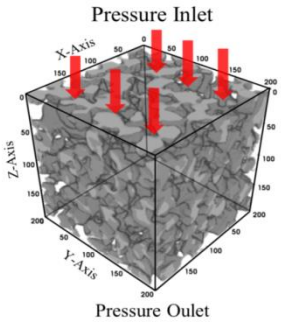


**Figure 16.** Conditions limites pour LBM

Quatre tailles différentes d'élément de volume représentatif (REV) ont été sélectionnées dans l'image binaire recadrée d'origine: 200 × 200 × 200 voxels, 150 × 150 × 150 voxels, 100 × 100 × 100 voxels et 50 × 50 × 50 voxels, comme illustré à la Fig. 17, correspondant respectivement aux volumes 1000 × 1000 × 1000 µm$^3$, 750 × 750 × 750 µm$^3$, 500 × 500 × 500 µm$^3$ et 250 × 250 × 250 µm$^3$. Ces 4 piles segmentées recadrées ont ensuite été utilisées

comme entrées pour la simulation numérique de la mesure de la perméabilité avec PALABOS. L'ensemble du processus a été répété pour tous les cas considérés dans l'étude.

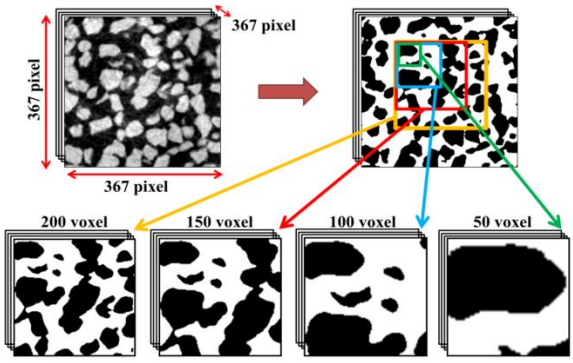


**Figure 17.** Élément de volume représentatif (RVE), pour spécimen BGLB

En effet, sur la figure 18, on peut observer que la valeur de perméabilité pour une image de 50 voxels est inférieure à celle de 100 voxels, de 150 voxels et de 200 empilements d'images de voxels pour tous les échantillons 3DP. Les valeurs de perméabilité approchaient d'une valeur de plateau lorsque la taille du RVE était supérieure à 100 voxels. Par conséquent, il est préconisé d'utiliser un volume d'entrée de 500 µm3, ce qui correspond à la taille de 3 à 4 couches équivalentes (3 × 190 µm ou 4 × 140 µm) de grains de silice pour les échantillons 3DP d'un diamètre moyen de 140 µm et 190 µm. Des tailles d'image plus grandes entraîneraient des temps de simulation plus longs sans amélioration significative de la précision.

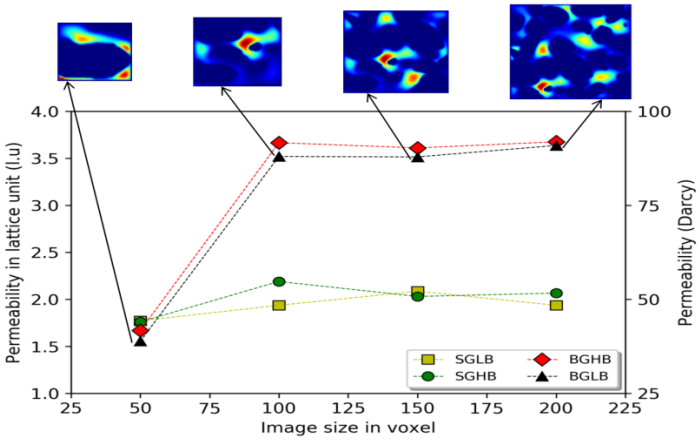


**Figure 18.** Effet du volume de géométrie en entrée sur la valeur de perméabilité calculée

Les résultats calculés de la perméabilité des échantillons 3DP avec PALABOS avec différents échantillons de pourcentage de grain et de liant peuvent être comparés aux résultats analytiques prévus et aux résultats d'analyse d'image. La concordance est bonne entre la

méthode analytique, l'analyse d'image et les résultats expérimentaux pour tous les spécimens 3DP (SGLB, SGHB, BGLB et BGHB). Les calculs de perméabilité obtenus avec PALABOS sont en bon accord avec les mesures expérimentales effectuées avec l'échantillon 3DP, comme indiqué dans le tableau 4.

**Tableau 4.** Résultats pour LBM

| **Taille de l'image (voxel)** | **Porosité (%)** | **Permeabilité ($m^2$)** | **Perméabilité (darcy)** |
|---|---|---|---|
| *Small Grain Low Binder (SGLB)* | | | |
| 50 | 51 | $4.431 \times 10^{-11}$ | 44.89 |
| 100 | 50 | $4.844 \times 10^{-11}$ | 49.08 |
| 150 | 51 | $5.215 \times 10^{-11}$ | 52.84 |
| 200 | 52 | $4.842 \times 10^{-11}$ | 49.06 |
| *Small Grain High Binder (SGHB)* | | | |
| 50 | 49 | $4.403 \times 10^{-11}$ | 44.61 |
| 100 | 51 | $5.475 \times 10^{-11}$ | 55.47 |
| 150 | 50 | $5.077 \times 10^{-11}$ | 51.44 |
| 200 | 53 | $5.166 \times 10^{-11}$ | 52.34 |
| *Big Grain Low Binder (BGLB)* | | | |
| 50 | 49 | $3.889 \times 10^{-11}$ | 39.41 |
| 100 | 51 | $8.801 \times 10^{-11}$ | 89.17 |
| 150 | 49 | $8.788 \times 10^{-11}$ | 89.04 |
| 200 | 52 | $9.092 \times 10^{-11}$ | 92.12 |
| *Big Grain High Binder (BGHB)* | | | |
| 50 | 49 | $4.171 \times 10^{-11}$ | 42.26 |
| 100 | 52 | $9.157 \times 10^{-11}$ | 92.78 |
| 150 | 53 | $9.027 \times 10^{-11}$ | 91.46 |
| 200 | 53 | $9.189 \times 10^{-11}$ | 93.11 |

### 4.3. Modélisation du réseau de pores

Dans cette étude, nous avons utilisé une image reconstruite d'un spécimen de sable 3DP pour extraire leurs réseaux de pores. La porosité de l'image reconstruite est de 49%. La figure 19

donne la comparaison visuelle de l'image reconstruite en 3D et d'une image micro-CT d'un spécimen 3DP.

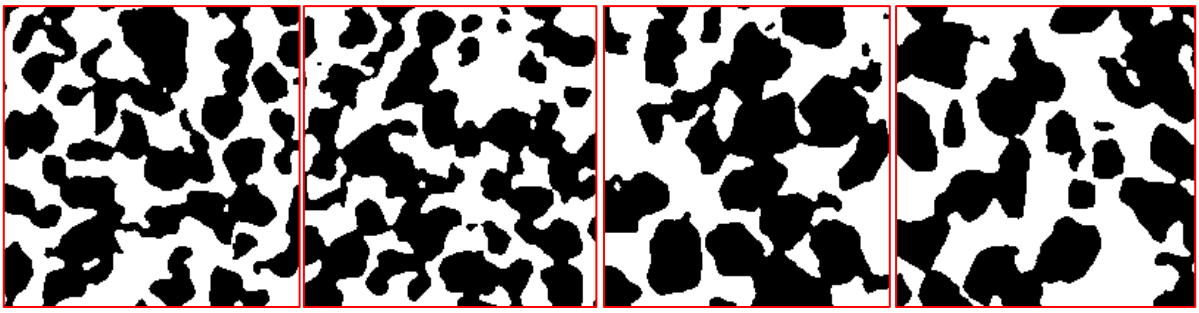

**Figure 19.** Tous les spécimens utilisés pour l'extraction du réseau de pores

Une approche PNM a été suivie afin de caractériser les dimensions des corps de pores et les constrictions des moules 3DP, en utilisant les images affichées à la figure 20 comme entrées.

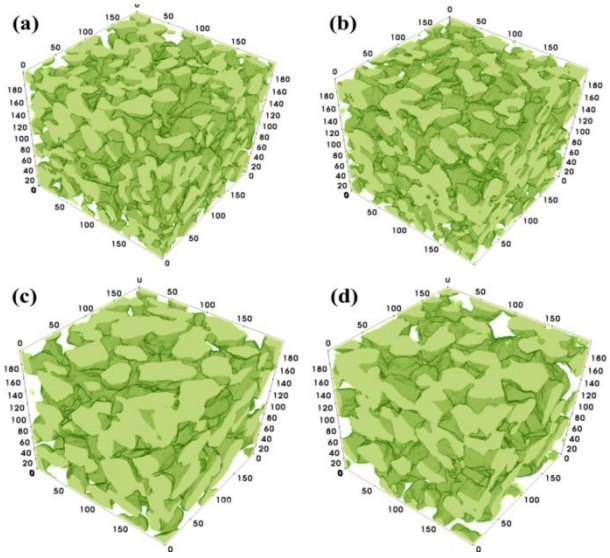


**Figure 20.** Image µ-CT aux rayons X pour tous les échantillons utilisés pour le PNM

La méthode d'extraction du réseau de pores commence par l'utilisation du code GETNET.py qui extrait un réseau de pores conventionnel à partir de l'image µ-CT fournie de la taille 200 du voxel. Il extrait tout d'abord la carte de distance de l'espace des pores (transformée en distance), puis un filtre. a été utilisé sur la carte des distances pour lisser l'image et pour supprimer les selles et les plateaux, en fusionnant les pics trop proches les uns des autres et en affectant le voxel vide aux pores appropriés à l'aide d'un algorithme de gestion des bassins versants basé sur des marqueurs.

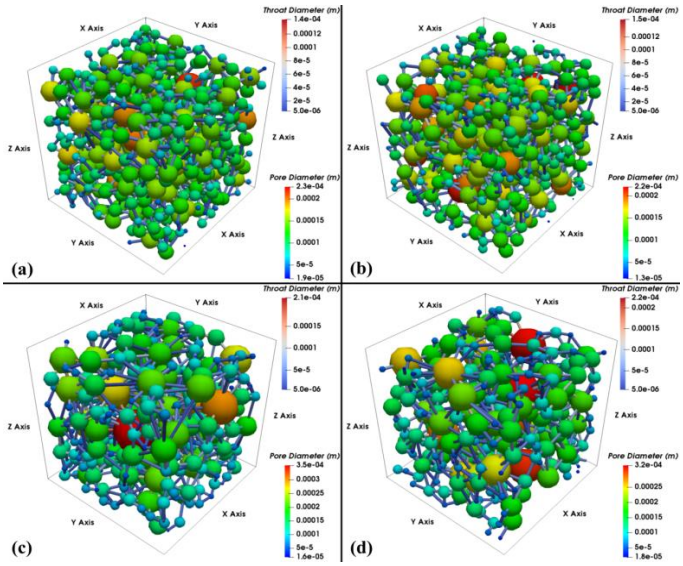


**Figure 21.** Réseau de pores extraits, (a) SGLB, (b) SGHB, (c) BGLB et (d) BGHB

Les distributions de la taille des pores en termes de diamètre des pores ont été extraites du réseau de pores générés (Fig. 21) et sont représentées sous forme d'histogramme, Fig. 22. Le diamètre des pores extraits pour le spécimen SGLB variait de ~ 19 µm à ~ 226 µm. , avec un diamètre de pore moyen de 105,84 µm et le diamètre de pore extrait pour le spécimen de SGHB variait de 14 µm à 220 µm, avec un diamètre de pore moyen de 108,05 µm. De même, le diamètre de pore extrait pour le spécimen de BGLB variait de ~ 16 µm à ~ 350 µm, avec un diamètre de pore moyen de 108,07 µm et le diamètre de pore extrait pour le spécimen de BGHB variait de ~ 18 µm à ~ 320 µm, avec un diamètre de pore moyen de 108,31 µm.

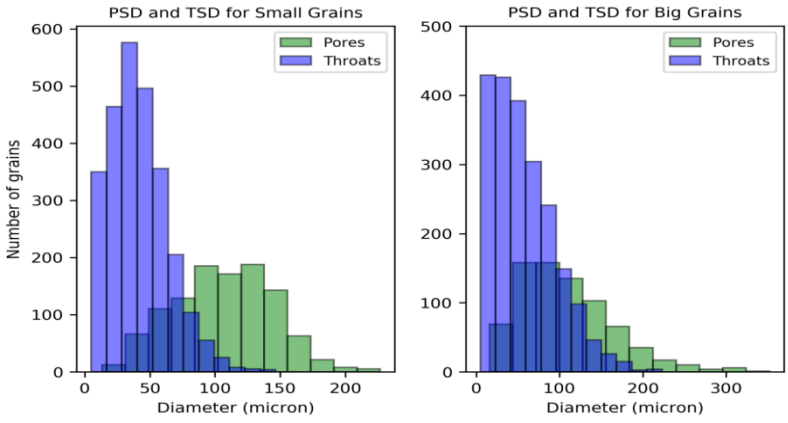


**Figure 22.** Taille des pores et des constrictions (à taux de liant élevé et faible) pour (a) les petits grains et (b) les gros grains

Les distributions de taille des constrictions en diamètre ont également été extraites du réseau de pores généré et ont ensuite été représentées sous la forme d'un histogramme cumulatif avec

le diamètre des constrictions, Fig. 22. Le diamètre de constriction extrait pour un échantillon de SGLB variait d'environ 5 µm. à environ 140 µm, avec un diamètre de constriction moyen de 38,66 µm et le diamètre de constriction extrait pour le spécimen de SGHB variait de ~ 5 µm à ~ 146 µm, avec un diamètre de constriction moyen de 44,43 µm. De même, le diamètre de constriction extrait pour le spécimen de BGLB variait de ~ 5 µm à ~ 214 µm, avec un diamètre de constriction moyen de 56,92 µm et le diamètre de constriction extrait pour le spécimen de BGHB variait de ~ 5 µm à ~ 220 µm, avec un diamètre moyen de constriction de 58,42 µm. Les valeurs de pic apparaissent lorsque la taille des pores est basse indique que la microstructure est complexe et que les détails structurels sont préservés. On peut observer pour les spécimens à gros grains que les constrictions et les pores se chevauchent, ce qui suggère l'existence de petits pores de taille similaire à ceux de la constriction. De plus, la distribution de la taille des constrictions pour tous les spécimens montre une distribution asymétrique à droite, avec une grande partie des petites constrictions (taille de la constriction maximale inférieure à la moyenne), qui construisent des trajets d'écoulement mineurs. À partir du diamètre de constriction équivalent moyen obtenu, la perméabilité a été calculée.

**Tableau 5.** Résultats du PNM

| **Échantillon** | **Taille moyenne de pore (µm)** | **Taille moyenne de constriction (µm)** | **Permeabilité ($m^2$)** | **Permeabilité (Darcy)** |
|---|---|---|---|---|
| *SGLB* | 105.84 | 38.66 | $4.666 \times 10^{-11}$ | 47.27 |
| *SGHB* | 108.05 | 44.43 | $6.168 \times 10^{-11}$ | 62.49 |
| *BGLB* | 108.07 | 56.92 | $1.012 \times 10^{-10}$ | 102.54 |
| *BGHB* | 108.31 | 58.42 | $1.066 \times 10^{-10}$ | 108.01 |

Par conséquent, les approches actuelles de fusion des mesures de perméabilité sur des échantillons de moules en sable 3DP avec extraction directe de la structure des réseaux de pores et de constrictions au moyen de la µ-CT à rayons X ont permis d'explorer et de mieux comprendre la structure des pores et son rôle sur le phénomène de transport de masse. Cela nous a également aidés à développer et à valider des modèles prédictifs plus fiables pour les paramètres de transport de masse, qui sont prometteurs pour effectuer des évaluations précises des risques liés aux contaminants toxiques produits lors du moulage des métaux dans l'industrie de la fonderie.

# 5. Sommaire, conclusions et perspectives

## 5.1. Sommaire

La technique de fabrication additive récemment mise au point, utilisée pour l'impression de moules à sable dans les procédés de moulage par alliage, est presque unique. Les pièces de l'ensemble de moules peuvent être fabriquées en contrôlant avec précision les paramètres du processus d'impression et les matériaux pouvant être produits avec des gaz toxiques dans le moule imprimé. Un moule fonctionnel peut être fabriqué avec la perméabilité aux gaz requise et la résistance requise, et garantit ainsi un taux de réussite élevé en fonderie avec une conception optimisée pour la réduction de poids. Il surmonte de nombreuses limitations de la conception de moules traditionnelle avec un nombre très limité de pièces dans l'assemblage de moules. Il n'a pas été possible de trouver un grand nombre de références dans la littérature traitant spécifiquement cette méthode de production innovante pour la fabrication additive.

Ce travail de doctorat portait sur une étude expérimentale des mécanismes régissant la réponse mécanique et microstructurale du moule 3DP à la variation de différents paramètres du procédé d'impression. Une approche innovante associant tomographie à rayons X et outils avancés d'analyse d'images a été utilisée pour extraire des informations à différentes échelles, notamment à l'échelle micro, c'est-à-dire à l'échelle des grains de sable. L'analyse quantitative du comportement du moule 3DP a fourni un ensemble précieux de données en trois dimensions par rapport auquel des approches théoriques et numériques ont été testées.

## 5.2. Conclusion

En conclusion, ce projet de thèse portait sur la maîtrise de la fabrication additive de moules en sable autour des quatre thèmes:

- ✓ Compréhension technologique des processus additifs avec identification des paramètres du procédé de l'imprimante 3D et des caractéristiques mécaniques des pièces imprimées en 3D.
- ✓ Connaissance du comportement de vieillissement et des propriétés du moule en sable imprimé en 3D.
- ✓ Méthodes de détermination et de caractérisation du moule 3DP en termes de résistance mécanique et de perméabilité.
- ✓ Caractérisation non destructive du moule en sable 3DP à l'aide de la tomographie à rayons X.

L’étude bibliographique a permis de comprendre la technique de fabrication additive, d’identifier les paramètres de contrôle et les variables à aspect qualitatif de leur influence sur la qualité du moule 3DP. Cette étude a montré que les variations des paramètres du procédé d'impression, telles que l'orientation de la construction, la vitesse du système de revêtement et le taux de liant, sont importantes pour la résistance et la perméabilité du moule en sable 3DP. Les premiers tests expérimentaux présentés dans ce travail ont établi les limites et les spécifications des paramètres du procédé d’impression et de l’effet de vieillissement du moule en sable imprimé en 3D.

Les résultats expérimentaux actuels sur la perméabilité et la 3PB concernant ce type de modèles 3DP sont à la pointe de la technologie et non publiés, car il n’y a pas beaucoup d’informations à ce sujet dans la littérature. Pour cette raison, il était essentiel de développer un perméamètre à écoulement de fluide, ce qui permettait de tester un écoulement de fluide unidirectionnel à travers le moule en sable 3DP afin de mesurer les propriétés de transport de masse dans différentes conditions de vieillissement. Celles-ci ont ensuite été étudiées en détail et comparées aux images de tomographie à rayons X afin de comprendre les mécanismes physiques qui régissent la variation de perméabilité pendant la phase de vieillissement des moules en sable 3DP. Les propriétés fonctionnelles du moule 3DP n'ont pas été non plus systématiquement étudiées dans la littérature. Afin d'améliorer la conception du moule fonctionnel et de limiter les défauts de coulée, nous avons répertorié les règles existantes et identifié un manque de connaissances sur l'effet de polymérisation et du pourcentage de liant en 3DP. En outre, une meilleure compréhension des caractéristiques du comportement du moule a été recherchée et des données physiques ont été obtenues à partir d'expériences de laboratoire. À cette fin, les principaux moyens et expériences visant à obtenir les caractéristiques du moule 3DP ont été identifiées. Les règles existantes ont été enrichies à l'aide des résultats expérimentaux obtenus. La continuité du travail a consisté en des itérations successives entre la tomodensitométrie à rayons X et des expériences, permettant de déterminer l’influence des paramètres du procédé sur les propriétés fonctionnelles du moule.

### 5.3. Perspectives

L'influence d'autres paramètres du procédé d'impression existants (type de poudre, taille du grain, vitesse d'impression, contenu de l'activateur, type de liant, épaisseur de la couche d'impression (axe Z), etc.) constitue également un domaine d'application important et doit être étudiée en détail. Il serait intéressant de répéter des tests de modèle similaires avec des moules

3DP avec différents paramètres de processus d'impression, comme expliqué ci-dessus. Les outils de tomodensitométrie utilisés dans cette thèse n'ont pas permis de révéler l'influence du liant sur la cinématique du grain et l'interface pont-résine. Il serait intéressant d'explorer et de comparer le comportement du grain de sable de silice et de l'interface du pont de résine pendant les phases de traction et de compression lors des essais de caractérisation mécanique. Les présentes conclusions représentent un pas en avant vers l'amélioration de la prédiction des propriétés de transport de masse des moules en sable 3DP. Cependant, pour caractériser la convergence du modèle actuel, il convient de procéder à une caractérisation plus poussée de la perméabilité de ces moules en sable fabriqués de manière additive. Pour une prédiction plus précise de la perméabilité, une approche différente pourrait également être envisagée, par exemple l'analyse par tomodensitométrie in situ en noyant de petits échantillons 3DP avec un gaz ayant un coefficient d'atténuation élevé, afin de détecter l'existence de les pores isolées qui ne contribuent pas à l'écoulement de gaz dans l'échantillon.

**Caractérisation expérimentale et numérique des propriétés fonctionnelles des moules sables produits par fabrication additive (procédé d'impression 3D par projection de liant) en fonderie rapid**


**RESUME :**

Les techniques traditionnelles pour la production des moules et des noyaux en sable utilisés en fonderie pour la coulée de métaux sont actuellement en cours de remplacement par des méthodes de fabrication additive, afin d'aider l'industrie aérospatiale/automobile à fabriquer des pièces de forme complexe d'une manière pratique. Le but de ce travail de recherche est d'étudier les propriétés fonctionnelles des moules imprimés en 3D utilisés lors de la coulée des pièces de forme complexe pour des applications d'ingénierie. Premièrement, le comportement mécanique des moules en sables imprimés en 3D a été analysé et caractérisé pour de différents paramètres du processus d'impression. Ensuite, les propriétés mécaniques et de transport de masse des moules en sable 3DP ont été étudiées. Les pièces imprimées en 3D pour la fonderie sont souvent fabriquées avec un type de technologie de fabrication additive appelé « powder-binder-jetting process » (processus de projection de liant de poudre). Des mesures sur trois points de la force de flexion, la densité, la porosité et la perméabilité, ont été effectués sur les moules fabriqués avec la technologie additive. En plus, l'influence de la température et de la fraction volumique du liant sur les propriétés mécaniques et de transport de masse a également été étudiée. Par ailleurs, la perméabilité des moules en sable imprimé a aussi été caractérisée par micro-tomographie de rayons X, permettant la modélisation avancée de la microstructure poreuse en suivant plusieurs étapes : 1) tomodensitométrie de petits échantillons de moules 3DP, 2) reconstruction volumétrique 3D de données, 3) simulation numérique pour la prédiction de la perméabilité à partir de volumes reconstruits et 4) modélisation du réseau de pores pour déterminer la distribution de la taille des pores et des constrictions. Des expériences ont également été conçues pour étudier les moules imprimés en 3D en termes de leur érosion lors de la coulée des métaux. Cela a permis d'identifier les paramètres optimaux du procédé d'impression 3D des moules, non seulement en termes de leurs propriétés mécaniques et de transport de masse, mais aussi pour minimiser l'érosion du moule durant la coulée métallique. Une méthode de détermination de la résistance à l'érosion des moules en sable a également été proposée, sur la base de la mesure du volume de la surface érodée à l'aide d'une technique d'ingénierie inverse moderne.



**Mots clés :** Fonderie; Fabrication additive; Moules sable impression 3D; Coulée métallique; Flexion trois points; Perméabilité; Distribution de tailles de grains; Tomographie par rayons X; Simulations numériques; Distribution de tailles de pores; Modélisation réseau de pores; Mold Erosion; Fonte;


**Experimental and numerical characterization of functional properties of sand molds produced by additive manufacturing (3D printing by binder-jetting) in a fast foundry**


**ABSTRACT :**

Nowadays, traditionally manufactured sand molds and cores for metal casting are being progressively replaced by additively processed sand molds in aerospace/automotive industry, facilitating the production of quality cast parts with complex shapes. The type of additive manufacturing technology used to manufacture 3DP parts in foundries is known as powder-binder-jetting process. In this technology, the molds are produced without the use of any kind of additive tools and in a completely automated way using the layer based construction method. One of the most popular binder systems used in the manufacturing of 3DP mold is a furan-based resin binder, which holds the grain particles together. Their amounts and ratios can influence significantly the 3D printed mold properties, affecting casting quality. Therefore, it is essential to characterize the effects process parameters on the functionality of the 3DP molds. In the present work, the mechanical behavior of 3DP sand molds with varying printing process parameters was first investigated, followed by mass transport properties. To do so, a series of three-point bending strength tests, density measurements, porosity measurements and permeability tests were performed on the 3DP molds. Furthermore, the influence of time, temperature and binder volume fraction on the mechanical and mass transport properties was also investigated. Advanced modelling of the pore space was performed by using the reconstructed images provided by X-ray computed tomography, following different steps: X-ray CT scanning of small 3DP mold specimen, 3D volumetric reconstruction of data, numerical simulations for the prediction of permeability from the reconstructed volume, and pore network modelling for the determination of the pore size distribution. Experiments were also designed to investigate the 3D printed molds in terms of mold erosion during metal casting, in order to select the molding parameters to print 3D printed parts not only with good mechanical and mass transport properties but also to minimize the mold erosion during metal casting. Furthermore, a reverse engineering method for determination of the erosion resistance of sand molds has been established, to study the volume of the eroded surface.



**Keywords** : Additive manufacturing; Binder jetting; 3D-printed casting sand mold; Casting; 3-Point bending strength; Permeability; Pore Size Distribution; Throat Size Distribution; X-ray tomography; Numerical simulations; Pore network modelling; Mold Erosion; Cast iron;

Arts et Métiers Sciences et Technologies

HESAM UNIVERSITÉ